

Cellular and Molecular Mechanisms of Macrophage Fusion

by

Arnat Balabiyev

A Dissertation Presented in Partial Fulfilment  
Of the Requirements for the Degree  
Doctor of Philosophy

Approved April 2021 by the  
Graduate Supervisory Committee:

Tatiana Ugarova, Chair

Robert Roberson

Douglas Chandler

Debra Page Baluch

ARIZONA STATE UNIVERSITY

May 2021

## ABSTRACT

Macrophage fusion resulting multinucleated giant cells (MGCs) formation is associated with numerous chronic inflammatory diseases including the foreign body reaction to implanted biomaterials. Despite long-standing predictions, there have been attempts to use live-cell imaging to investigate the morphological features initiating macrophage fusion because macrophages do not fuse on clean glass required for most imaging techniques. Consequently, the mechanisms of macrophage fusion remain poorly understood. The goal of this research project was to characterize the early and late stages of macrophage multinucleation using fusogenic optical quality substrate. Live-cell imaging with phase-contrast and lattice-light sheet microscopy revealed that an actin-based protrusion initiates macrophage fusion. WASp-deficient macrophages and macrophages isolated from myeloid cell-specific *Cdc42*<sup>-/-</sup> mice fused at very low rates. In addition, inhibiting the Arp2/3 complex impaired both the formation of podosomes and macrophage fusion.

Analyses of the late stages of macrophage multinucleation on biomaterials implanted into mice revealed novel actin-based zipper-like structures (ZLSs) formed at contact sites between MGCs. The model system that was developed for the induction of ZLSs *in vitro* allowed for the characterization of protein composition using confocal and super-resolution microscopy. Live-cell imaging demonstrated that ZLSs are dynamic formations undergoing continuous assembly and disassembly and that podosomes are precursors of these structures. It was further found that E-cadherin and nectin-2 are involved in ZLS formation by bridging the plasma membranes together.

Macrophage fusion on implanted biomaterials inherently involves their adhesion to the implant surface. While biomaterials rapidly acquire a layer of host proteins, a biological substrate that is required for macrophage fusion is unknown. It was shown that mice with fibrinogen deficiency as well as mice expressing fibrinogen incapable of fibrin polymerization displayed a dramatic reduction of macrophage fusion on biomaterials. Furthermore, these mice were protected from the formation of the dense collagenous capsule enveloping the implant. It was also found that the main cell type responsible for the deposition of collagen in the capsule were mononuclear macrophages but not myofibroblasts. Together, these findings reveal a critical role of the actin cytoskeleton in macrophage fusion and identify potential targets to reduce the drawbacks of macrophage fusion on implanted biomaterials.

## DEDICATION

This dissertation is dedicated to my parents, my wife, my children, and my friends who have supported me throughout the process. I deeply appreciate the support they have provided me.

## ACKNOWLEDGEMENTS

I would like to deeply appreciate my academic advisor Dr. Tatiana Ugarova for her support, guidance and encouragement that she has provided throughout the last five years. I would not be able to complete my projects on time without her since her participation was tremendous. I have learned from Dr. Tatiana Ugarova to plan, conduct, and analyze the experiments. During my difficult times her motivation held me straight and helped me to overcome critical moments in the projects. I also would like to express my appreciation for all collaborators who were interested in my projects and wished to improve them by providing essential tools. They helped me to broaden my skills and significantly contributed to collecting the data. Moreover, I would like to express my gratitude to my committee members, Dr. Robert Roberson, Dr. Douglas Chandler and Dr. Page Baluch for supporting me with their guidance and brilliant ideas in polishing my project.

Furthermore, I am grateful to my lab members, Dr. Nataly Podolnikova, Dr. Valeryi Lishko, and Aibek Mursalimov for sharing their expertise in biochemistry and molecular biology and for involvement in my projects. In addition, I would like to thank Dr. Robert Ros for providing me with an opportunity to collect data on atomic force microscopy and analyzing the acquired data. I also appreciate the assistance from David Lowry for helping me in sample preparation and data acquisition using TEM and SEM. Lastly, I would like to thank my former laboratory partner, Dr. James “Bo” Faust for teaching me confocal microscopy techniques, image analysis and for encouraging me to become a cell biologist.

## TABLE OF CONTENTS

	Page
LIST OF TABLES .....	viii
LIST OF FIGURES .....	ix
CHAPTER	
1 INTRODUCTION .....	1
1.1 The role of cell-cell fusion in biology of eukaryotic organism .....	1
1.1.1 Types of cell-cell fusion .....	1
1.1.2 Cellular and molecular mediators of cell-cell fusion .....	2
1.2 Macrophage fusion and the formation of macrophage-derived multinucleated giant cells .....	7
1.2.1 Physiological role of macrophages .....	8
1.2.2 Multinucleated giant cells/Foreign Body Giant Cells .....	10
1.3 The role of the actin cytoskeleton in cell-cell fusion .....	11
1.4 Macrophage fusion in disease .....	18
1.5 The foreign body reaction to biomaterials.....	20
1.6 Key unanswered questions about the mechanisms of macrophage fusion that has been investigated in this thesis.....	27

CHAPTER	Page
2 AN ACTIN-BASED PROTRUSION ORIGINATING FROM A PODOSOME-ENRICHED REGION INITIATES MACROPHAGE FUSION .....	33
2.1 Abstract .....	33
2.2 Introduction .....	34
2.3 Results.....	37
2.4 Discussion.....	54
2.5 Materials and methods.....	61
2.6 Acknowledgement.....	66
3 TRANSITION OF PODOSOMES INTO ZIPPER-LIKE STRUCTURES IN MACROPHAGE-DERIVED MULTINUCLEATED GIANT CELLS.....	67
3.1 Abstract.....	67
3.2 Introduction.....	68
3.3 Results.....	71
3.4 Discussion.....	91
3.5 Materials and methods.....	101
3.6 Acknowledgment.....	108
4 FIBRIN POLYMER ON THE SURFACE OF BIOMATERIAL IMPLANTS DRIVES THE FOREIGN BODY REACTION.....	109
4.1 Abstract.....	109
4.2 Introduction.....	110

CHAPTER	Page
4.3 Results.....	113
4.4 Discussion.....	133
4.5 Materials and methods.....	140
4.6 Acknowledgement.....	148
5 CONCLUSION AND OUTLOOK.....	149
REFERENCES.....	155
APPENDIX	178
A. CHAPTER 2 SUPPLEMENTAL MATERIAL .....	178
B. CHAPTER 3 SUPPLEMENTAL MATERIAL .....	183
C. CHAPTER 4 SUPPLEMENTAL MATERIAL .....	191



## LIST OF TABLES

Table	Page
1. APPENDIX A: CHAPTER 2: Table 1. Parameters of fusion competent protrusions .....	182
2. APPENDIX A: CHAPTER 2 Table 2. Patterns of macrophage fusion .....	182
3. APPENDIX B: CHAPTER 3 Supplemental Table 1. Viability of macrophages cultured under different conditions .....	184

## LIST OF FIGURES

Figure	Page
1.1 Models of membrane fusion .....	3
1.2 Simplified versions of various types of cell-cell fusion events .....	8
1.3.1 Lamellipodia structure .....	14
1.3.2 Filopodia structure .....	15
1.3.3 Invadopodia structure .....	16
1.3.4 Podosome structure .....	17
1.5 A general concept of the foreign body response to biomaterials .....	26
2.3 Figure 1. Phase-dense protrusions initiate macrophage fusion .....	40
2.3 Figure 2. Quantification of the length of fusion-competent protrusions, fusion time and spreading of fusing macrophages .....	41
2.3 Figure 3. An actin-based protrusion precedes macrophage fusion .....	43
2.3 Figure 4. Mixing macrophages expressing eGFP-LifeAct and mRFP-LifeAct shows asymmetric actin integration .....	46
2.3 Figure 5. Cytochalasin B treatment reduces macrophage fusion.....	47
2.3 Figure 6. WASp is required for macrophage fusion <i>in vitro</i> .....	49

Figure	Page
2.3 Figure 7. Loss of Cdc42 in macrophages results in impaired fusion <i>in vitro</i> ...	51
2.3 Figure 8. Inhibition of actin assembly by CK-636 and CK-548 decreases macrophage fusion and podosome formation .....	52
2.3 Figure 9. Fusion of WASp- and Cdc42-deficient macrophages is severely impaired <i>in vivo</i> .....	53
2.3 Figure 10. Model for macrophage fusion initiated by an actin-based protrusion. .....	57
3.3 Figure 1. Formation of zipper-like structures (ZLSs) in MGCs following biomaterial implantation .....	73
3.3 Figure 2. Kinetics of macrophage fusion and ZLS formation <i>in vitro</i> .....	74
3.3 Figure 3. Three-dimensional pattern of actin distribution in ZLS .....	78
3.3 Figure 4. Podosomes as potential precursors of ZLSs .....	80
3.3 Figure 5. Live-cell imaging of ZLS formation .....	81
3.3 Figure 6. Large globules in the ZLS grow by the addition of podosomes.	82
3.3 Figure 7. Localization of podosome-specific proteins in ZLSs .....	85

Figure	Page
3.3 Figure 8. The role of organizers of actin polymerization in ZLS formation.....	88
3.3 Figure 9. Analyses of junctional proteins within ZLS .....	89
3.3 Figure 10. Analyses of E-cadherin expression in fusing macrophages and its role in ZLS formation .....	90
3.3 Figure 11. Schematic drawing of the organization of actin and associated proteins in a ZLS .....	95
4.3 Figure 1. $Fg^{-/-}$ mice display reduced FBGC formation .....	115
4.3 Figure 2. The lack of granulation tissue around the implants in $Fg^{-/-}$ mice .....	117
4.3 Figure 3. Western blot analysis of proteins deposited on the surface and in the fibrinous capsule of materials implanted in WT mice .....	118
4.3 Figure 4. Precoating the implants with fibrinogen and various fibrin(ogen) species rescues macrophage fusion on materials implanted in $Fg^{-/-}$ mice .....	121
4.3 Figure 5. Thrombin inhibitor reduces macrophage fusion but does not affect the capsule formation .....	123

Figure	Page
4.3 Figure 6. The formation of FBGCs and not the production of granulation tissue is compromised in Fib <sup>AEK</sup> mice .....	125
4.3 Figure 7. Distribution of fibrinogen and fibrin in the capsule formed on the surface of implants in WT and Fib <sup>AEK</sup> mice .....	128
4.3 Figure 8. Deposition of collagen in the capsule formed on the surface of implants in WT and Fib <sup>AEK</sup> mice .....	130
4.3 Figure 9. Macrophages within the fibrous capsule express $\alpha$ SMA and CD68 .....	131
4.3 Figure 10. Macrophages within the fibrous capsule express collagen ....	132
Appendix A: Supplemental Figure 1. Phase-dense protrusions initiating Type 1 fusion.....	179
Appendix A: Supplemental Figure 2: eGFP-LifeAct faithfully reports the distribution of F-actin in TG-elicited macrophages.....	180
Appendix A: Supplemental Figure 3. eGFP-LifeAct puncta in macrophages are podosomes.....	180
Appendix A: Supplemental Figure 4. Distribution of the podosome size in samples of live and fixed macrophages.....	181

Figure	Page
Appendix B: Supplemental Figure 1. Determination of the MGC surface area.....	185
Appendix B: Supplemental Figure 2. Dimensional parameters of ZLSs.....	185
Appendix B: Supplemental Figure 3. Actin puncta in the vicinity of ZLSs are podosomes.....	186
Appendix B: Supplemental Figure 4. Correlation between the ZLS turnover time and ZLS length.....	187
Appendix B: Supplemental Figure 5. Large globules in the ZLS grow by the addition of podosomes.....	188
Appendix B: Supplemental Figure 6. Distribution of Myosin II (A) and SIRP $\alpha$ (B) within the ZLS structures.....	189
Appendix B: Supplemental Figure 7. The kinetics of nectin-2 mRNA expression in fusing macrophages.....	190
Appendix C: Supplemental figure 1. The number of cells in the inflamed peritoneum of WT and Fg <sup>-/-</sup> mice.....	192
Appendix C: Supplemental figure 2. The FBR to implant ed PTFE biomaterials.....	193
Appendix C: Supplemental figure 3. Analyses of multinucleation and the granulation	

Figure	Page
tissue formation of implants precoated with plasma.....	194
Appendix C: Supplemental figure 4. Effect of argatroban on the total number of cells adherent to the surface of PCTFE biomaterials implanted in WT mice.....	195
Appendix C: Supplemental figure 5. The number of cells in lavage obtained from WT and Fib <sup>AEK</sup> mice.....	195
Appendix C: Supplemental figure 6. Western blot analysis of fibrin(ogen) species deposited on the surface and in the capsule formed around PCTFE sections implanted into Fib <sup>AEK</sup> mice.....	196
Appendix C: Supplemental figure 7. Deposition of fibrillin and elastin in the capsule formed around the implants in WT and Fib <sup>AEK</sup> mice.....	197
Appendix C: Supplemental figure 8. Detection of collagen expression in macrophages isolated from the fibrous capsule.....	198
Appendix C: Supplemental figure 9. Macrophages express fibrillin and elastin .....	199

## CHAPTER 1

### INTRODUCTION

#### **1.1 The role of cell-cell fusion in biology of eukaryotic organism**

Cell-cell fusion is the process of physical merging of phospholipid bilayers of two adjacent cells, followed by mixing the cytoplasmic content. The process of cell-cell fusion is essential for variety of eukaryotic organisms because the fusion process is at least involved in the life cycle of many eukaryotes (Radzvilavicius et al., 2016). The difference in the fusion events is based on the composition of the membrane, the proteins involved in regulation, and the condition under they proceed. Although the mechanisms of fusion events have not been elucidated yet, the presence of fusion proteins must present on both or either one of the membranes. The essential feature of fusion proteins is their necessity and sufficiency for the fusion events. In other words, the presence of these fusion proteins is required for the fusion and incorporation of them into non-fusing membranes is sufficient for the progression of fusion. Both features characterize the essence of the fusion proteins (Weber et al., 1998).

##### **1.1.1 Types of cell-cell fusion**

In general, cell-cell fusion diverges into sexual and asexual subtypes. For instance, the mating of the unicellular yeast *Saccharomyces cerevisiae*, the fusion of the egg and sperm in all vertebrates, or the process of fertilization in plants, protists, and invertebrates is a result of the fusion of two cells (Hartwell et al., 1980). Asexual type of fusion events is mechanistically and functionally diverse compared to sexual. This type of fusion is



widely observed among somatic cells. Various physiological aspects of human body rely on the fusion of somatic cells. For example, osteoclast fusion occurs during bone reabsorption, the fusion of myoblasts is required to form muscle tissue, or the fusion of trophoblast cells is essential for the formation of the placenta. Even though the fusion of cells is part of human physiology, they are also a part of some pathological conditions and associated with diseases like tuberculosis, rheumatoid arthritis, and cancer (Anderson et al., 2000).

Cell-cell fusion is additionally classified into homo and heterotypic subdivisions. Sexual cell-cell fusion belongs to heterotypic cell-cell fusion due to differences in fusing cells' phenotypes, whereas asexual cell-cell fusion belonging to somatic cells is mainly homotypic and includes with occasional exceptions when fusing cells are different.

### **1.1.2 Cellular and molecular mediators of cell-cell fusion**

Intracellular cell-cell fusion is highly regulated to avoid spontaneous fusion that otherwise would lead to randomized fusion events. Fusion is mediated by fusion proteins situated on the plasma membrane of fusion competent cells. Although many fusion proteins have been identified the precise mechanisms of cell-cell fusion remain unknown. Fusion proteins vary depending on the type of cells that undergo fusion. However, the basic steps preceding the cell-cell fusion, adhesion on a substrate, the contact of fusion competent cells, and fusion of two phospholipid bilayers are similar for many fusion types. Hemagglutinin HA2 protein subunit of influenza envelope and SNARE protein on intracellular membranes are the best described models of fusion proteins. (Stein, 2009).

HA2 on a viral envelope assembles into a six helical bundle and that is inserted into the host membrane bilayer whereas SNARE form four-helical bundle because of the assembly of proteins from two interacting membranes. Upon integration into the endosomes, the viral fusogens undergo proteolytic cleavage enabling them to be inserted into the host membrane. Further, the inserted viral fusogen undergoes a pH-dependent conformational change that facilitates folding, bringing two membranes close together (Eckert et al., 2001; Hernandez et al., 1996). The canonical SNARE proteins that catalyze the reaction of membrane fusion in vesicles transport is an intracellular example of fusion proteins. They act in complementary manner involving v-SNAREs and t-SNAREs consisting of one and three polypeptide chains correspondingly. The interaction of v-SNAREs and t-SNAREs resulting in pulling the membranes close to each other and squeezing the water molecules mediates the fusion of two membranes (McNew et al., 2000) (Figure 1.1).

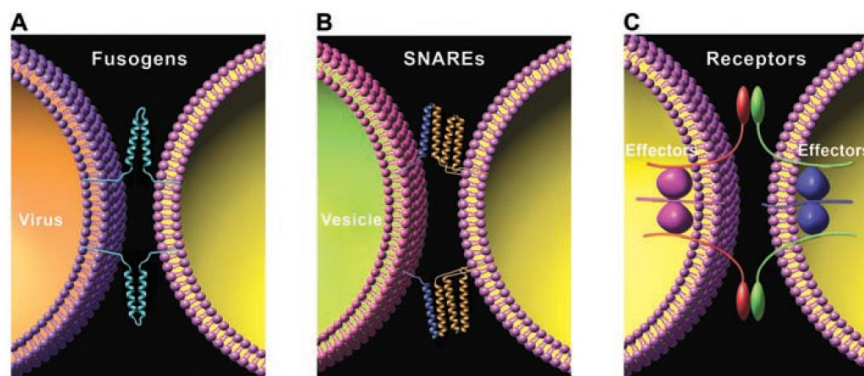


**Figure 1.1 Models of membrane fusion (Chen et al., 2005).**

The fusion of two cell membranes was hypothesized to proceed similarly, using a fusion protein(s). However, it has been shown that most of the fusion proteins do not share

structural similarities with well-studied fusion proteins discovered in viral envelopes and intracellular compartments. Hence, the fusion proteins utilized by different variety of fusing cells might involve distinct ways of fusion. The evolution of fusion proteins might have proceeded parallel to the evolution of organisms and further diverged giving rise to many subtypes, hypothetically resulting in the discrete versions of fusion mechanisms. A brief classification of fusing cells along with potent fusion proteins is provided below.

1. Yeast cell mating is an excellent example of the sexual subtype of fusion. It has been shown that the pheromone-regulated membrane proteins (Prms) display significant importance in the cell-cell fusion process. The structure of Prms lacks hydrophobic fusion peptides and does not resemble any of the viral fusion proteins (Mackay et al., 1974; Bardwell et al., 2005). Presumably, the yeast cell fusion mechanism utilizes different types of mechanisms that are distinct from viral envelope membrane fusion (Figure 1.2).

2. About 30 percent of nematode cells undergo cell-cell fusion and form 44 multinucleated syncytia. This process plays a vital role in the developmental process, where some of the organs are formed due to cell-cell fusion events. Among several candidates for the fusogens responsible for the fusion events, eff-1 (epithelial fusion failure gene) has been identified as the most potent, demonstrating its ability to mediate the fusion events in epithelial cells. Compared to viral fusion proteins, eff-1 contains a different extracellular domain that does not act to penetrate the membrane but only facilitates the proper positioning of the eff-1. Thus, the fusion mechanism is thought to be distinct from

the fusion mechanism utilized by viruses and intracellular vesicles (Podbilewicz et al., 2006) (Figure 1.2).

3. The muscle differentiation, growth and regeneration in *Drosophila* requires myoblast fusion to form multinucleated muscle fibers. The myoblast fusion in *Drosophila* belongs to heterotypic cell-cell fusion, where a founder cell attracts fusion-competent feeder cells for the fusion event. There are two main classes of potent fusion proteins involved in the fusion of myoblasts. The first class corresponds to the Ig-domain containing proteins facing the extracellular side of the cell. Duff and Rst are essential for founder cells, and Sns and Hbs proteins are mostly encoded in fusion-competent cells. The second type of proteins that are involved in myoblast fusion is categorized as intracellular. Specifically, these proteins are involved in signal transduction and are thought to regulate the cytoskeletal rearrangement that facilitates bringing the cell membranes close to each other (Haralalka et al., 2010; Lee et al., 2019). On the contrary, the myoblast fusion in vertebrates occurs with no differentiation to founder and fusion competent cells. Vertebrate myoblasts utilize the Myomaker and Myomerger transmembrane proteins to facilitate the fusion, distinct from what was identified in *Drosophila* (Abmayr et al., 2003; Horsley et al., 2004). It has been shown that the presence of both Myomaker and Myomerger on fibroblast plasma membranes results in fusion (Leikina et al., 2018).

4. Fertilization is the most common and unique type of cell-cell fusion within vertebrates. Before the actual membrane fusion event, the sperm cell penetrated the egg's outer layer to reach the egg cell membrane. Although many potential genes involved in

fertilization have been discovered, only CD9 directly contributes to sperm and egg membrane fusion events. Interestingly, CD9 lacks both hydrophobic and coiled-coiled extracellular domains used by viral fusogens. Hence, it was believed that CD9 is solely essential for organizing multiprotein fusion complex facilitating the fusion process (Kaji et al., 2002) However, further studies demonstrated the role of CD9 to be more associated with microvilli organization (Runge et al., 2007) (Figure 1.2). Another transmembrane protein, Izumol, residing on the sperm acrosomal membrane has been shown to be important for egg and sperm fusion event even though its presence is insufficient for membrane fusion (Inoue et al., 2005).

5. Although the placenta in mammals is only a transient organ formed during fetal development, the trophoblast fusion is essential to formation of placental villi. (Cross et al., 1994). Specifically, trophoblast cells fuse to form the syncytiotrophoblast, a layer of cells that can exceed 10 m<sup>2</sup> surface area and includes ~10 billion nuclei. The cell layer formed as a result of the fusion events separates fetal and maternal blood vessels. Even though trophoblast fusion is observed in almost all placental mammals, not many proteins are identified as fusogens. Syncytin, an endogenous retroviral protein has been identified to have a key role in the fusion. It is a single-pass transmembrane protein that is hypothesized to have evolved from HERV-W envelope due to its highly identical structure. Human and mouse placental cells express homologous syncytin proteins classified as syncytins (1 and 2) and syncytins (A and B), respectively (Blond et al., 1999; Dupressoir et al., 2005). Recently, it has been reported that the fusion of trophoblasts mediated by syncytins occurs by the formation of membrane protrusions morphologically like

podosomes (Wang et al., 2014). The correlation of syncytin location at a specific membrane spots and the growth of membrane protrusions as well as the mechanistic machinery governing the fusion remains unknown (Figure 1.2).

6. Macrophages are another model of cells capable of fusion. There are two distinct types of multinucleated cells originating from the fusion of macrophages: osteoclasts and multinucleated giant cells. Osteoclasts are involved in bone reabsorption during the development and maintenance of the bone tissues. The formation of giant osteoclasts takes place in the presence of macrophage colony stimulating factor and RANKL by the fusion of preosteoclasts derived from the monocyte/macrophage lineage. As for trophoblasts, preosteoclast fusion is mediated by the membrane protrusions. In addition, the fusion of preosteoclasts is facilitated by CD9, dynamin 2, clathrin, AP-2 and Syn1. Cell-cell contact is one of the prerequisites for macrophage fusion and thus several transmembrane proteins have been identified to be involved in the fusion events, such as SIRP $\alpha$  (MFR), CD47, CD44, E-cadherin and others. Recently, we have shown that integrin Mac-1 highly expressed in macrophages was important for the fusion in IL-4 added *in vitro* model. Importantly, we have further shown that SIRP $\alpha$  is a ligand for Mac-1 and may be involved in macrophage fusion. (Anderson et al., 2000; Vignery et al., 2000; Podolnikova et al., 2019) (Figure 1.2). Nevertheless, the fusion machinery complex mediating the macrophage fusion is poorly understood.

## **1.2 Macrophage fusion and the formation of macrophage-derived multinucleated giant cells**

Multinucleated giant cells are unique type of cell that derive from monocyte or macrophage fusion. They are actively involved in bone remodeling and in foreign body reaction. The different subtypes of multinucleated giant cells arise from monocyte/macrophages activated by distinct sets of chemical stimuli. Hence, the physiological role of macrophages and macrophage derived giant cells are interconnected and will be addressed in the next section.

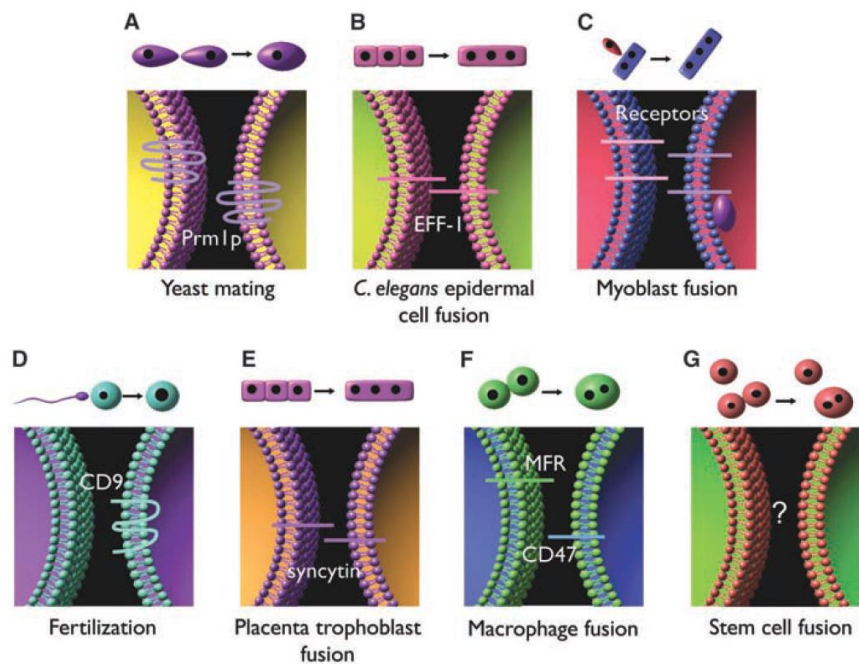


Figure 1.2. Simplified versions of various types of cell-cell fusion events (Chen et al., 2005).

### 1.2.1 Physiological roles of macrophages

Macrophages, monocytes, and dendritic cells belong to the mononuclear phagocyte system (MPS) that is the part of the immune cells with phagocytic ability (Strauss et al., 2015). Upon being derived from bone marrow monoblasts, monocytes enter the bloodstream and circulate up to three days and consequently infiltrate into the surrounding

tissue. Once they reach tissue, monocytes differentiate into macrophages (Hamilton et al., 2008). Even though it was believed that macrophages differentiate only from blood monocytes, new studies have shown differentiation of liver and spleen macrophages from embryonic precursors (Yona et al., 2013).

Macrophages are the immune system's effector cells that both participate in the initial defense by phagocytosis of microorganisms and trigger the adaptive immune system. In addition, macrophages are essential for tissue repair and tissue remodeling processes (Mosser et al., 2008). Depending on the location macrophages reside, they differentiate into peritoneal macrophages, microglial cells in the central nervous system, alveolar macrophages in lungs, histiocytes in connective tissue, and Kupffer cells in liver and osteoclasts in bones. Thus, the anatomical location defines the heterogeneity of macrophage function. The heterogeneity of macrophage function is based on chemical stimuli in the area they reside.

Macrophages possess a distinctive role during inflammation where they may act both as pro-inflammatory and anti-inflammatory cells. It has been demonstrated that type-1 helper T-cell cytokines induce macrophages to become classically activated M1 macrophages promoting inflammation. In contrast, cytokines secreted by type-2 helper T-cell promote alternatively activated M2 macrophages suppressing inflammation by switching to repair and tissue remodeling mode. IFN-gamma and TNF-alpha (tumor necrosis factor-alpha) are the main cytokines in converting macrophages to the M1 phenotype, whereas macrophages differentiate into the M2 phenotype via IL-4 and IL-10



activation (Gordon et al., 2003 and 2005; Yang et al., 2013). Upon differentiation into M1 or M2 phenotypes, macrophages change the gene expression profile and thus start to encode M1 or M2 specific markers. iNOS, SOCS3 and TLR4 are the main markers of M1 whereas Arg-1, Fizz1, MMR and others belong to M2 phenotype markers. In addition, M1 and M2 have distinctive cytokine and chemokine secretion profile (Duluc et al., 2007).

Classifying inflammatory macrophages into M1 and M2 phenotypes has been widely accepted, however, Mosser and Edwards have proposed an alternative strategy to classify macrophages. They proposed to classify macrophages based on their functions rather than markers, such as wound healing, immune regulation, and host defense (Mosser et al., 2008).

Another unique feature of macrophages is the plasticity and ability to polarize. In response to different environmental conditions, macrophages may switch their phenotypic and functional properties. It has been proposed that M1 and M2 macrophages possess the ability to change their phenotypes. Specifically, it has been demonstrated that the same population of pro-inflammatory macrophages (M1) may acquire an anti-inflammatory phenotype at the end of the inflammatory response. It has also been suggested that M2 macrophages may switch to M1 phenotype in the presence of LPS (lipopolysaccharide). These findings demonstrate that M1 and M2 phenotypes are interchangeable (Porcheray et al., 2005; Zheng et al., 2013).

### **1.2.2 Multinucleated Giant Cells/Foreign Body Giant Cells**

Multinucleated giant cells (MGCs) are extensively large cells formed due to monocytes/macrophages' fusion. The number of nuclei within a giant cell can reach over 200, depending on the conditions under which it was formed. Despite the existence of different nomenclature for giant cells, such as multinucleated giant cells, foreign body giant cell (FBGC), multinucleated cells, or even "foam" cell, all of them are derived from the same precursor cells. Giant cells vary morphologically and functionally depending on the chemical environment and thus share features like macrophage plasticity. For instance, osteoclasts are derived from monocytes/macrophages in the presence of CSF-1 (Colony-stimulating factor-1) and RANKL (Receptor activator of nuclear factor kappa-B ligand). In contrast, other multinucleated giant cells can be formed from monocytes, M1, and M2 phenotype macrophages under another set of cytokine combinations (Vignery et al., 2000; Gordon et al., 2005).

### **1.3 The role of the actin cytoskeleton in cell-cell fusion**

Most if not all prerequisite steps preceding macrophage fusion require substantial reorganization of actin microfilaments (Helming and Gordon et al., 2009). Well established actin inhibitors such that cytochalasin B and D have been shown to inhibit cell-cell fusion rate, indicating an essential role of actin in fusion (DeFife et al., 1999). The actin network's importance in macrophage fusion was additionally demonstrated by inhibiting the activity of Rac-1, a small GTP ase involved actin reorganization. Inhibiting Rac-1 resulted in a significant drop in cell-cell fusion events and a drop in the number of nuclei within MGCs. (Jay et al., 2007). It was also shown that the loss of function of main actin regulatory

proteins blocked the pore formation during myoblast fusion in *Drosophila* (Brugnera et al., 2002). It has been hypothesized that actin cytoskeleton contributes to cell-cell fusion by transporting proteins to the site of fusion or being involved in the membrane's stability, forming a scaffold enhancing the membrane interactions between the fusion competent cells (Chen et al., 2005). On the other hand, osteoclast formation from monocytes and myoblast fusion in *Drosophila* was facilitated by forming actin-based membrane protrusions (Shin et al., 2014). Thereby, actin's role is more than transporting the material to the site of fusion or mechanical support as a scaffold at the cell-cell contact sites, but rather the direct protruding force applied to a neighboring cell.

To evaluate the importance of actin cytoskeleton in macrophage fusion, distinguishing between different types of membrane protrusions in actively migrating cells is essential. Several known types of membrane protrusions have been identified in crawling cells, such as lamellipodia, filopodia, and invadopodia. Interestingly, several types of membrane protrusions may coexist at the leading edge of the cell. Most migrative cell types utilize these membrane protrusions since the cell's movement on any substrate requires the plasma membrane's extension to create the leading edge. All three types of membrane protrusions are actively involved in cell migration depending on the cells' environment (Ridley et al., 2011).

The leading edge of migrating cells forms a thin sheet-like structure, the lamellipodium. Previous studies by Abercrombie et al. showed that lamellipodia are made of actin filaments and lack microtubules (Abercrombie et al., 1971). Since then, it has been

established that actin polymerization drives the lamellipodia's growth pushing the membrane forward, thus, creating a protrusion at the plasma membrane. Lamellipodia can extend an extensive distance and can be used for tracking the cell through the extracellular matrix. These structures are highly dynamic and have a short turnover time. Lamellipodia structures are backed up by lamella, more stable structures that have strong adhesive force to a substratum due to presence of adhesive structures on the ventral membrane. Thus, lamella and lamellipodia formation play a key role in the process of cell migration.

The initiation of lamellipodia formation is initiated upon Rac-1 activation and subsequent activation of the WAVE complex. Consequently, the WAVE complex acts as an activator of the Arp2/3 complex responsible for the generation of branched actin filaments. Further extension of branched F-actin is mediated by formins which are activated by Cdc42, another regulatory protein. However, formins can initiate the nucleation of unbranched actin and do not depend on the Arp2/3 complex (Ridley et al., 2011) (Figure 1.3.1).

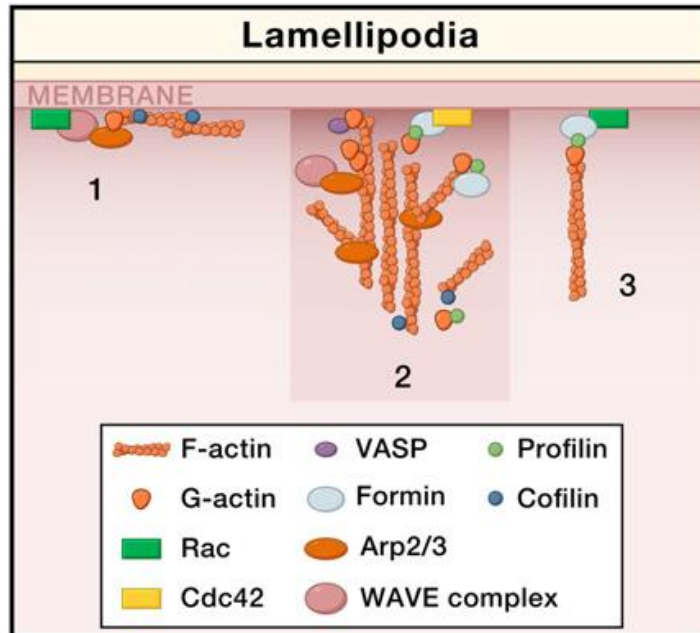
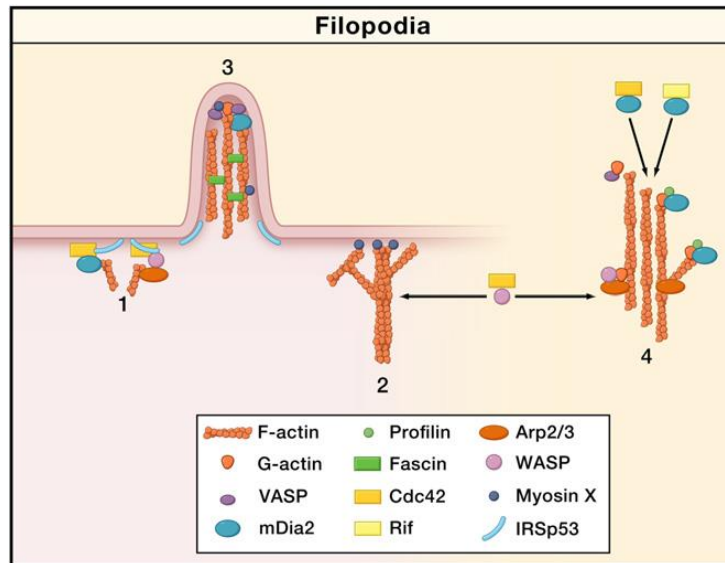


Figure 1.3.1. Lamellipodia structure (Ridley et al., 2011)

The second type of membrane protrusions often seen at the leading edge of migrating cells are filopodia extensions. These extensions are used for exploratory purposes to guide the cells where to grow and elongate. The filopodial structure's size is smaller than that of lamellipodia and invadopodia and utilizes a different combination of actin regulatory proteins. The initial step in filopodia formation is primed by IRSp53 (I-BAR) protein that bends the membrane. Cdc42 and downstream targets mDia2 and WASP/N-WASP further result in F-actin growth (Machesky and Li et al., 2010). The actin bundles' stability is supported by fascin, another distinct feature of filopodia compared to lamellipodia. Additionally, filopodia and lamellipodia can coexist close to each other, where the core of actin filaments is provided directly from lamellipodia (Gupton and Gertler et al., 2007) (Figure 1.3.2).



**Figure 1.3.2. Filopodia structure (Ridley et al., 2011).**

The third type of membrane protrusion, invadopodia, is an actin-based protrusion located at the cell's ventral side and involved in matrix degradation. They were first observed in Rous sarcoma virus-transformed fibroblasts (Chen et al., 1989). The key distinctive feature of invadopodia is the secretion of matrix-degrading metalloproteases and might require microtubules for vesicle delivery (Schoumacher et al., 2010). Additionally, invadopodia share similar actin-regulatory proteins found in aforementioned membrane protrusion types. The dependence of invadopodia on actin polymerization is unarguable since the extensions formed by invadopodia grow three-dimensionally and require force to invade the tissue. The assembly of invadopodia starts from the activation of N-WASP/WASP (in hematopoietic cells) by Cdc42. Upon activation, N-WASP/WASP activates the Arp2/3 complex downstream of the pathway, which initiates the actin nucleation. The elongation of F-actin in invadopodia requires the active involvement of formins and profilin bound G-actin monomers. As in filopodia, F-actin filaments are

bundled by fascin to stabilize the actin core of the protrusion (Machesky and Li et al., 2010) (Figure 1.3.3).

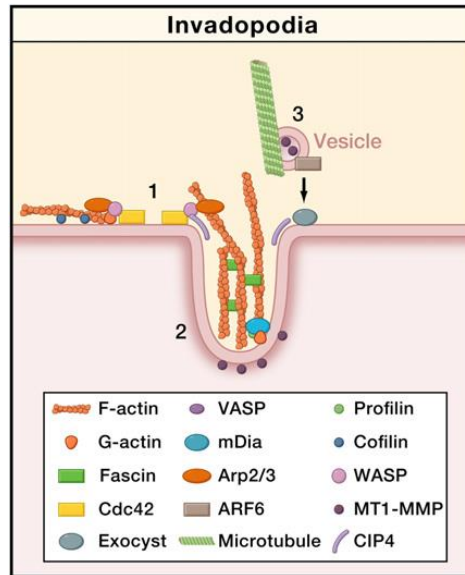


**Figure 1.3.3. Invadopodia structure (Ridley et al., 2011).**

The podosome is a subtype of invadopodia and situated at the ventral side of specific cells derived from monocytes. It consists of the actin core surrounded by proteins such as vinculin, talin, and integrins that form ring structures around the core (Linder et al., 2000; Kaverina et al., 2003). The role of podosomes is to adhere, migrate and secrete different proteases and reactive oxygen species to degrade the extracellular matrix (Linder et al., 2000). During foreign body reactions, the podosome secretions can severely damage the implanted biomaterial (Anderson et al., 2000). It has also been discovered that metastatic cancer cells may acquire podosome-like structures named invadosomes that facilitate the migration through the extracellular matrix to facilitate the metastasis through surrounding tissue (Linder et al., 2000).

Interestingly, the essential regulatory proteins involved in lamellipodia and filopodia formation also participate in podosome formation. All three types of membrane protrusions are scaffolded by nucleation and branching of the actin cytoskeleton at the plasma membrane site. Thereby, the participation of podosome structure in macrophage fusion might be essential (Figure 1.3.4).

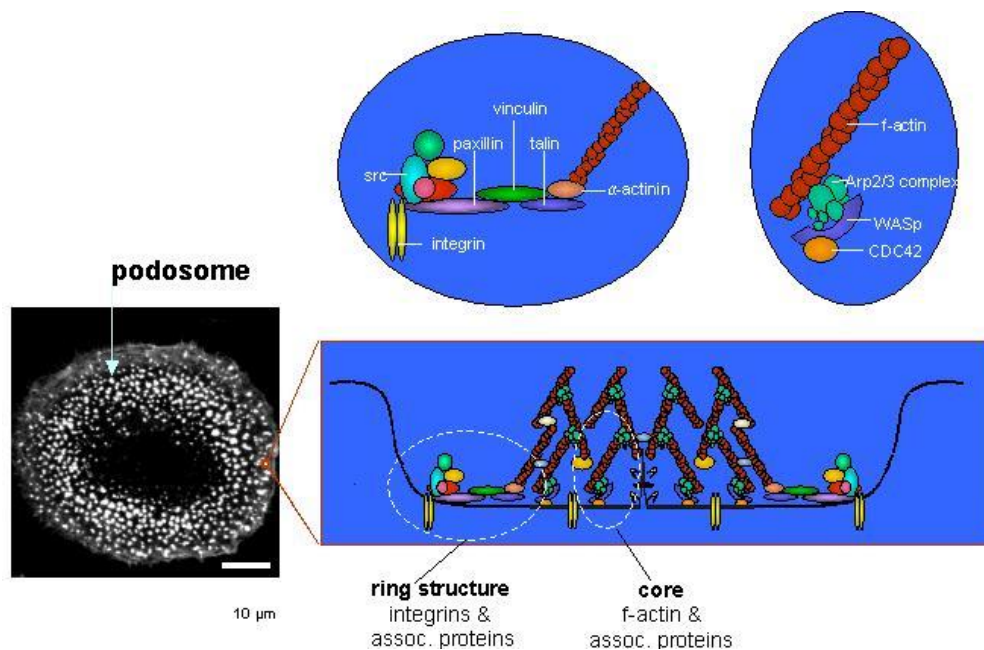


**Figure 1.3.4 Podosome structure (Linder et al., 2000)**

The involvement of actin-based protrusions in cell-cell fusion has been shown in osteoclastogenesis and myoblast fusion in *Drosophila* (Shilagardi et al., 2013; Oikawa et al., 2012). Oikawa and his colleagues have demonstrated that the fusion of macrophages during osteoclast formation is mostly driven by membrane protrusions that emerge from the sealing belt formed by podosome clusters circumventing the cell near the plasma



membrane. In rare events, finger-like extensions facilitated the fusion of RAW264.7 cells and later were named fusopods (Wang et al., 2015). Another actin-based protrusion was revealed during myoblast fusion in *Drosophila*. One or several finger-like protrusions were found at cell-cell contact sites of a founder cell and a fusion-competent myoblast (Abmayr and Pavlath et al., 2012; Aguilar et al., 2013).

#### **1.4 Macrophage fusion in diseases.**

Multinucleated giant cells are often observed as osteoclasts in bone tissues and play important role in reabsorption of bone. However, giant cells are also associated with several distinct pathological conditions.

#### **Multinucleated giant cells in mycobacterium induced granulomas.**

The multinucleated giant cells have always been associated with tuberculous granulomas. *In vitro* model of human tuberculous granuloma showed that mycobacterium virulence strength correlated with the extend of multinucleation of giant cells. Interestingly, although mycobacterium's highly virulent subtype, *M. tuberculosis*, resulted in MGC formation they lacked phagocytic activity and kept high antigen-presenting capability levels. The formation of MGCs with more than 15 nuclei demonstrated the terminal stage of MGC differentiation, thus identifying the stage of granulomatous structures (Lay et al., 2007). The glycolipid content of the mycobacterial cell wall was necessary for the progression of granulomatous infection. Particularly, pro-inflammatory glycolipids were able to induce giant cell formation from granuloma macrophages. Such multinucleation process was driven through Toll-Like Receptor-2, ADAM9, and integrins. Lastly, similar

pathways were upregulated during foreign body giant cell formation on biomaterials (Anderson and Brodbeck et al., 2009).

### **Multinucleated giant cells in atherosclerosis**

Atherosclerosis is a pathological condition when the arteries become narrow due to the accumulation of plaque on the walls. The plaque content is heterogeneous and may contain cholesterol, fat, and calcium, which harden over time. Additionally, the development of calcifying arteries during atherosclerosis involves the macrophages. Specifically, the inner layer of arteries accumulates monocytes that further differentiate into alternatively activated M1 macrophages (Tintut et al., 2002; Shioi et al., 2002). Consequently, M1 macrophages upon ingestion of modified lipoproteins give rise to lipid-rich macrophages or "foam cells" as a result of fusion and further facilitate the lipid core accumulation. It was also shown that M1 macrophages differentiate into M2 macrophages that cause calcification of arteries. It is not clear why M1 macrophages shift into the M2 on artery walls, although suggestions to repolarize M2 to M1 macrophages have already been proposed to prevent the calcification process (Oh et al., 2012)

### **Multinucleated giant cells and cancer**

Cancer progression is driven by many factors where chromosomal instability and genetic mutation accumulation are only a part of them (Yokota et al., 2003). The existence of cancer-cancer cell fusion and the fusion of cancer cells with non-cancer cells have previously been shown. As a result of such fusion events, cancer cells give rise to polyploid giant cancer cells (PGCCs) that acquire additional characteristics with a higher potential

threat to the human body. The fact that cancer cells can gain the potential to fuse with a variety of cell types makes them even more heterogeneous. This heterogeneity facilitates them to become genetically unstable, gain metastatic potential and acquire drug resistance (Lu et al., 2009; Seyfried et al., 2013). Possibly, gaining metastatic ability due to cancer-macrophage fusion may be the worst scenario compared to other additional acquired characteristics. The records show that ~90% of cancer death was due to metastatic consequences (Chaffer et al., 2011). Thus, there are several hypotheses as to how cancer cells gain metastatic phenotype. The first hypothesis suggests that epithelial type cells transition into mesenchymal, thus acquiring enhanced migration capabilities and reduced apoptosis (Kalluri et al., 2003). The second scenario suggests the involvement of macrophages in the transition of non-metastatic cancer cells into metastatic. For instance, tumor-associated macrophages (TAM) significantly contribute to metastasis by creating a pre-metastatic, inflammatory, and angiogenic environment (Hanahan et al., 2012).

Lastly, like TAMs, M1 macrophages trigger tumorigenesis by initiation of inflammatory environment around the tumor. On the other hand, M2 macrophages involved in angiogenesis can fuse with cancer cells (Seyfried et al., 2013). The fusion of M2 macrophages with tumor cells can proceed both by direct fusion and by engulfing the cell, followed by subsequent abortion of cellular digestion, giving rise to a new hybrid polyploid cell (Pawelek et al., 2008).

## **1.5 The foreign body reaction to biomaterials**

### **The fundamental concept of the foreign body reaction.**

Chronic inflammation is well known to be associated with the formation of multinucleated giant cells. In fact, MGCs have been an indicator of chronic inflammation. The triggers of chronic inflammation may be a persistent presence of bacterial, viral, or parasitic infections. Nevertheless, giant cells can also occur even when the exact trigger is unknown, as in rheumatoid arthritis and sarcoidosis (Anderson, 2008). When the immune system detects a non-phagocytosed foreign body, the giant cells are formed on the foreign body's surface from invading macrophages. The foreign body reaction is often observed when an implant is placed into the body. The foreign body giant cells formed on the implants' surface can remain for prolonged periods. Even though foreign body giant cells are often not able to phagocyte the implants, they can severely damage the surface of some types of biomedical polymers (Sheikh et al., 2015).

### **Provisional matrix formation on biomaterial.**

The foreign body reaction is initiated upon the insertion of an implant into the host tissue, preceded by the influx of blood proteins on the implant's surface. Not all, but most of the blood proteins are adsorbed to the surface and act as a substrate for monocyte and neutrophil attachment (Figure 1.5). Less adhesive blood proteins are replaced by more adhesive within the first period of FBR initiation (Williams et al., 2009). The initial provisional matrix formed due to the adsorption of blood-derived proteins to the implant surface has a thickness of ~ 5 nm (Zhang et al., 2013). Subsequently, most fibrinogen molecules are converted into fibrin and create fibrin-dominated provisional matrix (Rivera-Chacon et al., 2013). The cells attached to the provisional matrix interact with the protein

surface, not the biomaterial itself. However, it does not lessen the importance of the biomaterial surface characteristics. Indeed, the surface chemistry of biomaterials dictates the level and constitution of the proteins to be adsorbed. Not all blood proteins share the same level of affinity to a substrate. Albumin is the first abundant protein to be attached to the biomaterial surface but is quickly replaced by fibrinogen, fibronectin, and vitronectin with comparably higher affinity (Vroman et al., 1980). If the amount of albumin and fibrinogen adsorbed on the biomaterial surface is relatively the same as their blood concentration, the adsorption of fibronectin and vitronectin proceeds in an accumulative manner. It has been shown that both vitronectin and fibronectin share great importance in mediating monocyte adhesion to biomaterials via integrins. In addition to these proteins, the monocytes and neutrophils of the provisional matrix releases cytokines and growth factors leading to the attraction of macrophages and other immune cells that directly contribute to FBR progression (Anderson et al., 2001).

The ability of proteins to adsorb on the biomaterial depends on the physicochemical properties of the implant. Several factors can affect the adsorption of proteins. Hydrophobicity of the surface is an essential aspect of protein adsorption. It was shown that a hydrophilic surface adsorbs less protein than a hydrophobic because water molecules quickly form a layer on the polar surfaces, decreasing the proteins' affinity to the implant's surface (Wilson et al., 2005). On the contrary, other studies have shown the importance of surface charge and the protein conformation in addition to the wettability of the implant surface (Vogler et al., 1998; Chinn et al., 2013). Besides, the acidity and the ionic strength of the implant environment influence the protein adsorption level (Ward et al., 1974).

Furthermore, the surface topography and roughness may contribute to protein adsorption. Proteins with the dimensions smaller or larger than the implant surface roughness undergo conformational changes (Hunter et al., 1995; Kyriakides et al., 2004). Lastly, mechanical stress applied to the biomaterial can trigger enhanced FBR. It turns out that stiffer biomaterials with a high elastic modulus compared to surrounding tissue exert stress at the biomaterial-tissue interface that results in enhanced inflammation and fibrous capsule formation (Griendling et al., 2003).

#### **Acute inflammation step.**

The recruitment of monocytes and macrophages to implantation sites occurs upon secretion of cytokines such as TGF- $\beta$ , PDGF, and IL-1 by platelets and degranulated mast cells (Anderson et al., 2008). Subsequently, successfully attached macrophages secrete other cytokines recruiting even larger numbers of macrophages to the site of injury. It is essential to mention that monocytes and neutrophils express different integrin family receptors, enabling them to interact with different blood proteins to form a proper attachment. The fibrinogen component of the provisional matrix undergoing conformational change appears to expose  $\alpha$ M $\beta$ 2 integrin-binding sites for PMN and macrophage adhesion (Sheng et al., 2000; Ugarova et al., 1998). During cell attachment the surface material dictates the signaling pathway to be turned on. Often these changes in signaling trigger the cytoskeletal rearrangements and formation of the main adhesion structure, podosomes. The primary factor impacting acute inflammation is the binding of

PMN (polymorphonuclear leukocytes) and macrophages to the provisional matrix (Williams et al., 2009).

### **Chronic inflammation step.**

Macrophages play an enormous role in triggering FBR. Upon adhesion of monocytes to the implant surface triggered by TGF- $\beta$ , PDGF, platelet Factor 4 (PF4), macrophage chemoattractant protein 1-4 (MCP -1,2,3,4), and macrophage inflammatory proteins, monocytes and macrophages differentiate into pro-inflammatory macrophages. B-1,  $\beta$ -2, and  $\beta$ -3-integrin receptors mediate macrophage adhesion to provisional matrix proteins, fibrinogen, vitronectin, and fibronectin. Hence, during the acute inflammatory period, we observe the prevalence of M1 macrophages on the surface of the bioimplant. Alternatively, activated M1 macrophages secrete various other cytokines, such as IL-1, IL-6, IL-8, and TNF- $\alpha$ . Further, M1 macrophages play a critical role in inflammation by releasing ROS and enzymes and actively attempting to phagocytose the implant material. As inflammation progresses, M1 macrophages differentiate into M2 macrophages triggered by secretion of IL-4 and IL-13 from mast cells and Th2-lymphocytes. M2 macrophages are further activated to become fusion competent and consequently form foreign body giant cells (FBGCs) as a result of repetitive fusion events. Macrophages together with FBGCs, may damage the surface of the material by releasing reactive species, proteases, and acids (Martinez et al., 2014; Tarique et al., 2015) (Figure 1.5). The speed and extend of damage depend on the type of material the implant is made.

### **Foreign body giant cell formation.**

The formation of FBGCs is a distinctive feature of the foreign body reaction that distinguishes it from regular chronic inflammation. FBGCs are characterized as macrophage-derived giant cells consisting of dozens of nuclei and results from the fusion of cells that have been in contact with the implant surface for extended periods of time. FBGCs are also formed due to "frustrated phagocytosis" when macrophages fail to engulf the extensive material and become fusion-competent under the direction of IL-4 and IL-13, thereby avoiding apoptosis

### **Fibrous capsule formation step**

Implanted biomaterials, upon placement into a host are expected to integrate into surrounding tissue, followed by complete regeneration. We observe an alternative scenario when biomaterial implantation is accompanied by chronic inflammation and formation of FBGCs. This scenario often results in formation of collagenous capsule that surrounds the implants from all sides. During the chronic stage of FBR, M2 macrophages and fibroblasts are critical for formation of the capsule due to their release of growth factors necessary for this process (Kanagaraja et al., 1996; Sun et al., 2014). These released factors act as an additional signal to attract more fibroblasts and endothelial cells on the site implantation to secrete more collagen to enhance the granulation tissue formation (Koh et al., 2011).



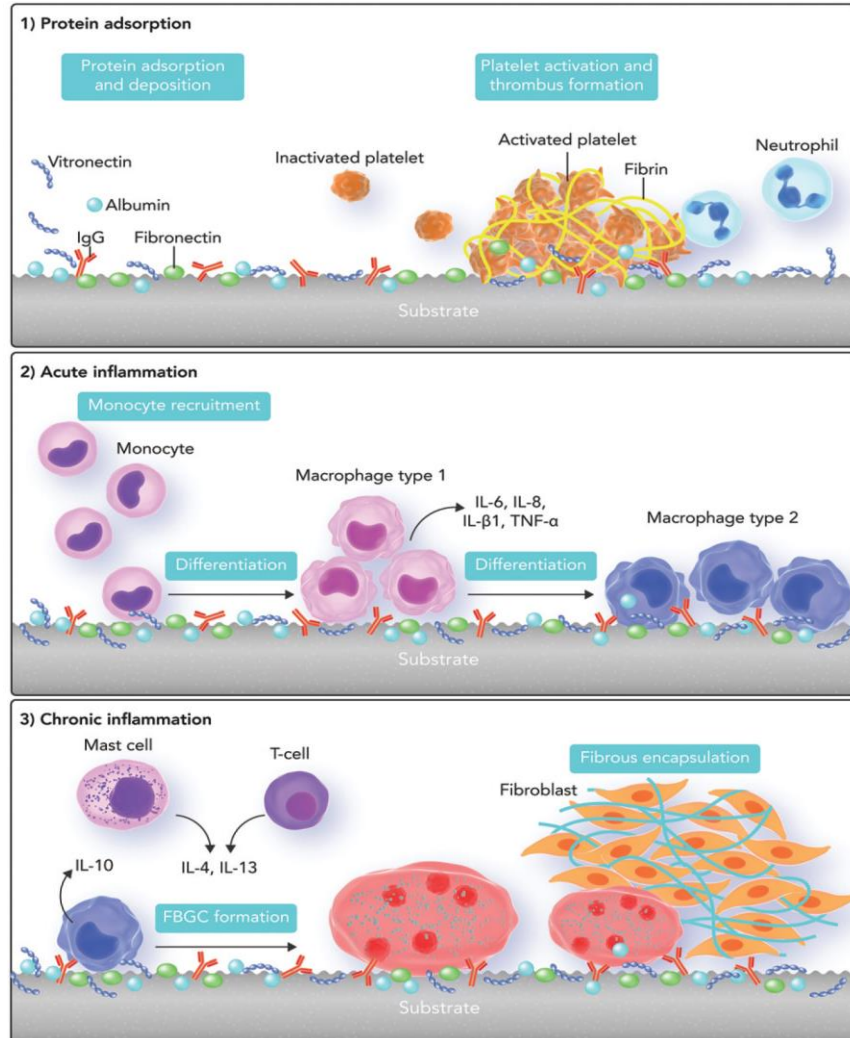


Figure 1.5. A general concept of the foreign body response to biomaterials (Rahmati et al., 2020).

### Drawbacks of Foreign Body Reaction.

Commonly, wound healing processes conclude with a resolution phase when myofibroblasts are cleared away by apoptosis, the process of neovascularization significantly is slowed down, and the deposited collagen mass is gradually removed by the proteolytic effect of fibrinolytic macrophages (Klopfleisch et al., 2017). However, the foreign body reaction lacks a resolution phase due to the presence of biomaterials, FBGCs,

and chronic inflammation at the injury site. Thus, the persistent presence of FBGCs, a pro-fibrotic condition, and a surrounding collagen capsule can significantly damage the biomaterial and its functionality. Depending on the biomaterial's chemical nature, FBGCs and macrophages in contact with their surface can gradually change the surface topography by secreting ROS, RNS and acids. Furthermore, collagen capsules formed around the biomaterial due to the pro-fibrotic response can block the implant's direct interaction with surrounding tissue, leading to the implant's functional failure in the case of implanted sensors such as to constantly measure the blood glucose level. Finally, fibroblasts differentiated into myofibroblasts by presence of TGF- $\beta$  within the capsule may contract and deform the capsule by applying mechanical stress (Jun et al., 2010; Ramachandran et al., 2012).

### **1.6 Key unanswered questions about the mechanisms of macrophage fusion that have been investigated in this thesis.**

#### **Technical limitations of studying macrophage fusion.**

Although multinucleated giant cells were discovered a long time ago, details of the macrophage fusion mechanism are still unknown. Despite there being candidate fusion proteins for mediating MGC formation, the complete fusion machinery remains elusive. One roadblock in determining the macrophage fusion mechanism has been the difficulty in high resolution imaging of the process in real time. Most of the studies have been performed on fixed samples, and only a few publications have observed the macrophage fusion using live specimens. For example, changes in macrophage morphology and cellular

machinery controlling the fusion *in vitro* have not been observed to date. The hurdle of studying macrophage fusion *in vitro* arises from the lack of a glass surface that can support the fusion. Conventional glass surfaces used for live-cell imaging are not suitable for studying macrophage fusion due to the cells' low fusion index. A well-established Permanox plastic surface used for studying macrophage fusion *in vitro* in the presence of IL-4 can only be used for phase-contrast live-cell imaging (Faust et al., 2017). These lenses were required to obtain sufficient numbers of fusion events for analysis. To visualize the actual macrophage fusion event, low magnification objectives were used since it was difficult to capture the fusion events by high magnification objective lenses. Thereby, the data acquisition from the imaging of live macrophage on permanox surface slides using low numerical aperture objectives became highly limited. In addition, the thickness of permanox plastic slides was not suitable for the use of high numerical aperture objectives. Hence, fusion supporting glass surface was needed for a more detailed study of macrophage fusion.

In this dissertation, I describe the preparation of new glass surface coatings which make possible to image live specimens using confocal and super-resolution microscopy equipped with high numerical aperture objectives, thus providing increased spatial resolution in imaging the fusion event. Recently, we have discovered the way to make the glass surface highly fusogenic. We have revealed that coating the glass surface with a long-chain hydrocarbon layer of organic material that facilitates a five-fold increase in the incidence of macrophage fusion making these events capable of being analyzed. This glass surface coating method enabled us to observe macrophage fusion for the first time with

high spatiotemporal resolution. Indeed, the discovery of the fusogenic glass surface has enabled us to study the distribution of critical regulatory proteins, rearrangement of cytoskeletal elements, and other vital elements involved in macrophage fusion using live-cell imaging as well as imaging of fixed samples.

### **Do cellular protrusions initiate macrophage fusion?**

Cell-cell fusion machinery depends not solely on single or multiple fusogenic proteins located on plasma membrane but also on active participation of actin filaments. Macrophage fusion being a multistage process that start from adhesion to a permissive substrate followed by cytoskeletal rearrangements, cell motility and cell-cell interaction depend on actin cytoskeleton. However, little is known regarding the participation of actin in the fusion machinery in macrophage fusion. Two decades ago, it was shown that cytochalasin B and D, common actin inhibitors, negatively affect the macrophage fusion (DeFife et al., 1999). Moreover, the role of Rac-1, a key regulatory protein in lamellipodia formation, in the attenuation of macrophage fusion, has already been described (Ridley et al., 2011). These studies suggest that the involvement of the actin cytoskeleton in macrophage fusion but prior to the studies reported here, there had been no direct evidence for cytoskeletal reorganization as a contributor to macrophage fusion. In contrast, recent studies on invertebrate and vertebrate myoblasts showed the presence of actin-based “podosome-like structures” membrane protrusions situated at the site of the cell-cell fusion (Sens et al., 2010; Chen et al., 2011). Yet other studies have revealed that most of the fusion events during osteoclastogenesis appear to be facilitated by extensive membrane

protrusions originating from the sealing belt circumventing the cell boundaries (Oikawa et al., 2012; Soe et al., 2015; Wang et al., 2015). However, there has not been any similar membrane protrusion identified during macrophage fusion yet.

In this research project we have identified direct involvement of actin-based membrane protrusions initiating macrophage fusion in the presence of IL-4. Firstly, live-cell imaging analysis by phase-contrast video microscopy showed that ~90% of all fusion events were accompanied by short membrane protrusions. More advanced imaging of live GFP- and RFP-LifeAct macrophages using lattice light-sheet microscopy demonstrated the actin-based composition of the membrane protrusions facilitating the fusion. Inhibition of Arp2/3 complex, a key regulatory protein involved in actin polymerization abrogated the fusion. *In vivo* studies on Cdc42 and WASp-deficient mice also resulted in the decrease of the FBGC formation on implanted biomaterials. Thus, we have discovered that most macrophage fusion events depend on actin-based protrusions, similar to structures identified during myoblast fusion and osteoclastogenesis.

### **What morphological changes do macrophages undergo during the late stages of multinucleation?**

There have always been numerous unanswered questions regarding the morphological changes that macrophages undergo during the late stages of FBR and during *in vitro* studies in the presence of IL-4. It has been stated that FBGCs live on biomaterial surface for a prolonged time avoiding apoptosis (Anderson et al., 2000). Yet the morphological changes that macrophages undergo during prolonged presence of IL-4 in

vitro has not been observed before. However, recent studies on osteoclastogenesis using RAW 264.7 cells activated by RANKL examined the changes podosomal structures undergo during the first 4 days culture *in vitro*. During these studies, podosomes formed ring structures and further arranged into sealing belts circumscribing the plasma membrane. Furthermore, additional actin-based zipper-like structures were identified in late-stage osteoclasts *in vitro* originating from podosome-like structures (Takito et al., 2012 and 2017). Given the involvement of podosome based structures in osteoclast formation, their possible involvement in macrophage fusion became an urgent question for which there was not yet an answer.

Indeed, in this dissertation I document a novel actin-based zipper-like structures (ZLS) originating at the late stage MGC-MGC contact sites on the bioimplant surface. Consequently, zipper-like structures appeared at late stage MGCs formed in the presence of IL-4 *in vitro*. Immunostaining analysis showed the presence of the major podosomal markers whereas live-cell imaging of GFP-LifeAct macrophages further demonstrated high dynamicity of the zipper-like structures assembling and disassembling from the fusion and fission of podosomes. We have also determined the dependence of zippering of the structures on E-cadherin, an adherens junction protein.

### **What is the role of the adhesive proteins deposited on the surface of biomaterials *in vivo* in driving the FBR?**

Upon insertion of bioimplants into the host tissue the surface of the implant is adsorbed by the blood proteins. Among others, fibrinogen, vitronectin and fibrinectin are

the most adhesive blood proteins to be determined on the bioimplant surface. *In vivo* experiments have shown the role of fibrinogen in the adhesion of neutrophils and macrophages to the surface of implanted material. Moreover, several other *in vitro* studies have shown the effect of vitonectin and fibronectin in the fusion of macrophages. Nonetheless, there are no studies that have demonstrated the direct involvement of any of blood proteins in trigerring the foreign body reaction.

Finally, we have discovered that lack of fibrinogen in the provisional matrix at the initial stage of FBR abrogates macrophage fusion and prevents granulation tissue formation, a precursor for encapsulation of the biomaterial. Unexpectedly, the fibrinogen gene mutation failed fibrin formation showed decreased FBGC formation but did not stop granulation tissue formation around implanted biomaterial. Granulation tissue was formed even when fibrin formation was abrogated. Nevertheless, the granulation tissue's physical characteristics were different due to less collagen deposited around the biomaterial. Intriguingly, mononuclear macrophages within granulation tissue turned out to be expressing collagen and fibroblast cells, which was supposed to be the only cell type expressing it. Thus, we revealed a novel role of fibrin polymer within the provisional matrix responsible for MGC formation and fibrous capsule formation during FBR.

## CHAPTER 2

### AN ACTIN-BASED PROTRUSION ORIGINATING FROM A PODOSOME- ENRICHED REGION INITIATES MACROPHAGE FUSION

#### **2.1 Abstract**

Macrophage fusion resulting in the formation of multinucleated giant cells occurs in a variety of chronic inflammatory diseases, yet the mechanism responsible for initiating this process is unknown. Here, we used live cell imaging to show that actin-based protrusions at the leading-edge initiate macrophage fusion. Phase-contrast video microscopy demonstrated that in the majority of events, short protrusions ( $\sim 3 \mu\text{m}$ ) between two closely apposed cells initiated fusion, but occasionally we observed long protrusions ( $\sim 12 \mu\text{m}$ ). Using macrophages isolated from LifeAct mice and imaging with lattice light sheet microscopy, we further found that fusion-competent protrusions formed at sites enriched in podosomes. Inducing fusion in mixed populations of GFP- and mRFP-LifeAct macrophages showed rapid spatial overlap between GFP and RFP signal at the site of fusion. Cytochalasin B strongly reduced fusion and when rare fusion events occurred, protrusions were not observed. Fusion of macrophages deficient in Wiskott-Aldrich syndrome protein and Cdc42, key molecules involved in the formation of actin-based protrusions and podosomes, was also impaired both *in vitro* and *in vivo*. Finally, inhibiting the activity of the Arp2/3 complex decreased fusion and podosome formation. Together these data suggest that an actin-based protrusion formed at the leading edge initiates macrophage fusion.



## 2.2 Introduction

Cell to cell fusion is an essential event in several biological processes such as fertilization, embryonic development, skeletal muscle and placenta formation, bone remodeling, and stem cell differentiation (Aguilar et al., 2013; Podbilewicz, 2014). Furthermore, cell–cell fusion has been observed in a number of pathological conditions. In particular, macrophage fusion resulting in the formation of multinucleated giant cells (MGCs) is associated with numerous chronic inflammatory diseases including granulomatous infection, the foreign body reaction to implanted biomaterials, atherosclerosis, amyotrophic lateral sclerosis, cancer, and others (Anderson et al., 2008; Helming and Gordon, 2008, 2009). MGCs are formed from blood monocytes recruited from the circulation to sites of inflammation where they differentiate into macrophages that undergo fusion as inflammation progresses to the chronic state. The T-helper 2 cytokine interleukin-4 (IL-4) promotes macrophages fusion in vivo (Kao et al., 1995) and when applied in cell culture can be used to study this process (McInnes and Rennick, 1988; McNally and Anderson, 1995). Although this in vitro cell system has proven invaluable to our understanding of the molecular mediators that orchestrate macrophage fusion (McNally and Anderson, 2002; Helming and Gordon, 2007; Jay et al., 2007; Milde et al., 2015), there is little information regarding the morphological changes that macrophages undergo to initiate fusion as well as the cellular mechanisms that govern this process.

MGC formation is thought to be a multistage process involving adhesion of cells to the substrate, the induction of a fusion-competent state, cellular motility, cell–cell

interaction, cytoskeletal rearrangements, and subsequent membrane fusion (Helming and Gordon, 2009). Most, if not all, of the steps involved in macrophage fusion appear to rely on contractile networks formed by the actin cytoskeleton. It has been shown that the fungal toxins cytochalasin B and D, which both prevent actin polymerization, inhibit MGC formation in a concentration-dependent manner (DeFife et al., 1999). The importance of the actin cytoskeleton has been further corroborated by studies indicating that IL-4 activated the Rac-1 signaling pathway (Jay et al., 2007). Rac-1 is known to reorganize actin networks resulting in the formation of membrane ruffles and extension of lamellipodia. Abrogation of Rac-1 activation by chemical and genetic approaches inhibited lamellipodia formation and attenuated MGC formation (Jay et al., 2007).

Several types of plasma membrane protrusions, including lamellipodia, filopodia, and invadosomes can form and coexist at the leading edge of migrating cells (for a review, see Ridley, 2011). The formation of these protrusions is a result of actin polymerization mediated by actin nucleation-promoting factors. The primary mediators of actin polymerization that induce the formation of branched networks in lamellipodia are the members of the Wiscott-Aldrich syndrome protein (WASp) family that activate the Arp2/3 complex (for a review, see Takenawa and Suetsugu, 2007). The Arp2/3 complex and WASp have also been implicated in filopodia formation (Takenawa and Suetsugu, 2007; Lee et al., 2010; Yang and Svitkina, 2011). Recent studies in myoblasts, cells that undergo fusion in arthropods and vertebrates, have revealed many proteins that participate in Arp2/3-mediated actin polymerization and are required for fusion (Chen, 2011; Aguilar et al., 2013). In these cells, Arp2/3-mediated actin polymerization is responsible for the

formation of F-actin-enriched structures protruding from one cell into another cell at the site of fusion (Sens et al., 2010; Haralalka et al., 2011; Shilagardi et al., 2013). The size and the molecular composition of these protrusions (Sens et al., 2010; Chen, 2011) clearly distinguish them from filopodia and lamellipodia (Mattila and Lappalainen, 2008). Based on the presence of an actin core with a surrounding ring of adhesive proteins and their protrusive nature, the protrusions in fusing myoblasts have been called “podosome-like structures” (PLS) (Onel and Renkawitz-Pohl, 2009; Sens et al., 2010). Podosomes and related structures invadopodia, collectively known as invadosomes, are ventral protrusions that form contacts with the extracellular matrix that have been identified in a variety of cell types (Linder et al., 2011; Murphy and Courtneidge, 2011). Podosomes are especially prominent in cells of the monocytic lineage, including macrophages and dendritic cells, where they have been associated with cell adhesion, migration, and matrix degradation. A defining feature of podosomes is a core of actin filaments nucleated by Arp2/3 complex (Linder et al., 2000; Kaverina et al., 2003) surrounded by adhesive plaque proteins such as talin, vinculin, integrins, and others (Zamboni-Zallone et al., 1989; Pfaff and Jurdic, 2001). In addition to activators of Arp2/3 complex, the endocytic protein dynamin plays an essential role in regulating actin polymerization in podosomes (Ochoa et al., 2000; Destaing et al., 2013) and has been shown to be involved in osteoclast fusion (Shin et al., 2014). Despite a requirement for actin polymerization in macrophage fusion, little is known about the role of actin-based protrusions during macrophage fusion.

In the present study, we reveal the existence of an actin-based protrusion that initiates IL-4-mediated macrophage fusion. Phase-contrast video microscopy

demonstrated that short phase-dense protrusions originating at the leading edge initiated ~90% of the fusion events with the remaining events having been initiated by long protrusions. Using macrophages isolated from LifeAct mice and imaging with lattice light sheet microscopy (LLSM), we observed short actin-based protrusions originating from regions enriched in podosomes prior to macrophage fusion. Inducing fusion in mixed populations of GFP- and mRFP-LifeAct macrophages showed rapid spatial overlap between GFP and RFP signals. Inhibiting actin polymerization with cytochalasin B impaired fusion, and when rare fusion events occurred, we observed no protrusions. Furthermore, Cdc42- and WASp-deficient macrophages fused at very low rates both in vitro and in vivo, and video analysis of fusion with these cells showed no clear evidence of protrusions. Finally, inhibiting the Arp2/3 complex not only reduced fusion but also rare fusion events did not appear to be dependent on protrusions.

## **2.3 Results**

### **1, Phase-dense protrusions at the leading edge precede macrophage fusion**

We recently developed optical-quality glass surfaces that enabled the first time-resolved views of IL-4-induced macrophage fusion and MGC formation (Faust *et al.*, 2017, 2018). Using these surfaces, we showed that macrophage fusion occurred between the intercellular margins of macrophages. Furthermore, we observed a founder population of mononuclear macrophages that initiates fusion with neighboring mononuclear macrophages (type 1 fusion). Early multinucleated cells then fuse with neighboring mononuclear macrophages (type 2 fusion), the most abundant event leading to MGC

formation. Finally, MGCs fuse with surrounding MGCs to form syncytia (type 3 fusion). However, due to the low-magnification views required to visualize the formation of large MGCs, the mechanism underlying this process remained obscure.

To visualize structures between the intercellular margins of fusing macrophages in detail, we initially used phase-contrast video microscopy with intermediate magnification objectives. In this series of experiments, we used primary macrophages isolated from the inflamed mouse peritoneum (Helming and Gordon, 2007; Podolnikova *et al.*, 2016) in order to avoid robust cell division observed in cultures of macrophage cell lines. Analyses of type 1 ( $n = 33$ ), type 2 ( $n = 93$ ), and type 3 ( $n = 36$ ) fusion events revealed the existence of phase-dense protrusions immediately preceding macrophage fusion. For the majority of events ( $n = 148$ ), short protrusions ( $2.8 \pm 0.8 \mu\text{m}$ ) initiated fusion (Supplemental Figure S1 for type 1 fusion and Figures 1A and 2A, and Supplemental Video S1 for type 2 fusion). However, we rarely observed long protrusions ( $11.6 \pm 6 \mu\text{m}$ ;  $n = 14$ ) (Figures 1B and 2A and Supplemental Video S2). No association of long protrusions with a specific type of fusion was found. Similar to short protrusions, long protrusions were observed in all three types of fusion. In a given cell, either a short or a long protrusion initiated fusion; the coexistence of protrusions was not observed. Within each type of fusion, the lengths of protrusions, both short and long, were similar (Table 1). Furthermore, as shown in [Figure 2A](#), there was no overlap between the distribution of lengths of short and long protrusions, further pointing to the existence of two populations of protrusions. Analyses of type 1 and type 2 of fusion showed no significant difference between spreading of mononuclear cells that fused via short ( $n = 116$ ) and long ( $n = 10$ ) protrusions (Figure 2B). Moreover, since

type 1 fusion occurs between mononuclear cells, which are poorly spread round cells, whereas type 2 and type 3 fusion events involve multinucleated cells, which are large well-spread cells (Table 1), spreading does not seem to influence the length of protrusion. Although a percentage of long protrusions slightly increased in the population of type 3 fusion, short protrusions remained the dominant structures (Table 1). As shown in Figure 2C, the time required from first intercellular contact until full nuclear integration between two macrophages that was mediated by short protrusions was similar for all three types of fusion ( $59 \pm 31$  min,  $48 \pm 22$  min, and  $68 \pm 48$  for type 1, type 2, and type 3, respectively), although the time for type 2 fusion tended to be shorter. The fusion times mediated by long protrusions were significantly shorter for type 2 and tended to be shorter for type 1 and type 3 fusion events than those mediated by short protrusions (Table 1).

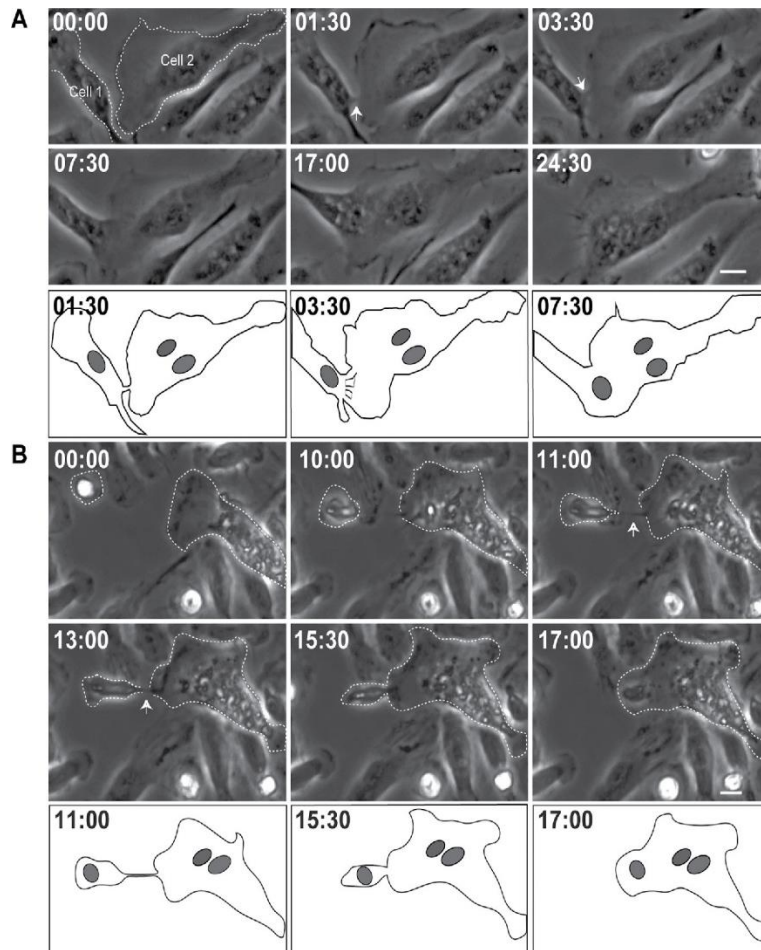


**Figure 1: Phase-dense protrusions initiate macrophage fusion.** (A) Live imaging of macrophages undergoing type 2 fusion. Macrophages were isolated from the mouse peritoneum 3 days after TG injection, plated on a 35-mm Fluorodish and fusion was induced by IL-4. Mononuclear macrophage (Cell 1) extends a short phase-dense protrusion (white arrow) toward MGC (Cell 2) immediately before fusion. The lower panel is a diagram of frames at 1:30, 3:30 and 7:30 min illustrating morphological aspects of the fusion process. In each micrograph, time is shown in minutes:seconds. The scale bar is 10  $\mu\text{m}$ . See also Video 1. (B) Macrophage undergoing type 2 fusion extends a long protrusion (white arrow) to initiate fusion. The lower panels show diagrams of frames at 11:00, 15:30 and 17:00 min. The scale bar is 10  $\mu\text{m}$ .

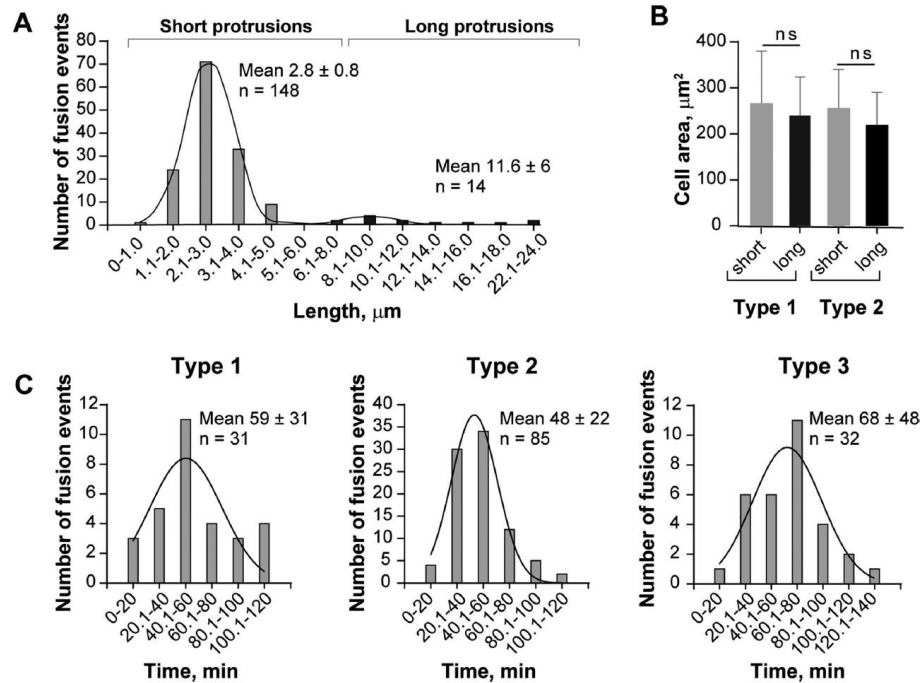


**Figure 2: Quantification of the length of fusion-competent protrusions, fusion time and spreading of fusing macrophages.** (A) Length distribution in the populations of short and long protrusions. Type 1, 2 and 3 fusion events were pooled. (B) Spreading of mononuclear macrophages mediating fusion through short and long protrusions in the population of cells undergoing type 1 and type 2 fusion. (C) The time required from first intercellular contact until full nuclear integration between two macrophages during fusion mediated by short protrusions.

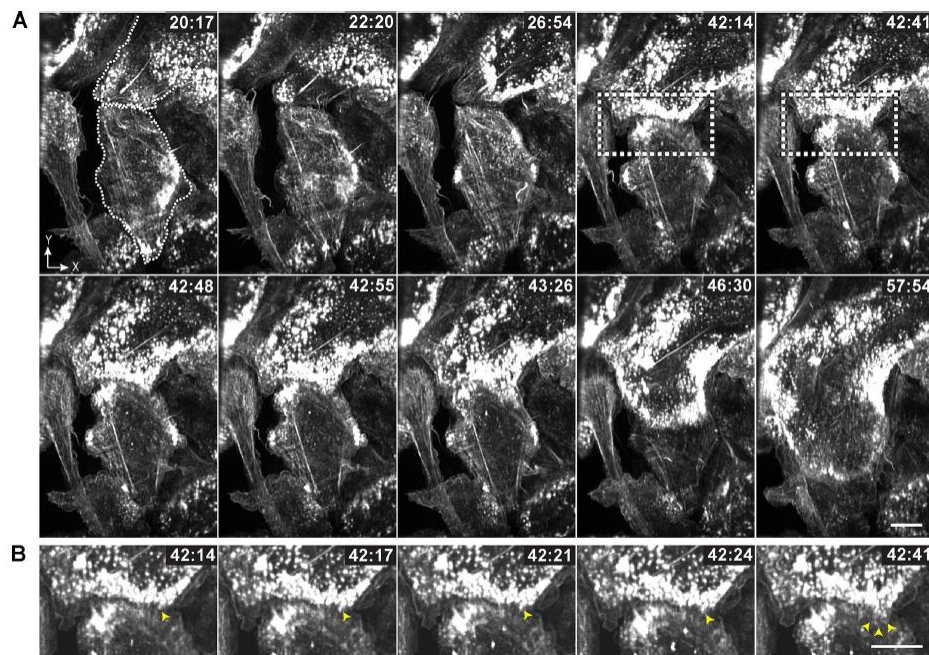
## 2, An actin-based protrusion initiates macrophage fusion

Membrane protrusions at the leading edge are actin-based structures. Furthermore, F-actin is known to be important for the formation of MGCs (DeFife et al., 1999; Jay et al., 2007). To determine if the protrusions we observed in phase-contrast micrographs were actin-based structures, we examined macrophages isolated from the inflamed peritoneum of LifeAct mice using LLSM (Chen et al., 2014). We first confirmed that LifeAct faithfully reported the distribution of F-actin in macrophages by comparing the distribution of eGFP-



LifeAct and Alexa 568– conjugated phalloidin (Supplemental Figure S2). Using LLSM, we reveal waves of eGFPLifeAct puncta emanating from the center of the cell to the cell periphery prior to fusion (Supplemental Video S6). At the time of apparent fusion, one wave of LifeAct puncta advanced into a neighboring cell (Figure 3A and Supplemental Video S6). In fixed specimens, actin puncta at cellular margins contained rings of vinculin and talin circumscribing a central actin core in both mononuclear macrophages and MGCs (Supplemental Figure S3), suggesting that structures we observed in living cells were podosomes. Furthermore, the size of individual podosomes determined in fixed samples (both GFP-LifeAct and phalloidin-labeled) and in living cells (Supplemental Figure S4) were similar. When we analyzed the site of fusion (Figure 3B, 42:14–42:41 min; boxed areas in Figure 3A) with the maximum temporal resolution achievable with LLSM under the conditions of our experiments (~1.5 s per image for several hours), we observed a finger-like enrichment of LifeAct that extended into the neighboring cell during fusion (Figure 3B, 42:14–42:24 min; yellow arrowhead). This protrusive structure fanned from the initial point of contact as fusion proceeded (Figure 3B, 42:41 min; yellow arrowheads). To visualize the dynamics of the actin cytoskeleton prior to fusion and observe the interface between fusing cells, we used a maximum intensity isosurface render of eGPF-LifeAct applied to the area shown in Figure 3A (Supplemental Video S7). We observed numerous thin protrusions between two interacting cells after initial contact (Figure 3C, 22:20 and 25:07 min). The protrusions appeared to contact apposing cells by rounds of extension and retraction, which continued until seconds before the cells fused (Figure 3C, 42:14– 42:55 min, individual protrusions are outlined; and Supplemental Video S7). Close apposition

of these cells in diffraction-limited space precluded visualizing the role of protrusions during the fusion process. Analysis of another area also revealed the presence of protrusions extending and retracting between two cells (Figure 3D, white outline; and Supplemental Video S8). In this case, however, the separation between the cells made it possible to observe an actin-based protrusion that initiated fusion (Figure 3D, 37:27–37:51 min; white arrowheads). The gradual expansion of the actin network that followed at this site could potentially be attributed to the local expansion of the protrusion, the formation of a fusion pore, or both (Figure 3D, 37:54–37:58 min; arrowheads).



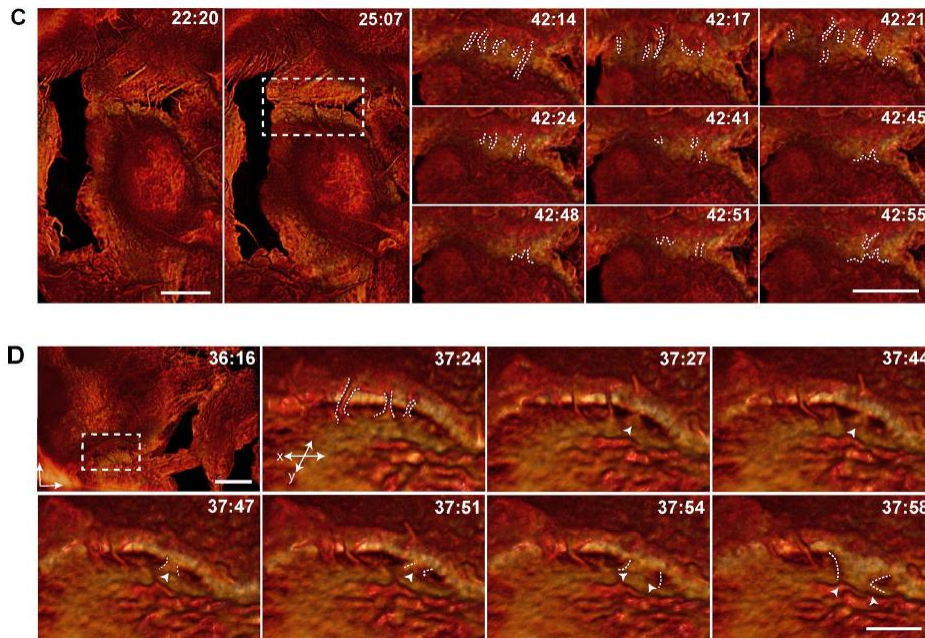


**Figure 3: An actin-based protrusion precedes macrophage fusion.** (A) Lattice light sheet microscopy of IL-4-induced fusion of macrophages expressing eGFP-LifeAct. All images shown are maximum-intensity projections. The scale bar is 10  $\mu\text{m}$ . See also Video 6. (B) Enlarged images of events occurring between 42:14 and 42:41 min (boxed regions in A). Yellow arrowheads point to the site of fusion. The scale bar is 10  $\mu\text{m}$ . (C) *En face* isosurface renders of LLSM data from A. The boxed region at 25:07 min corresponds to the subsequent micrographs showing the fusion progress (42:14-42:41 min). Note numerous protrusions (outlined by white dashes) formed between apposing cells. The scale bar is 10  $\mu\text{m}$ . See also Video 7. (D) Surface renders of LLSM data from another area of fusing macrophages showing contact of a fusion-competent protrusion (a single white arrowhead; 37:27-37:51 min) followed by its apparent expansion (two white arrowheads; 37:54-37:58 min). The scale bar is 5  $\mu\text{m}$ . The boxed area at 36:16 min (scale bar, 10  $\mu\text{m}$ ) corresponds to the subsequent micrographs (37:24-37:58 min). Time in each micrograph is shown as minutes:seconds.

### 3, F-actin incorporation is asymmetric during macrophage fusion

To determine how actin is integrated during the fusion process, we mixed equal numbers of eGFP-LifeAct and mRFP-LifeAct macrophages, induced fusion, and imaged the process with LLSM (Supplemental Video S9). When we visualized cells in this mixing assay at early time points, we observed no overlap of GFP and RFP emission in diffraction limited space (Figure 4A, 5:57 min; two adjacent mononuclear cells in the right bottom quadrant are outlined). However, at the time of apparent fusion (Figure 4A, 06:14 min), we

observed overlap of GFP and RFP in overlays at the cell margins, which became more apparent as fusion proceeded (Figure 4A, 6:31–7:22 min). Further, we observed reorganization of actin in cells undergoing fusion that first clearly appeared at 11:20 min and was completed by 23:48 min, suggesting mixing of the cytoplasm. Separating GFP and RFP emission and analyzing fusion in the two cells outlined in green and red revealed an asymmetry in the fusion process (Figure 4B and Supplemental Video S10). Prior to fusion (5:57 min), we observed no GFP signal in the cell outlined in red and vice versa. However, at 6:14 min, the signal from RFP appeared in the green outline traversing the entire length of the cell (Figure 4B; magnified inset shows the outline of the eGFP-LifeAct macrophage). At the same time, we were unable to detect a green signal within the outline of the red cell. Only after an additional 17 s (6:31 min) did we begin to see low levels of GFP signal spatially overlapping boundaries of the cell outlined in red, which appeared to enrich as time progressed (6:48 min). Thus, it appears that one of the two cells more actively integrates cytoplasm than the other does.

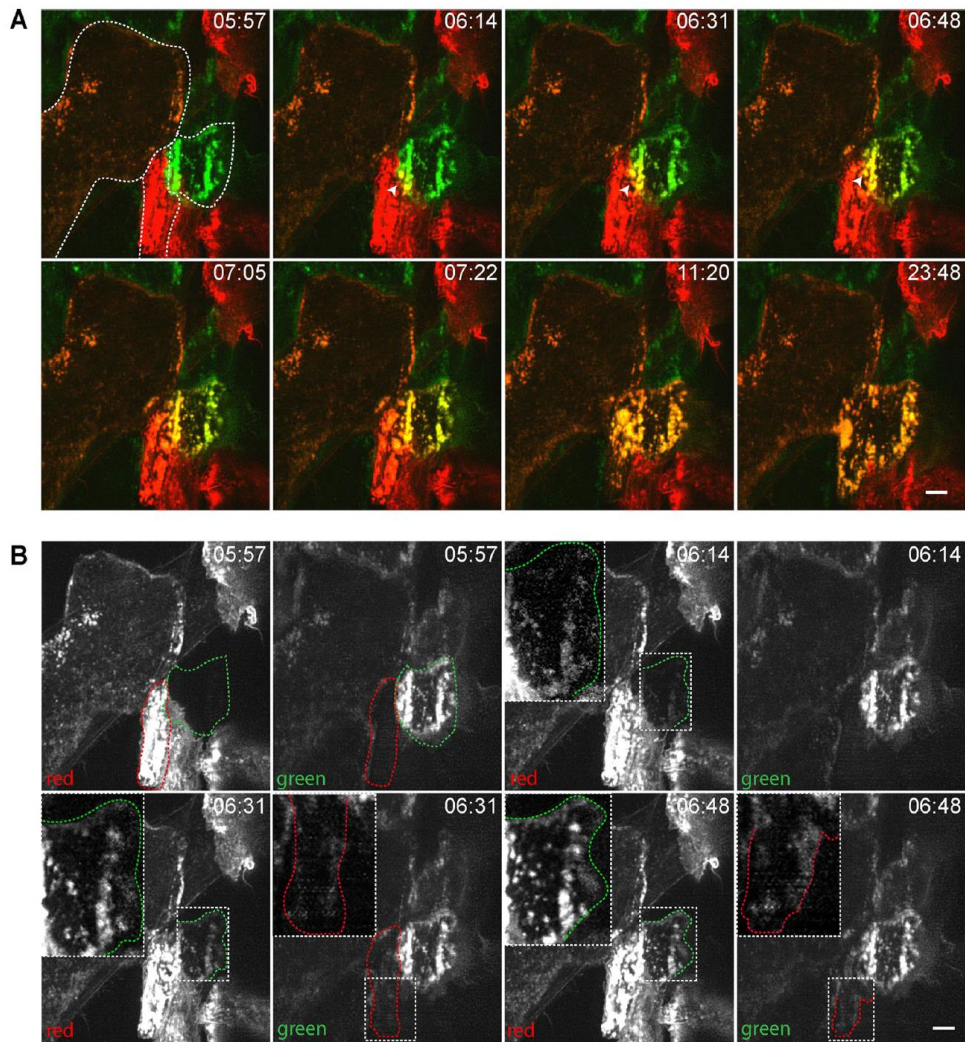


**Figure 4: Mixing macrophages expressing eGFP-LifeAct and mRFP-LifeAct shows asymmetric actin integration.** (A) Macrophage fusion in a mixed population of eGFP/mRFP-LifeAct macrophages. Two mononuclear cells expressing eGFP-LifeAct and mRFP-LifeAct undergoing fusion are outlined in the image taken at 5:57 min. A site of eGFP- and mRFP-LifeAct integration is indicated by white arrowheads at 6:14 and 6:48 min. (B) Split-channel view of the fusion event shown in A. The boxes outlined in white dashed lines in the images taken at 6:14-6:48 min correspond to the areas where integration of mRFP-LifeAct into the eGFP-LifeAct-containing cells is observed. The enlarged images of the same areas are shown as insets. The scale bars are 5  $\mu$ m.

#### 4, Organizers of actin-based protrusions are critical for macrophage fusion in vitro

Since protrusions precede macrophage fusion, we sought to determine whether these actin-based structures are causal mediators of macrophage fusion. As a first step, we examined the role of F-actin, the cytoskeleton underlying membrane protrusions, in

macrophage fusion. Consistent with previous data (DeFife et al., 1999), treatment of cells with cytochalasin B reduced MGC formation.

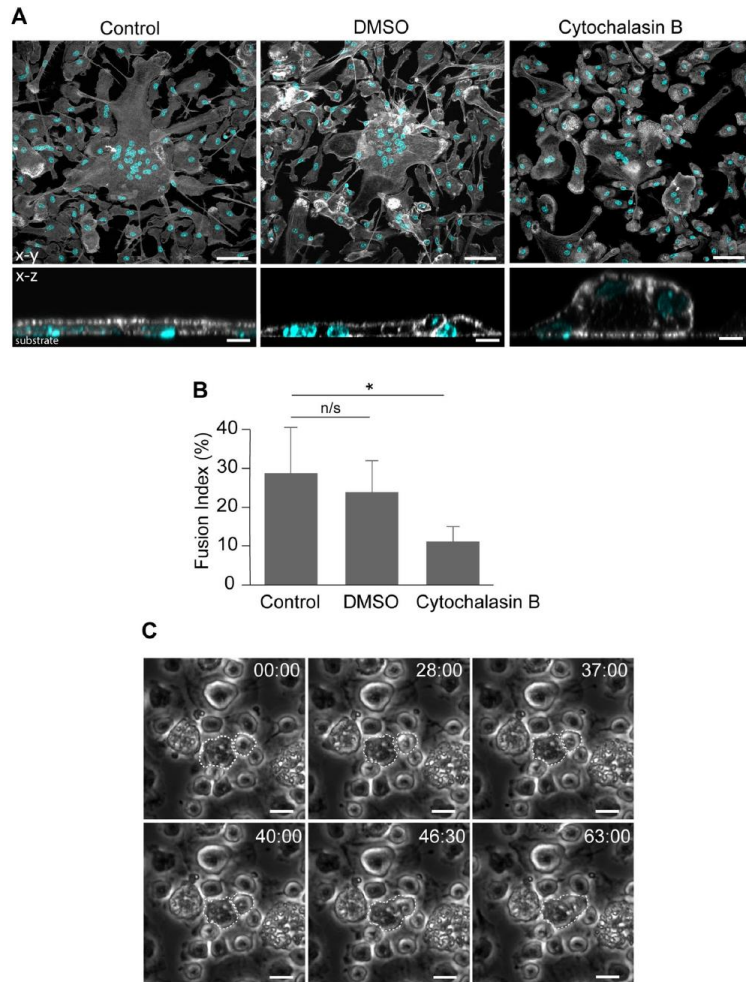


**Figure 5: Cytochalasin B treatment reduces macrophage fusion.** (A) Confocal micrographs of control (untreated and DMSO-treated) as well as cytochalasin B-treated (2.5  $\mu$ M) macrophages 24 hours after incubation in the presence of IL-4. The cells were labeled with Alexa Fluor 488-conjugated phalloidin (white) and DAPI (teal). The bottom panels show the x-z sections of control untreated (*left*), control DMSO-treated (*middle*) and cytochalasin B-treated (*right*) MGCs. The scale bars are 50  $\mu$ m and 10  $\mu$ m in the upper and lower panels, respectively. (B) Quantification of the fusion index in the population of untreated and cytochalasin B-treated macrophages. DMSO was used as vehicle control for cytochalasin B treatment. Three to five random 20x fields per sample were used to count nuclei (100-150 nuclei/field; total ~1500 nuclei). Results shown are mean  $\pm$  SD from three independent experiments. \* $p$ <0.01. (C) Single cytochalasin B-treated macrophages that undergo fusion do not form protrusions. The cells that fuse are outlined. The scale bars are 10  $\mu$ m.

Quantification of the fusion index indicated that at a concentration as low as 2.5  $\mu$ M, cytochalasin B decreased fusion by approximately threefold from  $29 \pm 10\%$  to  $10 \pm 5\%$  for untreated versus treated cells, respectively (Figure 5, A and B). Furthermore, the majority of treated cells had a bulbous shape compared with a flattened shape of untreated cells (Figure 5A, bottom panels). Importantly, when we recorded fusion in the presence of cytochalasin B using phase-contrast video microscopy, we were unable to observe phase-dense protrusions preceding fusion. Rather, some cells in close apposition appeared to passively undergo fusion (Figure 5C). It is well known that Cdc42 orchestrates filopodia formation. In addition, Cdc42 and PIP2 activate WASp to trigger downstream Arp2/3-mediated actin polymerization to form lamellipodia, podosomes, and other protrusions (Mattila and Lappalainen, 2008; Campellone and Welch, 2010; Linder et al., 2011). If actin-based protrusions are involved in macrophage fusion, then perturbing the function of these upstream regulatory proteins should inhibit macrophage fusion. To test this prediction, we isolated macrophages from a WASp<sup>-/-</sup> mouse and examined IL-4-induced macrophage fusion at various time points. Figure 6, A and B, shows that fusion of WASp-deficient macrophages was strongly impaired. Compared to wildtype (WT) macrophages, the degree of fusion of WASp-deficient macrophages at every time point tested (24, 48, and 72 h) was approximately sixfold less. WASp deficiency also inhibited the formation of podosomes in fusing macrophages (Figure 6C). Gross morphology and the degree of macrophage adhesion after 2.5 h in culture did not appear to be significantly different from WT macrophages (Figure 6A; t = 0). Using phase-contrast video microscopy performed during the first 24 h after IL-4 addition, we were able to observe rare fusion

events, which appear to have occurred by a protrusion-independent mechanism (Figure 6D).

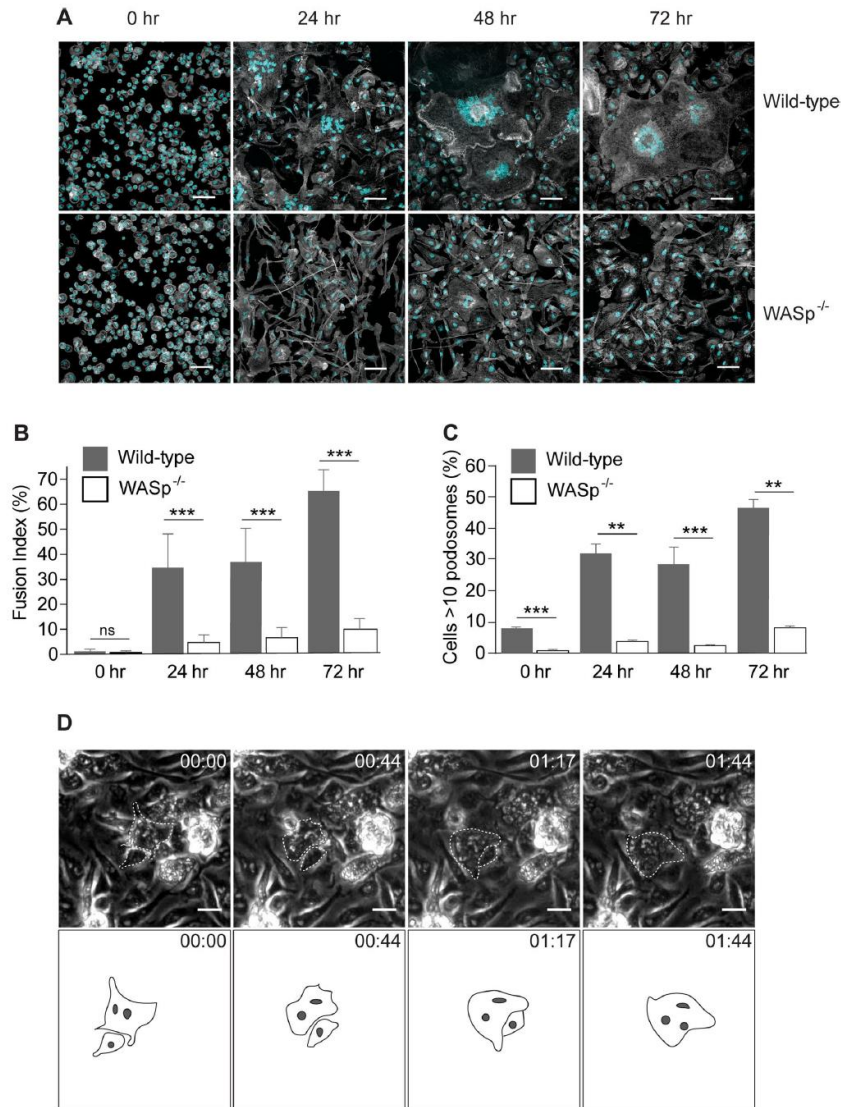


**Figure 6: WASp is required for macrophage fusion *in vitro*.** (A) Fusion of wild-type and WASp-deficient macrophages at various time points after the addition of IL-4. After 24, 48 and 72 hours, cells were fixed and labeled with Alexa 488-conjugated phalloidin (white) and DAPI (teal). The scale bars are 50  $\mu$ m. (B) The time-dependent fusion indices for wild-type and WASp-deficient macrophages. Results shown are mean  $\pm$  SD from three independent experiments. Three to five random 20x fields per sample were used to count nuclei (100-150 nuclei/field; total 1500 nuclei). \*\*\* $p$ <0.001. (C) The time-dependent podosome formation in fusing macrophages. The fraction of cells with >10 podosomes for each time point was calculated. Four random 20x fields each containing ~200-300 cells were used to count podosomes. \*\* $p$ <0.01, \*\*\* $p$ <0.001. (D) Live imaging of IL-4-treated WASp-deficient macrophages. In each micrograph, time is shown in hours:minutes. A rare fusion event detected in the population consisting of ~1200 macrophages is shown.



We next examined whether Cdc42 is required for macrophage fusion using macrophages isolated from myeloid cell-specific Cdc42<sup>-/-</sup> mice (Figure 7, A and B). As shown in Figure 7, C and D, at 24–72 h, we observed an approximately twofold decrease in fusion of Cdc42-deficient macrophages compared with control Cdc42<sup>loxP/loxP</sup> counterparts. Similar to WASp, Cdc42 deficiency also strongly reduced the formation of podosomes (Figure 7E). We next determined whether inhibition of Arp2/3 results in impaired macrophage fusion. As shown in Figure 8, A and C, the Arp2/3-specific inhibitors CK-636 and CK-548 (Nolen et al., 2009) blocked macrophage fusion in a dose-dependent manner. The IC<sub>50</sub> values for CK-636 and CK-548 inhibition were  $13 \pm 0.5$  and  $15 \pm 0.7$   $\mu$ M, respectively, for 72-h cultures. In addition, consistent with previous reports (Nolen et al., 2009), inhibition of Arp2/3 decreased the number of podosomes with both inhibitors exerting similar effects (IC<sub>50</sub> =  $9.5 \pm 0.5$   $\mu$ M for CK548 and  $12 \pm 0.5$   $\mu$ M for CK636; Figure 8, B and C). Although ~40% fusion was observed in the presence of 15  $\mu$ M CK-636, MGCs did not account for the majority of fusion events. Rather, binucleated cells were the predominant cell type, which formed by a protrusion-independent mechanism (Figure 8D). WASp- and conditional Cdc42-deficient mice do not initiate a robust foreign body response to implanted materials. Further evidence for the involvement of WASp and Cdc42 in macrophage fusion was obtained by in vivo experiments. Macrophage fusion leading to the formation of MGCs is a hallmark of the foreign body reaction that follows the implantation of vascular grafts and other engineered devices (Anderson et al., 2008; McNally and Anderson, 2011). To confirm that WASp and Cdc42 are important for the

formation of MGCs *in vivo*, we implanted polychlorotrifluoroethylene (PCTFE) into the peritoneum of WT, WASp<sup>-/-</sup>, and conditional Cdc42-deficient mice and retrieved the

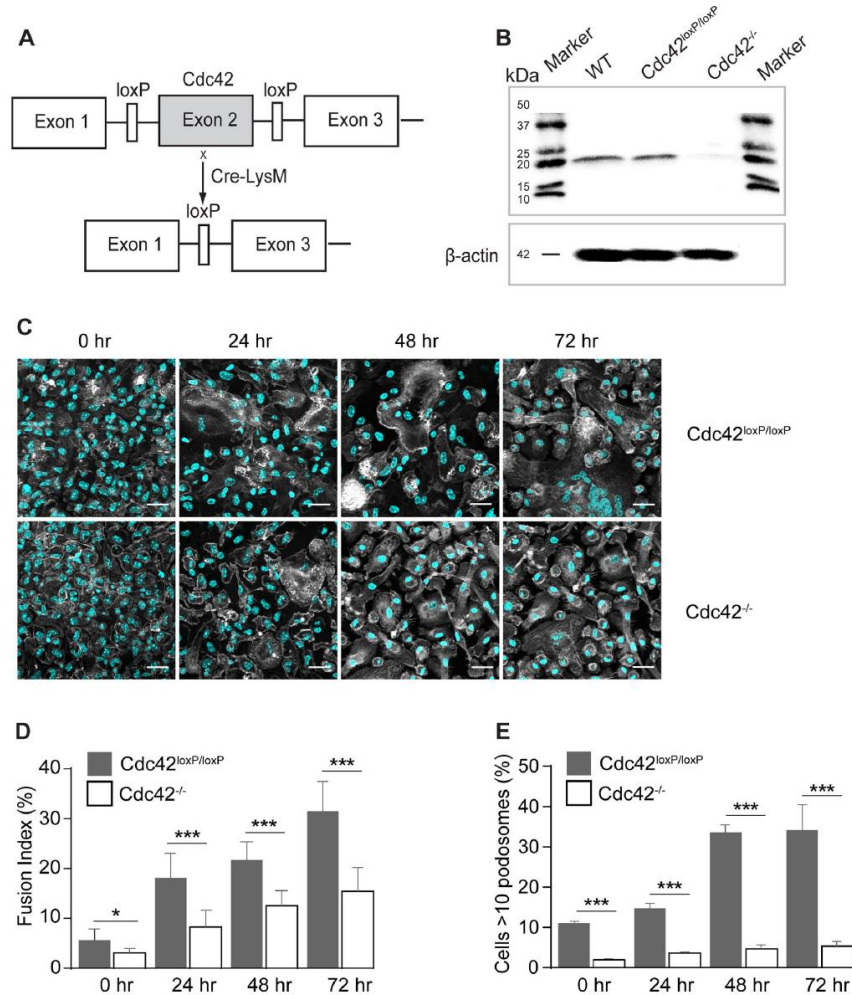


**Figure 7: Loss of Cdc42 in macrophages results in impaired fusion *in vitro*.** (A) Schematic diagram of the generation of a myeloid cell-specific Cdc42<sup>-/-</sup> mouse. Conditional gene-targeted mice with exon 2 of *Cdc42* gene flanked by a pair of loxP sequences (Yang et al., 2007) were cross-bred with LysMcre mice to allow *Cdc42* gene excision in myeloid cells. (B) Cdc42 deletion in isolated macrophages was examined by SDS-PAGE (11% gel) followed by Western blotting using anti-Cdc42 rabbit monoclonal antibody (ab187643; Abcam). (C) Fusion of wild-type and Cdc42-deficient macrophages at various time points after the addition of IL-4. Cells were fixed after 24, 48 and 72 hours and labeled with Alexa 488-conjugated phalloidin (white) and DAPI (teal). The scale bars are 50 μm. (D) Time-dependent fusion indices of wild-type and Cdc42-deficient macrophages. Results shown are mean ± SD from three independent experiments. Four to five random 20x fields per sample were used to count nuclei (300 nuclei/field; total ~4050 nuclei).

\* $p < 0.05$ , \*\*\* $p < 0.001$ . **(E)** The time-dependent podosome formation in fusing macrophages. The fraction of cells with  $>10$  podosomes for each time point was calculated. Four random 20x fields each containing  $\sim 200$ -300 cells were used to count podosomes. \*\*\* $p < 0.001$ .

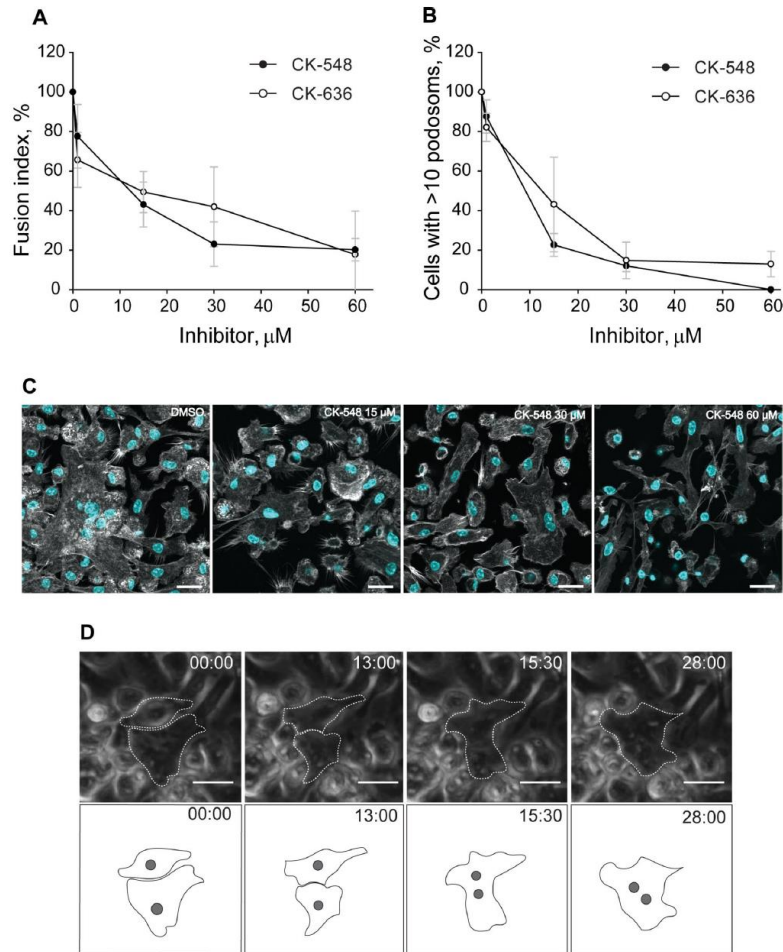


**Figure 8: Inhibition of actin assembly by CK-636 and CK-548 decreases macrophage fusion and podosome formation.** **(A)** Different concentrations of the Arp2/3 inhibitors CK-636 and CK-548 were added to macrophages at the onset of fusion induction with IL-4. Control cells were treated with DMSO. The fusion rates were determined after 72 hours from confocal images of samples labeled with Alexa 488-conjugated phalloidin and DAPI. Results shown are mean  $\pm$  SD from three independent experiments. Three to five random 20x fields per sample were used to count nuclei (250-300 nuclei/field; total  $\sim 3600$  nuclei). Fusion of control (DMSO-treated) cells was assigned a value of 100%. **(B)** Effect of inhibitors (each at 15  $\mu\text{M}$ ) on podosome formation. The fraction of cells with  $>10$  podosomes was calculated and normalized to DMSO control. Results shown are mean  $\pm$  SD from three independent experiments with three to five random 20x fields used per sample to count cells (100-150 cells/field). **(C)** Representative confocal micrographs of control (DMSO-treated) and CK 548-treated (15-60  $\mu\text{M}$ ) macrophages 72 hours after incubation in the presence of IL-4. The cells were labeled with Alexa Fluor 488-conjugated phalloidin (white) and DAPI (teal). **(D)** Live imaging of macrophages treated with 15  $\mu\text{M}$  Arp2/3 inhibitor CK-548. In each micrograph, time is shown in minutes:seconds. A single fusion event detected is shown.

implants 14 d later. Visualization of cells covering the surface of explants revealed a large number of MGCs on materials implanted into WT, but not WASp<sup>-/-</sup> mice (Figure 9, A and B). We found an approximately fivefold difference in the fusion index between WT and WASp-deficient macrophages ( $36 \pm 6\%$  vs.  $7 \pm 4\%$  for WT and WASp-deficient cells, respectively) (Figure 9B). No significant difference in the number of cells recruited into the peritoneum of WT and WASp<sup>-/-</sup> mice (Figure 9C) as well as in the number of cells attached to the retrieved implants was found (Figure 9D). Conditional deletion of Cdc42 also strongly impaired multinucleation with an approximately sixfold difference between Cdc42<sup>loxP/loxP</sup> and Cdc42<sup>-/-</sup> cells ( $33\% \pm 12$  vs.  $5.9\% \pm 4.0$ ) (Figure 9, E and F). The number of cells in the peritoneum 14 d after implantation (Figure 9G) and the number of cells on explants (Figure 9H) were not significantly different between the two strains of mice. Together, these data indicate that WASp and Cdc42 are essential *in vivo* for a robust foreign body reaction.

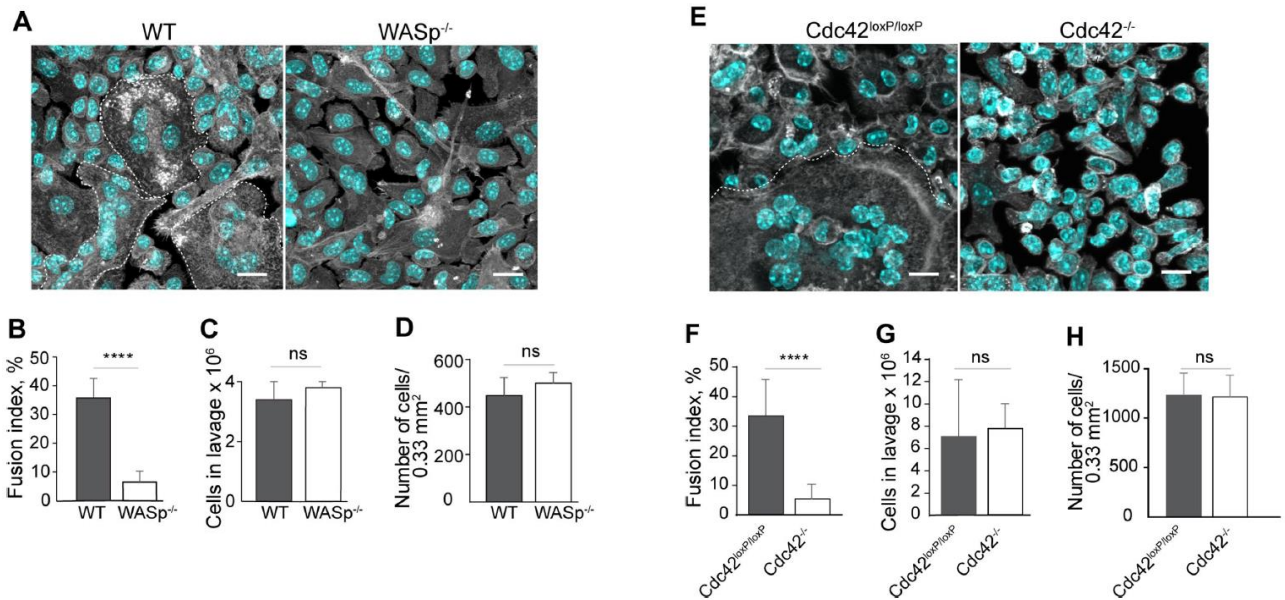


**Figure 9: Fusion of WASp- and Cdc42-deficient macrophages is severely impaired *in vivo*.** (A) Micrographs of macrophages on PCTFE surfaces retrieved 14 days after implantation in wild-type and WASp<sup>-/-</sup> mice. Three MGCs in the left panel are outlined. The scale bars are 7.5 μm. (B) Quantification of the fusion index of macrophages on PCTFE surfaces retrieved from wild-type and WASp<sup>-/-</sup> mice. Results shown are mean ± SD from three independent experiments. Six to eight random 20x fields per sample were used to count nuclei (250-300 nuclei/field; total 6000 nuclei). \*\*\*\*p < 0.0001. (C) A number of cells collected from the peritoneum of wild-type and WASp<sup>-/-</sup> mice before implants were retrieved. Results shown are mean ± SD from three independent experiments. No significant difference was observed. (D) A number of cells on the surface of explants retrieved from wild-type and WASp<sup>-/-</sup> mice. Results shown are mean ± SD from three independent experiments. No significant difference was observed. (E) Micrographs of macrophages on PCTFE surfaces retrieved 14 days after implantation in Cdc42<sup>loxP/loxP</sup> mice and mice with Cdc42-deficiency in myeloid cells. A single MGC in the left panel is outlined. The scale bars are 7.5 μm. (F) Quantification of the fusion index of macrophages on surfaces implanted into Cdc42<sup>-/-</sup> mice. Results shown are mean ± SD from three independent experiments. Six to eight random 20x fields per sample were used to count nuclei (300 nuclei/field; total 6600 nuclei). \*\*\*\*p < 0.0001. (G) A number of cells collected from the peritoneum of wild-type and Cdc42<sup>-/-</sup> mice before implants were retrieved. Results shown are mean ± SD from three independent experiments. Three to five random 20x fields were used per sample to count cells. No significant difference was observed. (H) A number of cells on the surface of explants retrieved from Cdc42<sup>loxP/loxP</sup> mice and mice with Cdc42-deficient macrophages. Results shown are mean ± SD from three independent experiments. No significant difference was observed

## 2.4 Discussion

Despite the long history of research on MGCs highlighted by the fact that these cells are often observed in many diseases, the molecular and cellular mechanisms of macrophage fusion remain poorly understood. While previous studies focused mainly on the identification of fusion effector molecules in macrophages (Helming and Gordon, 2009; Vignery, 2011), little effort has been expended to elucidate the involvement of the actin cytoskeleton, which has been shown to be a driving force in other types of cells undergoing fusion (Aguilar et al., 2013; Podbilewicz, 2014). Here, we used live cell imaging of macrophages to visualize actin-based structures formed at the site of contact between two fusing cells. We show for the first time that IL-4-induced macrophage fusion is initiated by a single protrusion that more often (~90% events) extends from the leading edge of one cell in contact with another cell. The majority (~90%) of fusion-competent

protrusions are short although long structures were also observed. Recently, a number of studies have reported the involvement of membrane extensions during osteoclastogenesis (Oikawa et al., 2012; Soe et al., 2015; Wang et al., 2015). Using RAW264.7 macrophages differentiated into osteoclasts by M-CSF and RANKL, Oikawa et al demonstrated that the majority of fusion events was mediated by membrane protrusions referred to as “podosome-related” that emerged from the sealing belt, a structure formed in large multinucleated osteoclasts from a ring of “circumferential” podosomes (Oikawa et al., 2012). Less frequently, “filopodia-like” protrusions that formed after a transient expansion of podosome-like protrusions and “long” protrusions were observed. Wang et al. (2015) have also observed finger-like extensions ( $\sim 2.5 \mu\text{m}$ ) in RAW264.7 cultures, which they termed fusopods (Wang et al., 2015). In that investigation, fusopods were the predominant structures, although some cells reportedly fused at contacts between broad surfaces. Thus, both IL-4– mediated fusion of natural mouse macrophages and RANKL-mediated osteoclastogenesis in RAW264.7 cultures are initiated by a protrusion. We demonstrated that macrophage fusion depends on F-actin and regulators of actin polymerization Cdc42 and its downstream effector WASp, inasmuch as the ability of macrophages to fuse was strongly impaired in the presence of cytochalasin B and in macrophages derived from WASp- and conditional Cdc42-deficient mice (Figures 5–7). In addition, inhibiting Arp2/3 activity also inhibited macrophage fusion (Figure 8). The decrease in fusion observed in cytochalasin B– and Arp2/3- treated as well as WASp- and Cdc42-deficient macrophages correlated with a lack of visible protrusions. Interestingly, a small portion of macrophages continued to fuse through a seemingly protrusion-independent way, the mechanism of

which remains to be determined. Importantly, fusion of WASp- and Cdc42-deficient macrophages was reduced not only in vitro but also in vivo, suggesting that protrusion-mediated fusion is not an artifact observed exclusively in cultured cells. It is known that macrophages derived from Wiskott-Aldrich syndrome patients are defective in chemotaxis and phagocytosis (Thrasher, 2002). The finding that WASp is also essential for fusion extends its known roles in macrophages. Our finding that the majority of fusion events in macrophages involved the leading edge of at least one cell (Table 2) and the observation of numerous thin protrusions at the site of contact between apposed cells (Supplemental Videos S7 and S8) are consistent with filopodia formation at this location. Indeed, thin finger-like filopodia are found at the leading edge of migrating cells and are an extension of the branched lamellipodia network (Svitkina et al., 2003). However, these protrusions did not seem to initiate fusion. Although extension and retraction of filopodia persisted for a prolonged period, fusion occurred only after podosomes concentrated at the leading edge. At that point one protrusion initiated fusion. Therefore, it may be possible to distinguish two types of protrusions during macrophage fusion: bona fide filopodia as pre-fusion protrusions and a fusion-competent protrusion that assembles in a region enriched in podosomes. Fusion-competent protrusions appear to have a different morphology being wider and shorter than filopodia (Figure 3D). Although the molecular composition and organization of the F-actin network within the two types of protrusions remain to be defined, our data suggest that several types of actin-based protrusions that have different functions may be involved in macrophage fusion. Fusion-competent short protrusions appear to originate from cells that become enriched in peripheral podosomes. In these cells,

podosomes emanate from the interior and move in a wave-like manner to the periphery where they accumulate at the site destined for fusion (Figure 3, A and B, and Supplemental Video S6). Before the arrival of podosomes, the interface between two apposing cells is filled with thin protrusions that undergo rounds of extension and retraction (Figure 3, C and D; Supplemental Video S7; and schematically shown in Figure 10A). This activity continues for some time until podosomes in the cell that initiates fusion align along the plasma membrane (Figure 10B). Shortly after, one of the protrusions initiates fusion (Figure 10, C and D). The association of podosomes with long protrusions is presently unclear.

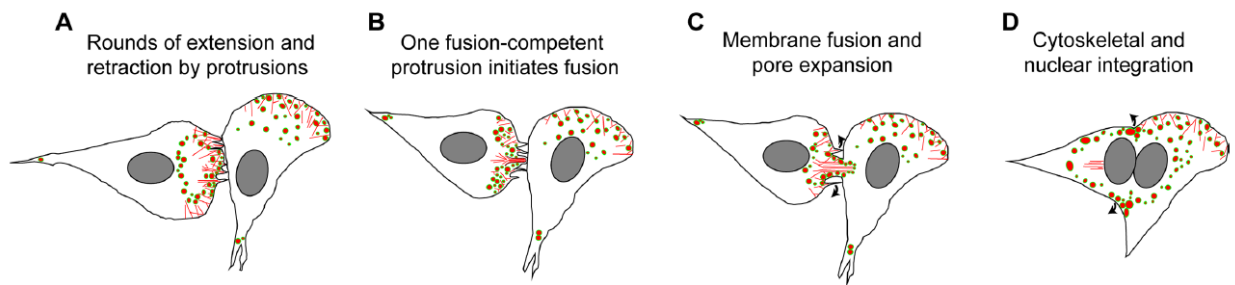


**Figure 10: Model for macrophage fusion initiated by an actin-based protrusion.** (A) The interface between two closely apposing macrophages contains numerous thin actin-based protrusions. A wave of podosomes moves from the interior of the cell that initiates fusion to the site of cell-cell contact. (B) Once podosomes arrive and align at the site of contact with the acceptor macrophage, membrane fusion is initiated by a single protrusion and podosomes from the donor macrophage advance into the acceptor macrophage. (C) The actin network at the site of fusion rapidly reorganizes to expand the initial pore. (D) The actin cytoskeleton and nuclei undergo directional integration.

Because of their paucity, we were unable to detect long protrusions in our LLSM experiments using LifeAct-containing macrophages. Nonetheless, although still constituting a small portion, long connections between two distant macrophages were



detected by phase-contrast video microscopy, which revealed that the pattern of fusion was rather different from cells that fuse through short protrusions. Interestingly, the long connections seemed to form by merging the tips of two protrusions arising from two macrophages (Supplemental Video S2). A similar mode of joining of two protrusions was observed in RAW264.7-derived osteoclasts (Oikawa et al., 2012). After establishing the long connection, fusion was accompanied by shortening and widening of this bridge, followed by fusion (Supplemental Video S2). At present, the differences between short and long protrusions and their origin remain to be defined. Previous studies have shown that Cdc42, WASp, and Arp2/3 have an important role in the formation of podosomes in macrophages (Linder et al., 1999, 2011; Dovas et al., 2009). In line with these investigations, our results demonstrated fewer podosomes in macrophages derived from WASp<sup>-/-</sup> and conditional Cdc42<sup>-/-</sup> mice (Figures 6 and 7). In addition, the number of podosomes was significantly decreased in macrophages treated with Arp2/3 inhibitors (Figure 8). Although podosomes were enriched at the site of fusion and abolishing the activity of critical podosomal proteins impaired fusion, the mechanistic link between fusion-competent protrusions and podosomes remains to be established. Podosomes are formed at the ventral side of the cell and typically protrude vertically into the substrate (Labernadie et al., 2010, 2014; Proag et al., 2015; Linder and Wiesner, 2016). Our current data suggest that the force driving the formation of fusion-competent protrusions may be delivered laterally toward the apposing cell in order to initiate fusion. It is possible that podosomes may directly or indirectly generate protrusive force during the fusion process. We speculate that when podosomes arrive at the leading edge, they anchor the ventral actin

network while allowing the lateral actin network to continue extending forward. Under these conditions, the cell would be unable to protrude along the entire leading edge and thus may focus the protrusive force to a limited region. Since the apposing macrophage presents an obstacle for the elongation of the protrusion, the protrusion may generate a pushing force and penetrate into the adjacent cell. It is presently unclear why only certain macrophages display the directional movement of podosomes and how it is associated with the formation of a fusion-competent protrusion. Long fusion-competent protrusions that we occasionally observed in our experiments (Figure 1 and Supplemental Figure S1) are visually reminiscent of tunneling nanotubes (TNTs). TNTs are long, thin membranous tubes with diameters of 50–800 nm connecting two cells that have been reported in numerous cell types, including macrophages (Rustom et al., 2004; Onfelt et al., 2006; Kimura et al., 2012; Hanna et al., 2017). Formation of TNTs requires F-actin and, as recently shown in macrophages, depends on the activity of Rac1, Cdc42, and WASp (Hanna et al., 2017). Despite the general requirement for F-actin and the activators of actin polymerization, there seem to be clear distinctions between TNTs and fusion-competent protrusions. In particular, we observed that contact initiated by a long protrusion with a neighboring macrophage was invariably followed by fusion. In contrast, TNTs that also form by extending long protrusions remain stable structures that connect two cells. Furthermore, while TNTs have been reported to form in short 4-h cultures of RAW/LR5 macrophages (Hanna et al., 2017), fusion of peritoneal macrophages begins 9 h after the addition of IL-4 (Faust et al., 2017). Finally, as revealed in our studies, short rather than long protrusions predominantly initiate macrophage fusion. Nevertheless, the requirement

for F-actin and actin nucleation promoting factors of both TNTs and long fusion-competent protrusions is intriguing and suggests that two phenomena may be connected by a general mechanism. The requirement for actin-based protrusions as initiators of cell–cell fusion seems to emerge as a unifying principle in several model systems, including fusion in osteoclasts (Oikawa et al., 2012; Shin et al., 2014; Wang et al., 2015) and fusion of muscle cells in flies, zebrafish, and mice (Chen, 2011; Abmayr and Pavlath, 2012; Gruenbaum-Cohen et al., 2012; Aguilar et al., 2013). In *Drosophila*, muscle fibers are formed through rounds of fusion between a myotube (founder cell) and a fusion-competent myoblast (FCM). The fusion interface between these cells was found to contain an F-actin enrichment referred to as a “focus,” which develops in FCM and then invades the myoblast with one or several finger-like protrusions (Abmayr and Pavlath, 2012; Aguilar et al., 2013). Numerous actin regulatory proteins, including WASp, WIP, SCAR/WAVE, and others have been found at the fusion site (Chen, 2011; Abmayr and Pavlath, 2012; Aguilar et al., 2013). Based on their invasiveness, size and the presence of the actin core with a surrounding ring of adhesive proteins, these structures were called PLS (Sens et al., 2010). While the molecular composition of the fusion-competent protrusions in macrophages and myoblasts may differ, their formation nevertheless requires Cdc42, WASp, and Arp2/3. Furthermore, although we did not observe stable F-actin foci in macrophages, fusion was initiated from sites where podosome clustered in large numbers (Figure 2, A and B). Recent studies have shown that actin-based protrusions, reconstituted together with adhesion molecules in *Drosophila* cells that normally do not undergo fusion, failed to recapitulate cell–cell fusion (Shilagardi et al., 2013). Expression of authentic fusion proteins, in

addition to cell–cell and cell-matrix adhesion molecules, was necessary to induce fusion. These findings suggest that actin-based protrusions are insufficient on their own to promote cell–cell fusion. Whether force production alone is sufficient or the presence of fusion proteins is required for macrophage fusion is currently unknown. Further studies of actin dynamics may help define a link between actinbased protrusions and podosomes in macrophage fusion.

## **2.5 Materials and methods**

### **1, Mice**

C57BL/6J, WASp<sup>-/-</sup>(B6.129S6-Wastm1Sbs/J), and Cdc42loxP/loxP mice were purchased from The Jackson Laboratory (Bar Harbor, ME). LysMcre mice were a gift from James Lee. LifeAct mice (Riedl et al., 2010) were a gift from Janice Burkhardt and used with permission from Roland Wedlich-Söldner. The conditional Cdc42loxP/loxP mice were generated by crossing Cdc42loxP/loxP mice with LysMcre mice and screening for Cdc42 excision in myeloid leukocytes. All animals were given ad libitum access to food and water and maintained at 22°C on a 12-h light/dark cycle. Experiments were performed according to animal protocols approved by the Institutional Animal Care and Use Committees at Arizona State University and the Mayo Clinic, Arizona, and the HHMI Janelia Research Campus.

### **2, Macrophage isolation**

Age- and sex-matched mice were injected with 0.5 ml of a sterile 4% solution of Brewer's thioglycollate (TG) (Sigma Aldrich, St. Louis, MO). All animals were humanely

killed 72 h later and macrophages were isolated by lavage with an ice-cold solution of phosphate-buffered saline (PBS, pH 7.4) supplemented with 5 mM EDTA. The cells were collected into tubes precoated with bovine serum albumin (BSA). Macrophages were counted with a Neubauer hemocytometer immediately thereafter.

### **3, IL-4-induced macrophage fusion**

Macrophage fusion was induced as previously described (Faust et al., 2017, 2018). Briefly, cells were applied to various surfaces at a concentration of  $5 \times 10^6$  cells/ml in DMEM/F12 supplemented with 15 mM HEPES (Cellgro, Manassas, VA), 10% fetal bovine serum (Atlanta Biological, Flowery Branch, GA), and 1% antibiotics (Cellgro, Manassas, VA) and incubated in 5% CO<sub>2</sub> at 37°C for 30 min. Nonadherent cells were removed by washing the culture 3–5× with Hank's balanced salt solution (HBSS; Cellgro, Manassas, VA) supplemented with 0.1% BSA. HBSS was removed and the cells were incubated in culture medium for 2 h. IL-4 (10 ng/ml; Genscript, Piscataway, NJ) was applied to cultures until the respective time points. The fusion index (McNally and Anderson, 1995) was used to determine the extent of macrophage fusion. The fusion index is defined as a fraction of nuclei within MGCs expressed as a percentage of total nuclei counted.

### **4, Phase-contrast videomicroscopy**

Macrophages were cultured on Permanox plastic (Thermo Scientific, Waltham, MA), Fluorodishes (World Precision Instruments, Sarasota, FL), or surfaces adsorbed with long-chain hydrocarbons as described previously (Faust et al., 2017). Dishes were

transferred from the cell culture incubator to a stage-top incubator calibrated to maintain a humidified atmosphere of 5% CO<sub>2</sub> in air at 37°C. Phasecontrast images were collected with a 20× or 40× objective every 30 s with an EVOS FL Auto (Thermo Scientific, Waltham, MA) and transferred to ImageJ to create movies.

## **5, LLSM**

The LLSM used in these experiments is housed in the Advanced Imaging Center at the Howard Hughes Medical Institute Janelia research campus. The system was configured and operated as previously described (Chen et al., 2014). Briefly, eGFP-LifeAct and/or mRFP-LifeAct peritoneal macrophages were applied to 5-mm cover glass surfaces adsorbed with long-chain hydrocarbons (Faust et al., 2017, 2018). IL-4 (10 ng/ml) was added and LLSM was conducted 8–10 h thereafter. Samples were illuminated by LLSM using 488- or 560-nm diode lasers (MPB Communications) through an excitation objective (Special Optics, 0.65 NA, and 3.74-mm WD). Fluorescent emission was collected by a detection objective (Nikon, CFI Apo LWD 25XW, 1.1 NA) and detected by an sCMOS camera (Hamamatsu Orca Flash 4.0 v2). Acquired data were deskewed as previously described (Chen et al., 2014) and deconvolved using an iterative Richardson-Lucy algorithm. Point-spread functions for deconvolution were experimentally measured using 200-nm TetraSpeck beads (Invitrogen) adhered to 5-mm glass coverslips for each excitation wavelength.

## **6, Biomaterial implantation**

Animal surgery was conducted according to AVMA Guidelines by protocols approved by both the Mayo Clinic and Arizona State University. Segments ( $1.5 \times 0.5$  cm) of sterile PCTFE were implanted into the peritoneum of age- and sex-matched mice as described (Jay et al., 2007). Animals were humanely killed 14 d later and explants were analyzed for the presence of MGCs. Prior to explantation, 2 ml of PBS containing 5 mM EDTA was aseptically injected into the peritoneum and cells in the peritoneum were collected by lavage. The number of cells in the peritoneum at the time of explantation was determined by counting with a Neubauer hemocytometer. Experiments were conducted in duplicate on three independent days (i.e., total six mice per experiment).

## **7, Immunofluorescence**

At the indicated time point, specimens were fixed with 2% formaldehyde in PBS for 30 min at room temperature. Samples were permeabilized with 2% formaldehyde, 0.1% Triton X-100 in PBS for 30 min, and then washed 3 $\times$  with PBS containing 1% BSA (PBS-BSA). Samples were incubated overnight at 4°C with primary antibodies directed against vinculin and talin (V9131 and T3287 for anti-vinculin and anti-talin, respectively; Sigma Aldrich) and 15 nM Alexa Fluor 488–conjugated phalloidin (Thermo Scientific). The specimens were washed 3 $\times$  with PBS-BSA and incubated with Alexa Fluor–conjugated secondary antibodies (Thermo Scientific) overnight at 4°C. Nuclei were labeled with DAPI according to the manufacturer’s recommendation (Thermo Scientific). Samples were mounted in Prolong Diamond (Thermo Scientific) and imaged with a Leica SP5 and Leica

SP8 laser scanning confocal microscopes. The effect of CK-636 and CK-548 on podosome formation in macrophages labeled with Alexa Fluor 488–conjugated phalloidin was assessed by counting a fraction of cells with >10 podosomes normalized to DMSO control, as previously described (Nolen et al., 2009).

## **8, Statistical analyses**

Unless indicated otherwise results are shown as the mean  $\pm$  SD from three independent experiments. Multiple comparisons were made via ANOVA followed by Tukey's or Dunn's posttest using GraphPad InStat software. Samples that passed the normal distribution test were analyzed by t test. The remaining samples were analyzed by the Mann-Whitney test. Data were considered significantly different if  $p < 0.05$ .



## **2.6 Acknowledgments**

We thank the members of the Ugarova laboratory and the ASU/Mayo Clinic Center for Metabolic and Vascular Biology for helpful discussions. We thank Satya Khuon at HHMI Janelia Research Campus for help with sample preparation for LLSM. During the preparation of this work, J.J.F. was supported by a T32 Fellowship (5T32DK007569-28). The AIC at HHMI Janelia is jointly funded by the Howard Hughes Medical Institute and the Gordon and Betty Moore Foundation. Image data were collected using a Leica TCS SP5 LSCM (National Institutes of Health [NIH] SIG award S10 RR027154) and Leica TCS SP8 LSCM (NIH SIG award S10 OD023691) housed in the W.M. Keck Bioimaging Facility at Arizona State University. This work was supported by NIH grant R01 HL-63199 to T.P.U.

## CHAPTER 3

### TRANSITION OF PODOSOMES INTO ZIPPER-LIKE STRUCTURES IN MACROPHAGE-DERIVED MULTINUCLEATED GIANT CELLS

#### 3.1 Abstract

Macrophage fusion resulting in the formation of multinucleated giant cells (MGCs) is a multistage process that requires many adhesion-dependent steps and involves the rearrangement of the actin cytoskeleton. The diversity of actin-based structures and their role in macrophage fusion is poorly understood. In this study, we revealed hitherto unrecognized actin-based zipper-like structures (ZLSs) that arise between MGCs formed on the surface of implanted biomaterials. We established an *in vitro* model for the induction of these structures in mouse macrophages undergoing IL-4-mediated fusion. Using this model, we show that over time MGCs develop cell-cell contacts containing ZLSs. Live-cell imaging using macrophages isolated from mRFP- or GFP-Lifeact mice demonstrated that ZLSs are dynamic formations undergoing continuous assembly and disassembly and that podosomes are precursors of these structures. Immunostaining experiments showed that vinculin, talin, integrin  $\alpha M\beta 2$ , and other components of podosomes are present in ZLSs. Macrophages deficient in WASp or Cdc42, two key molecules involved in actin core organization in podosomes, as well as cells treated with the inhibitors of the Arp2/3 complex failed to form ZLSs. Furthermore, E-cadherin and nectin-2 were found between

adjoining membranes, suggesting that the transition of podosomes into ZLSs is induced by bridging plasma membranes by junctional proteins.

### **3.2 Introduction**

Cell-cell fusion is a fundamental property of multicellular organisms and occurs in many physiological processes, such as fertilization, bone remodeling, skeletal muscle and placenta formation, and stem cell differentiation (Chen *et al.*, 2007; Aguilar *et al.*, 2013; Podbilewicz, 2014). In addition, cellular fusion has been observed in numerous pathological conditions. In particular, the homotypic fusion of macrophages, leading to the formation of multinucleated giant cells (MGCs), occurs in tissues affected by chronic inflammation, including infectious and non-infectious granulomas (Helming and Gordon, 2007b). Furthermore, MGCs are a prominent component of the foreign body reaction of the host to implanted biomaterials, and their accumulation at the tissue-material interface may persist throughout the lifetime of the implant (Anderson *et al.*, 2008). MGCs adherent to biomaterials is known to produce potent cellular products that have been proposed to degrade the biomaterial, eventually leading to device failure (Zhao *et al.*, 1991; Anderson *et al.*, 2008; Sheikh and Nash, 1996). MGCs are formed from blood monocytes recruited from the circulation to implant surface, where they differentiate into macrophages that undergo fusion. The T-helper 2 cytokine interleukin-4 (IL-4) participates in macrophage fusion *in vivo* (Kao *et al.*, 1995) and is broadly used to study monocyte/macrophage fusion in cell cultures (McInnes and Rennick, 1988; McNally and Anderson, 1995; Moreno *et al.*, 2007; Skokos *et al.*, 2011; Milde *et al.*, 2015).

Cellular fusion is a multistage process, which starts with the cytokine induction of intracellular signaling that programs cells into a fusion-competent state. Adhesion of fusion-competent cells to a permissive substrate, cytoskeletal rearrangements, cell motility, and cell-cell interactions are all important determinants of macrophage fusion (Helming and Gordon, 2009). Most, if not all, of the steps involved in macrophage fusion, appear to rely on the actin cytoskeleton. It has long been known that cytochalasins B and D that prevent actin polymerization also inhibit macrophage fusion (DeFife *et al.*, 1999; Faust *et al.*, 2019). The polymerization of actin filaments is known to be involved in the formation of diverse cellular protrusions, including lamellipodia, filopodia, and podosomes (for review see Ridley, 2011 and Svitkina, 2013). However, the precise targets of actin-disrupting agents that inhibit macrophage fusion have not been identified. Recently, we have characterized the early steps of IL-4-mediated macrophage fusion and showed that an actin-based protrusion at the leading edge initiates macrophage fusion (Faust *et al.*, 2019). Furthermore, we have found that fusion-competent protrusions form at the sites enriched in podosomes.

Podosomes are dot-shaped adhesion complexes formed at cell-matrix contact sites that have been identified in many cell types. Podosomes are especially prominent in cells of the monocytic lineage, including macrophages and dendritic cells, where they are associated with cell adhesion, migration, and matrix degradation (for review see Linder *et al.*, 2011; Murphy and Courtneidge, 2011). Structurally, podosomes consist of a core of Arp2/3-mediated branched actin filaments and actin-regulatory proteins, including WASp and cortactin. The actin core is surrounded by a ring of cytoskeletal adaptor proteins, such as talin, vinculin, and paxillin. Moreover, integrin receptors have been localized in the ring

(Zambonin-Zallone *et al.*, 1989; Pfaff and Jurdic, 2001), with integrin  $\alpha_M\beta_2$  being the predominant integrin in macrophages (van den Dries *et al.*, 2013b) and dendritic cells (Burns *et al.*, 2004). The core and ring are linked by a myosin-IIA-containing network of unbranched actin filaments (Luxenburg *et al.*, 2007; Akisaka *et al.*, 2008; van den Dries *et al.*, 2013b). An additional subset of unbranched actin filaments connects individual podosomes into groups (Bhuwania *et al.*, 2012). Furthermore, a cap at the tip of the actin core consists of formins, fascin, and other proteins (Mersich *et al.*, 2010; Van Audenhove *et al.*, 2015; Panzer *et al.*, 2016; Bhuwania *et al.*, 2012). Podosomes are dynamic structures that give rise to different morphologies in diverse cells (for review see Linder *et al.*, 2011). In v-Src-transformed fibroblasts, podosomes form rosettes in cell extensions. In macrophage-derived osteoclasts, initial clusters of podosomes reorganize into rings, which then fuse and finally stabilize as a continuous sealing belt. Recent studies of murine macrophages undergoing osteoclastogenesis in the presence of RANKL and osteoclasts induced in mouse bone marrow cells by RANKL/M-CSF have demonstrated podosome-related actin-based zipper-like structures (Takito *et al.*, 2012; Takito *et al.*, 2017) that form at the site of cell-cell contact. Podosomes are especially dynamic in macrophages where they undergo continuous turnover. Studies on the reorganization of podosomes in mononuclear mouse and human macrophages under nonfusogenic conditions have shown that individual podosomes can fuse into larger structures and then disassemble into smaller clusters (Evans *et al.*, 2003; Kopp *et al.*, 2006; Poincloux *et al.*, 2006). However, little is known about the fate of podosomes in MGCs as these cells undergo maturation *in vitro* and *in vivo*.

In this study, we revealed actin-based zipper-like structures (ZLSs) that form over time

between MGCs undergoing fusion on the surface of biomaterials implanted into mice. We established an *in vitro* model for the induction of these structures in MGCs formed by the IL-4-mediated fusion of mouse macrophages. Using this model, we found that podosomes were the precursors of ZLSs. Moreover, in addition to actin, ZLSs contained other proteins typically found in podosomes. The transition of podosomes into ZLSs appeared to be induced upon the bridging of two plasma membranes by the junctional proteins E-cadherin and nectin-2. Thus, a novel actin-based structure was identified in macrophages undergoing fusion on implanted biomaterials, which may provide a potential target for blocking MGC formation.

### **3.3 Results**

#### **1, Zipper-like actin structures formed in MGCs following biomaterial implantation**

While studying the foreign body reaction to implanted biomaterials in mice, we observed heretofore unrecognized actin-based structures formed at the contact sites between MGCs. In these experiments, polychlorotrifluoroethylene (PCTFE) sections were implanted into the peritoneal cavity of C57BL/6J mice, and the formation of MGCs was monitored after 3, 7, and 14 days by labeling recovered explants with Alexa Fluor 568-conjugated phalloidin and DAPI. Analyses of the samples revealed a progressive accumulation of MGCs on the biomaterial surface (Figure 1A). Furthermore, many MGC-MGC contact sites in the samples retrieved after 7 or 14 days of implantation contained areas with a seemingly symmetric and periodic actin distribution that visually resembled a zipper (Figures 1B). Based on this appearance, we hereafter call this actin pattern the zipper-like structure (ZLS). The ZLSs were first observed on day 7 as assessed by the

measurements of the total ZLS length per high-power field (0.15 mm<sup>2</sup>), and their numbers increased by day 14 (Figure 1C). The majority of ZLSs were observed between MGCs, although they were infrequently seen at the contact sites of MGCs with mononuclear macrophages.

## **2, Formation of ZLSs *in vitro***

To investigate the mechanism of ZLS formation, we established an *in vitro* system that allowed us to generate ZLSs reproducibly. Since PCTFE plastic is not amenable to most imaging techniques, we took advantage of recently developed optical-quality glass surfaces prepared by adsorption of long-chain hydrocarbons such as paraffin that promote high levels of macrophage fusion (Faust *et al.*, 2017; Faust *et al.*, 2018). In this series of experiments, rather than macrophage cell lines, we used primary macrophages isolated from the inflamed mouse peritoneum (Helming and Gordon, 2007a; Podolnikova *et al.*, 2016; Faust *et al.*, 2019) to avoid the robust proliferation observed in the cultures of macrophage cell lines. Using phase-contrast video microscopy, we determined that the kinetics of IL-4-induced macrophage fusion on paraffin-coated glass (P-surface) were similar to that on PCTFE (Figure 2A and B). The cell fusion began 8–9 h on both surfaces after the addition of IL-4, and the maximum number of fusion events occurred after 16–20 h and then gradually declined. Furthermore, as determined by the measurements of the fusion index, the period between hours 9 and 24 was the most active period of fusion on both surfaces (Figure 2C).

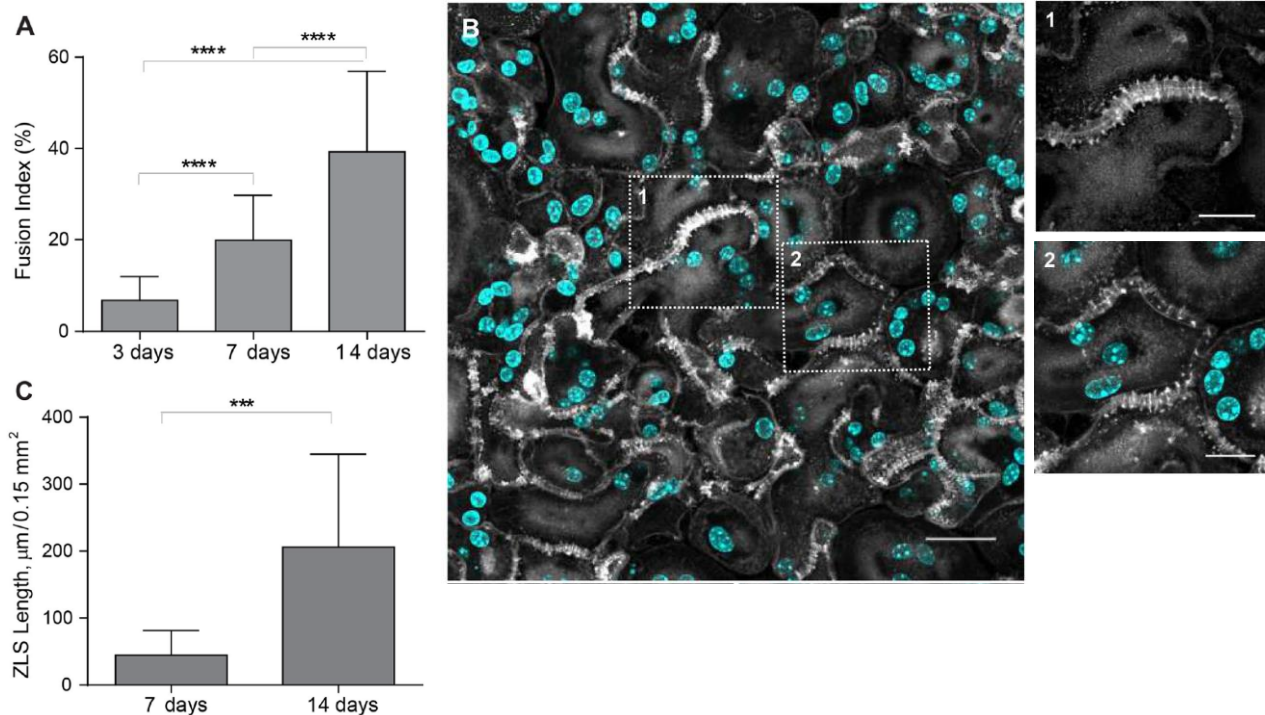
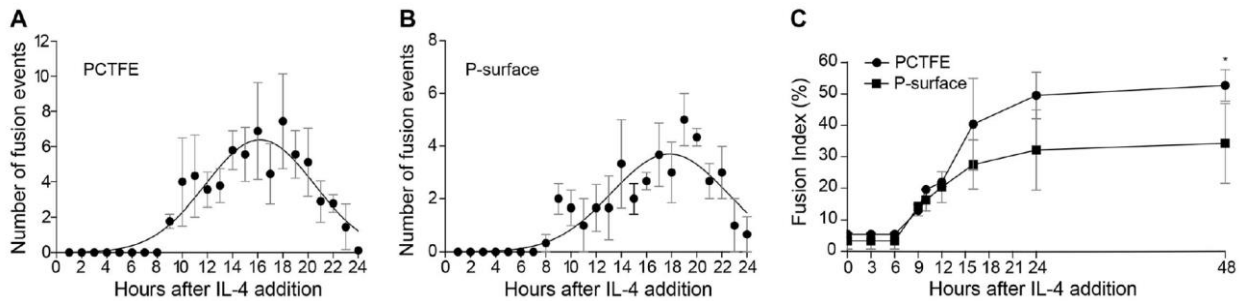


**Figure 1. Formation of zipper-like structures (ZLSs) in MGCs following biomaterial implantation.** (A) Sections of the PCTFE implanted into the peritoneal cavity of mice were recovered 3, 7, and 14 days after surgery. Explants were fixed and labeled with Alexa Fluor 546-conjugated phalloidin (white) and DAPI (teal). Macrophage fusion was assessed as a fusion index, which determines the percent of cells with three or more nuclei. Results shown are mean  $\pm$  S.D. of three independent experiments. Three-to-five random 20 $\times$  fields were used per sample to count nuclei. \*\*\*\* $p < .0001$ . (B) Upper panel, a representative image of MGCs formed on the surfaces of the implants recovered at day 14 post-surgery. The scale bar is 20  $\mu\text{m}$ . Bottom panels, high magnification views of the boxed areas 1 and 2 shown in B. The scale bars are 10  $\mu\text{m}$  and 15  $\mu\text{m}$  for images 1 and 2, respectively. (C) The time-dependent formation of ZLSs on the PCTFE sections explanted at days 7 and 14 post-surgery. The formation of ZLSs was assessed as the total length of ZLSs per high-power field (0.15  $\text{mm}^2$ ), and the determination was made using ImageJ. Results shown are mean  $\pm$  SD of three independent experiments. \*\*\* $p < .001$ .



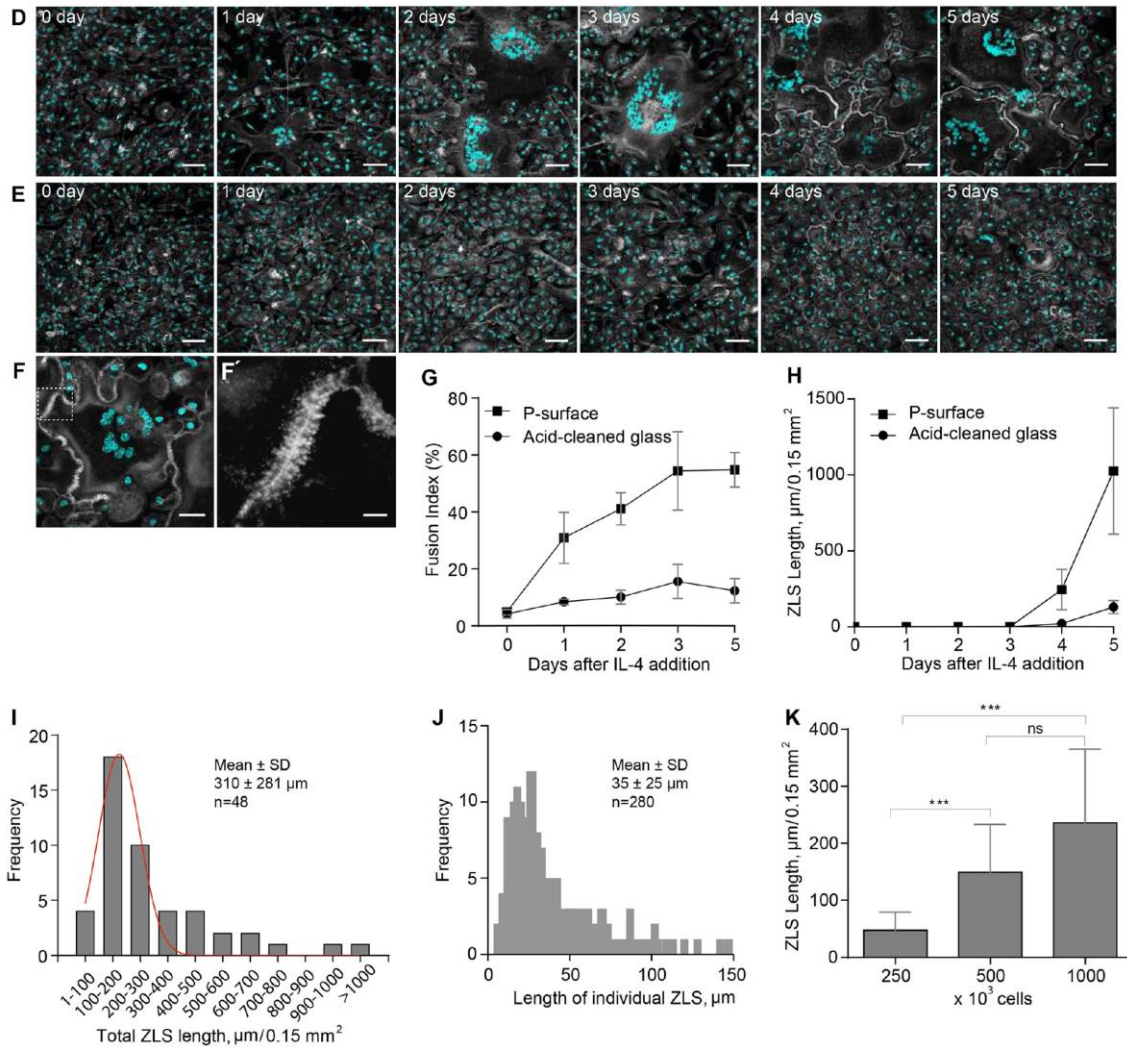


**Figure 2. Kinetics of macrophage fusion and ZLS formation *in vitro*.** (A, B) Macrophages were isolated from the mouse peritoneum 3 days after TG injection and plated on PCTFE sections (20 × 20 mm) or paraffin-coated cover glasses (P-surface) at 5000 cells/mm<sup>2</sup> in DMEM/F12 supplemented with 10% FBS, and fusion was induced by the addition of IL-4 (10 ng/ml). The number of fusion events at different times was determined using phase-contrast video microscopy. Results shown are mean ± SD of three-four independent experiments. (C) The fusion indices of macrophages plated on PCTFE or P-surface determined at different time points. Results shown are mean ± SD of three independent experiments. Three-to-five random 20× fields were used per sample to count nuclei (total ~6000 nuclei). (D, E) TG-elicited peritoneal macrophages were seeded at 5000 cells/mm<sup>2</sup> on paraffin-coated (D) or acid-cleaned (E) cover glasses and fusion was induced by the addition of IL-4 (10 ng/ml). Representative images of fusing macrophages taken at different time points are shown. The scale bars are 50 μm. (F) A representative image of an MGC formed in the 5-day culture of fusing macrophages on the P-surface. The scale bar is 30 μm. (F') High magnification view of a boxed area in F. The scale bar is 5 μm. (G) The time-dependent fusion of IL-4-induced macrophages on the P-surface or acid-cleaned glass. Results shown are mean ± SD of three independent experiments. (H) The total lengths of ZLSs in MGCs formed on the P-surface or acid-cleaned glass for 5 days. Results shown are

mean  $\pm$  SD of three independent experiments. Three-to-five random 20 $\times$  fields were used per sample to determine the ZLS length by Image J. **(I)** The frequency distribution of the total ZLS lengths/high power field in MGCs formed in the 5-day culture (n = 48). **(J)** The frequency distribution of individual ZLS lengths (n = 280). **(K)** The total lengths of ZLSs formed in the 5-day cultures of macrophages plated at different densities. Results shown are mean  $\pm$  SD of three independent experiments. Three-to-five random 20 $\times$  fields were used per sample to determine the length. \*\*\* $p < .001$ ; ns, nonsignificant.

Based on this similarity, we used P-surfaces in subsequent experiments. Since we were unable to detect ZLSs after 48 h, the duration of incubation was extended to 5 days. Although the size of MGCs did not significantly change after 2 days (Supplemental Figure 1), they acquired a more round morphology by day 4 relative to the irregularly shaped MGCs formed at earlier times (Figure 2D). In addition, contacts between apposing MGCs became more frequent, with many regions displaying ZLSs (Figure 2D and F, F'). ZLS formation appeared to have correlated with the fusion index inasmuch as only the limited number of ZLSs was detected on poorly fusogenic acid-cleaned glasses (Fig. 2E, G and H). The total length of ZLSs at day 5 ranged between a minimum of  $\sim 50$   $\mu\text{m}$  and a maximum of  $\sim 1460$   $\mu\text{m}$ /high power field (Figure 2I), and the average length of individual ZLSs was  $35 \pm 25$   $\mu\text{m}$  and varied between 6  $\mu\text{m}$  and  $\sim 150$   $\mu\text{m}$  (Figure 2J). Furthermore, increasing the seeding cell density increased the total ZLS length (Figure 2K), suggesting that contact between cells is essential for ZLS formation. After 5 days, the MGCs and mononuclear macrophages attached to P-surface remained viable as determined by the trypan blue exclusion test (Supplemental Table 1). Based on the examination of confocal images (Figures 1B and 2, D and F), the pattern of actin distribution within ZLSs formed *in vitro* and *in vivo* appeared to be indistinguishable. In subsequent experiments, the 5-day time point was chosen to allow for sufficient ZLS formation.

### **3, The three-dimensional pattern of the actin distribution in ZLS**

To examine whether ZLSs had a specific pattern, we determined their dimensional parameters using samples from 5-day MGC cultures labeled with Alexa Fluor 568-conjugated phalloidin. The periodicity of the actin distribution in ZLSs was determined from the x-y planes (Figure 3, A and B), and the height and width from the scans of fluorescence intensity of the x-z sections (Figure 3C). Actin was organized into large and small globules that formed two closely spaced “humps” originating from each MGC (Figure 3C). The average maximum height of the humps was  $2.9 \pm 0.5 \mu\text{m}$  ( $n = 64$ ; 40 cells), and the average width was  $4.8 \pm 0.9 \mu\text{m}$  ( $n = 196$ ; 30 cells). The distribution of the height and width values of the actin humps is shown in Supplemental Figure 2. The humps were closely abutting at the site of cell-cell contact. (Figure 3C). The average height of the region of close apposition was  $1.2 \pm 0.3 \mu\text{m}$  ( $n = 40$ ; 20 cells). The average periodicity of the main actin foci seen in ZLSs was  $2.1 \pm 0.4 \mu\text{m}$  ( $n = 71$ ; 30 cells) (Figure 3B, arrowheads, and Figure 3F). By fitting the diameter value distribution of the bottommost region of the large globules with a bimodal Gaussian formula, two populations were identified (Figure 3G) with average diameters of  $1.2 \pm 0.2 \mu\text{m}$  and  $2.0 \pm 0.3 \mu\text{m}$  ( $n = 100$ ). Another feature observed in the x-y plane was the areas of actin organization that appeared as closely spaced small globules lying along the plasma membrane of two apposing MGCs (Figure 3B, arrows). The images acquired by structured illumination microscopy (SIM) showed additional details of this area (Figure 3, D and E). The space between the plasma membranes was clearly seen with small actin globules ( $0.24 \pm 0.06 \mu\text{m}$  in diameter) positioned at seemingly regular intervals ( $0.2 \pm 0.1 \mu\text{m}$ ) at the cytosolic face of the

membrane (Figure 3H). In the x-y plane, it appeared that large foci were connected to small foci by thin filaments, although such filaments were not clearly seen in some locations. Together, these analyses suggest that the actin distribution pattern in ZLS is relatively uniform.

#### **4, ZLSs are transient actin-based arrangements formed from podosomes**

Upon close examination of adjoining cells (Figures 4), we noticed that the regions of the plasma membranes just preceding the ZLSs contained actin puncta (Figure 4, enlarged boxes 1 and 2, arrows). Furthermore, actin puncta were seen in the vicinity of ZLSs (Figure 4, enlarged boxes 1 and 2, arrowheads). The actin puncta contained rings of vinculin and talin circumscribing a central actin core (Supplemental Figure 3), suggesting that these structures were podosomes, a characteristic feature of macrophages. Podosomes were often assembled into clusters of two or three podosomes which were also surrounded by vinculin and talin. The size of individual podosomes (~0.7  $\mu\text{m}$ ), as well as those in clusters, was in agreement with that determined previously in living MGCs and in fixed samples (Faust et al, 2019). Mononuclear macrophages that were observed close to MGCs also contained numerous circumferential podosomes (Figure 4, left bottom quadrant). While mononuclear macrophages occasionally formed short ZLSs with MGCs (Figure 4, enlarged box 3), they did not form ZLSs with each other. The presence of podosomes in close proximity to the site of the MGC-MGC apposition suggested that podosomes might be precursors of ZLSs. To examine whether ZLSs originate from podosomes, we performed live-cell imaging using mRFP- or eGFP-LifeAct macrophages, which were fused by IL-4 induction for 5 days. Surprisingly, ZLSs were not as stable as appeared in

the fixed specimens

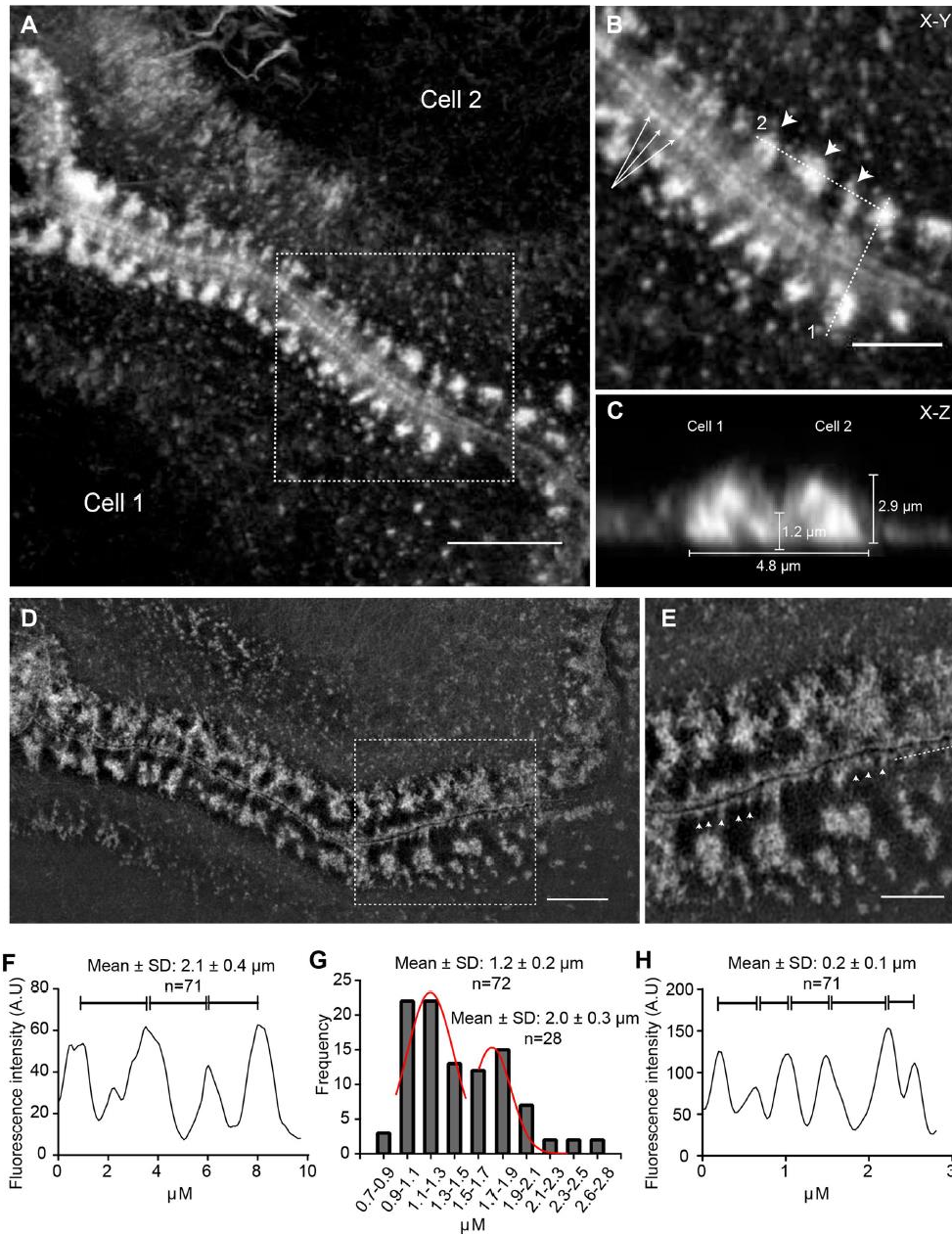


**Figure 3. Three-dimensional pattern of actin distribution in ZLS.** (A) MGCs formed in a 5-day culture were labeled with Alexa Fluor 568-conjugated phalloidin, and confocal images were used to analyze actin distribution in ZLSs. A representative deconvolved x-y confocal plane of a ZLS close to the substrate is shown. The scale bar is 5  $\mu\text{m}$ . (B) High magnification image of the boxed area in A. The arrowheads point to the main actin foci, and arrows point to small actin globules adjacent to the plasma membranes. The scale bar is 2.5  $\mu\text{m}$ . (C) The z-scan through line 1 in B demonstrates a cross-section through the ZLS and illustrates the localization of actin in two adjacent humps. Numbers indicate the averaged dimensional parameters of

the ZLS. **(D)** Imaging of MGCs labeled with Alexa Fluor 568-conjugated phalloidin using SIM. The scale bar is 5  $\mu\text{m}$ . **(E)** A high magnification image of the boxed area in **D**. Arrowheads indicate membrane-adjacent actin globules. The scale bar is 2.5  $\mu\text{m}$ . **(F)** The scan of fluorescence intensity (in arbitrary units) along dotted line 2 indicated in **B**. **(G)** The size distribution of the large actin globules. **(H)** The scan of the fluorescence intensity (in arbitrary units) along a dotted line shown in **E**.

analyzed by immunofluorescence but were rather dynamic. The ZLSs formed from actin puncta, remained seemingly stable for some time and then disassembled into actin puncta. As shown in Figure 5A and Video 1, a nascent ZLS (00:00 min; yellow and white arrows show the top and bottom borders of the ZLS, respectively) was undergoing further organization and elongation (2:00–06:00 min). The subsequent growth of this ZLS downward from a pool of adjacent podosomes was concomitant with its disassembly upstream (Figure 5A, 10:00–22:00 min). A cloud of actin puncta emerging from the disassembled ZLS remained near the plasma membrane. Another area of the ZLS assembly and disassembly is shown in Figure 5B and Video 2. The dismantlement of the ZLS, in this case, resulted in the separation of the two MGCs (Figure 5B; 35:00 min). The amount of time during which the membranes between different MGCs remained joined by ZLSs was  $12.8 \pm 3.5$  min ( $n = 20$ ). No correlation between the length of the ZLSs and time was found (Supplemental Figure 4). To determine whether podosomes give rise to large actin globules in the ZLS we conducted a series of live-cell imaging experiments performed with a better temporal resolution ( $\sim 7$ -s per image for 15-20 min). Tracking individual podosomes showed a single actin punctum moving toward the ZLS and then fusing with a nascent large globule, suggesting that large globules grow by sequential addition of actin from podosomes (Figure 6A and Video 3). The large globules could also grow by accumulating small clusters consisting of two or three podosomes (Supplemental Figure 5). We

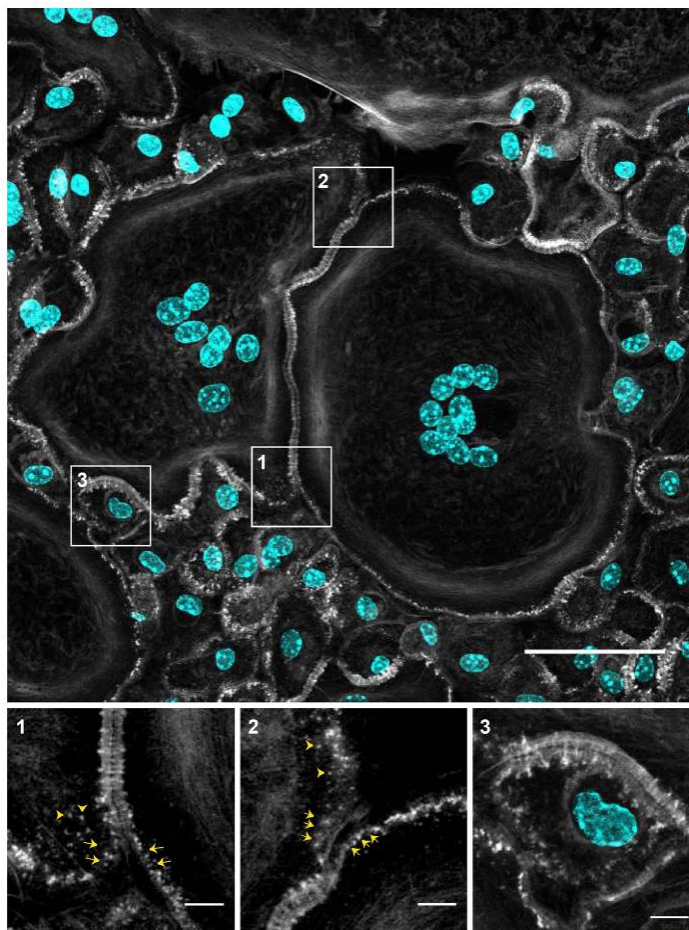


**Figure 4. Podosomes as potential precursors of ZLSs.** A representative image of MGCs formed in the 5-day culture of fusing macrophages. Cells were labeled with Alexa Fluor 488-conjugated phalloidin (white) and DAPI (teal). Many areas of contact between MGCs and MGC-mononuclear cells contain ZLSs, which are observed at the sites where two plasma membranes decorated with podosomes adjoin. The scale bar is 50  $\mu\text{m}$ . High magnification images of the boxed areas (1-3) illustrate the possible formation of ZLSs from podosomes. The scale bars are 5  $\mu\text{m}$ .

also observed that large globules can be fragmented into actin puncta. As shown in Figure 6B and Video 4, a large globule began to fragment into two smaller globules that were still associated with the ZLS. This behavior suggests that ZLSs are highly dynamic with large globules undergoing continuous turnover.

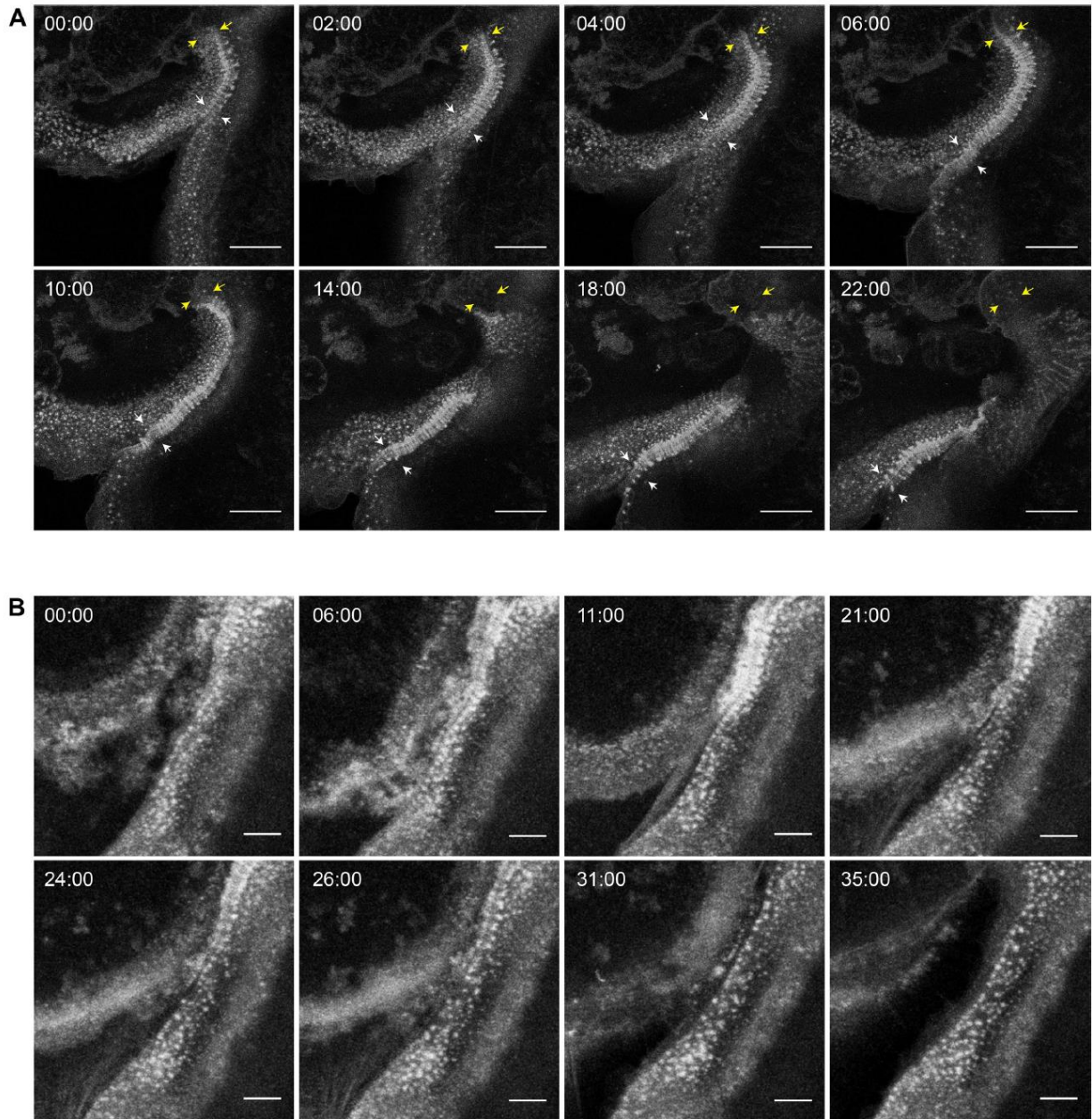


**Figure 5. Live-cell imaging of ZLS formation.** (A) Frames from a representative live-cell imaging experiment showing the formation of a ZLS between two MGCs formed in a 5-day culture of IL-4-induced macrophages isolated from mice expressing mRFP-LifeAct. Yellow and white arrows indicate the initial upper and bottom boundaries of the nascent ZLS, respectively (00:00 min). After the period of maturation and elongation (02:00-10:00 min), the upper part of the ZLS disassembles (10:00-22:00 min). The scale bar is 20  $\mu$ m. See also Video 1. (B) Frames from a movie showing the formation and disassembly of another ZLS between MGCs derived from EGFP-LifeAct macrophages. The scale bar is 5  $\mu$ m.



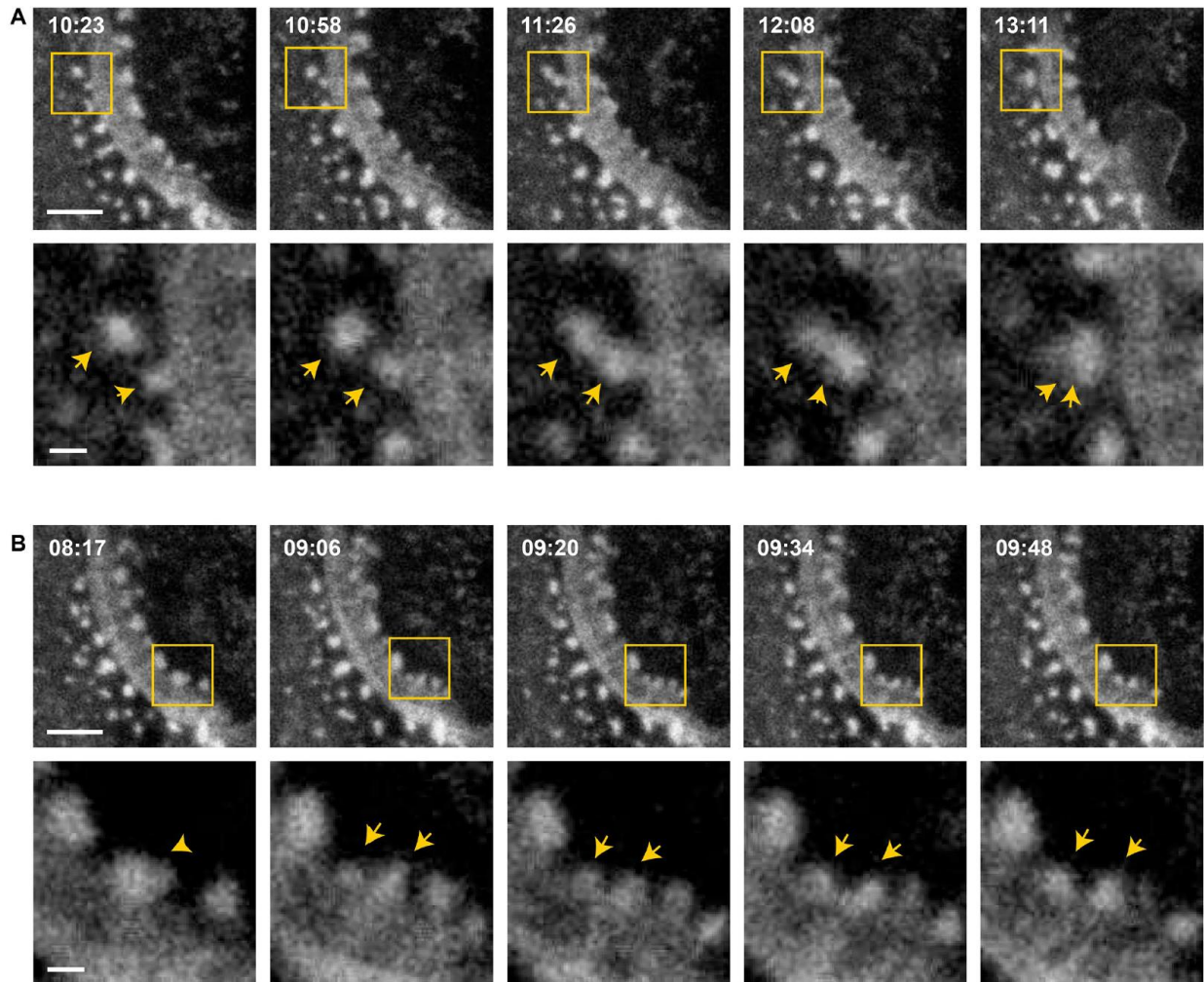
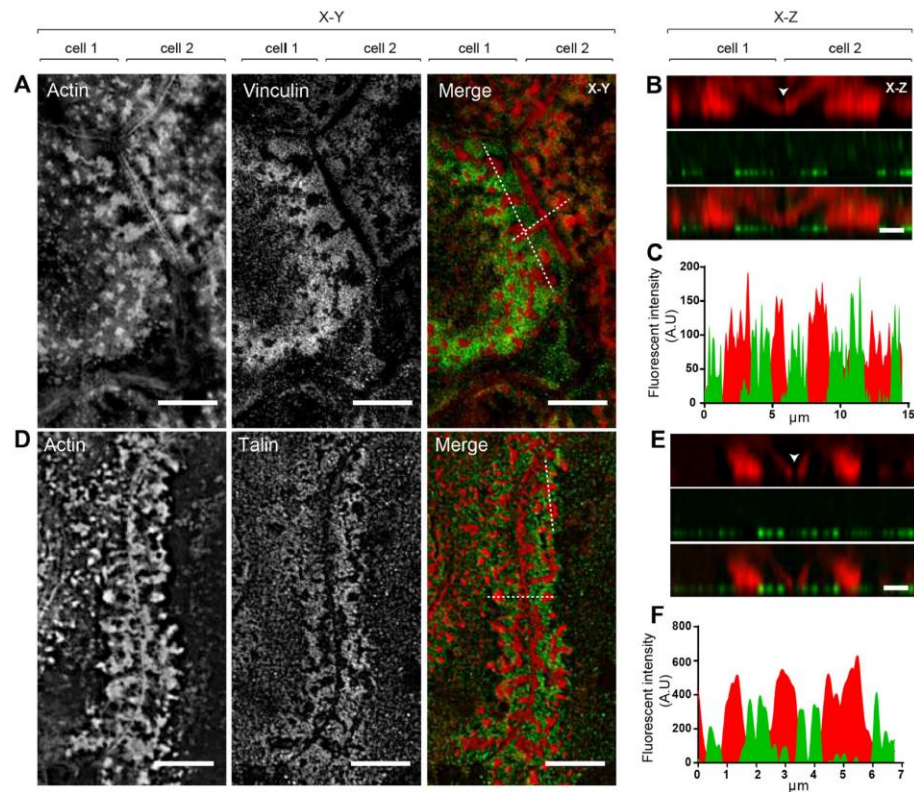


**Figure 6. Large globules in the ZLS grow by the addition of podosomes.** (A) Frames from a representative live-cell imaging experiment (n=9) showing fusion of a single podosome with a nascent large globule in the ZLS (*upper panel*). *Bottom panels*: high magnification images of the boxed areas. Arrows indicate two fusing actin puncta. The scale bars in the upper panels are 5  $\mu\text{m}$  and 1  $\mu\text{m}$  in the lower panels. (B) Frames from a representative live-cell imaging experiment (n=10) showing fragmentation of a large globule (*upper panels*). *Bottom panels*: high magnification images of the boxed areas. Arrowheads indicate an initial large globule which is fragmented giving rise to a smaller daughter globule (arrows). The scale bars in the upper panels are 5  $\mu\text{m}$  and 1  $\mu\text{m}$  in the lower panels.

## **5, ZLSs contain proteins found in podosomes**

Further evidence for the podosome origin of ZLSs was obtained by immunofluorescence experiments using antibodies that recognize proteins usually found in podosomes. The defining feature of podosomes is the presence of the core of actin filaments (Linder et al., 2000; Kaverina et al., 2003) surrounded by adhesive plaque proteins, such as talin, vinculin, and integrins (Zambonin-Zallone et al., 1989; Pfaff and Jurdic, 2001). As shown in Figure 7, vinculin, talin, paxillin, cortactin, and integrin  $\alpha\text{M}\beta\text{2}$  were detected in ZLSs. Furthermore, actin and podosome proteins were enriched on both sides of the plasma membranes. Among the podosome proteins, vinculin and talin localized in the humps, and both proteins encircled the large actin globules (Figure 7, A-F). No colocalization of vinculin or talin with actin was observed in the small globules (Figure 7, B and E). Paxillin was also found to surround the large globules (Figure 7, G and G'). Cortactin colocalized with actin in the large globules and was present in the small globules near the midline between the two MGC membranes (Figure 7, H and H'; arrow in the z section). The area between the humps corresponding to the site of close apposition between the plasma membranes appeared to be void of podosome-associated proteins, except for  $\alpha\text{M}\beta\text{2}$  (Figure 7I and I'). The integrin  $\alpha\text{M}\beta\text{2}$  was present in the midline and also decorated the plasma membrane above the humps. Myosin II, which has been shown to localize in the area surrounding the actin core (Labernadie et al., 2010; van den Dries et al., 2013a) and to enrich in the regions of high podosome turnover (Kopp et al., 2006), was also found in ZLSs (Supplemental Figure 6A). It is known that the Arp2/3 complex and its activators Cdc42 and WASp nucleate the core of actin filaments in podosomes (Linder et al., 2000).

We previously demonstrated that deficiency of WASp or Cdc42, or inhibition of Arp2/3 strongly reduces macrophage fusion and podosome formation (Faust et al., 2019). To examine the importance of these actin regulators in ZLS formation, we isolated macrophages from WASP<sup>-/-</sup> and myeloid-cell-specific Cdc42<sup>-/-</sup> mice and tested their ability to assemble ZLSs. We observed that WASp<sup>-/-</sup> (Figure 8, A, B, E, and F) or Cdc42<sup>-/-</sup> deficient macrophages (Figure 8, C, G, and H) lost their capacities to form ZLSs in correlation with their reduced fusion capacities. In addition, the treatment of wild-type macrophages with wiskostatin, a



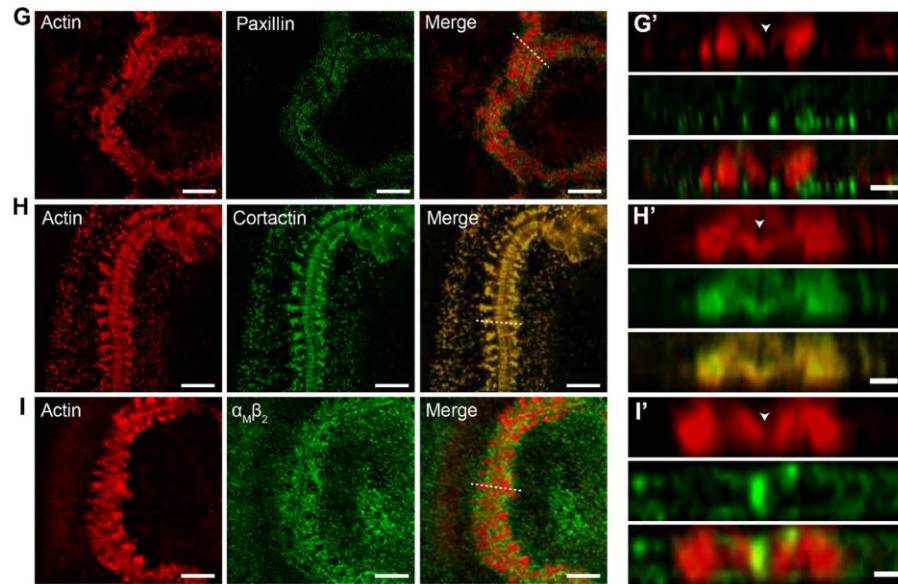


**Figure 7. Localization of podosome-specific proteins in ZLSs.** Representative SIM images of MGCs in the 5-day culture induced by the addition of IL-4 (10 ng/ml) and incubated with anti-vinculin (A), anti-talin (D), anti-paxillin (G), anti-cortactin (H) and anti- $\alpha_M\beta_2$  (I) antibodies followed by corresponding secondary antibodies conjugated to Alexa Fluor 488. Actin was labeled with Alexa Fluor 568-conjugated phalloidin. Confocal x-y planes close to the substrate-attached cell surface show the distribution of actin and podosome-specific proteins. (B, E, G', H', I') The z-scans across the horizontal dotted lines in the merged images shown in A, D, G, H, and I illustrate the distribution of actin and podosome-specific proteins in the humps. The midline, which defines the position of adjoining plasma membranes, is indicated by arrowheads. (C, F) Scans of fluorescence intensity of actin/vinculin and actin/talin, respectively, across the vertical dotted lines (x-y plane) shown in A and D. The scale bars are 5  $\mu\text{m}$  in all x-y sections and 2  $\mu\text{m}$  in all x-z sections.

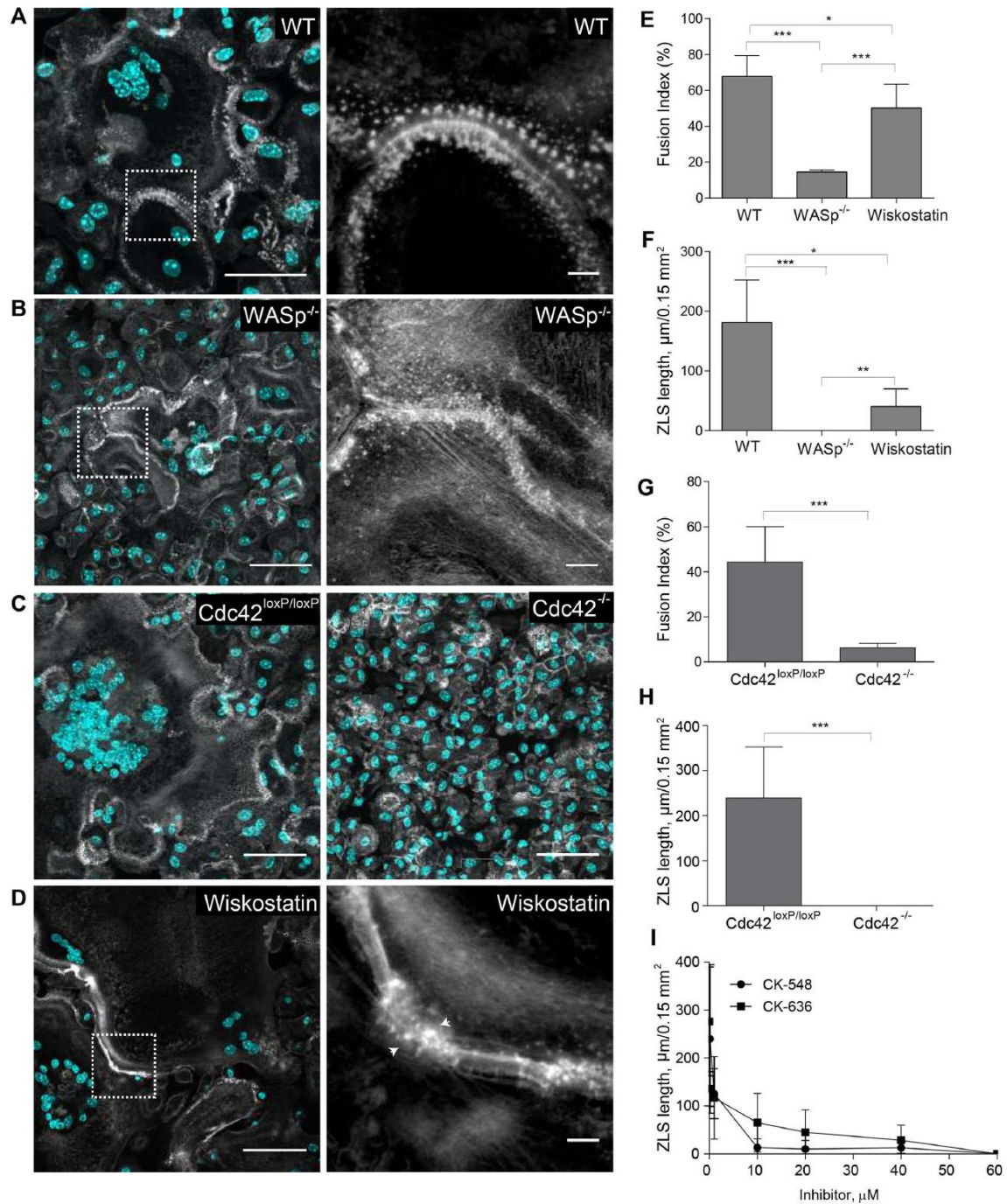
specific inhibitor of WASp, decreased the fusion and total length of the ZLSs (Figure 8D and E, F). Next, we examined whether inhibition of Arp2/3 impaired the ability of wild-type macrophages to form ZLS. As shown in Figure 8I, the Arp 2/3-specific inhibitor CK-636 or CK-548 blocked ZLS formation in a dose-dependent manner. Together with live-cell video microscopy results, these data suggest that ZLSs originate from podosomes.

## 6, Analyses of the junctional proteins within ZLS

Analyses of actin distribution shown in Figure 3 revealed a narrow space between adjoined MGCs, suggesting a very close apposition between the plasma membranes within ZLSs. To examine the interface between the membranes at a higher resolution, we performed transmission electron microscopy (TEM) to examine MGCs formed in the 5-day culture. Analyses of the sections taken parallel the site of the cell attachment to substrate revealed segments of closely apposed plasma membranes with a spacing of  $7.7 \pm 1.3$  nm ( $n= 30$ ) (Figure 9A). Interestingly, the space between two membranes was not empty but filled with a material, which displayed striation in some areas (Figure 9A, inset in the left panel). To determine the nature of these electron-dense “ladders”, we performed confocal microscopy using antibodies against selected proteins, including E-cadherin, nectin-2, JAM-A, and connexin43, which are known to mediate homophilic cell-cell interactions (Figure 9, C-F). The presence of these proteins has previously been reported in activated macrophages (Liu et al., 2000; Eugenin et al., 2003; Pende et al., 2006; Moreno et al., 2007; Van den Bossche et al., 2009). We also labeled cells with the lipophilic membrane stain DiD to mark the midline, which separates the two halves of the ZLS (Figure 9B, arrowhead in the right panel). Labeling with a mAb against the ectodomain of E-cadherin revealed this protein in the ZLSs (Figure 9C). E-cadherin was detected in the midline (x-y plane) and at the apposition site between the humps (x-z section). E-cadherin was also present at the ventral sides of the humps but was mainly excluded from the bodies of the humps. Both nectin-2 (Figure 9D) and JAM-A (Figure 9E) were detected in ZLSs. However, only nectin-2 was found in both the midline and at the apposition site, whereas

JAM-A appeared to have colocalized with actin in the humps. Labeling for afadin, a cytosolic adaptor protein which associates with nectin-2 (Takai et al., 2008), showed its colocalization with actin in the humps (Figure 9F). Connexin43 was not detected in ZLSs. Since the tight junction protein ZO-1 has also been found in macrophages, we labeled ZLSs with antiZO-1 antibody; however, we were unable to detect this protein.

Investigations of E-cadherin and nectin-2 expression during macrophage fusion showed that E-cadherin (Figure 10A) and nectin-2 mRNAs (Supplemental Figure 7) were barely expressed in freshly isolated macrophages. E-cadherin transcript was detected 3 hours after incubation of macrophages in the presence of IL-4. A ~10-fold increase was observed after 12 hours, and this level did not change after 5 days (Figure 10B). Likewise, E-cadherin was poorly expressed on the surface of macrophages before their treatment with IL-4 but gradually increased after the addition of IL-4 (Figure 10, C and D). To investigate the contribution of E-cadherin to the adjoining of the plasma membranes within the ZLS, we treated the cells in a 5-day culture with 1 mM EGTA. As shown in Figures 10, E and F, the treatment of cells with 1 mM EGTA for 5 min resulted in almost complete dissociation of ZLSs. The effect of EGTA was dose-dependent with the concentration of EGTA as low as 0.06 mM reducing the formation of ZLSs by ~90% (Figure 10G). As expected, anti-E-cadherin mAb DECMA-1 strongly inhibited the ZLS formation while isotype control IgG was ineffective (Fig. 10H). These data indicate that E-cadherin is required for generating ZLSs and suggest that this junctional molecule is the chief mediator of ZLS formation.



respectively. **(D)** Effect of wiskostatin (1  $\mu$ M) on the formation of ZLS. Wiskostatin was added simultaneously with IL-4. **(E-H)** Fusion index and the lengths of ZLSs in MGCs derived from WASp- or Cdc42-deficient macrophages or in macrophages treated with wiskostatin. Results shown are mean  $\pm$  SD of three independent experiments. \* $p$  < .05, \*\* $p$  < .05, \*\*\* $p$  < .001 **(I)** Effect of the Arp2/3 inhibitor CK-548 or CK-636 on ZLS formation. The total lengths of ZLSs per high power field (0.15 mm<sup>2</sup>) were determined in MGCs formed in the 5-day cell culture.

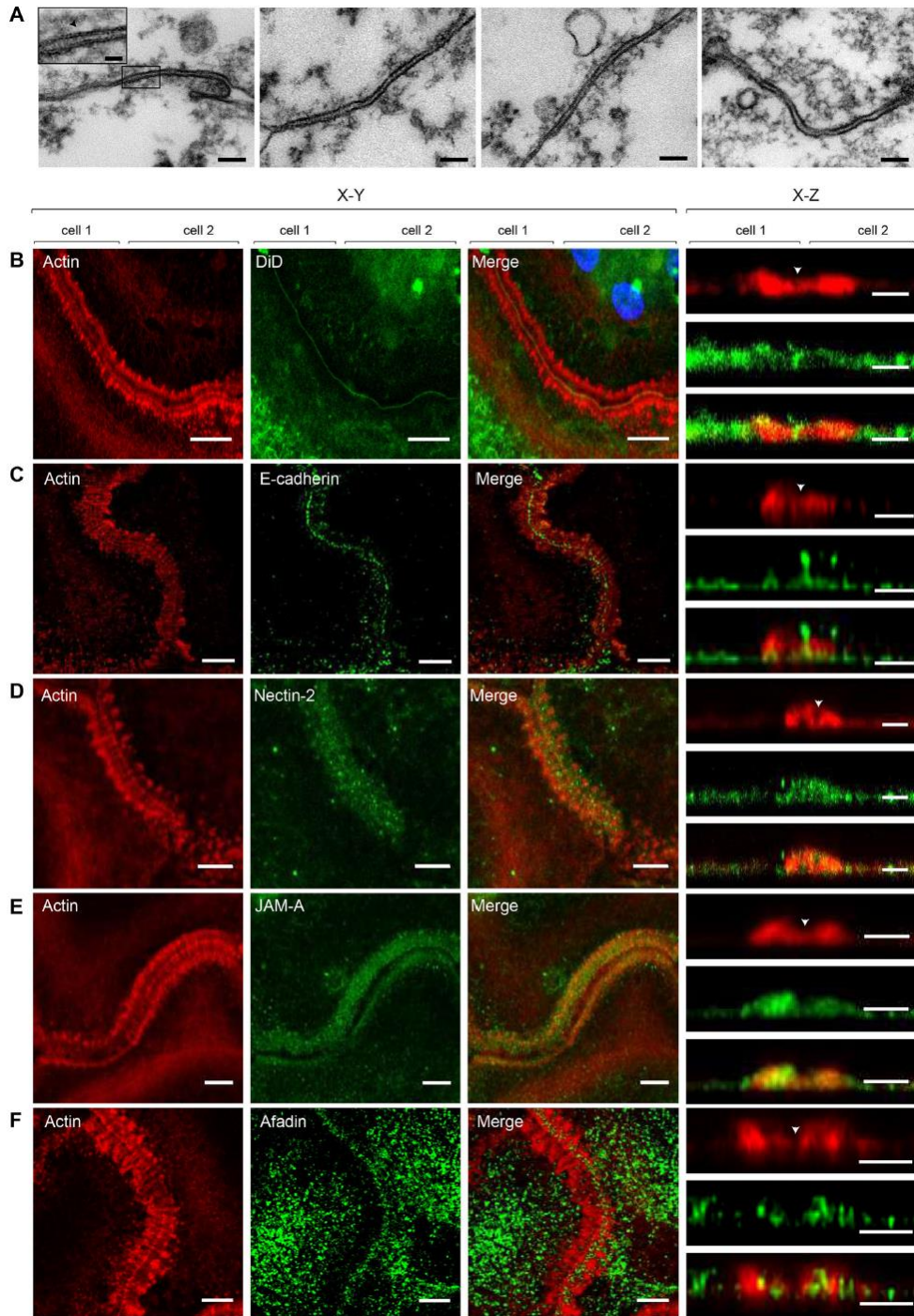




**Figure 9. Analyses of junctional proteins within ZLS.** (A) Ultrastructural details of the intercellular junctions formed in a 5-day MGC examined by TEM. Representative TEM micrographs of the sections prepared by cutting the specimen parallel to the substratum. The scale bar is 100 nm. *Inset* in the left panel is a higher magnification view of the boxed area. The scale bar is 20 nm. (B-F) MGCs in the 5-day culture were labeled with DiD (B) or incubated with anti-E-cadherin (C), anti-nectin-2 (D), JAM-A (E), or anti-afadin (F) antibody followed by corresponding secondary antibodies conjugated to Alexa Fluor 488. Actin was labeled with Alexa Fluor 568-conjugated phalloidin. The x-y confocal planes close to the cell-substratum attachment side (200 nm; *left panels*) and the x-z sections of the z stack (*right panels*) are shown. The scale bars are 5  $\mu\text{m}$  and 2.5  $\mu\text{m}$  for the x-y and x-z planes, respectively.

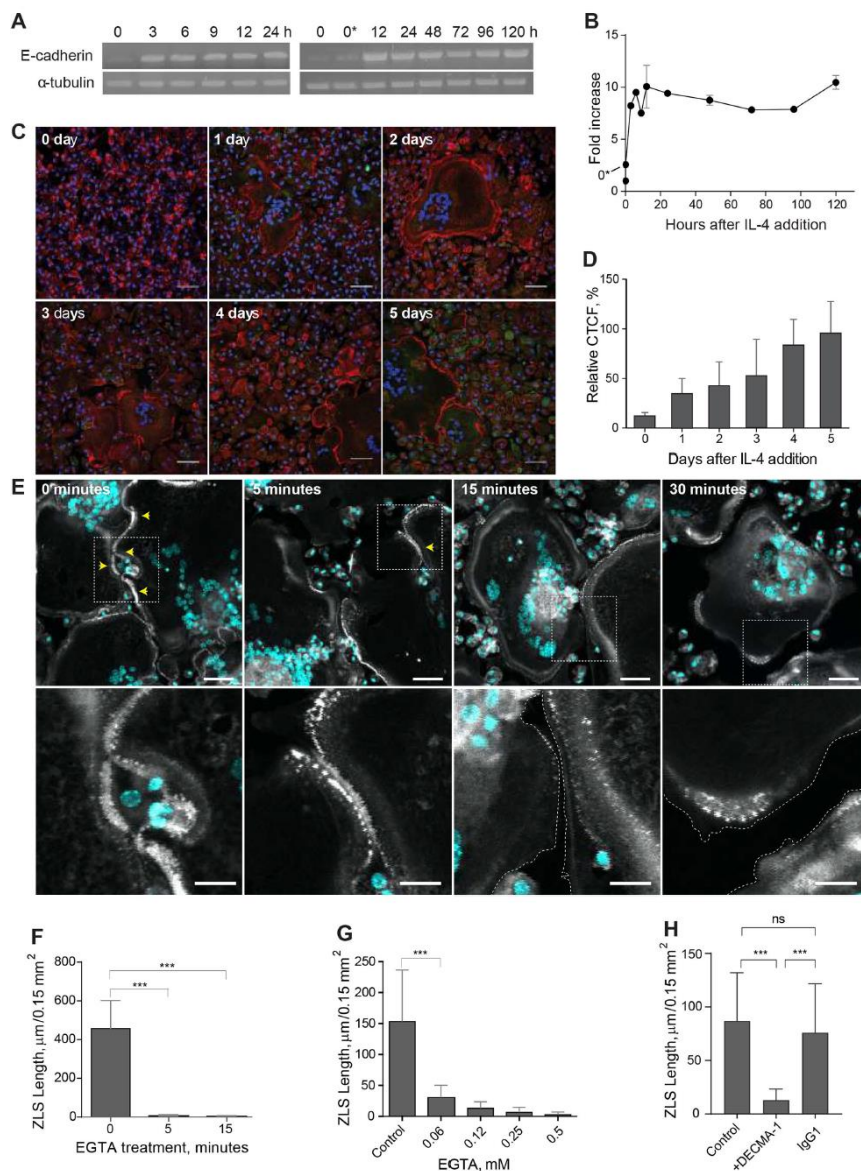


**Figure 10. Analyses of E-cadherin expression in fusing macrophages and its role in ZLS formation.** (A, B) A time course of E-cadherin mRNA expression in macrophages undergoing fusion in the presence of IL-4, as determined by RT-PCR. Signal intensities were normalized to that of  $\alpha$ -tubulin mRNA, and fold change was determined relative to the control mRNA levels in freshly isolated TG-elicited macrophages (0). 0\*, unstimulated macrophages adherent for 2 h before the addition of IL-4. Results shown are mean  $\pm$  SD of three independent experiments. (C) Time-dependent expression of E-cadherin in fusing macrophages was quantified using immunofluorescence with anti-E-cadherin mAb followed by a secondary Alexa Fluor 546-conjugated goat anti-mouse antibody. Nuclei are stained with DAPI (teal). Representative images of E-cadherin expression for each time point are shown. The scale bar is 50  $\mu$ m. (D) Quantification of fluorescence intensities of images of E-cadherin expression shown in C. Data shown are mean  $\pm$  SD of three independent experiments. (E) Effect of EGTA on ZLS formation. Cells in the 5-day culture of IL-4-induced macrophages were treated with 1 mM EGTA for various periods (5–30 min). Vehicle buffer (0 min) was added to the control cells. *Upper panel:* After washing, samples were fixed and labeled with Alexa Fluor 546-conjugated phalloidin (white) and DAPI (teal). *Bottom panel:* High magnification views of the boxed areas shown in the upper panel. (F) The total lengths of ZLSs in the control (0 min) and EGTA-treated cells. Results shown are mean  $\pm$  SD of three independent experiments. (G) Dose-dependent effect of EGTA on ZLS formation. Cells in the 5-day culture of IL-4-induced macrophages were treated with different concentrations of EGTA (0–0.5 mM) for 5 min, and the total lengths of ZLSs were determined. Results shown are mean  $\pm$  SD of three independent experiments. (H) Effect of the anti-E-cadherin mAb DECMA-1 on ZLS formation. DECMA-1 (10  $\mu$ g/ml) or isotype control IgG (10  $\mu$ g/ml) were added to MGCs in the 5-day culture for 1 hour before fixing the cells. Results shown are mean  $\pm$  SD of three independent experiments. \*\*\* $p < .001$

### 3.4 Discussion

In this study, using an *in vivo* biomaterial implantation model we revealed actin-based zipper-like structures that arise at the sites of contact between large macrophage-derived MGCs. We reproduced the process of the formation of these structures *in vitro* and characterized their composition. Several lines of evidence indicate that ZLSs are transient dynamic structures that are formed from podosomes and disassembled into podosomes. First, the plasma membranes of two cells immediately preceding the ZLS are arrayed with podosomes. Second, podosome-specific proteins talin, vinculin, paxillin, cortactin, and integrin  $\alpha$ M $\beta$ 2 are the components of ZLSs. Third, live-cell imaging using macrophages isolated from eGFP- or mRFP-LifeAct mice enabled direct visualization of the origin of ZLS from podosomes. Lastly, the organization of ZLSs requires the Arp2/3 nucleation-promoting factors WASp and Cdc42, and the Arp2/3 complex, three proteins that are also involved in podosome formation. The intercellular space between the apposing plasma

membranes within ZLSs is filled with the junctional proteins E-cadherin and nectin-2, suggesting that homophilic interactions between these molecules induce ZLS assembly. In three dimensions, ZLSs show a characteristic pattern of actin distribution. Actin is mainly concentrated in large globules that are distributed with a regular spacing of  $\sim 2.1 \mu\text{m}$  on each side of the plasma membrane of two abutting cells (Figure 3 and schematically shown in Figure 11). In addition, actin forms the second array consisting of small globules positioned in the immediate proximity to the plasma membrane. Video recordings revealed that large actin globules are assembled from podosomes or small podosome clusters that concentrate in the vicinity of nascent ZLSs (Figures 5 and 6, and Videos 1-3). Dynamic clusters of podosomes have previously been reported in LPS- and  $\text{INF}\gamma$ -stimulated IC-21 mouse macrophages in which podosomes fuse to form transient actin-containing clusters that vary in size (Evans et al., 2003). Likewise, LPS/ $\text{INF}\gamma$  treatment of human monocyte-derived macrophages causes podosomes to cluster (Poincloux et al., 2006). The size heterogeneity of the actin core has also been observed in dendritic cells, in which a population of podosomes undergoes fusion or fission (van den Dries et al., 2013a). Therefore, it appears that large actin globules in ZLSs arise by acquiring new podosomes. As determined from the fluorescence micrographs of fixed specimens (Figure 3G), two populations of large globules were identified with average diameters of  $1.2 \pm 0.2 \mu\text{m}$  and  $2.0 \pm 0.3 \mu\text{m}$ . These diameters are greater than that of individual podosomes ( $0.7 \pm 0.2 \mu\text{m}$ ), suggesting that at the cell-substrate surface, large globules may contain 2–3 individual podosomes. However, since the height of large globules is  $\sim 2.9 \mu\text{m}$  and the reported height of podosomes is  $0.4\text{--}0.6 \mu\text{m}$  (Linder, 2007; Labernadie et al., 2010), the calculated volume

of large globules and podosomes is  $\sim 1.2 \mu\text{m}^3$  and  $\sim 0.17 \mu\text{m}^3$ , respectively, based on the assumption of their shape as a circular, slightly truncated cone (Linder, 2007). These values imply that large globules can theoretically accumulate actin from  $\sim 7$  individual podosomes. However, while podosome clusterization at the cell-substrate surface can be readily envisioned, how large globules grow in the z dimension is unclear. Nonetheless, the relatively uniform dimensions of ZLSs suggest that only a limited number of podosomes can supply actin to large globules, indicating that their size is regulated. A striking feature of ZLSs is that actin foci, large or small, are correctly aligned against each other on both sides of the cell-cell interface and equidistant from the plasma membrane, implicating undefined scaffold proteins in ZLS formation. It is worth noting that a distinctive pattern of actin distribution is clearly seen only in the x-y plane and cannot be easily discerned in the z-direction, especially in the region adjacent to the plasma membrane (Figure 3 and schematically shown in Figure 11). The z scans show that actin within large globules is connected with actin in small globules, although its nature, as well as that of small globules, is not clear. The humps formed of large and small actin globules also contain proteins typically found in podosomes, including talin, vinculin, paxillin, cortactin, and integrin  $\alpha\text{M}\beta 2$  (Figures 7 and 11). Among these proteins, talin and vinculin encircle actin cores in large foci (Figure 7, A-F). The distribution of cortactin and  $\alpha\text{M}\beta 2$  differs from that of other proteins (Figure 7). Interestingly, both cortactin and  $\alpha\text{M}\beta 2$  were observed in the midline, suggesting that these proteins are positioned close to the membrane. However, since  $\alpha\text{M}\beta 2$  was detected using mAb M1/70 directed against the ligandbinding domain of integrin, these data indicate that  $\alpha\text{M}\beta 2$  is present in the intercellular space. In the scheme shown in

Figure 11, we take this distribution of actin and ZLS-associated vinculin and talin into account, although further studies are required to determine the complex organization of a ZLS. The ZLSs formed only after a prolonged period of adhesion of MGCs to the surface of biomaterials *in vivo* and after several days of incubation with IL-4 in a culture medium *in vitro*. By this time, the majority of MGCs appear as large spread cells that form extensive contacts with each other, apparently facilitating ZLS formation. Our live-cell is apparently enacted by E-cadherin and nectin-2, which are detected in the intercellular space of ZLSs. In agreement with previous data (Moreno et al., 2007; Van den Bossche et al., 2009), E-cadherin mRNA was poorly detected in freshly isolated macrophages but was gradually expressed. The live-cell imaging analyses revealed that ZLSs are dynamic structures with an average lifespan of ~13 min. Notably, the assembly of ZLSs seems to occur in a sequential manner, visually resembling a fastener that moves in one direction, “zippering up” plasma membranes. The zippering mechanism peaked within 12 hours of IL-4 addition and remained stable after 5 days. Moreover, while the protein was weakly expressed on the surface of freshly plated macrophages, its expression was readily detectable by 24 h and gradually upregulated over 5 days (Figure 10). Since ZLSs were first detected at day 4, either the critical level of E-cadherin or the required level of cell spreading or both may be an essential requisite of ZLS formation.

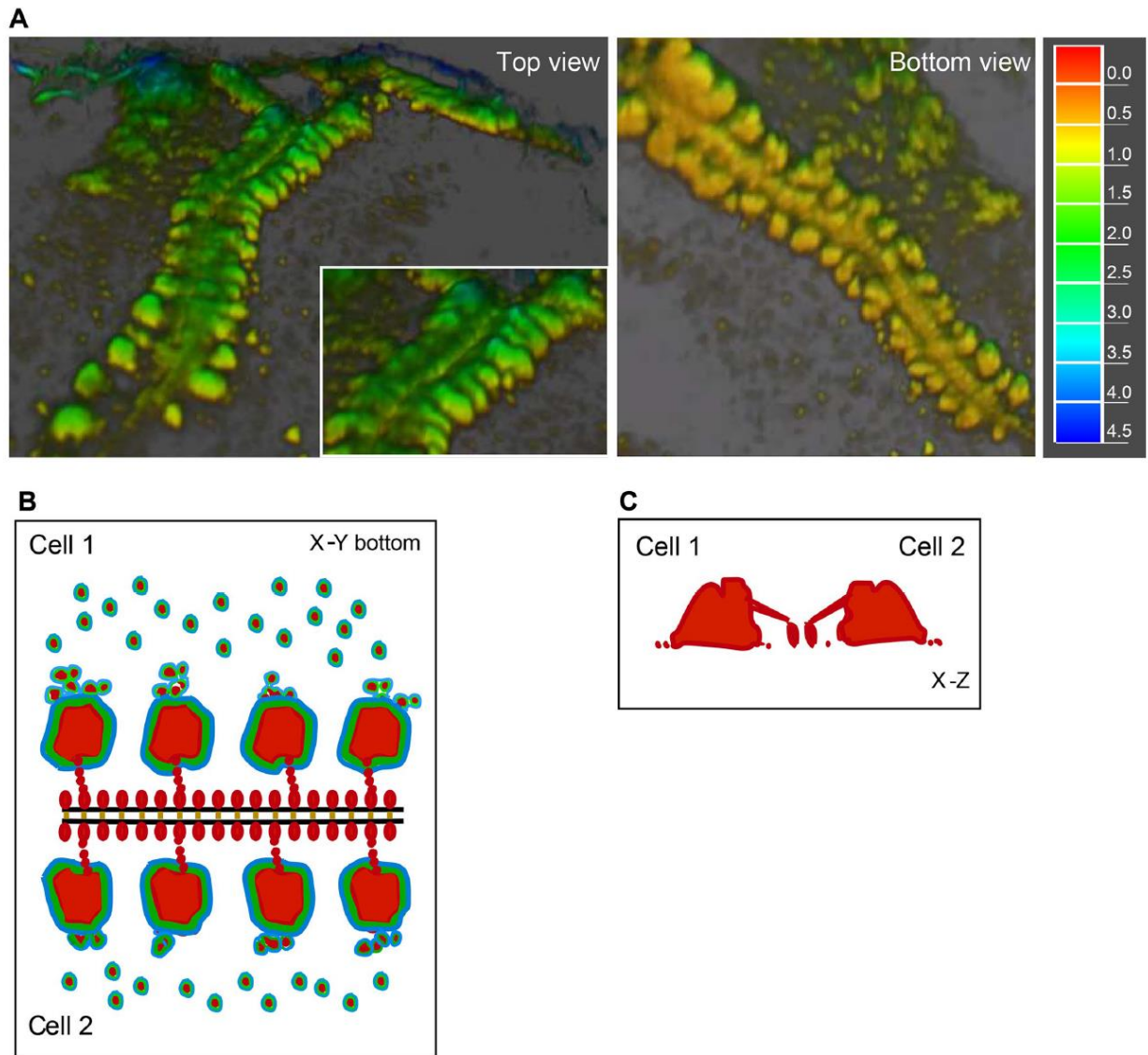


**Figure 11. Schematic drawing of the organization of actin and associated proteins in a ZLS.** (A) The 3D reconstruction of actin distribution in a ZLS formed by two abutting cells, based on confocal and structured illumination microscopy using cell labeling with Alexa-Fluor-conjugated phalloidin. *Left panel:* top view. *Right panel:* bottom view. The representation of data as a heat map is shown on the right ( $\mu\text{m}$ ). (B) The distribution of actin (red) within the large and small membrane-proximal globules in a ZLS. Based on live-cell video microscopy, large globules form from a pool of individual podosomes present in the vicinity of the plasma membranes. The podosome proteins vinculin (green) and talin (blue) surround the actin cores in large globules and individual podosomes. E-cadherin (orange) holds the two plasma membranes (black lines). Afadin (not shown) and other unknown scaffold proteins may organize actin and its associated proteins into highly symmetrical ZLS structures. (C) A vertical section across two large actin globules in a ZLS.

Similar to E-cadherin, nectin-2 mRNA was not detected in freshly isolated macrophages but expressed several hours after incubation in the presence of IL-4. Nonetheless, E-cadherin appears to play a dominant role in ZLS formation inasmuch as sequestration of Ca<sup>2+</sup> by EGTA or blocking E-cadherin with an anti-E-cadherin antibody effectively disrupted ZLSs (Figure 10). E-cadherin and nectin-2 are typical components of adherens junctions (AJ) in epithelial and other cells (Takai et al., 2008; Harris and Tepass, 2010; Takeichi, 2014). In AJs, Ca<sup>2+</sup>-dependent cadherin molecules associate with the actin cytoskeleton, strengthening intercellular adhesions. Moreover, another intercellular adhesion system consisting of the Ca<sup>2+</sup>-independent nectin molecules and nectin-binding adaptor protein afadin, which connects nectin to actin, plays a role in the organization of AJs, either cooperatively with or independently of cadherin (Takai et al., 2008). E-cadherin and nectin-2 have previously been identified in monocytes/macrophages (Pende et al., 2006; Moreno et al., 2007; Van den Bossche et al., 2009). The surprising finding of the present study is that these molecules, together with afadin, were found in ZLSs suggesting that they can form adherens junction-like structures in mature MGCs. Epithelial AJs have traditionally been classified into two major groups based on their dynamics and on how they associate with actin filaments (Franke, 2009; Takeichi, 2014). The linear adherens junctions (lAJ) that connect mature epithelial cells link with a bundle of linear actin filaments that runs parallel to the cell borders and are relatively stable. The punctate adherens junctions (pAJ) that are found at the edges of epithelial colonies and in other cell types, associate with radial actin bundles and are mobile, morphologically unstable structures (Takai et al., 2008; Takeichi, 2014; Indra et al., 2018). Ecadherin is also observed

at lateral cell-cell contacts below IAJ, where it associates with an amorphous actin network (Takeichi, 2014). There are several notable differences between the ZLStype junctions in MGCs and AJs in epithelial cells. First, in contrast to AJs, the transient nature of the ZLS-type junctions suggests that they are held by weak interactions. Although pAJs have been described as mobile structures, this behavior is referred to as the ability of cadherin molecules to be released and then reassemble within cadherin clusters (Indra et al., 2018). Hence, the dynamic behavior of pAJ is related to the continuous turnover of cadherin molecules while still maintaining their overall stability. In contrast, an entire ZLS can form and disassemble in one location while a new ZLS appears in another location. Second, the distribution of actin in ZLSs is distinct from that observed in AJs. Neither parallel actin filaments similar to those in IAJ nor pAJ-associated long filaments that perpendicularly terminate at the plasma membrane have been detected in ZLSs. Rather, actin is organized within regular foci that resemble large podosome clusters observed in nonfusing mouse macrophages (Evans et al., 2003). Third, in contrast to IAJs that may encircle cells, ZLSs form discontinuous segments at the sites where MGCs contact each other. In this regard, ZLSs are reminiscent of cell-cell junctions formed in fibroblasts and other motile cells, in which they are observed as punctate and streak-like structures (Yonemura et al., 1995; Takeichi, 2014). Fourth, the inter-membrane space in a ZLS determined by TEM was  $7.7 \pm 1.3$  nm, significantly narrower than  $\sim 15\text{--}25$  nm in epithelial AJs (Farquhar and Palade, 1963; Miyaguchi, 2000). Thus, despite the presence of some typical AJ proteins and actin, many features of the ZLStype junctions in MGCs distinguish them from AJs and other cell-cell junctions, suggesting that these adhesive structures may represent a novel type of AJ.



Recently, a report has shown that mononuclear macrophages in the granuloma of zebrafish infected with mycobacteria can form adherens junctions (Cronan et al., 2016). Since MGCs are the characteristic feature of granulomas in tuberculosis and E-cadherin expression has been detected in macrophages from human and mouse samples (Cronan et al., 2016), it will be interesting to examine whether MGCs in granulomas also form ZLSs. In addition to E-cadherin and nectin-2, integrin  $\alpha M\beta 2$ , which is known to associate with podosomes in macrophages (Duong and Rodan, 2010; van den Dries et al., 2013a), was found in the intercellular space of ZLSs. Integrin  $\alpha M\beta 2$  is a multi-ligand receptor that can engage several counter-receptors, including members of the ICAM and JAM protein families (Diamond et al., 1990; Santoso et al., 2002). This receptor may contribute to heterophilic interactions that hold two membranes in the ZLS together. We have recently demonstrated that  $\alpha M\beta 2$  can interact with SIRP $\alpha$  (also known as the macrophage fusion receptor, MFR) which, similarly as ICAMs and JAMs, belongs to the Ig superfamily (Podolnikova et al., 2019). However, while SIRP $\alpha$  was strongly expressed in ZLSs (Supplemental Figure 6B), it was not present in the midline, suggesting that SIRP $\alpha$  and  $\alpha M\beta 2$  do not colocalize. At present, the counter-receptor of  $\alpha M\beta 2$  and its contribution to ZLS formation remain to be determined. We have recently demonstrated that in vitro macrophage fusion occurs in three overlapping steps (Faust et al., 2017). Several hours after IL-4 induction, a founder population of mononuclear macrophages initiates fusion with neighboring mononuclear macrophages. These early multinucleated cells then fuse with neighboring mononuclear macrophages and, finally, MGCs fuse with surrounding MGCs to form syncytia. Our current studies suggest that the formation of ZLSs is a late-stage event in multinucleation.

Since similar structures form in late MGCs on the surfaces of implanted biomaterials, these data indicate that ZLSs are not in vitro artifacts. However, the role of these enigmatic structures is unclear. It is well-known that when motile cells establish cell-cell junctions they cease movement and proliferation, a phenomenon referred to as contact inhibition of cell movement and proliferation (Fisher and Yeh, 1967; Bell, 1978). Since peritoneal macrophages do not divide, it is unlikely that ZLSs function in blocking cell proliferation signals. Therefore, the role of ZLSs in suppressing migration of MGCs as well as mononuclear cells that occasionally form ZLSs with MGCs can be theoretically envisioned. Our studies demonstrate that MGCs remain viable after establishing ZLSs. This observation is consistent with a well-known fact that cells that establish cell-cell junctions and stop moving continue to survive. Another possibility is that ZLSs may be involved in proteolysis. Podosomes have been associated in vitro with ECM degradation in many cell types, including macrophages (Linder et al., 2011). This is achieved by the recruitment and localized release of MMPs as well as serine and cathepsin proteinases. Among MMPs, MT1-MMP has been shown to degrade ECM in primary macrophages (Wiesner et al., 2010; Wiesner et al., 2014). However, although we observed MT1-MMP in mononuclear macrophages and early MGCs, we were not able to detect this protease in ZLSs (Supplemental Figure 6C). At present, the involvement of other proteases that can be recruited with podosomes to ZLSs remains to be defined. Recent studies have demonstrated zipper-like structures in cultures of the murine macrophage cell line RAW267.4 undergoing osteoclastogenesis in the presence of RANKL and in osteoclasts induced in mouse bone marrow cells by RANKL/M-CSF (Takito et al., 2012; Takito et al., 2017).

Although osteoclast ZLSs and the ZLSs observed in the current study share similar features, such as overall visual appearance, transient nature, and association with podosomal proteins, there are clear differences between these two structures. First, two types of ZLSs have been found in osteoclasts. The first type has been observed at the ventral membrane of a single multinucleated osteoclast that formed as a result of fusion of mononuclear cells and was interpreted as the structure joining actin rings of individual cells remaining after fusion. Such compartmentalization of the ventral membrane was not observed in IL-4-induced MGCs. We invariably observed ZLSs only between the plasma membranes of two large apposing MGCs (and rarely between an MGC and mono/binuclear cell). The ZLS structures in our experiments seem to resemble another type of ZLS that was observed in mature osteoclasts (Takito et al., 2017). Second, in contrast to MGCs, the ZLSs in osteoclasts were negative for E-cadherin,  $\beta$ -catenin, and nectin-2 staining (Takito et al., 2012). Third, the dimensional parameters of ZLSs in mature osteoclasts are different from those in MGCs, with the average width of the ZLSs in osteoclasts being almost twice larger than that in MGCs (~8.4  $\mu\text{m}$  vs. ~4.8  $\mu\text{m}$ , respectively). Fourth, perhaps the most striking difference between the ZLSs in MGCs and those in osteoclasts is the mechanisms of their formation. Although both structures are highly dynamic, the ZLSs in MGCs are formed from podosomes or podosome clusters and disassemble into podosomes, whereas the ZLSs in osteoclasts result from continuous retrograde actin flow and are independent of the dissolution and reformation of podosomes (Takito et al., 2017). It has been proposed that this actin flow generates forces that push the plasma membranes of neighboring osteoclasts at cell-cell contact sites to generate the ZLSs. While this is an attractive

possibility, our results also suggest the formation of ZLSs in MGCs is triggered by the interaction of E-cadherin molecules through the zippering mechanism. Finally, the ZLSs in osteoclasts have been proposed to be involved in cell-cell fusion (Takito et al., 2012). This scenario differs from our findings. Since the ZLSs in MGCs materialize only in extended IL-4-induced cultures by the time the cell fusion largely ceases (Figure 2, G and H), it is unlikely that they are involved in fusion. Indeed, among the twenty ZLSs analyzed by live-cell imaging, we were able to detect only one fusion event that occurred at the site of the ZLS. Thus, the kinetics and morphological differences between ZLSs in osteoclast and MGCs indicate that the definitive description of ZLSs during osteoclastogenesis and MGC formation and their functional roles may require further analysis. In conclusion, our in vivo and in vitro studies demonstrate the formation of highly ordered actin-based zipper-like structures that originate from podosomes and link the plasma membranes of two large MGCs. Given the fact that macrophage-derived MGCs and their secreted products may modulate the foreign body reaction to implanted biomaterials and ultimately wound healing (Anderson et al., 2008; Jones et al., 2008), the mechanisms underlying the assembly of podosome-derived ZLSs and their role in the foreign body reaction merit further analyses.

### **3.5 Materials and methods**

#### **1, Reagents**

The rat mAb M1/70, which recognizes the mouse  $\alpha$ M integrin subunit, was purified from the conditioned media of hybridoma cells (obtained from The American Tissue Culture Collection, Manassas, VA) using protein A agarose. The mouse anti-talin (catalog #T3287), anti-vinculin (catalog #V9131) mAbs, and rabbit anti-I/S-afadin polyclonal

antibody (catalog #A0224) were from Sigma (St. Louis, MO). The rabbit anti-paxillin (catalog #32084) and anti-JAM-A (catalog #180821) polyclonal antibodies and rabbit anti-cortactin mAb conjugated to Alexa Fluor 555 were from Abcam (Cambridge, MA). The rat anti-nectin-2 (catalog #sc-502-57) mAb and the rat anti-E-cadherin mAb DECMA-1 (catalog #sc-59778) were from Santa Cruz Biotechnology (Dallas, TX). The mouse anti-E-cadherin mAb (catalog #3195T), rabbit anti-Myosin IIa polyclonal antibody (catalog #34035), and the mouse IgG1 isotype control (catalog #5415) were from Cell Signaling (Danvers, MA). The rat anti-SIRP $\alpha$ /CD172a polyclonal antibody (catalog #552371) was from BD Bioscience (San Jose, CA). The rabbit anti-MT1-MMP-14 polyclonal antibody (catalog #14552-1-AP) was from Proteintech (Rosemont, IL). The rabbit anti-ZO-1 polyclonal antibody (catalog #61-7300) and secondary antibodies Alexa Fluor 488-conjugated goat anti-rabbit IgG and Alexa Fluor 633-conjugated goat anti-rat IgG were from Invitrogen (Carlsbad, CA). Vibrant DiD membrane-labeling reagent was from Thermo Fisher (Waltham, MA). Brewer's thioglycollate (TG), wiskostatin, and the Arp2/3 inhibitors CK-548 and CK-636 were from Sigma (St. Louis, MO). IL-4 was from Genscript (Piscataway, NJ).

## **2, Mice**

C57BL/6J and WASp<sup>-/-</sup> (B6.129S6-Wasm1Sbs/J) mice were purchased from The Jackson Laboratory (Bar Harbor, MA). EGFP- and mRFP-LifeAct mice (Riedl et al., 2010) were gifts from Dr. Janice Burkhardt and were used with permission from Dr. Roland Wedlich-Söldner. Myeloid cell-specific Cdc42<sup>-/-</sup> mice were generated by crossing Cdc42loxP/loxP mice with LysMcre mice, followed by screening the progeny for Cdc42

excision in myeloid leukocytes as previously described (Faust et al., 2019). All animals were given ad libitum access to food and water and maintained at 22 °C on a 12-hour light/dark cycle. Experiments were performed according to animal protocols approved by the Institutional Animal Care and Use Committees at Arizona State University.

### **3, Biomaterial implantation**

Segments (1.5 × 0.5 cm) of sterile polychlorotrifluoroethylene (PCTFE) were implanted into the peritoneum of age- and sex-matched mice. Animals were humanely sacrificed 3, 7 and 14 days later, and explants were analyzed for the presence of MGC as previously described (Faust et al., 2019). Prior to explantation, 2 ml of PBS containing 5 mM EDTA was aseptically injected into the peritoneum, and cells in the peritoneum were collected by lavage. The number of cells in the peritoneum at the time of explantation was determined by counting with a Neubauer hemocytometer. Experiments were conducted in triplicate on three independent days.

### **4, Macrophage isolation**

Macrophages were isolated from 8-12-week-old male and female age- and sex-matched mice injected (I.P.) with 0.5 mL of a sterile 4% Brewer's thioglycollate (TG) solution. All animals were humanely sacrificed 72 h later, and macrophages were isolated by lavage with ice-cold phosphatebuffered saline (PBS, pH 7.4) containing 5 mM EDTA. Macrophages were counted with a hemocytometer immediately thereafter.

### **5, IL-4-induced macrophage fusion**

Macrophage fusion was induced as previously described (Faust et al., 2019). Briefly, peritoneal cells ( $5 \times 10^6$  cells/ml) in Hank's Balanced Salt Solution (HBSS;

Cellgro, Manassas, VA) supplemented with 0.1% bovine serum albumin (BSA) were applied to acid-cleaned or paraffin-24 coated glass coverslips [prepared as described by Faust et al. (2017 and 2018)]. Cells were incubated in 5% CO<sub>2</sub> at 37 °C for 30 min. Non-adherent cells were removed by washing the culture three times with HBSS, and then the adherent cells were cultured with DMEM/F12 containing 15 mM HEPES (Cellgro, Manassas, VA), 10% FBS (Atlanta Biological, Flowery Branch, GA) and 1% antibiotics (Cellgro, Manassas, VA). After 2 h, 10 ng/ml IL-4 was added to the cultures until the indicated time points. For the 5-day cultures, media were changed on day 3. The fusion indices were determined from the images of cells labeled with Alexa Fluor 568- conjugated phalloidin and DAPI as previously described (Faust et al., 2019). The fusion index is defined as the fraction of nuclei within MGCs and expressed as the percentage out of the total nuclei counted. A total of 18–20 images (40×) that contained approximately 100–200 cells were analyzed for each experimental condition. The lengths of ZLSs were determined with ImageJ software (National Institutes of Health). Photomicrographs of representative fields were obtained with a Leica SP8 microscope (Leica Microsystems Inc. Buffalo Grove, IL).

## **6, Phase-Contrast Video-Microscopy**

Wild-type, WASp-deficient, and Cdc42-deficient macrophages ( $5 \times 10^6$  /ml) isolated from the peritoneum of mice 3 days after TG injection were plated on the surface of paraffin-coated coverslips or a section of polychlorotrifluoroethylene (PCTFE), and cell fusion was induced by adding 10 ng/ml IL-4. Dishes were transferred from the cell culture incubator to a stage-top incubator calibrated to maintain a humidified atmosphere of 5%

CO<sub>2</sub> in air at 37 °C. Phasecontrast images were collected with a 20× objective every 30 s using an EVOS FL Auto (Thermo Scientific, Waltham, MA) and transferred to ImageJ to generate movies.

## **7, Live-cell fluorescence microscopy**

EGFP- or mRFP-LifeAct macrophages were isolated from the peritoneum of TG-induced mice. Macrophages (10<sup>6</sup> /0.5 ml) were plated on the surface of coverslips adsorbed with paraffin and 25 incubated in the presence of 10 ng/ml IL-4. After 3 days, half of the DMEM/F12 medium was replaced with fresh medium without IL-4, and the cell culture was incubated for an additional 2 days. The dish was placed into a live-cell imaging chamber supplied with 5% CO<sub>2</sub> at 37 °C, and live-imaging was conducted for 6 h. Images were acquired by Leica SP8 using a 40×/1.3 NA oil objective every minute using a HyD hybrid detector. The acquired images were processed and converted into movies using ImageJ software.

## **8, Immunofluorescence**

At the indicated time points, cells cultured on clean glass or paraffin-coated coverslips were fixed with 2% paraformaldehyde in PBS for 30 minutes, permeabilized with 0.2% Tween-20 in PBS for 15 min at 22 °C, and then washed with PBS. The permeabilization step was omitted for the staining of transmembrane proteins. The cells were incubated overnight at 4 °C with the primary antibodies using the dilutions recommended by the manufacturers. Incubations with Alexa Fluor (488, 568, or 647)-conjugated secondary antibodies were performed at room temperature for 4 h. Cells were also stained with 15 nM Alexa Fluor 568-conjugated phalloidin (Thermo Scientific,



Waltham, MA) for 30 min at 22 °C to detect F-actin. Cells were washed twice with PBS and incubated with DAPI. ProLong Diamond Antifade Mountant was used to mount the cells on a glass slide (Thermo Scientific, Waltham, MA). Images were acquired by using Leica SP8 and Zeiss LSM800 confocal microscopes (Carl Zeiss Vision Inc., San Diego, CA) with 40×/1.3 NA and 60×/1.4 oil immersion objectives, respectively. Super-resolution images were acquired using a Nikon SIM (Nikon Instruments Inc., Melville, NY) with an SR Apo TIRF 100×/1.49 NA oil immersion objective.

### **9, RT-PCR analysis of E-cadherin and Nectin-2 expression**

Macrophages were induced to fuse by IL-4 for the indicated periods. Total RNA was extracted using TRIzol reagent (Invitrogen) and resuspended in 20 µl of RNase-free water supplemented with 0.1 mM EDTA. 1 µg of total RNA was used to generate cDNA using SuperScript III Reverse Transcriptase (Invitrogen). PCR was performed with the generated cDNA and premixed 2× Taq polymerase solution (Promega) in an MJ Mini Thermal Cycler (BioRad). The levels of target mRNAs were normalized by the Tuba1b mRNA level. The primer sets for PCR analyses were purchased from Integrated DNA Technologies (Iowa, USA) and included those for Tuba1b, 5'CAGGTCTCCAGGGCTTCTTG-3' (forward) and 5'-GAAGCATCAGTGCCTGCAAC-3' (reverse); for Cdh1 5'-CGGGACTCCAGTCATAGGGA-3' (forward) and 5'ACTGCTGGTCAGGATCGTTG-3' (reverse); and for Nectin2 5'GTTTCAGCAAGGACCGTCTGTC-3' (forward) and 5'-ATCGTAGGATCCTCTGTCGC-3' (reverse). The semi-quantitative digital analysis was performed using ImageJ software. Pixel density for each band was calculated in arbitrary

units and expressed as a fold change relative to the target mRNA level in macrophages in suspension (denoted 0).

## **10, TEM**

TG-elicited peritoneal macrophages were seeded on a PCTFE section (Welch Fluorocarbon, Dover, NH) and cultured in DMEM/F12 supplemented with 15 mM HEPES, 10% FBS, and 1% antibiotics. After 2 h, 10 ng/ml IL-4 was added to cultures, and cells were incubated for 5 days. Cells were fixed with 2.5% glutaraldehyde in 0.1 M PBS (pH 7.4) at 4 °C overnight and then treated with 1% OsO<sub>4</sub> in 0.1 M PBS for 1 h. Subsequently, cells were washed with 0.1 M PBS and then dehydrated using acetone. Finally, cells were flat-embedded into Spur's EPOXY Resin, and 70-nm sections were obtained by slicing parallel to the site of the cell attachment to substrate. Sections were post-stained with uranyl acetate and Sato's lead citrate. Micrographs were taken using a Philips CM 12 TEM with a Gatan model 791 camera.

## **11, Statistical Analyses**

Unless otherwise indicated, results are shown as mean  $\pm$  SD of three independent experiments. Multiple comparisons were made by using ANOVA followed by Tukey's or Dunn's post-test using GraphPad InStat software. Where applicable, means were compared with each other by using Student's t-test. Data were considered significantly different if  $p < .05$ .

### **3.6 ACKNOWLEDGMENT**

We thank James Faust for helpful advice on performing phase-contrast live-cell video experiments and Page Baluch for anti-ZO-1 antibodies. We acknowledge the use of facilities within the Eyring Materials Center at Arizona State University supported in part by NNCI-ECCS-1542160. Image data were collected using a Leica TCS SP5 LSCM (the National Institutes of Health SIG award S10 RR027154) and Leica TCS SP8 LSCM (the NIH SIG award S10 OD023691) housed in the W.M. Keck Bioimaging Facility at Arizona State University.

## CHAPTER 4

### FIBRIN POLYMER ON THE SURFACE OF BIOMATERIAL IMPLANTS DRIVES THE FOREIGN BODY REACTION

#### 4.1 Abstract

Implantation of biomaterials and medical devices in the body triggers the foreign body reaction (FBR) which is characterized by macrophage fusion at the implant surface leading to the formation of foreign body giant cells and the development of the fibrous capsule enveloping the implant. While precedent adsorption of fibrin(ogen) on the surface of implants is required for macrophage adhesion, it is unknown whether fibrin(ogen) is involved in the development of FBR. Here we show that mice with genetically-imposed fibrinogen deficiency display a dramatic reduction of macrophage fusion on implanted biomaterials and are protected from the formation of fibrin-containing granulation tissue, a precursor of the fibrous capsule. Furthermore, macrophage fusion on biomaterials implanted in Fib<sup>AEK</sup> mice that express a mutated form of fibrinogen incapable of thrombin-mediated polymerization was strongly reduced. Surprisingly, despite the lack of fibrin, the capsule was formed in Fib<sup>AEK</sup> mice, although it had a different composition and distinct mechanical properties than that in wild-type mice. Specifically, while mononuclear  $\alpha$ SMA<sup>+</sup>/CD68<sup>+</sup>/CD11b<sup>+</sup> cells embedded in the capsule of both strains of mice secreted collagen, the amount of collagen and its density in the tissue of Fib<sup>AEK</sup> mice was reduced. These data identify fibrin polymer as a key biological substrate driving the development of the FBR.

## 4.2 Introduction

Implantation of biomaterials and medical devices in the body triggers the foreign body reaction (FBR) which represents an end-stage of the inflammatory and wound healing responses following injury (Anderson *et al.*, 2008; Anderson and Cramer, 2015; Ratner, 2015). The FBR is characterized by macrophage fusion at the implant surface leading to the formation of foreign body giant cells (FBGCs) and the development of the fibrous capsule enveloping the implant. FBGC-mediated damage of the biomaterial surface and the formation of a dense fibrous capsule that isolates the implant from the host is the common underlying cause of implant failure.

The very early events following tissue injury caused by implantation include the interaction of blood with the biomaterial surface resulting in adsorption of plasma proteins and the formation of a provisional matrix (Anderson *et al.*, 2008). This matrix serves as an adhesive substrate for neutrophils and monocytes that are recruited out of the vasculature to the implant site with latter cells undergoing differentiation into macrophages. Subsequently, as the acute inflammatory response progresses to chronic inflammation, macrophages at the biomaterial interface fuse to form multinucleated giant cells, also known as foreign body giant cells (FBGCs). Macrophage fusion requires both the presence of large foreign surfaces and a microenvironment generated in proximity to the implanted biomaterial. In particular, cytokines IL-4 and IL-13 have been shown to program macrophages into a fusion-competent state *in vitro* (McInnes and Rennick, 1988; McNally and Anderson, 1995; Skokos *et al.*, 2011), and IL-4 and IL-13 were identified at the implant site (Kao *et al.*, 1995; Higgins *et*

*al.*, 2009) (Ward *et al.*, 2008). In addition, the chemokine MCP-1 which participates in macrophage fusion *in vitro* and *in vivo* (Kyriakides *et al.*, 2004) is secreted by biomaterial-adherent macrophages (Jones *et al.*, 2007).

The formation of macrophage-derived giant cells is concomitant with the growth and remodeling of granulation tissue around the implant which is gradually populated by fibroblasts that transform into myofibroblasts (Kenneth Ward, 2008; Anderson and Cramer, 2015). Fibroblasts are thought to be attracted by potent soluble mediators released from activated biomaterial-adherent mononuclear macrophages and FBGCs. Both macrophages and FBGCs also secrete pro-fibrogenic factors that enhance fibrogenesis by myofibroblasts (Hernandez-Pando *et al.*, 2000; Song *et al.*, 2000; Barron and Wynn, 2011). According to current dogma, the secretion of collagen and other matrix proteins by myofibroblasts results in the production of a fibrous capsule that envelops the implanted device. The capsule containing a dense, avascular layer of collagen is considered an adverse factor of the bioimplant performance because it is impermeable to most molecules in the surrounding environment, thus isolating the implant from the local tissue environment and preventing full healing and incorporation of the implant (Ratner, 2002; Langer, 2009; Jones, 2015; Anderson, 2016; Scatena *et al.*, 2017). Furthermore, FBGCs themselves are viewed as a significant negative factor contributing to long-term failures in implanted medical devices. FBGCs may cause biomaterial surface damage by releasing potent degradative cellular products such as reactive oxygen intermediates, enzymes, and acid (Zhao *et al.*, 1991; Matheson *et al.*, 2004; Santerre *et al.*, 2005; Ratner, 2011). Thus, strategies that limit FBGC formation and development of the fibrous capsule are highly desirable.

It is well known that immediately after implantation, biomaterials spontaneously acquire a layer of host proteins that provide an adhesive substrate for arriving inflammatory cells (Wilson *et al.*, 2005; Horbett, 2012). Among them, fibrin(ogen), a principal adsorbed protein, triggers an early arrival and adhesion of phagocytic cells (Tang and Eaton, 1993; Tang *et al.*, 1996; Hu *et al.*, 2001). Using the intraperitoneal implantation model, Eaton and colleagues have shown that mice made severely hypofibrinogenemic by injection of anicrod do not mount an acute inflammatory response to the implanted biomaterial unless the material is coated with fibrinogen or animals are injected with fibrinogen before implantation (Tang and Eaton, 1993). Although it has not been determined whether adsorbed fibrinogen or fibrin was responsible for phagocyte recruitment, both proteins can support integrin  $\alpha_M\beta_2$  (Mac-1)- and  $\alpha_5\beta_1$ -mediated adhesion of neutrophils and monocyte/macrophages (Altieri *et al.*, 1988; Tang *et al.*, 1996; Lu *et al.*, 1997; Loike *et al.*, 1999; Flick *et al.*, 2004). Whether fibrinogen or fibrin are also required for macrophage fusion and formation of the fibrous capsule during the FBR is unclear.

In this study, we have shown that macrophage fusion on biomaterials implanted in fibrinogen-deficient ( $Fg^{-/-}$ ) mice was almost completely abrogated and no granulation tissue, a precursor of the fibrous capsule was found around the biomaterials. We further found that  $Fib^{AEK}$  mice that express mutated fibrinogen that is incapable of thrombin-mediated polymerization (Prasad *et al.*, 2015) also exhibit a defect in macrophage fusion. Furthermore, although the thickness of granulation tissue in  $Fib^{AEK}$  mice was comparable to that in WT mice, both matrices had a different composition and mechanical properties. In particular, fibrin-containing capsules formed in WT mice contained greater amounts of collagen than

those formed in Fib<sup>AEK</sup> mice. The cells producing collagen and other extracellular matrix proteins during the early FBR were mononuclear macrophages embedded in granulation tissue. These data indicate that fibrin polymer deposited on the surface of implants is responsible for macrophage fusion and implicate fibrin matrix in organizing a dense fibrous capsule.

### 4.3 Results

#### 1, Formation of FBGCs on implanted biomaterials is abrogated in Fg<sup>-/-</sup> mice

To assess how fibrinogen might affect macrophage fusion, we used an intraperitoneal implantation model to induce the FBR in Fg<sup>-/-</sup> mice. In these experiments, sterile polychlorotrifluoroethylene (PCTFE) sections were implanted into the peritoneal cavity of WT and Fg<sup>-/-</sup> mice and the formation of FBGCs was determined after 3, 7, and 14 days. At the time of retrieval, the implanted biomaterial segments were coated by a fibrinous material that appeared as a white film that formed on both sides of the implant in WT mice. Macrophage fusion on the surface of PCTFE implants was determined after the removal of the fibrinous capsule and labeling cells with Alexa Fluor 568-conjugated phalloidin and DAPI. Macrophage fusion in Fg<sup>-/-</sup> mice was strongly reduced at all time points compared to WT mice (Fig. 1, A and B). On all days, a ~5-6-fold difference between fusion indices of FBGCs formed in WT and Fg<sup>-/-</sup> was found. As shown in Fig. 1B, the fusion index in WT mice was increased from  $17 \pm 8\%$  to  $57.0 \pm 5\%$  from day 3 to day 14 whereas macrophage fusion in Fg<sup>-/-</sup> increased from  $3.3 \pm 2.5\%$  to  $9.4 \pm 3.9\%$ . The defect in macrophage fusion in Fg<sup>-/-</sup> mice was not due to the number of macrophages adherent to the implant as even greater



numbers of cells (determined as the total number of nuclei) were found on the implants retrieved from  $Fg^{-/-}$  mice at days 3 and 7, and equal numbers of cells were found at day 14 (Fig. 1C). Macrophage adhesion and spreading are known to be required for macrophage fusion (Helming and Gordon, 2009). The degree of mononuclear macrophage spreading to materials implanted into WT mice for 3 days was ~2-fold greater than in  $Fg^{-/-}$  ( $187 \pm 57$  vs.  $84 \pm 37 \mu m^2$ ), although it was not significantly different after 7 and 14 days (Fig. 1D). In addition, the migration of leukocytes in  $Fg^{-/-}$  mice in response to implantation was not compromised. A trend toward a higher number of cells in the lavage obtained from the peritoneum of  $Fg^{-/-}$  mice was noted, but the difference was not significant (Fig. 1E). To examine whether fibrinogen deficiency affects leukocyte migration in another model of inflammation, the leukocyte flux into the peritoneum was induced by the thioglycolate injection. A similar trend was observed, i.e. the total number of monocytes in the peritoneum of  $Fg^{-/-}$  mice on day 3 was slightly higher than that in WT mice (Fig. S1). This result is consistent with an increased monocyte/macrophage recruitment into the peritoneum 3 days after thioglycollate injection reported recently by other investigators (Silva *et al.*, 2019). Histological analyses showed that the thickness of the fibrinous capsule formed around PCTFE material implanted in WT mice gradually increased (Fig. 2, A and B). The capsule was composed of a layer of adherent FBGCs and numerous mononuclear cells embedded into granulation tissue.

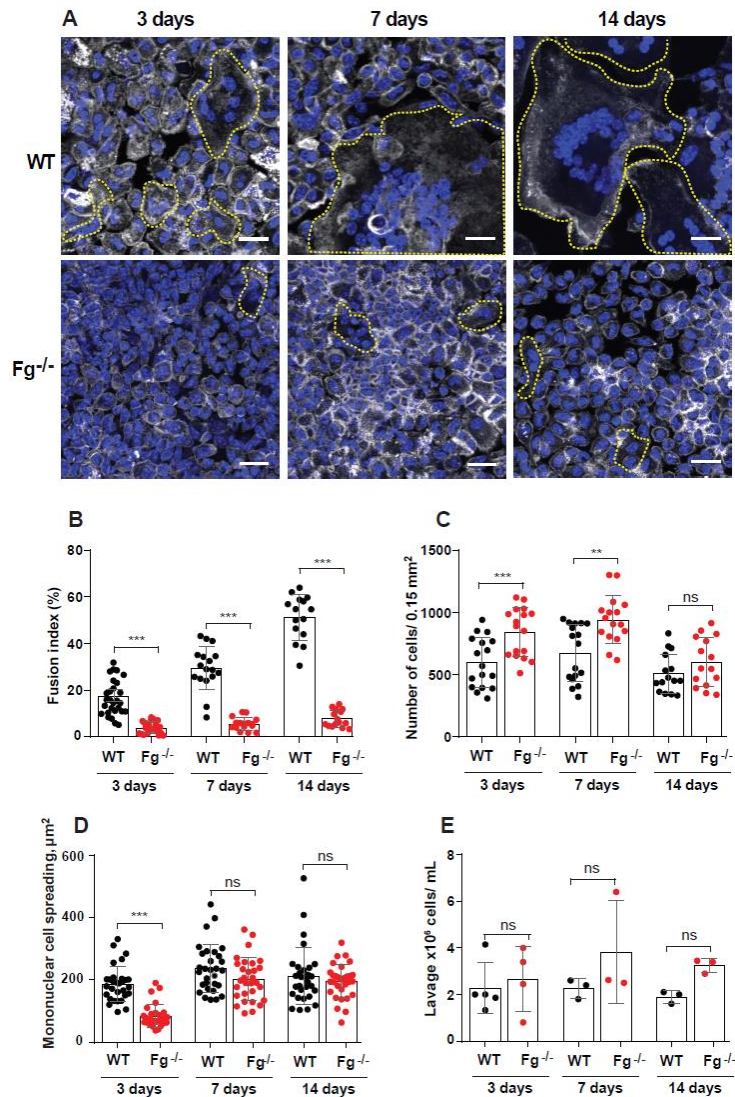


**Figure 1. Fg<sup>-/-</sup> mice display reduced FBGC formation.** PCTFE sections were implanted in the peritoneum of wild type and Fg<sup>-/-</sup> mice for 3, 7, and 14 days and analyzed by immunocytochemistry. (A) Explants were separated from the surrounding fibrinous capsule, fixed, and incubated with Alexa Fluor 546-conjugated phalloidin (white) and DAPI (teal). Representative confocal images are shown. FBGCs are outlined (yellow). The scale bar is 20 μm. (B) Macrophage fusion was assessed as a fusion index, which determines the fraction of nuclei within FBGCs expressed as the percentage of the total nuclei counted. Five to six random 20× fields were used per sample to count nuclei. (C) The number of cells on the surface of explants retrieved at various time points was determined by counting nuclei in mononuclear cells and FBGCs. (D) Spreading of mononuclear macrophages on the surface of explants. Six to eight random 20x fields per sample were used to determine the cell area (5-6 cells/field). (E) The number of cells in lavage recovered from the mouse peritoneum before explantation. Results shown are mean ± S.D. of four independent experiments. ns, not significant, \*\**p* < .01, \*\*\**p* < .001 when compared with WT mice.

The capsule was absent around the implants retrieved from  $Fg^{-/-}$  mice (Fig. 2, A and B). Even 14 days after implantation, the surface of the implant in  $Fg^{-/-}$  mice was only coated with adherent macrophages. Similar results were obtained with polytetrafluoroethylene (PTFE), a biomaterial commonly used for the manufacturing of vascular grafts (Fig. S2). Since PTFE, as compared to PCTFE, is a non-transparent material that precludes direct visualization of macrophages, we used PCTFE in subsequent experiments. Together, these results indicate that macrophage fusion on the surface of the implant and the formation of the granulation tissue, a precursor of the collagenous fibrous capsule, require fibrin(ogen).

It is generally believed that recruitment and adhesion of leukocytes to the surface of biomaterials implanted into the peritoneum during acute inflammation depends on adsorbed fibrinogen (Tang and Eaton, 1993). It is possible though that adsorbed fibrinogen is converted into fibrin by thrombin generated at sites of implantation. Therefore, it is not clear whether fibrinogen or the fibrin polymer initiates the foreign body reaction.

## **2, Analyses of fibrinogen and fibrin deposited on the surface of implants and in granulation tissue surrounding the implants deposited on the surface of implants mediate macrophage fusion.**

Furthermore, the fibrinous capsule formed above adherent macrophages in WT mice, which was conspicuously absent in  $Fg^{-/-}$  mice, may contribute to macrophage fusion. To

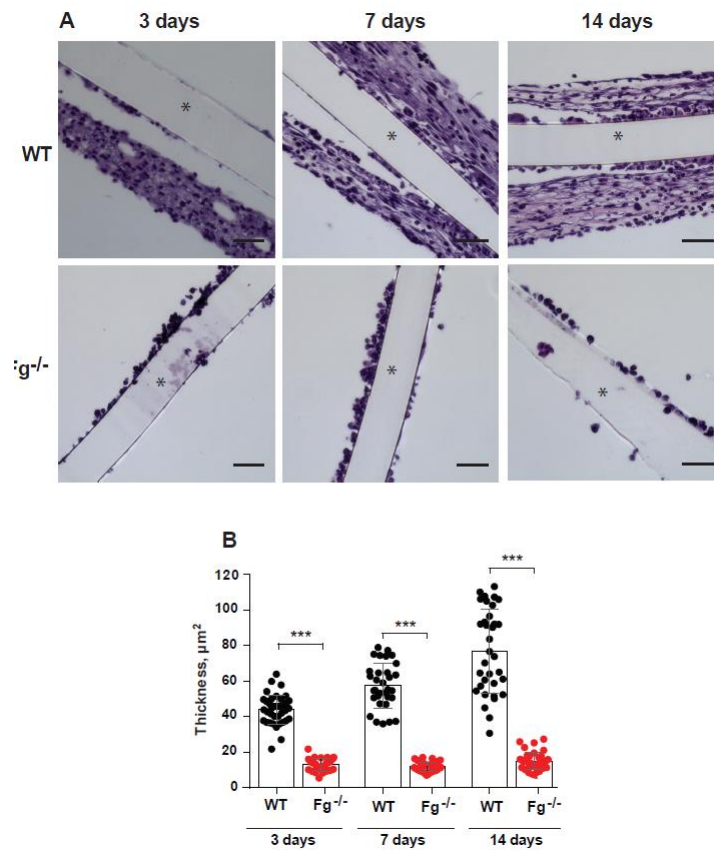


**Figure 2. The lack of granulation tissue around the implants in Fg<sup>-/-</sup> mice.** (A) PCTFE sections were implanted in the peritoneum of wild type and Fg<sup>-/-</sup> mice for 3, 7, and 14 days and analyzed by histochemistry. Explants were fixed, paraffin-embedded, sectioned, and stained according to a standard H&E method. Representative images of stained cross-sections are shown. The scale bar is 50 μm. (B) The thickness of granulation tissue around the implants retrieved from WT and Fg<sup>-/-</sup> mice was determined using ImageJ software. Ten random fields were used per sample to measure the thickness of cross-sections. Results shown are mean ± SD from four independent experiments. \*\*\**p* < .001

investigate these questions, we first examined the presence of fibrinogen and fibrin on the surface of implants and in the capsule (schematically shown in Fig. 3A) using Western blotting with antibodies that recognize the fibrinopeptide A in intact fibrinogen (anti-FpA) and fibrin (anti-Fibrin; mAb 59D8) (Fig. 3B). As expected, the total fibrin(ogen) antigen with a molecular weight of 340 kDa corresponding to intact fibrinogen was detected on the

surface of implants (Fig. 3C, *left panel*). The lack of reactivity with anti-FpA antibodies indicated that fibrinogen was converted into fibrin (Fig. 3C, *the second panel from the left*).

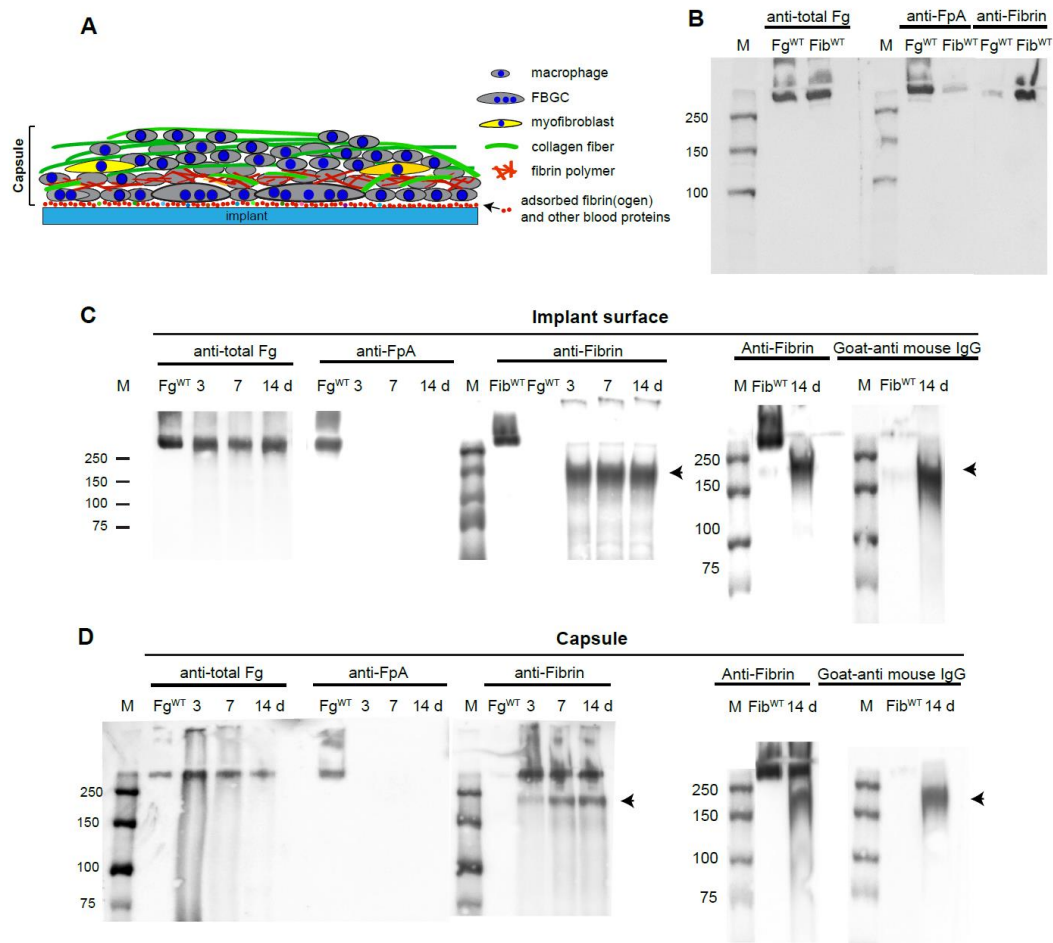


**Figure 3. Western blot analysis of proteins deposited on the surface and in the fibrinous capsule of materials implanted in WT mice.** (A) Schematic representation of the explant components used for analyses. The implants were retrieved after various days and the fibrinous capsule was removed from the explants. The exposed sections and the capsule were analyzed separately. (B) The specificity of antibodies recognizing total fibrinogen (anti-total Fg; 1: 50,000 dilution), fibrinopeptide A in intact fibrinogen (anti-FpA; 1:2000 dilution), and the N-terminus of the  $\beta$ -chain in fibrin after the cleavage of fibrinopeptide B (anti-Fibrin; 1  $\mu$ g/ml). Purified mouse fibrinogen and fibrin-monomer were electrophoresed on 7.5% polyacrylamide gel followed by Western blotting using fibrinogen- and fibrin-specific antibodies. (C) Analysis of the implant surfaces retrieved 3, 7, and 14 days after surgery. The sections were placed into PBS containing protease inhibitors followed by the addition of SDS-PAGE loading buffer. The samples were analyzed by Western blotting using anti-fibrinogen (anti-total Fg), anti-FpA, and anti-fibrin antibodies. The right panel shows the analysis of the material obtained from the surface of the 14-day implant probed with anti-fibrin antibody followed by the secondary antibody or secondary goat anti-mouse IgG only. The arrowhead indicates a band corresponding to a ~150-180 kDa product reactive

with a secondary goat-anti mouse IgG. The data shown are representative of samples obtained from four mice. (D) Analysis of proteins present in the fibrinous capsule formed at different time points. The right panel shows the analysis of the material obtained from the capsule of the 14-day implant probed with anti-fibrin followed by the secondary antibody or secondary anti-total IgG only. The IgG-reactive product is indicated by the arrowhead. M, molecular weight markers.

However, the reactivity with fibrin-specific mAb 59D8, which recognizes the N-terminal end of the  $\beta$ -chain in fibrin after cleavage of the fibrinopeptide B (FpB) by thrombin was also not observed (Fig. 3C, *the third panel from the left*). This finding suggests that fibrin molecules on the surface of implants lost the epitope for mAb 59D8 due to proteolysis or the epitope is not exposed in the surface-deposited fibrin. A protein band with a molecular weight of ~150-180 kDa was detected in blots incubated with mAb 59D8 (Fig. 3C, *right panel, indicated by an arrowhead*). In the absence of the primary antibody, this product interacted with a secondary rabbit anti-mouse antibody, suggesting that this protein is IgG. In line with this finding, previous studies showed that IgG is readily adsorbed from serum on the surface of various materials (Jenney and Anderson, 2000).

Analyses of the material deposited in the fibrinous capsule (Fig. 3D) revealed fibrin as evidenced by the presence of the protein with the molecular weight of ~340 kDa which interacted with mAb 59D8, but not anti-FpA. The IgG-immunoreactive 150-180 kDa protein was also detected in the capsule (Fig. 3D, *right panel*).

### **3, Coating the implant with fibrinogen derivatives rescues the fusion defect in $Fg^{-/-}$ mice**

To substantiate the role of fibrin(ogen) in macrophage fusion and determine whether fibrinogen or fibrin was required for this process, materials were coated with purified mouse fibrinogen or fibrin and implanted in  $Fg^{-/-}$  mice for 7 days. Also, to determine

whether fibrin-monomer vs. fibrin polymer was responsible for macrophage fusion, a layer of polymerized fibrin gel was deposited on the surface of the material by applying a solution of fibrinogen and thrombin. As shown in Fig.4, A and C, implantation of either fibrinogen- or fibrin-monomer-coated materials in  $Fg^{-/-}$  mice rescued macrophage fusion by ~65% of the level observed in WT mice. However, the extent of multinucleation determined as the number of nuclei accumulated in FBGCs, although tended to be higher, was not significantly different from that observed on uncoated surfaces (Fig. 4D). Implantation of sections coated with the fibrin polymer fully restored macrophage fusion (Fig. 4, A and C) and, interestingly, the extent of multinucleation was higher than that in WT mice (Fig. 4D). In addition, pre-coating PCFTE sections with plasma obtained from WT mice and implanted them in  $Fg^{-/-}$  mice for 3 days restored macrophage fusion to the level comparable to that in WT mice ( $15.2 \pm 4.6$  vs.  $18.5 \pm 5.7$  we can change the places: WT (18.5) vs Plasma coated (15.2)) (Fig. S3, A and C), although the extent of multinucleation was ~2-fold lower (Fig. S3D). Since all of the explanted surfaces contained a similar number of cells as determined by the number of nuclei, the difference in the rescue effect appears to be due to the form of the fibrin(ogen) substrate and/or its physical properties. Of note, despite the lack of host fibrinogen in  $Fg^{-/-}$  mice, a small fibrinous capsule was formed around materials coated with fibrinogen, fibrin-monomer, and fibrin polymer (Fig. 4B and E) with the capsule around sections coated with fibrin-monomer and fibrin polymer being larger. A small capsule was also formed around the implant coated with plasma (Fig. S3, B and E). To test whether inhibition of fibrin polymer formation could reduce the FBR, we examined the effect of the thrombin inhibitor argatroban on macrophage fusion and the fibrin capsule formation in WT mice. Two

concentrations of argatroban (9 and 18 mg/kg/day) were injected for 5 days before implantation of biomaterials and then daily for 7 days post-surgery, after which materials were explanted and analyzed.

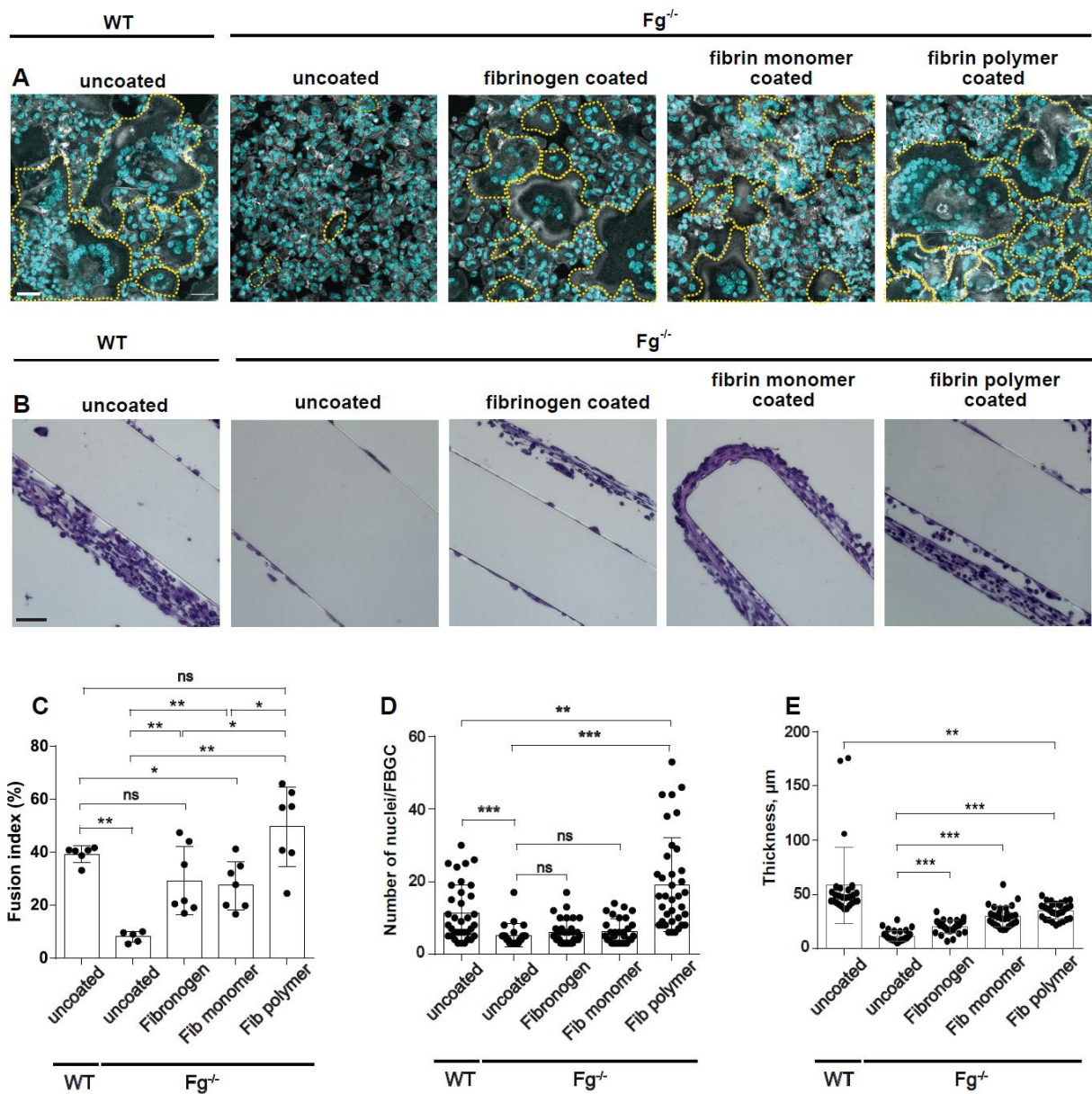




**Figure 4. Precoating the implants with fibrinogen and various fibrin(ogen) species rescues macrophage fusion on materials implanted in  $Fg^{-/-}$  mice.** PCFTE sections were precoated with mouse fibrinogen (1 mg/ml), fibrin-monomer (1 mg/ml), or fibrin polymer and implanted into  $Fg^{-/-}$  mice for 7 days after which time the implants were removed and analyzed for the presence of FBGCs (A) and granulation tissue formation (B). Uncoated material implanted in WT mice served as a control. (C) Fusion indices were determined as described in Materials and Methods. (D) The extent of multinucleation was determined by counting the number of nuclei per FBGC. ~70-140 FBGCs were analyzed from 10-15 random fields. (E) The thickness of granulation tissue formed around the plasma-precoated implants was determined using ImageJ software. Ten random fields were used per sample to measure the thickness of cross-sections. Results shown are mean  $\pm$  SD from 3 independent experiments. The scale bar is 30  $\mu$ m in A and 50  $\mu$ m in B. ns, not significant, \* $p < .05$ , \*\* $p < .01$ , \*\*\* $p < .001$ .

In a pattern analogous to that observed for implants in  $Fg^{-/-}$  mice, treatment of WT mice with argatroban significantly reduced macrophage fusion compared to untreated controls (~1.8- and 2-fold for 9 and 18 mg/kg, respectively; Fig. 5A and 5C), even though a slightly larger number of cells was present on the surface of materials implanted in treated mice (Fig. S4). FBGCs on the surface of implants in argatroban-treated mice contained fewer nuclei (Fig. 5, D and E) and were smaller (Fig. 5F and G). However, the thickness of the capsule formed around materials in treated and untreated mice was similar (Fig. 5, B and H). Together, these data suggest that fibrin-polymer deposited on the surface of implants is required for macrophage fusion but is dispensable for the capsule formation.

#### **4, Macrophage fusion on materials implanted in $Fib^{AEK}$ mice carrying a mutation in the thrombin-cleavage site in the $A\alpha$ chain of fibrinogen**

To directly determine the role of fibrin polymer in mediating macrophage fusion, PCTFE sections were implanted in  $Fib^{AEK}$  mice and various parameters of the FBR were

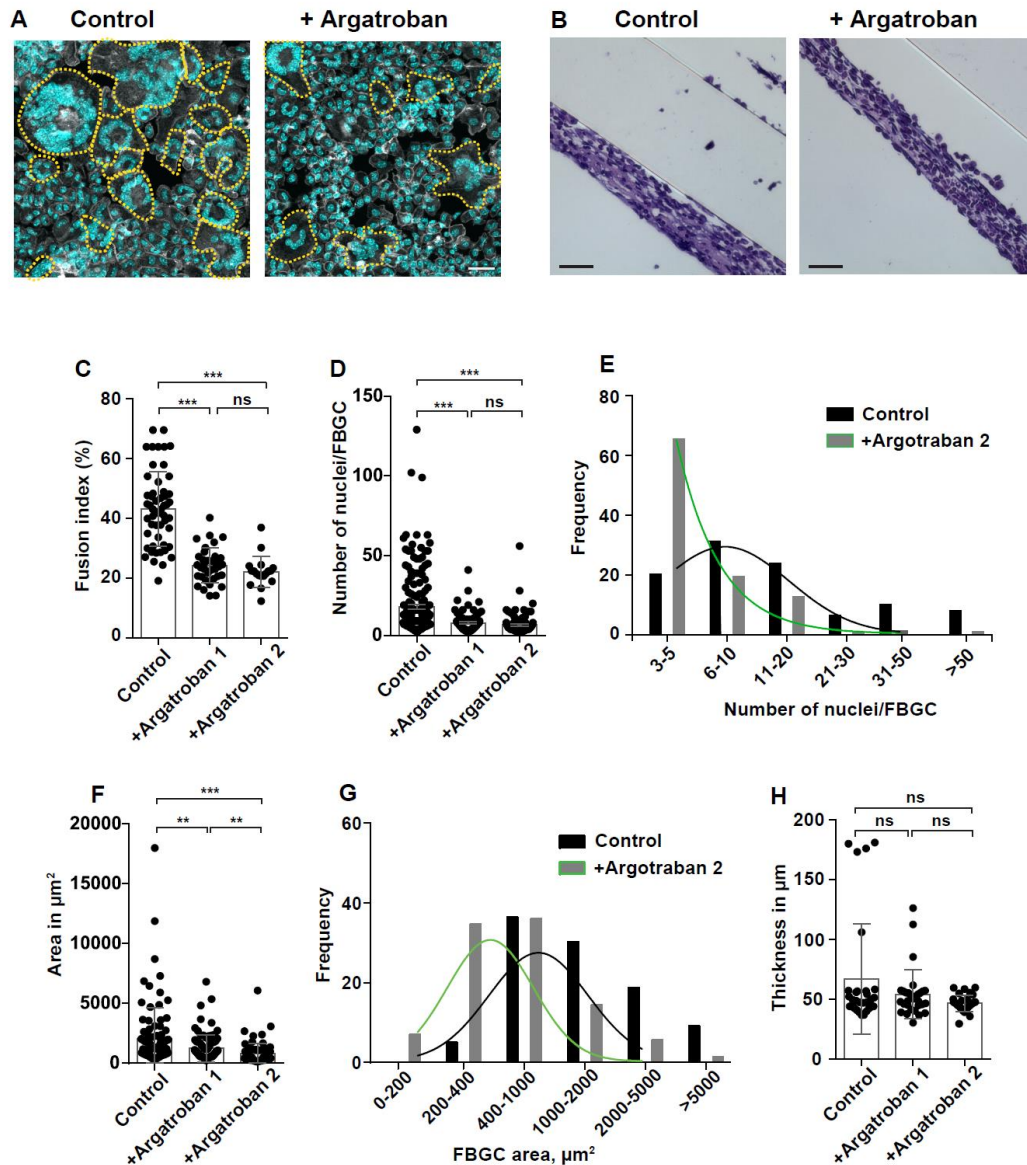


**Figure 5. Thrombin inhibitor reduces macrophage fusion but does not affect the capsule formation.** (A) Representative confocal images showing that treatment with argatroban, as compared with the untreated control, reduces FBGC formation. Argatroban (9 mg/kg and 18 mg/kg; termed argatroban 1 and 2, respectively) was injected i.p. for 5 days before implantation of materials for 7 days post-surgery. Control mice were injected with PBS. (B) Granulation tissue argatroban-treated mice was determined using ImageJ software. Ten random fields were used per sample to measure the thickness of cross-sections. Results shown are mean  $\pm$  SD from three independent experiments (6 mice per each group). ns, not significant, \*\* $p < .01$ , \*\*\* $p < .001$

determined. In these mice, the six A $\alpha$  chain amino acid residues upstream of the thrombin cleavage site (Glu<sup>P6</sup>-Gly-Gly-Gly-Val-Arg<sup>P1</sup>) were mutated to prevent the removal of FpA

thus incapacitating the ability of fibrinogen to polymerize (Prasad *et al.*, 2015). Similar to the FBR observed in  $Fg^{-/-}$  mice, macrophage fusion was impaired (Fig. 6A and 6C) with the fusion index being ~6-fold lower at day 14 in  $Fib^{AEK}$  mice compared to WT mice. Furthermore, similar to  $Fg^{-/-}$  mice, the reduced fusion in  $Fib^{AEK}$  mice was not due to a difference in the number of macrophages adherent to the surface of implants (Fig. 6D). However, in contrast to  $Fg^{-/-}$  mice, where a difference between mononuclear macrophage spreading on implanted surfaces was observed only at day 3, cell spreading on surfaces retrieved from  $Fib^{AEK}$  mice was significantly reduced at all times (Fig. 6E). No significant difference between the number of leukocytes in the lavage of WT and  $Fib^{AEK}$  mice was found (Fig. S5).

Western blot analyses of fibrinogen species deposited on the surface of implants demonstrated the availability of total fibrinogen antigen with a molecular weight of 340 kDa (Fig. S6B). No reactivity with anti-FpA was detected (Fig. S6B, *middle panel*). The lack of reactivity with anti-FpA mAb can potentially arise from the substitution of six amino acid residues in the FpA rather than the cleavage of the peptide. Indeed, fibrinogen isolated from  $Fib^{AEK}$  mice failed to interact with the anti-FpA antibody (Fig. S6A, *right panel*). Moreover, consistent with failed fibrin polymerization, we were unable to produce fibrin from fibrinogen isolated from  $Fib^{AEK}$  mice and consequently detect the interaction of anti-fibrin mAb 59D8 with this protein. Hence, no interaction of mAb 59D8 with proteins deposited on the surface of implants was found (Fig. S6B). Similar to WT mice, the presence of a product with a molecular weight of ~150-180 kDa reactive with a secondary antibody was observed.

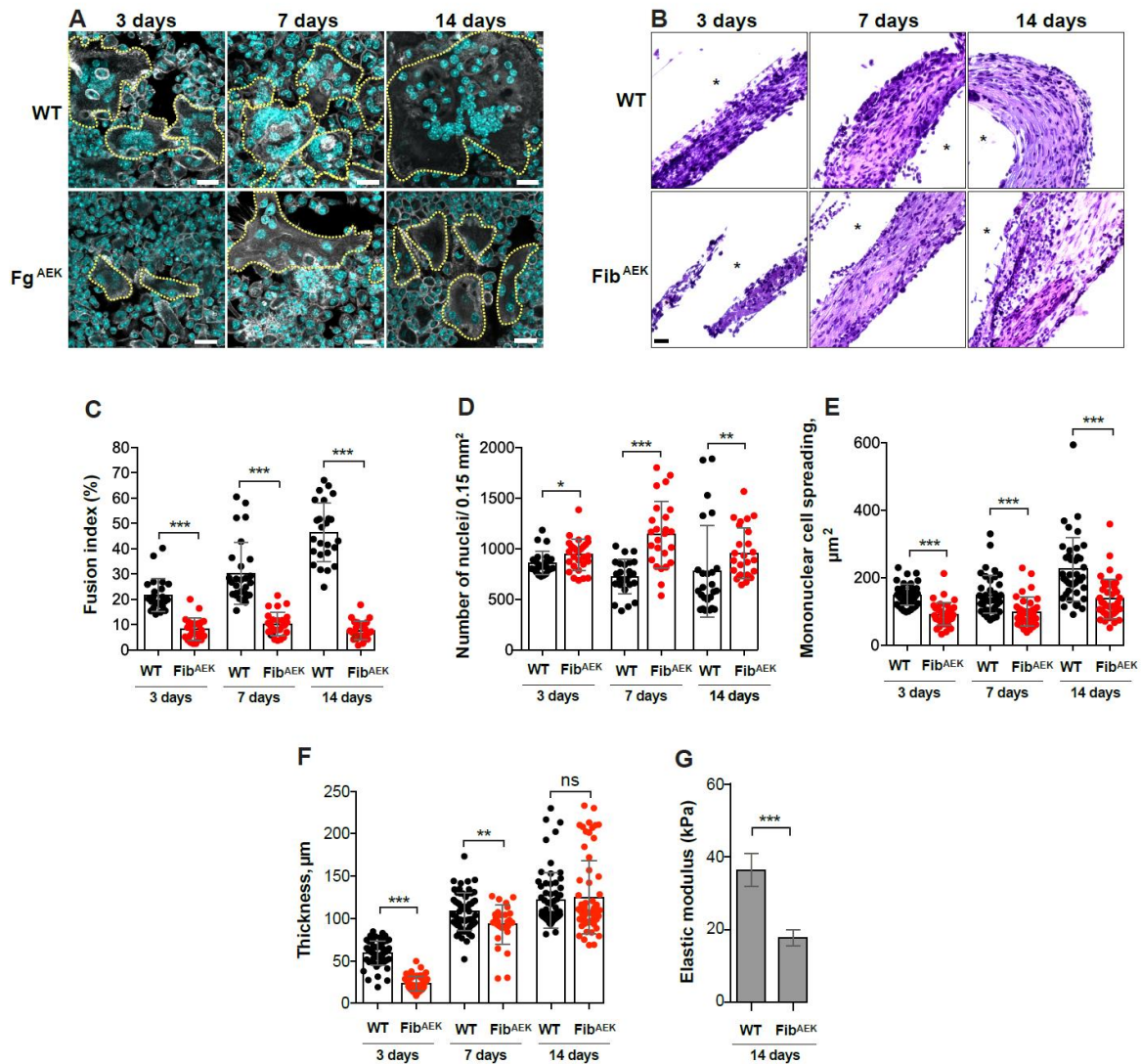


**Figure 6. The formation of FBGCs and not the production of granulation tissue is compromised in Fib<sup>AEK</sup> mice.** PCTFE sections were implanted in WT and Fib<sup>AEK</sup> mice for 3, 7, and 14 days. (A) Explants retrieved after selected time points were separated from the surrounding fibrinous capsule, fixed, and incubated with Alexa Fluor 546-conjugated phalloidin (white) and DAPI (teal). Representative confocal images are shown. The scale bar is 20 μm. (B) Representative images of the H&E stained cross-sections of implants retrieved from the peritoneum of WT and Fib<sup>AEK</sup> mice. The scale bar is 20 μm. (C) Fusion indices of macrophages formed on the surface of implants that have been retrieved at different time points from WT and Fib<sup>AEK</sup> mice. (D) The density of cells on the surface of explants retrieved at various time points as determined by counting the number of nuclei. (E) Spreading of the mononuclear cells on the surface of implants. (F) The thickness of granulation tissue formed on the surface of implants retrieved from WT and Fib<sup>AEK</sup> mice. Results shown are mean ± S.D. of four independent experiments. ns, not significant, \**p* < .05, \*\**p* < .01, \*\*\**p* < .001. (G) Mechanical properties of the 14-day capsules formed around implants retrieved from WT and Fib<sup>AEK</sup> mice were determined

by measuring the elastic moduli (expressed in Pa) using AFM as described in Materials and Methods. Results are mean and S.E. of 300 force-indentation curves on each sample.

Surprisingly, although less robust on day 3, granulation tissue-like material was formed around PCTFE sections implanted in Fib<sup>AEK</sup> mice and its thickness was comparable to that in WT mice at days 7 and 14 (Fig. 6, B and F). Western blotting showed that the material present in the capsule contained fibrinogen as evidenced by the interaction with an antibody directed against the total protein and an IgG-immunoreactive 150-180 kDa product (Fig. S6C).

Grossly, the capsules retrieved from WT and Fib<sup>AEK</sup> mice were indistinguishable but Fib<sup>AEK</sup>-derived material was softer and more fragile, indicating that the mechanical properties of these matrices were different. To quantitatively assess the difference, we determined the stiffness of each tissue using AFM. The analysis showed that the elastic modulus of granulation tissue isolated from WT mice was 2.3-times greater than that of tissue retrieved from Fib<sup>AEK</sup> mice ( $37.0 \pm 2.2$  kPa vs.  $16.2 \pm 0.6$  kPa; Fig. 6G).

## **5, Analysis of the fibrinous capsule formed around implants in WT and Fib<sup>AEK</sup> mice**

Since granulation tissue-like material was formed around implants in Fib<sup>AEK</sup> mice in the absence of fibrin polymerization we sought to determine its composition. Because fibrinogen was detected by Western blotting, we first examined its spatial distribution within the capsule and compared it with the capsule retrieved from WT mice using immunohistochemistry. As shown in Fig. 7A and 7B, the extensive deposition of fibrinogen and fibrin were detected in the capsule retrieved from WT mice. Examination of granulation tissue in Fib<sup>AEK</sup> mice

revealed the presence of total fibrinogen antigen that increased by day 14 (Fig. 7C). Consistent with the results of Western blotting, no fibrin was detected (Fig. 7D).

Next, we determined whether other proteins may organize granulation tissue-like material in Fib<sup>AEK</sup> mice. Since granulation tissue is a precursor of the fibrous collagenous capsule, we examined the time-dependent deposition of collagen in both WT and Fib<sup>AEK</sup> mice using a mAb directed to Type 1 $\alpha$  collagen. The collagen density in the capsule was quantified by measuring the green-pixel coverage per 400  $\mu\text{m}^2$  area. While no collagen was detected in the 3-day capsule formed in both strains of mice, it was detectable on day 7 and its amount strongly increased on day 14 in WT mice (Fig. 8, A and C). In comparison, the amount of collagen was significantly less in the capsule from Fib<sup>AEK</sup> mice (Fig. 8, B and C). Additional investigations of the capsule organization using transmission electron microscopy (TEM) confirmed the presence of abundant collagen fibrils in WT mice that were organized into fibers that ran approximately at right angles to one another (Fig. 8D, shown for day 14). Collagen fibrils were also observed in the capsule of Fib<sup>AEK</sup> mice (Fig. 8D); however, fibrils were significantly shorter than in WT mice ( $590\pm 343$  nm vs.  $1515\pm 697$  nm) (Fig. 8E). Moreover, the density of fibrils determined as the distance between individual fibrils was significantly greater in WT- than in Fib<sup>AEK</sup>-derived tissue ( $18.2\pm 3.9$  nm vs.  $27.2\pm 4.5$  nm) (Fig. 8F). We also found that material retrieved from the WT and Fib<sup>AEK</sup> capsules contained

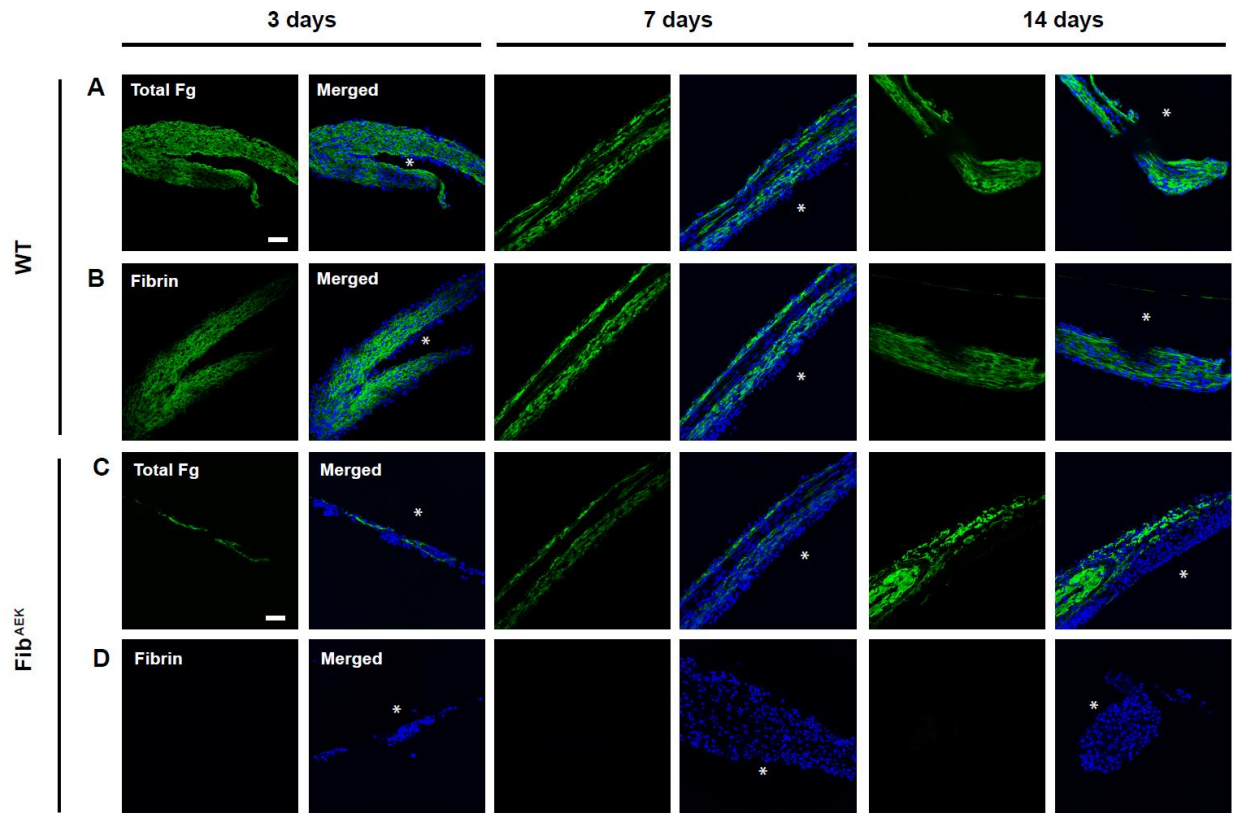


**Figure 7. Distribution of fibrinogen and fibrin in the capsule formed on the surface of implants in WT and Fib<sup>AEK</sup> mice.** Representative confocal images of granulation tissue formed on the surface of implants 3, 7, and 14 days after surgery. The samples were incubated with antibodies that recognize total fibrinogen (A, C) and fibrin (B, D). The scale bar is 50  $\mu$ m.

fibrillin and elastin, typical components of the extracellular matrix of connective tissue (Fig. S7, A-D). These proteins were first detected as early as day 3 and their amounts increased by day 14. The density of fibrillin and elastin in the capsule from WT mice was greater than in Fib<sup>AEK</sup> mice on day 3 and was not significantly different at later time points (Fig. S7, E and F).

It is generally believed that mononuclear macrophages and FBGCs recruit fibroblasts that begin to invade granulation tissue after 2-3 weeks after implantation, differentiate into myofibroblasts, and initiate collagen deposition (Anderson, 2001; Ratner, 2002). The

absence of cells with morphological features of fibroblasts/myofibroblasts in the TEM images and rather an early deposition of collagen in the capsule from WT and Fib<sup>AEK</sup> mice suggested that other cells may secrete collagen. To identify these cells, we labeled granulation tissue retrieved from WT and Fib<sup>AEK</sup> mice with a mAb recognizing  $\alpha$  smooth muscle actin ( $\alpha$ SMA), a myofibroblast marker, and CD68, a macrophage marker. Many cells in the capsules retrieved at 3-14 days appeared to show the presence of both proteins (Fig. 9, A-D). However, the tight packing of cells in the capsule precluded the quantification of cells that expressed only  $\alpha$ SMA, only CD68, or both proteins.



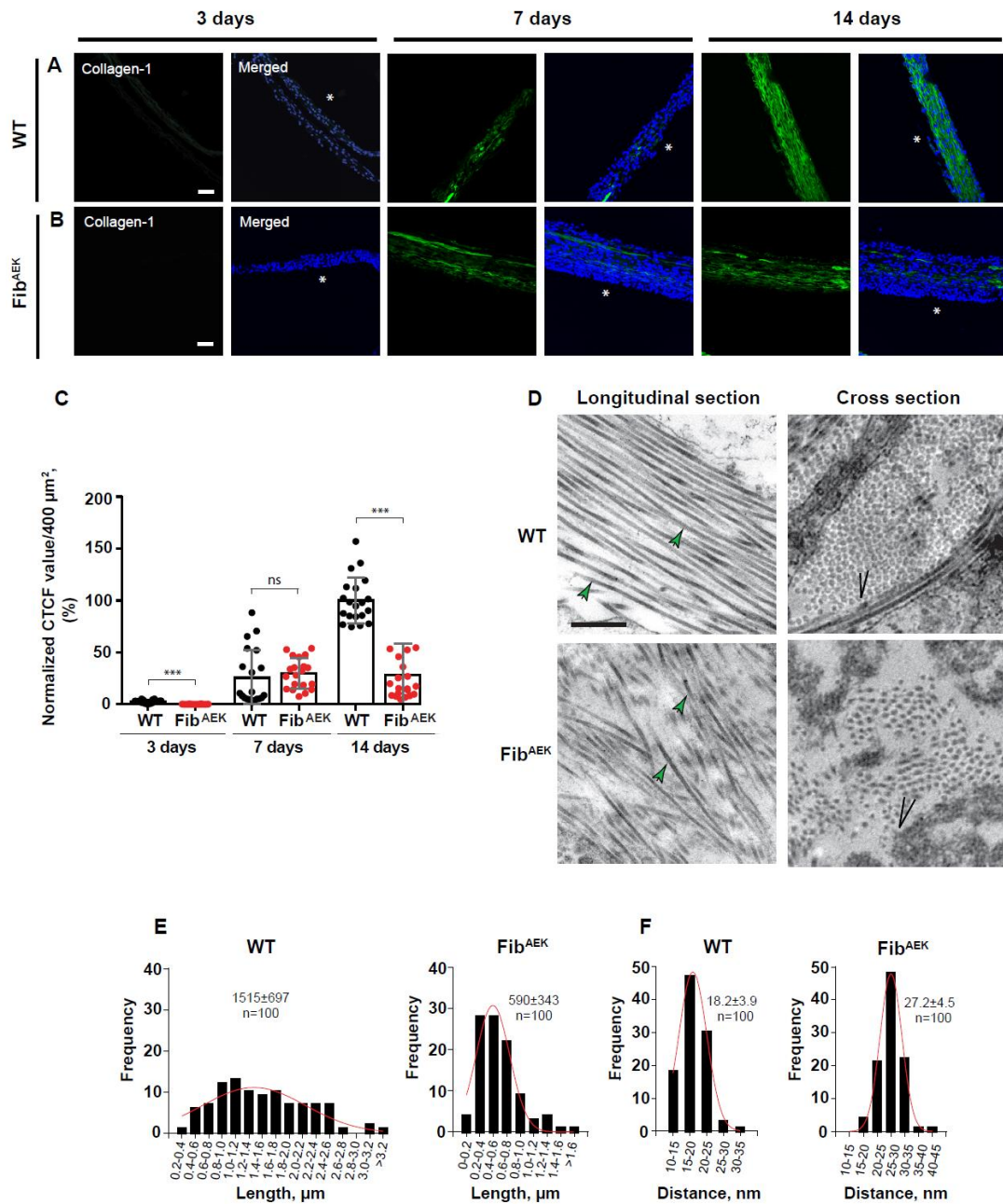


**Figure 8. Deposition of collagen in the capsule formed on the surface of implants in WT and Fib<sup>AEK</sup> mice.** PCTFE sections were implanted in WT and Fib<sup>AEK</sup> mice for 3, 7, and 14 days and the capsules formed were analyzed for the presence of collagen. (A, B) Representative immunofluorescence images of the samples incubated with antibodies that recognize collagen 1a. The scale bars are 50 μm. (C) Quantification of fluorescence intensities of images of collagen deposition shown in A and B. CTCF (correlated total cell fluorescence) values were determined by ImageJ software using the following formula: Integrated Density-

(Area of selected region x Mean fluorescence of background readings). Collagen expression in the 14-day capsule was assigned a value of 100%. Results shown are mean  $\pm$  SD of 3 independent experiments. (D) The ultrastructural details of the capsule were examined by TEM. Representative TEM micrographs of the sections prepared by cutting the specimen parallel (*longitudinal*) and vertical (*cross*) to the substratum are shown. The scale bar is 500 nm. (E) The frequency distribution of the collagen fiber lengths in the capsule from WT and Fib<sup>AEK</sup> mice. (F) The frequency distribution of the collagen fiber densities in the capsule from WT and Fib<sup>AEK</sup> mice.

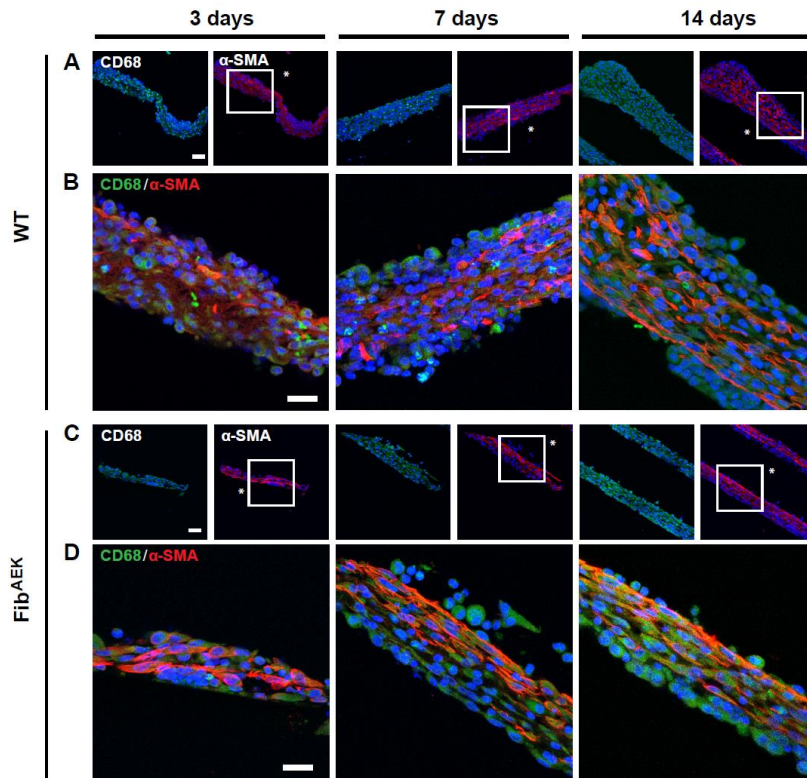


**Figure 9. Macrophages within the fibrous capsule express  $\alpha$ SMA and CD68.** PCTFE sections were implanted in WT (A, B) and Fib<sup>AEK</sup> (C, D) mice for 3, 7, and 14 days. Representative images of the capsule samples incubated with anti-CD68 (green) and anti- $\alpha$ SMA (red) antibodies are shown. High magnification views of boxed areas in A and C are shown in B and D. The scale bars are 50  $\mu$ m (A and C) and 20  $\mu$ m (B and D).

Therefore, we isolated cells from the 14-day capsules and analyzed them by immunocytochemistry using mAbs directed to  $\alpha$ SMA and CD68. The analyses showed that a small population of isolated cells ( $\sim$ 6%) expressed  $\alpha$ SMA and were negative for CD68

(Fig. 10, A and B; shown for cells isolated from a 14-day WT capsule). Based on these features and the presence of actin stress fibers, these cells were identified as myofibroblasts (Fig. 10 A, *upper panel*). The main population of cells (~ 93%) isolated from the WT and Fib<sup>AEK</sup> capsules expressed  $\alpha$ SMA and CD68, displayed podosomes, and were thus identified as monocyte/macrophages (Fig. 10, A and B). MAb M1/70 which recognizes myeloid-specific CD11b/CD18 (integrin Mac-1) also labeled these cells (Fig. 10C, *bottom panel*).

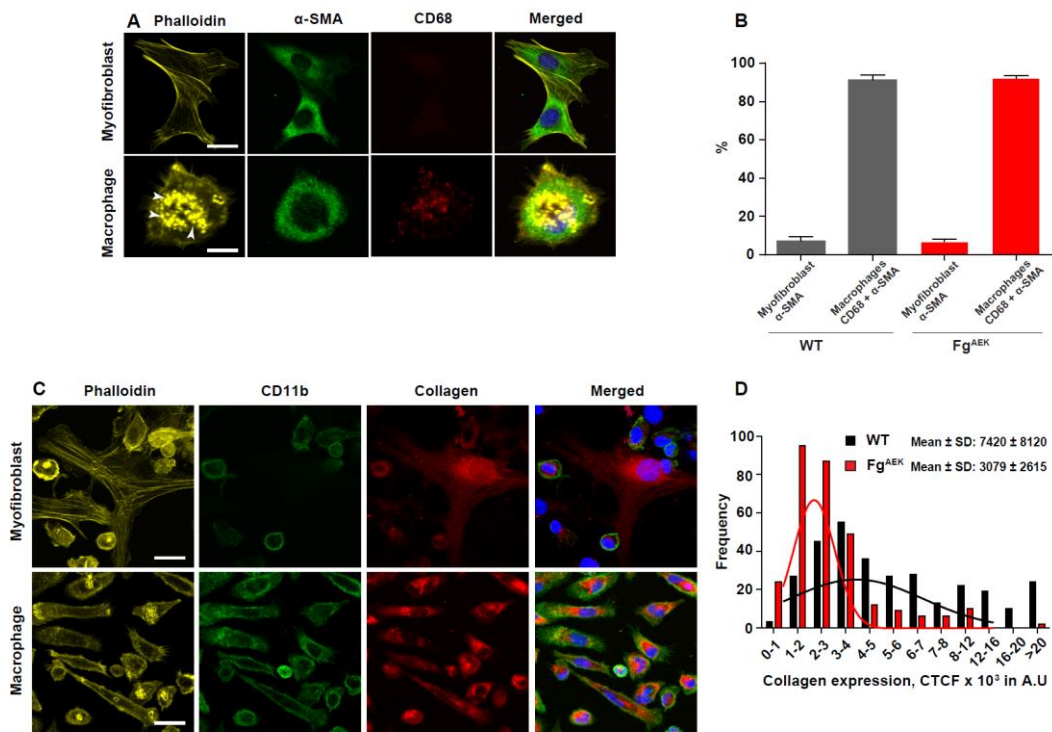


**Figure 10. Macrophages within the fibrous capsule express collagen.** PCTFE sections were implanted in WT and Fib<sup>AEK</sup> mice for 14 days and the cells accumulated within the capsules were isolated as described in the Materials and Methods. (A) The cells were allowed to adhere to the surface of a FluoroDish, fixed, and incubated with Alexa Fluor 568-conjugated phalloidin, anti- $\alpha$ SMA, and anti-CD68 antibodies. Representative confocal images of myofibroblasts and macrophages isolated from the capsule retrieved from WT mice are shown. Arrowheads point to podosomes seen in macrophages incubated with phalloidin-Alexa Fluor 568. The scale bar is 10  $\mu$ m. (B) Quantification of cells expressing  $\alpha$ SMA, CD68, or both. (C) The cells isolated from the capsule obtained from WT mice were incubated with mAb M1/70 and anti-collagen I antibodies. The scale bar is 20  $\mu$ m. (D) The frequency distribution of fluorescence intensities for collagen I in macrophages isolated from the capsules retrieved from WT and Fib<sup>AEK</sup> mice was expressed as CTCF arbitrary units (A.U).

Both fibroblasts and monocyte/macrophages were stained for collagen I (Fig. 10C). Interestingly, collagen expression in WT macrophages was ~2.4-fold greater than in their Fib<sup>AEK</sup> counterparts (Fig. 10D). Macrophages also expressed fibrillin and elastin; however, expression of these proteins did not differ between WT and Fib<sup>AEK</sup> capsules (Fig. S8). Together, these results suggest that cells of monocyte origin present in the capsule are the main cell type responsible for collagen production and that WT monocytes secrete more collagen than cells accumulated in the Fib<sup>AEK</sup> capsule.

#### **4.4 Discussion**

The foreign body reaction (FBR) to implanted biomaterials begins with the spontaneous adsorption of host proteins within seconds after contact with body fluids (Anderson *et al.*, 2008). This process initiates the recruitment and accumulation of phagocytes on the surface of implants. Among adsorbed proteins, fibrin(ogen) is chiefly responsible for this early inflammatory response (Tang and Eaton, 1993). In the present study, we have examined the role of fibrino(gen) in mediating the later stages of FBR, including macrophage fusion and the fibrous capsule formation. Several lines of evidence indicate that fibrin polymer deposited on the surface of implants is required for macrophage fusion. First, the presence of fibrinogen, a fibrin precursor, is indispensable for the formation of macrophage-derived FBGCs since the implantation of materials into the peritoneum of Fg<sup>-/-</sup> mice resulted in the almost complete lack of macrophage fusion. However, despite the presence of intact fibrinogen in Fib<sup>AEK</sup> mice that express a mutated form of fibrinogen incapable of thrombin-mediated polymerization, macrophage fusion was also strongly reduced. Second,

implantation in  $Fg^{-/-}$  mice of materials coated with fibrin polymer fully rescued the fusion defect whereas coating with fibrinogen or fibrin-monomer partially normalized macrophage fusion. Third, inhibition of thrombin with argatroban reduced macrophage fusion. These findings indicate that fibrin polymer is a major determinant of FBGCs formation.

Previous studies conducted in mice made hypofibrinogenemic by injections of ancrod, a thrombin-like protease from the venom of Malayan pit viper showed almost no phagocyte accumulation on materials implanted for 16 hours in the mouse peritoneum and this defect could be normalized by coating materials with fibrinogen or by injection of purified fibrinogen (Tang and Eaton, 1993). In addition, studies conducted in  $Fg^{-/-}$  mice showed a ~two-fold decrease in the number of phagocytes adherent to implanted biomaterial 18 hours after implant (Busuttill *et al.*, 2004). Our data showed that 3 days after implantation, when macrophage fusion begins, the surfaces implanted in WT and  $Fg^{-/-}$  mice contain similar numbers of mononuclear cells (Fig. 1C), suggesting that at later times, adsorption of other plasma proteins can support phagocyte adhesion. However, only the absence of fibrin(ogen) in  $Fg^{-/-}$  mice resulted in the dramatic defect in macrophage fusion. Moreover, analyses of the surfaces explanted from WT mice showed that adsorbed fibrinogen converted into fibrin as was evidenced by the presence of the product with the molecular weight of ~340 kDa that lacked FpA (Fig. 3B). Fibrin deposited on the surface was not intact though but was missing the epitope for mAb 59D9 which recognizes the N-terminal portion of the  $\beta$ -chain of fibrinogen after cleavage of FpB. This finding can be explained by the propensity of the  $\beta$ -chain to undergo rapid degradation by various proteases releasing the  $\beta$ 15-41 and  $\beta$ 42-53 fragments (Takagi and Doolittle, 1975; Etscheid *et al.*, 2018).

Consistent with the requirement for fibrin, coating of materials with fibrin polymer normalized macrophage fusion in  $Fg^{-/-}$  mice. Importantly, since the coating of implants with purified fibrinogen or fibrin-monomer only partially restored macrophage fusion, the polymeric state of fibrin seems to be essential for effective fusion. The requirement for fibrin polymer rather than adsorbed fibrinogen in mediating macrophage fusion is puzzling since it is generally believed that adsorbed fibrinogen, due to its partial unfolding, has altered conformation and shares many properties with fibrin, including expression of the binding sites for integrins, monoclonal antibodies, and other molecules (Zamarron *et al.*, 1991; Lishko *et al.*, 2002). The fusion-promoting effect of the fibrin network deposited on the surface of implants may be indirect and involve trapping of specific cytokines and chemokines involved in the induction of the fusion program. Alternatively, the physical properties of the fibrin matrix *versus* adsorbed fibrinogen can potentially influence macrophage fusion by initiating a specific mechanotransduction response. In this regard, numerous studies demonstrated that the physical properties of extracellular matrices, including those made of fibrin(ogen) influence intracellular signaling and cell responses (Wang *et al.*, 1993; Parsons *et al.*, 2010; Podolnikova *et al.*, 2010; Cantini *et al.*, 2020). Indeed, we have observed that mononuclear cell spreading, a sign of integrin-mediated signaling, and the ensuing actin cytoskeleton rearrangement was lower on the surfaces implanted in  $Fib^{AEK}$  mice compared to WT mice (Fig. 6E). The actin cytoskeleton is known to be actively involved in macrophage fusion (DeFife *et al.*, 1999; Jay *et al.*, 2007; Faust *et al.*, 2019) and thus the interaction of macrophage integrins with fibrin matrices may initiate alterations of the actin cytoskeleton conducive to fusion. Yet another possibility is that fibrin

polymerization results in the exposure of sequences that are not present in the soluble and adsorbed forms of fibrinogen and which may serve as binding sites for cellular structures involved in macrophage fusion. This proposal is based on a precedent established by studies showing that binding of t-PA and VE-cadherin is mediated by fibrin-specific sequences, not accessible in fibrinogen (Nieuwenhuizen *et al.*, 1990; Chalupowicz *et al.*, 1995; Yakovlev *et al.*, 2000). At this juncture, the basis for the differential effect of fibrinogen and fibrin remains speculative and further studies may help to define the mechanisms underlying the fusion-promoting activity of fibrin polymer.

Our data show that fibrinogen is required for the formation of granulation tissue and, ultimately, the fibrous capsule surrounding the implant. Only a layer of adherent cells but a complete lack of the capsule was detected around materials implanted in  $Fg^{-/-}$  mice (Fig. 2). At the same time, although fibrin polymerization was compromised, the formation of the capsule in  $Fib^{AEK}$  mice was not impaired, suggesting that fibrinogen was required for the capsule formation (Fig. 6F). Furthermore, a small capsule was formed around the materials coated with fibrinogen, fibrin-monomer, and fibrin polymer that were implanted into  $Fg^{-/-}$  mice (Fig. 4). In agreement with these data, biomaterials coated with polyethylene oxide-like compounds that are known to be ultra-low fouling and inhibit fibrinogen adsorption (Shen *et al.*, 2001) reduced the fibrous capsule thickness (Ward *et al.*, 2002). Analogously, zwitterionic materials with ultralow-fouling properties (Jiang and Cao, 2010) resisted the capsule formation for several months after subcutaneous implantation (Zhang *et al.*, 2013). Therefore, the deposition of fibrin(ogen) on the surface of implants seems to nucleate the fibrous capsule formation.

Analyses of the capsule formed in WT and Fib<sup>AEK</sup> mice showed that in addition to fibrinogen it contains collagen and other proteins typically present in the extracellular matrix of connective tissue, including fibrillin and elastin. However, the amount of collagen in the capsule from WT mice was significantly higher and collagen fibers were longer and packed into denser bundles than in the capsule from Fib<sup>AEK</sup> mice. These morphological features were reflected in the different mechanical properties of both matrices. Based upon the measurement of the elastic modulus, the matrices formed in WT mice were about 2.3-fold stiffer than those in Fib<sup>AEK</sup> mice. These findings suggest that fibrin polymer abundantly deposited in the capsule of WT mice may organize collagen and other proteins into a dense matrix. This is, to the best of our knowledge, the first evidence for a critical role of fibrin polymer in the organization of the fibrous capsule.

It is generally believed that cells responsible for collagen production and deposition in the fibrous capsule are  $\alpha$ SMA-expressing myofibroblasts. Our data show that cells producing collagen I and other connective tissue proteins indeed express  $\alpha$ SMA. However, these cells also express CD68 and integrin Mac-1 (CD11b/CD18), suggesting that these cells are of monocyte/macrophage origin. This finding is corroborated by the fact that collagen I was deposited in the capsule between 3-7 days and fibrillin and elastin were detected as early as 3 days after implantation, i.e. much faster than would be expected for the secretion of these proteins by recruited fibroblast/myofibroblasts. Indeed, myofibroblasts were identified only in a 14-day capsule and their proportion was small (~6%) (Fig. 10B). Given this small number, it seems unlikely that the staining of capsule-derived cells for collagen I was due to the uptake of collagen secreted by myofibroblasts.



Recent murine and human studies provided evidence that monocyte-derived cells at sites of injury express  $\alpha$ SMA and secrete collagen I (Keeley *et al.*, 2010; Reilkoff *et al.*, 2011; Duffield *et al.*, 2013). These cells originate from a subset of circulating monocytes that express collagen I, a mesenchymal marker, and CD45 and CD11b/CD18, hematopoietic markers (Bucala *et al.*, 1994; Quan *et al.*, 2004; Suga *et al.*, 2014). Cells that combine a gene expression profile of macrophages with that found in fibroblasts and have both the inflammatory features of macrophages and the tissue remodeling properties of fibroblasts have been termed fibrocytes (Bucala *et al.*, 1994; Keeley *et al.*, 2010; Reilkoff *et al.*, 2011). Fibrocytes participate in both physiological wound healing and pathological fibrosis (Keeley *et al.*, 2010; Reilkoff *et al.*, 2011). Furthermore, fibrocyte-like cells have been detected in the vicinity of biomaterials (Mooney *et al.*, 2010; Thevenot *et al.*, 2011). Mooney *et al.* showed that cells within the capsule formed in response to implantation of a foreign object in the peritoneal cavity express  $\alpha$ SMA protein (Mooney *et al.*, 2010) and also express genes typically found in macrophages (Mooney *et al.*, 2014). It is presently unclear whether  $\alpha$ SMA<sup>+</sup>/CD68<sup>+</sup>/CD11b<sup>+</sup>/Col<sup>+</sup> cells infiltrating the capsule in our implant model are recruited from blood or originate from other sources. Although further studies are needed to elucidate the phenotype of these cells and their origin, this is the first demonstration that cells expressing both hematopoietic and stromal markers are involved in the deposition of collagen and other extracellular matrix proteins in the capsule during the FBR.

Previous studies revealed many aspects of macrophage fusion, including the requirement for adhesion, the induction of specific intracellular signaling, and the role of specific molecules (Helming and Gordon, 2009). The majority of this information was generated *in*

*vitro* experiments using macrophages cultured on various surfaces, including biomaterials, with only a few studies performed *in vivo* models of implantation (Takeda *et al.*, 2003; Kyriakides *et al.*, 2004; Tsai *et al.*, 2005; Yagi *et al.*, 2005; MacLauchlan *et al.*, 2009; Doloff *et al.*, 2017). Moreover, with the exception of plasma fibronectin (pFN), little consideration has been given to proteins that may serve as adhesive substrates for fusing macrophages *in vivo*. Using pFN conditional knock-out mice, Keselowsky *et al* demonstrated that the number of FBGCs on biomaterials implanted subcutaneously was three times higher than in WT mice (Keselowsky *et al.*, 2007). The mechanism by which pFN exerts this effect remains elusive and the role of cellular fibronectin which was not depleted needs to be investigated. McNally *et al* showed that among several plasma proteins that might adsorb on the surface of implants, vitronectin mediated the greatest IL-4-induced fusion of cultured monocyte/macrophages (McNally *et al.*, 2008). While vitronectin can serve as important adhesive ligands mediating initial macrophage adhesion to the surface of implants, its role in macrophage fusion has not been corroborated in the present study as the deficiency of a single protein, fibrinogen, completely abrogated macrophage fusion. More importantly, studies conducted in a unique Fib<sup>AEK</sup> mouse model allowed us to conclude that it is fibrin rather than intact fibrinogen *per se* that drives the FBR.

It is well established that the physical and chemical properties of materials modulate their ability to acquire a protein coat (Latour, 2008; Horbett, 2012) and this, in turn, can alter the extent of macrophage fusion and macrophage/FBGC phenotype (Anderson *et al.*, 1999) (Brodbeck *et al.*, 2002a; Brodbeck *et al.*, 2002b; Shen *et al.*, 2004; Jones *et al.*, 2007). This concept has been mainly explored *in vitro* studies; however, implantation in mammals of

materials with diverse surface properties elicits a very similar FBR and results in an essentially identical healing response (Ratner, 2002, 2015). It is possible that almost unavoidable adsorption of fibrinogen on the surface of all implanted materials and its rapid conversion into fibrin polymer would largely negate the unique surface properties of materials. Hence, macrophages will likely interact with fibrin-coated material rather than directly with the material. The physical and adhesive properties of fibrin matrices deposited on the surface of various materials implanted in different locations and their ability to support FBGC formation remain to be elucidated. Nonetheless, given the role of fibrin polymer in promoting macrophage fusion, inhibition of thrombin may be a useful strategy to control the adverse effects of FBGCs. Furthermore, inhibition of fibrin formation leading to the reduced density of collagen in the fibrous capsule may be especially beneficial for certain medical devices, including biosensors and controlled drug delivery systems that often fail due to the formation of a diffusion barrier.

## **4.5 Materials and methods**

### **1, Reagents**

The hybridoma producing mouse mAb 59D8, which recognizes the N-terminal end of the  $\beta$ -chain of human and mouse fibrin was previously described (Hui *et al.*, 1983). The mAb was purified using Protein A agarose and characterized by ELISA as previously described (Owaynat *et al.*, 2015). The rat mAb M1/70 which recognizes mouse CD11b/CD18 (integrin Mac-1) was purified from conditioned media of hybridoma cells obtained from the American Tissue Culture Collection (Manassas, VA) and then conjugated

to Alexa Fluor 488 (catalog number A20181) according to the manufacturer's instructions (Thermo Fisher Scientific, Waltham, MA). The rabbit polyclonal antibody (catalog number PA5-29734), which recognizes mouse fibrinogen was purchased from Thermo Fisher Scientific (Waltham, MA) and the rabbit polyclonal antibody directed against the mouse fibrinopeptide A (catalog number ab103648) was from Abcam (Cambridge, MA). The mouse anti-collagen 1 $\alpha$  (catalog number sc-293182) and anti-elastin (catalog number sc-58756) mAbs were from Santa Cruz Biotechnology (Dallas, TX). The mouse anti- $\alpha$ SMA mAb (catalog number MAB1420-SP) was from R&D systems and the rat anti-CD68 mAb (catalog number 14-0681-82) was from Invitrogen (Carlsbad, CA). The mouse anti-fibrillin-1 mAb (catalog number MAB2502) was purchased from Millipore (Temecula, CA). The secondary antibodies, Alexa Fluor 647-conjugated goat anti-rabbit IgG and Alexa Fluor 488-conjugated goat anti-mouse IgG, were obtained from Invitrogen (Carlsbad, CA). Thrombin inhibitor argatroban monohydrate (catalog number A0487) was from Sigma Aldrich (St. Louis, MO). The protease inhibitor cocktail was purchased from Thermo Fisher Scientific (Waltham, MA). Mouse fibrinogen (catalog number ab92791) was obtained from Abcam (Cambridge, MA) or purified from freshly isolated mouse blood. Fibrin-monomer was prepared by dissolving the fibrin clot in 20 mM acetic acid as previously described (Belitser *et al.*, 1980).

## **2, Mice**

Wild type (WT) C57BL/6J mice were purchased from The Jackson Laboratory (Bar Harbor, ME). Fibrinogen-deficient ( $Fg^{-/-}$ ) and fibrin-deficient ( $Fib^{AEK}$ ) mice were previously described (Suh *et al.*, 1995; Prasad *et al.*, 2015). All animals were given *ad libitum* access to food and water and maintained at 22 °C on a 12-h light/dark cycle. Experiments were performed according to animal protocols approved by the Institutional Animal Care and Use Committees at Arizona State University.

### **3, Thioglycollate-induced peritonitis**

Eight- to twelve-week-old male and female mice were used in all experiments with age- and sex-matched WT and  $Fg^{-/-}$  animals selected for side-by-side comparison. Peritonitis in mice was induced by the intraperitoneal injection of 0.5 ml of a 4% Brewer thioglycollate (TG) solution (Sigma-Aldrich, St. Louis, MO) as described (Podolnikova *et al.*, 2016). Cells were collected 3 days after TG injection by peritoneal lavage with 5 ml ice-cold PBS with 5 mM EDTA. The total number of cells in the lavage fluid was counted using a hemocytometer.

### **4, Biomaterial implantation and analyses of the retrieved explants**

As an *in vivo* model for assessing the FBR to biomaterials, a well-characterized (Freyria *et al.*, 1991; Tang and Eaton, 1993) intraperitoneal implantation model was used. The peritoneal cavity provides a good site for studying the cell reactions caused by implantation because of the minimal contact with the interstitium of the normal tissue. Sections (1.5×0.5 cm) of sterile polychlorotrifluoroethylene (PCTFE) or polytetrafluoroethylene (PTFE) were implanted into the peritoneum of mice as previously described (Faust *et al.*, 2019). Ten- to twelve-week old male and female mice were used in

all experiments with age- and sex-matched wild-type and deficient animals selected for side-by-side comparison. Animals were humanely sacrificed 3, 7, and 14 days later, and retrieved explants were divided into two parts. One part was used for calculating the fusion index by immunofluorescence and the other part was used for histological analyses. The fibrinous material that covered the explant (capsule) retrieved from WT and Fib<sup>AEK</sup> mice was carefully removed to expose the surface and saved for analyses of the protein composition by Western blotting. Before explantation, 2 ml of ice-cold PBS containing 5 mM EDTA was aseptically injected into the peritoneum, cells in the peritoneum were collected by lavage and counted. The percentage of macrophages in the lavage was determined by differential analysis of cytopsin preparations dyed with Wright stain. The material deposited around the implant in the form of a fibrinous capsule was collected for Western blot, histological, ultrastructural, and AFM analyses.

## **5, Preparation of plasma- and protein-coated PCTFE surfaces**

The plasma for coating of PCTFE surfaces and isolation of fibrinogen was prepared from blood isolated from WT and Fg<sup>-/-</sup> mice by cardiac puncture. Blood (0.3-0.6 ml) was drawn from each mouse using a 23G needle and insulin syringe. Anticoagulant citrate/dextrose solution was added to the blood at a 1:7 ratio. The blood was centrifuged at 3000 g for 15 min and the plasma was purified from the potential endotoxin contamination using high capacity endotoxin removal spin columns (ThermoFisher Scientific, Waltham, MA; 88274). The isolated plasma, purified mouse fibrinogen, and fibrin-monomer used in the “rescue” experiments were tested for endotoxin using Pierce<sup>TM</sup> Chromogenic Endotoxin

Quant kit (ThermoFisher Scientific; A39552S) and the results showed that proteins contained < 0.7 EU/ml.

## **6, Histological analyses**

Retrieved implants with a surrounding capsule were fixed in 10% formalin for 24 h at 22 °C. After fixation, the materials were embedded in paraffin, sectioned, and stained according to a standard histological H&E procedure. The sections were mounted on a cover glass and imaged using the EVOS FL Auto (Thermo Scientific, Waltham, MA) wide-field microscope and a 40x objective.

## **7, Isolation of cells from the capsule**

On days 7 and 14 after surgery, the PCTFE sections were explanted from the mouse peritoneum. The capsule was removed and placed into a 35-mm dish (FluoroDish™; World Precision Instruments, Sarasota, FL) filled with the warm DMEM/F-12 medium for 24 hours in a cell culture incubator. During this time the majority of the cells migrated out of the cap. The remaining cells in the cap were removed by incubating the cap in a collagenase D solution (1 mg/ml) for 2 hours at 37 °C followed by collecting the cells by centrifugation at 300 x g for 3 minutes. The cells were resuspended in DMEM/F-12 and added to the initial pool of cells in a Fluorodish. Adherent cells were fixed with 2% formaldehyde in PBS for 30 minutes, permeabilized with 0.1% Triton X-100 for 30 minutes, blocked with 1% BSA for 1 hour at 22 °C, and used for immunofluorescence.

## 8, Immunofluorescence

To determine the fusion index, retrieved PCTFE sections were fixed with 2% formaldehyde in PBS for 30 min at 22 °C. Adherent cells were permeabilized with 0.1% Triton X-100 in PBS for 30 min and then washed three times with PBS containing 1% BSA. Nuclei were labeled with DAPI and actin was labeled with Alexa Fluor 488/568-conjugated phalloidin according to the manufacturer's recommendation (Thermo Scientific, Waltham, MA). Samples were mounted in Prolong Diamond (Thermo Scientific, Waltham, MA) and imaged with a Leica SP5 or Leica SP8 laser scanning confocal microscopes using 40x/1.3 NA oil objective. The fusion index was determined as previously described (Faust *et al.*, 2018) and is defined as the fraction of nuclei within FBGCs expressed as the percentage of the total nuclei counted. Five to six fields imaged by a 40×objective that contained ~100–200 cells were analyzed for each experimental condition. The macrophage spreading was assessed using NIH ImageJ software by quantitating the surface area ( $\mu\text{m}^2$ ) of adherent macrophages.

To examine the presence of various extracellular matrix proteins in the capsule, paraffin blocks were cut and the sections deparaffinized followed by dehydration in ethanol. After incubation in PBS+1% BSA, the sections were incubated with primary antibodies (anti-fibrinogen, anti-fibrin, anti- $\alpha$ SMA, anti-CD68, anti-collagen 1 $\alpha$ , anti-fibrillin, and anti-elastin) for 1 h at 22 °C followed by secondary antibodies conjugated to Alexa Fluor 647. In addition to the above-mentioned primary antibodies, cells isolated from the capsule were incubated with mAb M1/70 directed to a mouse integrin Mac-1. Samples were mounted in



Prolong Diamond mounting solution (Thermo Scientific) and imaged with a 40x oil objective using an SP5 confocal microscope.

## **9, Western blotting**

The implants inserted into WT, Fg<sup>-/-</sup> and Fib<sup>AEK</sup> mice were explanted after 3, 7 and 14 days and the fibrinous capsule was removed from the surface (it is easily detachable with no adhesive resistance). The retrieved material sections and fibrinous capsules were placed in PBS containing protease inhibitors and then the loading buffer containing SDS (1% final concentration), 8 M urea, and 10 mM N-ethylmaleimide was added. Samples were electrophoresed on 7.5% SDS-polyacrylamide gels and proteins were transferred onto the Immobilon-P membrane (Millipore, New Bedford, MA). Blots were probed with anti-fibrinogen polyclonal antibody (1:100,000 dilution), anti-fibrinopeptide A polyclonal antibody (1:1000 dilution) and fibrin-specific mAb 59D8 (1 µg/ml) followed by goat anti-rabbit and rabbit anti-mouse secondary antibodies conjugated with horseradish peroxidase (1:10,000 dilution). Bound antibodies were detected by reaction with a SuperSignal West Pico Chemiluminescent Substrate (Thermo Scientific, Grand Island, NY; Cat. No 34577).

## **10, TEM analysis of the capsule**

1.5 cm x 0.5 cm PCTFE pieces implanted into mouse peritoneum were explanted after 14 days, fixed with 2.5% glutaraldehyde in 0.1 M PBS (pH 7.4) at 4 °C overnight, and then treated with 1% OsO<sub>4</sub> in 0.1 M PBS for 1 h. Subsequently, cells were washed with 0.1 M PBS and then dehydrated using acetone. Finally, the implants with the surrounding capsule were flat-embedded into Spurr's epoxy Resin, and 70-nm sections were obtained by

longitudinal or vertical sectioning of the sample. Sections were post-stained with uranyl acetate and Sato's lead citrate. Micrographs were taken using a Philips CM 12 TEM with a Gatan Model 791 camera.

## **11, Atomic Force Microscopy (AFM)**

An Asylum Research MFP-3D-BIO AFM was used to conduct the force-indentation measurements. AFM probes with sphere-cone geometry were used (LRCH-750 Team NanoTec, Villingen-Schwenningen, Germany). The spring constants (nominal  $k \sim 0.2 \text{ N.m}^{-1}$ ) were determined using the thermal energy dissipation method built-in the Asylum Research image acquisition software. Samples were measured at room temperature in DPBS. Quasi-static measurements with cantilever approach and retraction speed  $2 \mu\text{m s}^{-1}$  were conducted to collect elastic modulus data. In areas in the center of the samples, 15 grids of  $5 \times 4$  indentations were acquired by applying a trigger force of 45 nN which resulted in 10-15  $\mu\text{m}$  of indentation. The force-indentation curves were fitted to a quasi-static contact model for a sphero-conical indenter (Staunton *et al.*, 2016; Saini *et al.*, 2020).

## **12, Statistical analyses**

Unless indicated otherwise results are shown as the mean  $\pm$  SD from three independent experiments. Multiple comparisons were made via ANOVA followed by Tukey's or Dunn's post hoc test using GraphPad Instat software. Samples that passed the normal distribution test were analyzed by t-test. The remaining samples were analyzed by the Mann-Whitney test. Data were considered significantly different if  $p < 0.05$ .

#### **4.6 ACKNOWLEDGMENT**

We acknowledge the use of instruments within the W.M. Keck Bioimaging Facility at Arizona State University. Image data were collected using a Leica TCS SP5 LSCM (the National Institutes of Health SIG award S10 RR027154) and Leica TCS SP8 LSCM (the NIH SIG award S10 OD023691). We also acknowledge the use of facilities within the Eyring Materials Center at Arizona State University supported in part by NNCI-ECCS-1542160.

## CHAPTER 5

### CONCLUSION AND OUTLOOK

This dissertation has provided several discoveries crucial to the cellular mechanisms of macrophage fusion. Novel actin-based structures were, for the first time, observed during the Foreign Body Response, and the role of fibrin polymers in the progression of FBR at later stages was determined. The studies presented in chapter 2 demonstrate that macrophage fusion is facilitated by actin-based protrusions emerging from a podosome-enriched region while the studies in chapter 3 established that macrophage fusion on implanted biomaterials depends on novel actin-based zipper-like structures which appear at the contact sites between closely apposed MGCs just prior to fusion. Further study of macrophage fusion during FBR on biomaterials (chapter 4) determined that the fibrin polymer formed on the provisional matrix played a dominant and necessary role in facilitating macrophage fusion and modulating the collagen deposition within surrounding granulation tissue.

The ability to study the cellular mechanisms of macrophage fusion on fusion-friendly, high-optical quality glass surfaces significantly impacted the study's outcome. For the first time, we could study macrophage fusion using live-cell imaging by phase-contrast and fluorescent microscopy with high spatiotemporal resolution. Live-cell imaging techniques addressed two different pieces of the picture. Using phase-contrast imaging, we determined that most of the fusion events between macrophages proceed by forming short

membrane protrusions. Further studies using the recently innovated technique of lattice light-sheet microscopy (LLSM) showed that these protrusions are driven by actin filaments and correlated with the podosome-enriched region. Most exciting, imaging of the fusion event at high speed by LLSM captured the moment at which the actin-based protrusive machinery created a pore between two fusing macrophages - details that have never been observed before. Revealing the fact that actin-based membrane protrusion was mechanistically linked to macrophage fusion provided us with the idea that the regulatory mechanisms of actin growth in this particular type of membrane protrusion might be similar to those in other types of membrane protrusions occurring at the leading edge of motile cells. As a result, we postulated and subsequently identified an integral role of Cdc42, WASp, and Arp2/3 complex proteins in regulating the actin-based protrusions involved in macrophage fusion. As a result, the correlation of such actin-based protrusions in macrophages with the growth of podosomes in motile cells is clear, but the mechanisms that govern this correlation are yet to be identified. Comparative study of lamellipodia, filopodia, podosomes, and the macrophage fusion facilitating protrusions could shed light on discovering specific regulatory proteins associated only with the macrophage fusion machinery. Hence, this particular specificity would provide a novel method to regulate the MGC formation *in vitro* and *in vivo*.

Furthermore, discovery of zipper like structures, another actin-based structure at the MGC-MGC contact sites seen in later stages of FBR, was intriguing since, based on our best knowledge, these structures are novel and have not been previously reported.

These structures demonstrate the importance of initiating future study of how localized remodeling of the actin cytoskeleton, in distinct steps, may underlie regulation of macrophage fusion and MGC formation on biomaterial implants.

Our use of IL-4 induced peritoneal macrophages plated on highly fusogenic paraffin-coated glass surfaces enabled us for the first time to establish the time course of macrophage fusion. As a result, we showed that the peak of fusion events takes place 24 hours after the addition of IL-4 into the media, and dramatically drops at the later stages. Starting from day 4 of incubation with IL-4, we noticed morphological changes in MGCs and macrophages. Prior to day four, MGCs and macrophages appeared to have long spike-like "arms", while on day 4 and afterwards, their morphology shifted to a more rounded shape. Starting from day four, we also noticed the formation of zipper-like actin structures between MGCs and on rare occasions at MGC-macrophage contact sites. During *in vivo* studies, these structures started to appear on day seven after implantation, wherein the morphology of MGCs and macrophages was similar to what we observed *in vitro*. In vitro, zipper-like actin structures were highly dynamic, assembling from podosomes and disassembling into podosomes, as shown by immunofluorescent staining of podosome markers and live-cell imaging at high spatiotemporal resolution by confocal microscopy. Although similar structures were identified in osteoclasts before, zipper-like actin structures discovered on biomaterials differ in structure, pattern of formation, and location. Most importantly, and despite the fact that formation of these zippering structures was mediated by the adherens junctional proteins, E-cadherin and Nectin-2, the adherens-like

junctions formed between MGCs were found to be different from conventional adherens junctions in structure and dynamics (Nagafuchi et al., 2001).

Even though we have elucidated the structure and composition of these novel zipper-like actin structures, there is still much to know regarding the functional role during FBR. For example, we speculate that the zipper-like actin structures transiently forming at MGC-MGC contact sites may contribute to the overall stability of MGCs, creating yet another mechanism by which the cells stay attached to the surface of the bioimplant. This might account for the observation that the MGCs/FBGCs formed during IL-4 and IL-13 induced fusion of M2 macrophages, live on bioimplants' surfaces for a prolonged amount of time, thereby avoiding apoptosis and provoking long term degradation of implant surfaces (Sun et al., 2014). It would be of further interest to know if these novel actin-based structures only assemble on biomaterials during FBR or if they are of more widespread occurrence and can also be found in other pathological conditions such as granulomatous infection during tuberculosis, in which the formation of MGCs is integral to the progression of the disease.

The discovery of the cellular mechanism of macrophage fusion through actin-based protrusion, along with the unidentified role of podosomes and discovery of novel zipper-like actin structures formed at the later stages of FBR may contribute to the development of additional approaches by which to regulate FBR. A case in point is that we revealed a critical role of fibrin(ogen) in FBR progression and fibrous capsule formation. Although previous studies have demonstrated the importance of vitronectin and fibronectin in MGC

formation on biomaterials *in vivo*. (Anderson et al., 2008), the possible role of fibrin(ogen) in these processes was entirely unknown. Using  $Fg^{-/-}$  and  $Fib^{AEK}$  mice, we demonstrated that the formation of FBGC, the hallmark of FBR, depended on the presence of the fibrin network that forms a provisional matrix upon biomaterial implantation. For the first time, it was shown that absence of a single host protein could dramatically inhibit FBR progression. Although, the drop in FBGC formation due to failure of fibrin polymer formation was not enough to entirely stop fibrous capsule formation, the resulting capsule was thinner, less stiff and had a markedly reduced amount of collagen compared to wild type controls.

Even though the fibrin deficiency did not stop bioimplant encapsulation, it would potentially benefit bioimplant longevity at least in two ways. Firstly, the drop in the number and size of FBGCs would positively affect the bioimplant surface integrity. For vascular grafts widely used in cardiovascular issues, the damage arising from FBGCs is tremendous. Thus, inhibition of macrophage fusion during FBR is critical for some classes of biomedical implants. Secondly, decreased density of collagen due to the absence of fibrin polymers within granulation tissue would prolong the life of specific biomedical sensors implanted within the body. For instance, subcutaneously implanted glucose sensors have started to be widely used for patients with diabetes. The average life of glucose sensor implants is around two weeks. The number of studies trying to increase the life of glucose sensors is exponentially increasing. Increasing the functionality of glucose sensors up to three months would be considered a considerable advancement in the biomaterial industry.



Thus, decreasing the density of collagen within the capsule and making it more permeable for small molecules would potentially prolong such sensors' functionality. We have also demonstrated the effect of thrombin inhibiting drugs on the progression of FBR. Administering the thrombin inhibitor argatroban directly into the mouse peritoneum resulted in a two-fold decrease in multinucleation level. Further study of the effect of thrombin inhibitors on fibrous capsule formation is yet another promising direction for future biomaterial research.

## REFERENCES

- Abercrombie, M.T.E.M., Heaysman, J.E. and Pegrum, S.M., (1971). The locomotion of fibroblasts in culture: IV. Electron microscopy of the leading lamella. *Experimental cell research*, 67(2), 359-367.
- Abmayr, S.M., Balagopalan, L., Galletta, B.J. and Hong, S.J., (2003). Cell and molecular biology of myoblast fusion. *International review of cytology*, 225, 33-89.
- Abmayr, S.M., and Pavlath, G.K. (2012). Myoblast fusion: lessons from flies and mice. *Development* 139, 641-656.
- Aguilar, P.S., Baylies, M.K., Fleissner, A., Helming, L., Inoue, N., Podbilewicz, B., Wang, H., and Wong, M. (2013). Genetic basis of cell-cell fusion mechanisms. *Trends in Genetics* 29, 427-437.
- Anderson, J.M., Rodriguez, A., and Chang, D.T. (2008). Foreign body reaction to biomaterials. *Semin.Immunol.* 20, 86-100.
- Akisaka, T., Yoshida, H., Suzuki, R., and Takama, K. (2008). Adhesion structures and their cytoskeleton-membrane interactions at podosomes of osteoclasts in culture. *Cell Tissue Res* 331, 625-641.
- Altieri, D.C., Bader, R., Mannucci, P.M., and Edgington, T.S. (1988). Oligospecificity of the cellular adhesion receptor MAC-1 encompasses an inducible recognition specificity for fibrinogen. *Journal of Cell Biology* 107, 1893-1900.
- Anderson, J.M. and Marchant, R.E., (2000). Biomaterials: factors favoring colonization and infection. *Infections associated with indwelling medical devices*, 89-109.
- Anderson, J., and Cramer, S. (2015). Perspectives on the Inflammatory, Healing, and Foreign Body Responses to Biomaterials and Medical Devices. In: *Host Response to Biomaterials*, ed. E. Inc., 13-36.
- Anderson, J.M. (2001). Biological Responses to Materials. *Annual Review of Materials Research* 31, 81-110.
- Anderson, J.M. (2016). Future challenges in the in vitro and in vivo evaluation of biomaterial biocompatibility. *Regen.Biomater.* 3, 73-77.
- Anderson, J.M., Defife, K., McNally, A., Collier, T., and Jenney, C. (1999). Monocyte, macrophage and foreign body giant cell interactions with molecularly engineered surfaces. *Journal of materials science. Materials in medicine* 10, 579-588.

Bardwell, L., (2005). A walk-through of the yeast mating pheromone response pathway. *Peptides*, 26(2), 339-350.

Bell, P.B., Jr. (1978). Contact inhibition of movements in transformed and nontransformed cells. *Birth Defects Orig Artic Ser* 14, 177-194.

Bhuwania, R., Cornfine, S., Fang, Z., Kruger, M., Luna, E.J., and Linder, S. (2012). Supervillin couples myosin-dependent contractility to podosomes and enables their turnover. *J Cell Sci* 125, 2300-2314.

Burns, S., Hardy, S.J., Buddle, J., Yong, K.L., Jones, G.E., and Thrasher, A.J. (2004). Maturation of DC is associated with changes in motile characteristics and adherence. *Cell Motil Cytoskeleton* 57, 118-132.

Barron, L., and Wynn, T.A. (2011). Fibrosis is regulated by Th2 and Th17 responses and by dynamic interactions between fibroblasts and macrophages. *American journal of physiology. Gastrointestinal and liver physiology* 300, G723-728.

Belitser, V.A., Pozdnjakova, T.M., and Ugarova, T.P. (1980). Light and heavy fractions of fragment D: preparation and examination of fibrin-binding properties. *Thrombosis Research* 19, 807-814.

Blond, J.L., Besème, F., Duret, L., Bouton, O., Bedin, F., Perron, H., Mandrand, B. and Mallet, F., (1999). Molecular characterization and placental expression of HERV-W, a new human endogenous retrovirus family. *Journal of virology*, 73(2), 1175-1185.

Brodbeck, W.G. and Anderson, J.M., (2009). Giant cell formation and function. *Current opinion in hematology*, 16(1), 53.

Brodbeck, W.G., Nakayama, Y., Matsuda, T., Colton, E., Ziats, N.P., and Anderson, J.M. (2002a). Biomaterial surface chemistry dictates adherent monocyte/macrophage cytokine expression in vitro. *Cytokine* 18, 311-319.

Brodbeck, W.G., Patel, J., Voskerician, G., Christenson, E., Shive, M.S., Nakayama, Y., Matsuda, T., Ziats, N.P., and Anderson, J.M. (2002b). Biomaterial adherent macrophage apoptosis is increased by hydrophilic and anionic substrates in vivo. *Proc Natl Acad Sci U S A* 99, 10287-10292.

Brugnera, E., Haney, L., Grimsley, C., Lu, M., Walk, S.F., Tosello-Tramont, A.C., Macara, I.G., Madhani, H., Fink, G.R. and Ravichandran, K.S., (2002). Unconventional Rac-GEF activity is mediated through the Dock180–ELMO complex. *Nature cell biology*, 4(8), 574-582.

Bucala, R., Spiegel, L.A., Chesney, J., Hogan, M., and Cerami, A. (1994). Circulating fibrocytes define a new leukocyte subpopulation that mediates tissue repair. *Molecular Medicine* 1, 71-81.

Busuttill, S.J., Ploplis, V.A., Castellino, F.J., Tang, L., Eaton, J.W., and Plow, E.F. (2004). A central role for plasminogen in the inflammatory response to biomaterials. *Journal of thrombosis and haemostasis: JTH* 2, 1798-1805.

Campellone, K.G., and Welch, M.D. (2010). A nucleator arms race: cellular control of actin assembly. *Nat.Rev.Mol.Cell Biol.* 11, 237-251.

Chaffer, C.L. and Weinberg, R.A., (2011). A perspective on cancer cell metastasis. *Science*, 331(6024), 1559-1564.

Chen, E.H. and Olson, E.N., (2005). Unveiling the mechanisms of cell-cell fusion. *Science*, 308(5720), 369-373.

Chen, W.T., (1989). Proteolytic activity of specialized surface protrusions formed at rosette contact sites of transformed cells. *Journal of Experimental Zoology*, 251(2), 167-185.

Chen, E.H. (2011). Invasive podosomes and myoblast fusion. *Curr.Top.Membr.* 68, 235-258.

Chen, E.H., Grote, E., Mohler, W., and Vignery, A. (2007). Cell-cell fusion. *FEBS Lett.* 581, 2181-2193.

Chinn, J.A. and Slack, S.M., (2013). Biomaterials: Protein—Surface Interactions. *The Biomedical Engineering Handbook*.

Cronan, M.R., Beerman, R.W., Rosenberg, A.F., Saelens, J.W., Johnson, M.G., Oehlers, S.H., Sisk, D.M., Jurcic Smith, K.L., Medvitz, N.A., Miller, S.E., Trinh, L.A., Fraser, S.E., Madden, J.F., Turner, J., Stout, J.E., Lee, S., and Tobin, D.M. (2016). Macrophage epithelial reprogramming underlies mycobacterial granuloma formation and promotes infection. *Immunity* 45, 861-876.

Cross, J.C., Hemberger, M., Lu, Y., Nozaki, T., Whiteley, K., Masutani, M. and Adamson, S.L., (2002). Trophoblast functions, angiogenesis and remodeling of the maternal vasculature in the placenta. *Molecular and cellular endocrinology*, 187(1-2), 207-212.

Cross, J.C., Nakano, H., Natale, D.R., Simmons, D.G. and Watson, E.D., 2006. Branching morphogenesis during development of placental villi. *Differentiation*, 74(7), 393-401.

Cantini, M., Donnelly, H., Dalby, M.J., and Salmeron-Sanchez, M. (2020). The Plot Thickens: The Emerging Role of Matrix Viscosity in Cell Mechanotransduction. *Advanced healthcare materials* 9, e1901259.

Chalupowicz, D.G., Chowdhury, Z.A., Bach, T.L., Barsigian, C., and Martinez, J. (1995). Fibrin II induces endothelial cell capillary tube formation. *J.Cell Biol* 130, 207-215.

Das, A., Sinha, M., Datta, S., Abas, M., Chaffee, S., Sen, C.K. and Roy, S., (2015). Monocyte and macrophage plasticity in tissue repair and regeneration. *The American journal of pathology*, 185(10), 2596-2606.

DeFife, K.M., Jenney, C.R., Colton, E., and Anderson, J.M. (1999). Disruption of filamentous actin inhibits human macrophage fusion. *FASEB Journal* 13, 823-832.

Destaing, O., Ferguson, S.M., Grichine, A., Oddou, C., De Camilli, P., Albiges-Rizo, C., and Baron, R. (2013). Essential function of dynamin in the invasive properties and actin architecture of v-Src induced podosomes/invadosomes. *PLoS One* 8, e77956.

Dovas, A., Gevrey, J.C., Grossi, A., Park, H., Abou-Kheir, W., and Cox, D. (2009). Regulation of podosome dynamics by WASp phosphorylation: implication in matrix degradation and chemotaxis in macrophages. *Journal of Cell Science* 122, 3873-3882.

Diamond, M.S., Staunton, D.E., de Fougerolles, A.R., Stacker, S.A., Garcia-Aguilar, J., Hibbs, M.L., and Springer, T.A. (1990). ICAM-1 (CD54)-a counter-receptor for Mac-1 (CD11b/CD18). *J Cell Biol* 111, 3129-3139.

Duong, L.T., and Rodan, G.A. (2010). Pyk2 is an adhesion kinase in macrophages, localized in podosomes and activated by  $\beta$ 2-integrin ligation. *Cell Motil Cytoskeleton* 47, 174-188.

Doloff, J.C., Veisheh, O., Vegas, A.J., Tam, H.H., Farah, S., Ma, M., Li, J., Bader, A., Chiu, A., Sadraei, A., Aresta-Dasilva, S., Griffin, M., Jhunjhunwala, S., Webber, M., Siebert, S., Tang, K., Chen, M., Langan, E., Dholokia, N., Thakrar, R., Qi, M., Oberholzer, J., Greiner, D.L., Langer, R., and Anderson, D.G. (2017). Colony stimulating factor-1 receptor is a central component of the foreign body response to biomaterial implants in rodents and non-human primates. *Nat.Mater.* 16, 671-680.

Duffield, J.S., Lupher, M., Thannickal, V.J., and Wynn, T.A. (2013). Host responses in tissue repair and fibrosis. *Annual review of pathology* 8, 241-276.

Dupressoir, A., Marceau, G., Vernochet, C., Bénit, L., Kanellopoulos, C., Sapin, V. and Heidmann, T., (2005). Syncytin-A and syncytin-B, two fusogenic placenta-specific murine envelope genes of retroviral origin conserved in Muridae. *Proceedings of the National Academy of Sciences*, 102(3), 725-730.

Eckert, D.M. and Kim, P.S., (2001). Mechanisms of viral membrane fusion and its inhibition. *Annual review of biochemistry*, 70(1), 777-810.

Eugenin, E.A., Branes, M.C., Berman, J.W., and Saez, J.C. (2003). TNF-alpha plus IFN-gamma induce connexin43 expression and formation of gap junctions between human monocytes/macrophages that enhance physiological responses. *J Immunol* 170, 1320-1328.

Evans, J.G., Correia, I., Krasavina, O., Watson, N., and Matsudaira, P. (2003). Macrophage podosomes assemble at the leading lamella by growth and fragmentation. *J Cell Biol* 161, 697-705.

Etscheid, M., Subramaniam, S., Lochnit, G., Zabczyk, M., Undas, A., Lang, I.M., Hanschmann, K.M., and Kanse, S.M. (2018). Altered structure and function of fibrinogen after cleavage by Factor VII Activating Protease (FSAP). *Biochimica et biophysica acta. Molecular basis of disease* 1864, 3397-3406.

Faust, J.J., Christenson, W., Doudrick, K., Heddleston, J., Chew, T.L., Lampe, M., Balabiyev, A., Ros, R., and Ugarova, T.P. (2018). Fabricating Optical-quality Glass Surfaces to Study Macrophage Fusion. *J.Vis.Exp.* 133, 56866

Faust, J.J., Christenson, W., Doudrick, K., Ros, R., and Ugarova, T.P. (2017). Development of fusogenic glass surfaces that impart spatiotemporal control over macrophage fusion: Direct visualization of multinucleated giant cell formation. *Biomaterials* 128, 160-171.

Farquhar, M.G., and Palade, G.E. (1963). Junctional complexes in various epithelia. *J Cell Biol* 17, 375-412.

Faust, J.J., Balabiyev, A., Heddleston, J.M., Podolnikova, N.P., Baluch, D.P., Chew, T.L., and Ugarova, T.P. (2019). An actin-based protrusion originating from a podosome-enriched region initiates macrophage fusion. *Mol Biol Cell* 30, 2254-2267.

Fisher, H.W., and Yeh, J. (1967). Contact inhibition in colony formation. *Science* 155, 581-582.

Franke, W.W. (2009). Discovering the molecular components of intercellular junctions--a historical view. *Cold Spring Harb.Perspect Biol* 1, a003061.

Flick, M.J., Du, X., Witte, D.P., Jirouskova, M., Soloviev, D.A., Plow, E.F., and Degen, J.L. (2004). Leukocyte engagement of fibrin(ogen) via the integrin receptor alphaMbeta2/Mac-1 is critical for host inflammatory response in vivo. *JCI* 113, 1596-1606.

Freyria, A.M., Chignier, E., Guidollet, J., and Louisot, P. (1991). Peritoneal macrophage response: an in vivo model for the study of synthetic materials. *Biomaterials* 12, 111-118.

Griendling, K.K. and FitzGerald, G.A., (2003). Oxidative stress and cardiovascular injury: Part II: animal and human studies. *Circulation*, 108(17), 2034-2040.

Gordon, S., (2003). Alternative activation of macrophages. *Nature reviews immunology*, 3(1), 23-35.

Gordon, S. and Taylor, P.R., (2005). Monocyte and macrophage heterogeneity. *Nature reviews immunology*, 5(12), 953-964.

Gruenbaum-Cohen, Y., Harel, I., Umansky, K.B., Tzahor, E., Snapper, S.B., Shilo, B.Z., and Schejter, E.D. (2012). The actin regulator N-WASp is required for muscle-cell fusion in mice. *Proc.Natl.Acad.Sci.U.S.A* 109, 11211-11216.

Gupton, S.L. and Gertler, F.B., (2007). Filopodia: the fingers that do the walking. *Science's STKE*, 2007(400), re5-re5.

Hamilton Jr, R.F., Thakur, S.A. and Holian, A., (2008). Silica binding and toxicity in alveolar macrophages. *Free Radical Biology and Medicine*, 44(7), 1246-1258.

Hanna, S.J., McCoy-Simandle, K., Miskolci, V., Guo, P., Cammer, M., Hodgson, L., and Cox, D. (2017). The Role of Rho-GTPases and actin polymerization during Macrophage Tunneling Nanotube Biogenesis. *Sci.Rep.* 7, 8547.

Hanahan, D. and Coussens, L.M., (2012). Accessories to the crime: functions of cells recruited to the tumor microenvironment. *Cancer cell*, 21(3), 309-322.

Haralalka, S. and Abmayr, S.M., (2010). Myoblast fusion in *Drosophila*. *Experimental cell research*, 316(18), 3007-3013.

Haralalka, S., Shelton, C., Cartwright, H.N., Katzfey, E., Janzen, E., and Abmayr, S.M. (2011). Asymmetric Mbc, active Rac1 and F-actin foci in the fusion-competent myoblasts during myoblast fusion in *Drosophila*. *Development* 138, 1551-1562.

Hartwell, L.H., (1980). Mutants of *Saccharomyces cerevisiae* unresponsive to cell division control by polypeptide mating hormone. *The Journal of Cell Biology*, 85(3), 811-822. Podbilewicz, B., Leikina, E.,

Helming, L., and Gordon, S. (2007). Macrophage fusion induced by IL-4 alternative activation is a multistage process involving multiple target molecules. *European Journal of Immunology* 37, 33-42.

Helming, L., and Gordon, S. (2008). The molecular basis of macrophage fusion. *Immunobiology* 212, 785-793.

Helming, L., and Gordon, S. (2009). Molecular mediators of macrophage fusion. *Trends in Cell Biology* 19, 514-522.

Harris, T.J., and Tepass, U. (2010). Adherens junctions: from molecules to morphogenesis. *Nat Rev Mol Cell Biol.* 11, 502-514.

Hernandez, L.D., Hoffman, L.R., Wolfsberg, T.G. and White, J.M., (1996). Virus-cell and cell-cell fusion. *Annual review of cell and developmental biology*, 12(1), 627-661.

Hernandez-Pando, R., Bornstein, Q.L., Aguilar Leon, D., Orozco, E.H., Madrigal, V.K., and Martinez Cordero, E. (2000). Inflammatory cytokine production by immunological and foreign body multinucleated giant cells. *Immunology* 100, 352-358.

Higgins, D.M., Basaraba, R.J., Hohnbaum, A.C., Lee, E.J., Grainger, D.W., and Gonzalez-Juarrero, M. (2009). Localized immunosuppressive environment in the foreign body response to implanted biomaterials. *The American journal of pathology* 175, 161-170.

Horbett, T.A. (2012). Adsorbed proteins on biomaterials. In: *Biomaterials Science: An Introduction to Materials in Medicine* (third ed), ed. B.D. Ratner: Elsevier Science & Technology, 34-408.

Horsley, V. and Pavlath, G.K., (2004). Forming a multinucleated cell: molecules that regulate myoblast fusion. *Cells Tissues Organs*, 176(1-3), 67-78.

Hu, W.J., Eaton, J.W., Ugarova, T.P., and Tang, L. (2001). Molecular basis of biomaterial-mediated foreign body reactions. *Blood* 98, 1231-1238.

Hui, K.Y., Haber, E., and Matsueda, G.R. (1983). Monoclonal antibodies to a synthetic fibrin-like peptide bind to human fibrin but not fibrinogen. *Science* 222, 1129-1132.

Hunter, A., Archer, C.W., Walker, P.S. and Blunn, G.W., (1995). Attachment and proliferation of osteoblasts and fibroblasts on biomaterials for orthopaedic use. *Biomaterials*, 16(4), 287-295.

Indra, I., Choi, J., Chen, C.S., Troyanovsky, R.B., Shapiro, L., Honig, B., and Troyanovsky, S.M. (2018). Spatial and temporal organization of cadherin in punctate adherens junctions. *Proc Natl Acad Sci U S A* 115, E4406-e4415.



Inoue, N., Ikawa, M., Isotani, A. and Okabe, M., 2005. The immunoglobulin superfamily protein Izumo is required for sperm to fuse with eggs. *Nature*, 434(7030), 234-238.

Jay, S.M., Skokos, E., Laiwalla, F., Krady, M.M., and Kyriakides, T.R. (2007). Foreign body giant cell formation is preceded by lamellipodia formation and can be attenuated by inhibition of Rac1 activation. *American Journal of Pathology* 171, 632-640.

Jones, J.A., McNally, A.K., Chang, D.T., Qin, L.A., Meyerson, H., Colton, E., Kwon, I.L., Matsuda, T., and Anderson, J.M. (2008). Matrix metalloproteinases and their inhibitors in the foreign body reaction on biomaterials. *J Biomed Mater Res A* 84, 158-166.

Jenney, C.R., and Anderson, J.M. (2000). Adsorbed serum proteins responsible for surface dependent human macrophage behavior. *Journal of biomedical materials research* 49, 435-447.

Jiang, S., and Cao, Z. (2010). Ultralow-fouling, functionalizable, and hydrolyzable zwitterionic materials and their derivatives for biological applications. *Advanced materials (Deerfield Beach, Fla.)* 22, 920-932.

Jones, J.A., Chang, D.T., Meyerson, H., Colton, E., Kwon, I.K., Matsuda, T., and Anderson, J.M. (2007). Proteomic analysis and quantification of cytokines and chemokines from biomaterial surface-adherent macrophages and foreign body giant cells. *Journal of biomedical materials research. Part A* 83, 585-596.

Jones, K. (2015). *Fibrotic Response to Biomaterials and all Associated Sequence of Fibrosis*. In: *Host Response to Biomaterials*: Elsevier Inc.

Jun, J.I. and Lau, L.F., (2010). The matricellular protein CCN1 induces fibroblast senescence and restricts fibrosis in cutaneous wound healing. *Nature cell biology*, 12(7), 676-685.

Kaji, K., Oda, S., Miyazaki, S. and Kudo, A., (2002). Infertility of CD9-deficient mouse eggs is reversed by mouse CD9, human CD9, or mouse CD81; polyadenylated mRNA injection developed for molecular analysis of sperm-egg fusion. *Developmental biology*, 247(2), 327-334.

Kanagaraja, S., Lundström, I., Nygren, H. and Tengvall, P., (1996). Platelet binding and protein adsorption to titanium and gold after short time exposure to heparinized plasma and whole blood. *Biomaterials*, 17(23), 2225-2232.

Kao, W.J., McNally, A.K., Hiltner, A., and Anderson, J.M. (1995). Role for interleukin-4 in foreign-body giant cell formation on a poly(etherurethane urea) in vivo. *J Biomed Mater Res* 29, 1267-1275.

Kalluri, R. and Neilson, E.G., (2003). Epithelial-mesenchymal transition and its implications for fibrosis. *The Journal of clinical investigation*, 112(12), 1776-1784.

Kaverina, I., Stradal, T.E., and Gimona, M. (2003). Podosome formation in cultured A7r5 vascular smooth muscle cells requires Arp2/3-dependent de-novo actin polymerization at discrete microdomains. *Journal of Cell Science* 116, 4915-4924.

Kimura, S., Hase, K., and Ohno, H. (2012). Tunneling nanotubes: emerging view of their molecular components and formation mechanisms. *Experimental Cell Research* 318, 1699-1706.

Kopp, P., Lammers, R., Aepfelbacher, M., Woehlke, G., Rudel, T., Machuy, N., Steffen, W., and Linder, S. (2006). The kinesin KIF1C and microtubule plus ends regulate podosome dynamics in macrophages. *Mol Biol Cell* 17, 2811-2823.

Koh, R.U., Oh, T.J., Rudek, I., Neiva, G.F., Misch, C.E., Rothman, E.D. and Wang, H.L., (2011). Hard and soft tissue changes after crestal and subcrestal immediate implant placement. *Journal of Periodontology*, 82(8), 1112-1120.

Keeley, E.C., Mehrad, B., and Strieter, R.M. (2010). Fibrocytes: bringing new insights into mechanisms of inflammation and fibrosis. *The international journal of biochemistry & cell biology* 42, 535-542.

Kenneth Ward, W. (2008). A review of the foreign-body response to subcutaneously-implanted devices: the role of macrophages and cytokines in biofouling and fibrosis. *Journal of diabetes science and technology* 2, 768-777.

Keselowsky, B.G., Bridges, A.W., Burns, K.L., Tate, C.C., Babensee, J.E., LaPlaca, M.C., and García, A.J. (2007). Role of plasma fibronectin in the foreign body response to biomaterials. *Biomaterials* 28, 3626-3631.

Klopfleisch, R. and Jung, F., (2017). The pathology of the foreign body reaction against biomaterials. *Journal of Biomedical Materials Research Part A*, 105(3), 927-940.

Kyriakides, T.R., Foster, M.J., Keeney, G.E., Tsai, A., Giachelli, C.M., Clark-Lewis, I., Rollins, B.J., and Bornstein, P. (2004). The CC chemokine ligand, CCL2/MCP1, participates in macrophage fusion and foreign body giant cell formation. *American Journal of Pathology* 165, 2157-2166.

Labernadie, A., Bouissou, A., Delobelle, P., Balor, S., Voituriez, R., Proag, A., Fourquaux, I., Thibault, C., Vieu, C., Poincloux, R., Charriere, G.M., and Maridonneau-Parini, I. (2014). Protrusion force microscopy reveals oscillatory force generation and mechanosensing activity of human macrophage podosomes. *Nat. Commun.* 5, 5343.

Labernadie, A., Thibault, C., Vieu, C., Maridonneau-Parini, I., and Charriere, G.M. (2010). Dynamics of podosome stiffness revealed by atomic force microscopy. *Proc.Natl.Acad.Sci.U.S.A* 107, 21016-21021.

Lee, D.M. and Chen, E.H., (2019). *Drosophila* myoblast fusion: invasion and resistance for the ultimate union. *Annual review of genetics*, 53, 67-91.

Lee, K., Gallop, J.L., Rambani, K., and Kirschner, M.W. (2010). Self-assembly of filopodia-like structures on supported lipid bilayers. *Science* 329, 1341-1345.

Leikina, Evgenia, et al. "Myomaker and myomerger work independently to control distinct steps of membrane remodeling during myoblast fusion." *Developmental cell* 46.6 (2018): 767-780.

Linder, S., Nelson, D., Weiss, M., and Aepfelbacher, M. (1999). Wiskott-Aldrich syndrome protein regulates podosomes in primary human macrophages. *Proc.Natl.Acad.Sci.U.S.A* 96, 9648-9653.

Linder, S., and Wiesner, C. (2016). Feel the force: Podosomes in mechanosensing. *Experimental Cell Research* 343, 67-72.

Linder, S. (2007). The matrix corroded: podosomes and invadopodia in extracellular matrix degradation. *Trends Cell Biol* 17, 107-117.

Linder, S., Higgs, H., Hufner, K., Schwarz, K., Pannicke, U., and Aepfelbacher, M. (2000). The polarization defect of Wiskott-Aldrich syndrome macrophages is linked to dislocalization of the Arp2/3 complex. *J Immunol* 165, 221-225.

Linder, S., Wiesner, C., and Himmel, M. (2011). Degrading devices: invadosomes in proteolytic cell invasion. *Ann Rev Cell Dev Biol* 27, 185-211.

Liu, Y., Nusrat, A., Schnell, F.J., Reaves, T.A., Walsh, S., Pochet, M., and Parkos, C.A. (2000). Human junction adhesion molecule regulates tight junction resealing in epithelia. *J Cell Sci* 113 (Pt 13), 2363-2374.

Luxenburg, C., Geblinger, D., Klein, E., Anderson, K., Hanein, D., Geiger, B., and Addadi, L. (2007). The architecture of the adhesive apparatus of cultured osteoclasts: from podosome formation to sealing zone assembly. *PloS One* 2, e179.

Langer, R. (2009). Perspectives and challenges in tissue engineering and regenerative medicine. *Adv.Mater.* 21, 3235-3236.

Latour, R.A. (2008). Biomaterials: Protein-Surface Interactions. In: *Encyclopedia of biomaterials and biomedical engineering*, eds. G. Wnek and G.L. Bowling, 270-284.

Lishko, V.K., Kudryk, B., Yakubenko, V.P., Yee, V.C., and Ugarova, T.P. (2002). Regulated unmasking of the cryptic binding site for integrin  $\alpha$ M $\alpha$ 2 in the  $\beta$  C-domain of fibrinogen *Biochemistry* 41, 12942-12951.

Loike, J.D., Cao, L., Budhu, S., Marcantonio, E.E., El Khoury, J., Hoffman, S., Yednock, T.A., and Silverstein, S.C. (1999). Differential regulation of  $\alpha$ 1 integrins by chemoattractants regulates neutrophil migration through fibrin. *Journal of Cell Biology* 144, 1047-1056.

Lu, H., Smith, C.W., Perrard, J., Bullard, D., Tang, L., Entman, M.L., Beaudet, A.L., and Ballantyne, C.M. (1997). LFA-1 is sufficient in mediating neutrophil emigration in Mac-1 deficient mice. *JCI* 99, 1340-1350.

Lu, J., Steeg, P.S., Price, J.E., Krishnamurthy, S., Mani, S.A., Reuben, J., Cristofanilli, M., Dontu, G., Bidaut, L., Valero, V. and Hortobagyi, G.N., (2009). Breast cancer metastasis: challenges and opportunities.

Machesky, L.M. and Li, A., (2010). Fascin: Invasive filopodia promoting metastasis. *Communicative & integrative biology*, 3(3), 263-270.

Mackay, V. and Manney, T.R., (1974). Mutations affecting sexual conjugation and related processes in *Saccharomyces cerevisiae*. I. Isolation and phenotypic characterization of nonmating mutants. *Genetics*, 76(2), 255-271.

Martinez, F.O. and Gordon, S., (2014). The M1 and M2 paradigm of macrophage activation: time for reassessment. *F1000prime reports*, 6.

Mattila, P.K., and Lappalainen, P. (2008). Filopodia: molecular architecture and cellular functions. *Nat.Rev.Mol.Cell Biol.* 9, 446-454.

McInnes, A., and Rennick, D.M. (1988). Interleukin 4 induces cultured monocytes/macrophages to form giant multinucleated cells. *Journal of Experimental Medicine* 167, 598-611.

McNally, A.K., and Anderson, J.M. (2002). Beta1 and beta2 integrins mediate adhesion during macrophage fusion and multinucleated foreign body giant cell formation. *American Journal of Pathology* 160, 621-630.

McNally, A.K., and Anderson, J.M. (2011). Macrophage fusion and multinucleated giant cells of inflammation. *Advances in Experimental Medicine and Biology* 713, 97-111.

Milde, R., Ritter, J., Tennent, G.A., Loesch, A., Martinez, F.O., Gordon, S., Pepys, M.B., Verschoor, A., and Helming, L. (2015). Multinucleated Giant Cells Are Specialized for Complement-Mediated Phagocytosis and Large Target Destruction. *Cell Rep.* 13, 1937-1948.

Mosser, D.M. and Edwards, J.P., (2008). Exploring the full spectrum of macrophage activation. *Nature reviews immunology*, 8(12), 958-969.

Murphy, D.A., and Courtneidge, S.A. (2011). The 'ins' and 'outs' of podosomes and invadopodia: characteristics, formation and function. *Nat.Rev.Mol.Cell Biol.* 12, 413-426.

McNally, A.K., and Anderson, J.M. (1995). Interleukin-4 induces foreign body giant cells from human monocytes/macrophages. Differential lymphokine regulation of macrophage fusion leads to morphological variants of multinucleated giant cells. *Am J Pathol* 147, 1487-1499.

Mersich, A.T., Miller, M.R., Chkourko, H., and Blystone, S.D. (2010). The formin FRL1 (FMNL1) is an essential component of macrophage podosomes. *Cytoskeleton (Hoboken, N.J.)* 67, 573-585.

Miyaguchi, K. (2000). Ultrastructure of the zonula adherens revealed by rapid-freeze deep-etching. *J Struct Biol* 132, 169-178.

Moreno, J.L., Mikhailenko, I., Tondravi, M.M., and Keegan, A.D. (2007). IL-4 promotes the formation of multinucleated giant cells from macrophage precursors by a STAT6-dependent, homotypic mechanism: contribution of E-cadherin. *J Leukoc Biol* 82, 1542-1553.

Mosser, D.M. and Edwards, J.P., (2008). Exploring the full spectrum of macrophage activation. *Nature reviews immunology*, 8(12), 958-969.

Murphy, D.A., and Courtneidge, S.A. (2011). The 'ins' and 'outs' of podosomes and invadopodia: characteristics, formation and function. *Nat Rev Mol Cell Biol* 12, 413-426.

MacLauchlan, S., Skokos, E.A., Meznarich, N., Zhu, D.H., Raouf, S., Shipley, J.M., Senior, R.M., Bornstein, P., and Kyriakides, T.R. (2009). Macrophage fusion, giant cell

formation, and the foreign body response require matrix metalloproteinase 9. *Journal of Leukocyte Biology* 85, 617-626.

McNally, A.K. and Anderson, J.M., (1995). Interleukin-4 induces foreign body giant cells from human monocytes/macrophages. Differential lymphokine regulation of macrophage fusion leads to morphological variants of multinucleated giant cells. *The American journal of pathology*, 147(5), p.1487.

McNally, A.K., Jones, J.A., Macewan, S.R., Colton, E., and Anderson, J.M. (2008). Vitronectin is a critical protein adhesion substrate for IL-4-induced foreign body giant cell formation. *J.Biomed.Mater.Res.A* 86, 535-543.

McNew, James A., et al. "Compartmental specificity of cellular membrane fusion encoded in SNARE proteins." *Nature* 407.6801 (2000): 153-159.

Matheson, L.A., Santerre, J.P., and Labow, R.S. (2004). Changes in macrophage function and morphology due to biomedical polyurethane surfaces undergoing biodegradation. *J.Cell Physiol* 199, 8-19.

Mooney, J.E., Rolfe, B.E., Osborne, G.W., Sester, D.P., van Rooijen, N., Campbell, G.R., Hume, D.A., and Campbell, J.H. (2010). Cellular plasticity of inflammatory myeloid cells in the peritoneal foreign body response. *The American journal of pathology* 176, 369-380.

Mooney, J.E., Summers, K.M., Gongora, M., Grimmond, S.M., Campbell, J.H., Hume, D.A., and Rolfe, B.E. (2014). Transcriptional switching in macrophages associated with the peritoneal foreign body response. *Immunology and cell biology* 92, 518-526.

Nolen, B.J., Tomasevic, N., Russell, A., Pierce, D.W., Jia, Z., McCormick, C.D., Hartman, J., Sakowicz, R., and Pollard, T.D. (2009). Characterization of two classes of small molecule inhibitors of Arp2/3 complex. *Nature* 460, 1031-1034.

Nieuwenhuizen, W., Schielen, W.J.G., Yonekawa, O., Tesser, G.I., and Voskuilen, M. (1990). Studies on the localization and accessibility of sites in fibrin which are involved in the acceleration of the activation of plasminogen by tissue-type plasminogen activator. *Advances in Experimental Medicine and Biology* 281, 83-91.

Oh, J., Riek, A.E., Weng, S., Petty, M., Kim, D., Colonna, M., Cella, M. and Bernal-Mizrachi, C., (2012). Endoplasmic reticulum stress controls M2 macrophage differentiation and foam cell formation. *Journal of Biological Chemistry*, 287(15), 11629-11641.

Ochoa, G.C., Slepnev, V.I., Neff, L., Ringstad, N., Takei, K., Daniell, L., Kim, W., Cao, H., McNiven, M., Baron, R., and De Camilli, P. (2000). A functional link between dynamin and the actin cytoskeleton at podosomes. *The Journal of Cell Biology* 150, 377-389.

Oikawa, T., Oyama, M., Kozuka-Hata, H., Uehara, S., Udagawa, N., Saya, H., and Matsuo, K. (2012). Tks5-dependent formation of circumferential podosomes/invadopodia mediates cell-cell fusion. *Journal of Cell Biology* 197, 553-568.

Onel, S.F., and Renkawitz-Pohl, R. (2009). FuRMAS: triggering myoblast fusion in *Drosophila*. *Dev.Dyn.* 238, 1513-1525.

Onfelt, B., Nedvetzki, S., Benninger, R.K., Purbhoo, M.A., Sowinski, S., Hume, A.N., Seabra, M.C., Neil, M.A., French, P.M., and Davis, D.M. (2006). Structurally distinct membrane nanotubes between human macrophages support long-distance vesicular traffic or surfing of bacteria. *Journal of Immunology* 177, 8476-8483.

Owaynat, H., Yermolenko, I.S., Turaga, R., Lishko, V.K., Sheller, M.R., and Ugarova, T.P. (2015). Deposition of fibrinogen on the surface of in vitro thrombi prevents platelet adhesion. *Thrombosis Research* 136, 1231-1239.

Pawelek, J.M. and Chakraborty, A.K., (2008). Fusion of tumour cells with bone marrow-derived cells: a unifying explanation for metastasis. *Nature Reviews Cancer*, 8(5), 377-386.

Proag, A., Bouissou, A., Mangeat, T., Voituriez, R., Delobelle, P., Thibault, C., Vieu, C., Maridonneau-Parini, I., and Poincloux, R. (2015). Working together: spatial synchrony in the force and actin dynamics of podosome first neighbors. *ACS Nano*. 9, 3800-3813.

Panzer, L., Trube, L., Klose, M., Joosten, B., Slotman, J., Cambi, A., and Linder, S. (2016). The formins FHOD1 and INF2 regulate inter- and intra-structural contractility of podosomes. *J Cell Sci* 129, 298-313.

Pende, D., Castriconi, R., Romagnani, P., Spaggiari, G.M., Marcenaro, S., Dondero, A., Lazzeri, E., Lasagni, L., Martini, S., Rivera, P., Capobianco, A., Moretta, L., Moretta, A., and Bottino, C. (2006). Expression of the DNAM-1 ligands, Nectin-2 (CD112) and poliovirus receptor (CD155), on dendritic cells: relevance for natural killer-dendritic cell interaction. *Blood* 107, 2030-2036.

Pfaff, M., and Jurdic, P. (2001). Podosomes in osteoclast-like cells: structural analysis and cooperative roles of paxillin, proline-rich tyrosine kinase 2 (Pyk2) and integrin  $\alpha$ V $\beta$ 3. *J Cell Sci* 114, 2775-2786.

Podbilewicz, B. (2014). Virus and cell fusion mechanisms. *Ann Rev Cell Dev Biol* 30, 111-139.

Podolnikova, N.P., Kushchayeva, Y.S., Wu, Y., Faust, J., and Ugarova, T.P. (2016). The role of integrins alphaMbeta2 (Mac-1, CD11b/CD18) and alphaDbeta2 (CD11d/CD18) in macrophage fusion. *Am J Pathol* 186, 2105-2116.

Podolnikova, N.P., Hlavackova, M., Wu, Y., Yakubenko, V.P., Faust, J.J., Balabiyev, A., Ugarova, T.P. (2019) The interaction between the macrophage receptors integrin Mac-1 ( $\alpha_M\beta_2$ , CD11b/CD18) and SIRP $\alpha$  (MFR) mediates fusion in heterologous cells. *J Biol Chem* 294, 7833-7849.

Poincloux, R., Vincent, C., Labrousse, A., Castandet, J., Rigo, M., Cougoule, C., Bordier, C., Le Cabec, V., and Maridonneau-Parini, I. (2006). Re-arrangements of podosome structures are observed when Hck is activated in myeloid cells. *Eur J Cell Biol* 85, 327-332.

Parsons, J.T., Horwitz, A.R., and Schwartz, M.A. (2010). Cell adhesion: integrating cytoskeletal dynamics and cellular tension. *Nature reviews. Molecular cell biology* 11, 633-643.

Podolnikova, N.P., Yermolenko, I.S., Fuhrmann, A., Lishko, V.K., Magonov, S., Bowen, B., Enderlein, J., Podolnikov, A., Ros, R., and Ugarova, T.P. (2010). Control of integrin  $\alpha IIb\beta_3$  outside-in signaling and platelet adhesion by sensing the physical properties of fibrin(ogen) substrates *Biochemistry* 49, 68-77.

Porcheray, F., Viaud, S., Rimaniol, A.C., Leone, C., Samah, B., Dereuddre-Bosquet, N., Dormont, D. and Gras, G., (2005). Macrophage activation switching: an asset for the resolution of inflammation. *Clinical & Experimental Immunology*, 142(3), 481-489.

Prasad, J.M., Gorkun, O.V., Raghu, H., Thornton, S., Mullins, E.S., Palumbo, J.S., Ko, Y.P., Hook, M., David, T., Coughlin, S.R., Degen, J.L., and Flick, M.J. (2015). Mice expressing a mutant form of fibrinogen that cannot support fibrin formation exhibit compromised antimicrobial host defense. *Blood* 126, 2047-2058.

Quan, T.E., Cowper, S., Wu, S.P., Bockenstedt, L.K., and Bucala, R. (2004). Circulating fibrocytes: collagen-secreting cells of the peripheral blood. *The international journal of biochemistry & cell biology* 36, 598-606.

Radzvilavicius, A.L., (2016). Evolutionary dynamics of cytoplasmic segregation and fusion: mitochondrial mixing facilitated the evolution of sex at the origin of eukaryotes. *Journal of Theoretical Biology*, 404, pp.160-168.



Rahmati, Maryam, et al. "Biological responses to physicochemical properties of biomaterial surface." *Chemical Society Reviews* 49.15 (2020): 5178-5224.

Ramachandran, S. and Prasad, N.R., (2012). Sesamol modulates ultraviolet-B-induced apoptotic and inflammatory signaling in human skin dermal fibroblasts. *International Journal of Nutrition, Pharmacology, Neurological Diseases*, 2(1), 31.

Ridley, A.J. (2011). Life at the leading edge. *Cell* 145, 1012-1022.

Riedl, J., Flynn, K.C., Raducanu, A., Gartner, F., Beck, G., Bosl, M., Bradke, F., Massberg, S., Aszodi, A., Sixt, M., and Wedlich-Soldner, R. (2010). Lifeact mice for studying F-actin dynamics. *Nat.Methods* 7, 168-169.

Rivera-Chacon, D.M., Alvarado-Velez, M., Acevedo-Morantes, C.Y., Singh, S.P., Gultepe, E., Nagesha, D., Sridhar, S. and Ramirez-Vick, J.E., (2013). Fibronectin and vitronectin promote human fetal osteoblast cell attachment and proliferation on nanoporous titanium surfaces. *Journal of biomedical nanotechnology*, 9(6), 1092-1097.

Runge, Kathryn E., et al. "Oocyte CD9 is enriched on the microvillar membrane and required for normal microvillar shape and distribution." *Developmental biology* 304.1 (2007): 317-325.

Rustom, A., Saffrich, R., Markovic, I., Walther, P., and Gerdes, H.H. (2004). Nanotubular highways for intercellular organelle transport. *Science* 303, 1007-1010.

Ratner, B.D. (2002). Reducing capsular thickness and enhancing angiogenesis around implant drug release systems. *J. Control Release* 78, 211-218.

Ratner, B.D. (2011). The biocompatibility manifesto: biocompatibility for the twenty-first century. *J.Cardiovasc.Transl.Res.* 4, 523-527.

Ratner, B.D. (2015). *The Biocompatibility of Implant Materials*. In: *Host Response to Biomaterials*: Elsevier Inc, 37-51.

Reilkoff, R.A., Bucala, R., and Herzog, E.L. (2011). Fibrocytes: emerging effector cells in chronic inflammation. *Nature reviews. Immunology* 11, 427-435.

Saini, H., Rahmani Eliato, K., Veldhuizen, J., Zare, A., Allam, M., Silva, C., Kratz, A., Truong, D., Mouneimne, G., LaBaer, J., Ros, R., and Nikkhah, M. (2020). The role of tumor-stroma interactions on desmoplasia and tumorigenicity within a microengineered 3D platform. *Biomaterials* 247, 119975.

Sapir, A., Valansi, C., Suissa, M., Shemer, G. and Chernomordik, L.V., (2006). The C. elegans developmental fusogen EFF-1 mediates homotypic fusion in heterologous cells and in vivo. *Developmental cell*, 11(4), 471-481.

Santerre, J.P., Woodhouse, K., Laroche, G., and Labow, R.S. (2005). Understanding the biodegradation of polyurethanes: from classical implants to tissue engineering materials. *Biomaterials* 26, 7457-7470.

Scatena, M., Eaton, K.V., Jackson, M.F., Lund, S.A., and Giachelli, C.M. (2017). Macrophages: The Bad, the Ugly, and the Good in the Inflammatory Response to Biomaterials: SPRINGER, 37.

Schoumacher, M., Goldman, R.D., Louvard, D. and Vignjevic, D.M., (2010). Actin, microtubules, and vimentin intermediate filaments cooperate for elongation of invadopodia. *Journal of Cell Biology*, 189(3), 541-556.

Seyfried, T.N. and Huysentruyt, L.C., (2013). On the origin of cancer metastasis. *Critical reviews in oncogenesis*, 18(1-2), 43.

Sens, K.L., Zhang, S., Jin, P., Duan, R., Zhang, G., Luo, F., Parachini, L., and Chen, E.H. (2010). An invasive podosome-like structure promotes fusion pore formation during myoblast fusion. *Journal of Cell Biology* 191, 1013-1027.

Sheng, N., Fairbanks, M.B., Heinrikson, R.L., Canziani, G., Chaiken, I.M., Mosser, D.M., Zhang, H. and Colman, R.W., (2000). Cleaved high molecular weight kininogen binds directly to the integrin CD11b/CD18 (Mac-1) and blocks adhesion to fibrinogen and ICAM-1. *Blood, The Journal of the American Society of Hematology*, 95(12), 3788-3795.

Shilagardi, K., Li, S., Luo, F., Marikar, F., Duan, R., Jin, P., Kim, J.H., Murnen, K., and Chen, E.H. (2013). Actin-propelled invasive membrane protrusions promote fusogenic protein engagement during cell-cell fusion. *Science* 340, 359-363.

Shin, N.Y., Choi, H., Neff, L., Wu, Y., Saito, H., Ferguson, S.M., De Camilli, P., and Baron, R. (2014). Dynamin and endocytosis are required for the fusion of osteoclasts and myoblasts. *The Journal of cell biology* 207, 73-89.

Soe, K., Hobolt-Pedersen, A.S., and Delaisse, J.M. (2015). The elementary fusion modalities of osteoclasts. *Bone* 73, 181-189.

Svitkina, T.M., Bulanova, E.A., Chaga, O.Y., Vignjevic, D.M., Kojima, S., Vasiliev, J.M., and Borisy, G.G. (2003). Mechanism of filopodia initiation by reorganization of a dendritic network. *Journal of Cell Biology* 160, 409-421.

Santoso, S., Sachs, U.J., Kroll, H., Linder, M., Ruf, A., Preissner, K.T., and Chavakis, T. (2002). The junctional adhesion molecule 3 (JAM-3) on human platelets is a counterreceptor for the leukocyte integrin Mac-1. *J Exp Med* 196, 679-691.

Sheikh, S., and Nash, G.B. (1996). Continuous activation and deactivation of integrin CD11b/CD18 during de novo expression enables rolling neutrophils to immobilize on platelets. *Blood* 87, 5040-5050.

Skokos, E.A., Charokopos, A., Khan, K., Wanjala, J., and Kyriakides, T.R. (2011). Lack of TNF-alpha-induced MMP-9 production and abnormal E-cadherin redistribution associated with compromised fusion in MCP-1-null macrophages. *Am J Pathol* 178, 2311-2321.

Svitkina, T.M. (2013). Ultrastructure of protrusive actin filament arrays. *Curr Opin Cell Biol* 25, 574-581.

Shen, M., Garcia, I., Maier, R.V., and Horbett, T.A. (2004). Effects of adsorbed proteins and surface chemistry on foreign body giant cell formation, tumor necrosis factor alpha release and procoagulant activity of monocytes. *Journal of biomedical materials research. Part A* 70, 533-541.

Shen, M., Pan, Y.V., Wagner, M.S., Hauch, K.D., Castner, D.G., Ratner, B.D., and Horbett, T.A. (2001). Inhibition of monocyte adhesion and fibrinogen adsorption on glow discharge plasma deposited tetraethylene glycol dimethyl ether. *Journal of biomaterials science. Polymer edition* 12, 961-978

Shioi, A., Katagi, M., Okuno, Y., Mori, K., Jono, S., Koyama, H. and Nishizawa, Y., (2002). Induction of bone-type alkaline phosphatase in human vascular smooth muscle cells: roles of tumor necrosis factor- $\alpha$  and oncostatin M derived from macrophages. *Circulation research*, 91(1), 9-16.

Silva, L.M., Lum, A.G., Tran, C., Shaw, M.W., Gao, Z., Flick, M.J., Moutsopoulos, N.M., Bugge, T.H., and Mullins, E.S. (2019). Plasmin-mediated fibrinolysis enables macrophage migration in a murine model of inflammation. *Blood* 134, 291-303.

Song, E., Ouyang, N., Hörbelt, M., Antus, B., Wang, M., and Exton, M.S. (2000). Influence of alternatively and classically activated macrophages on fibrogenic activities of human fibroblasts. *Cell Immunol* 204, 19-28.

Staunton, J.R., Doss, B.L., Lindsay, S., and Ros, R. (2016). Correlating confocal microscopy and atomic force indentation reveals metastatic cancer cells stiffen during invasion into collagen I matrices. *Scientific reports* 6, 19686.

Stein, Alexander, et al. "Helical extension of the neuronal SNARE complex into the membrane." *Nature* 460.7254 (2009): 525-528.

Strauss, O., Dunbar, P.R., Bartlett, A. and Phillips, A., (2015). The immunophenotype of antigen presenting cells of the mononuclear phagocyte system in normal human liver—A systematic review. *Journal of hepatology*, 62(2), 458-468.

Suga, H., Rennert, R.C., Rodrigues, M., Sorkin, M., Glotzbach, J.P., Januszyk, M., Fujiwara, T., Longaker, M.T., and Gurtner, G.C. (2014). Tracking the elusive fibrocyte: identification and characterization of collagen-producing hematopoietic lineage cells during murine wound healing. *Stem cells (Dayton, Ohio)* 32, 1347-1360.

Suh, T.T., Holmbäck, K., Jensen, N.J., Daugherty, C.C., Small, K., Simon, D.I., Potter, S., and Degen, J.L. (1995). Resolution of spontaneous bleeding events but failure of pregnancy in fibrinogen-deficient mice. *Genes & development* 9, 2020-2033.

Sun, J., Ling, M., Wang, Y., Chen, D., Zhang, S., Tong, J. and Wang, S., (2014). Quasi-static and dynamic nanoindentation of some selected biomaterials. *Journal of Bionic Engineering*, 11(1), 144-150.

Takai, Y., Ikeda, W., Ogita, H., and Rikitake, Y. (2008). The immunoglobulin-like cell adhesion molecule nectin and its associated protein afadin. *Ann Rev Cell Dev Biol* 24, 309-342.

Takeichi, M. (2014). Dynamic contacts: rearranging adherens junctions to drive epithelial remodeling. *Nat Rev Mol Cell Biol* 15, 397-410.

Takito, J., Nakamura, M., Yoda, M., Tohmonda, T., Uchikawa, S., Horiuchi, K., Toyama, Y., and Chiba, K. (2012). The transient appearance of zipper-like actin superstructures during the fusion of osteoclasts. *J Cell Sci* 125, 662-672.

Takito, J., Otsuka, H., Inoue, S., Kawashima, T., and Nakamura, M. (2017). Symmetrical retrograde actin flow in the actin fusion structure is involved in osteoclast fusion. *Biol Open* 6, 1104-1114.

Takenawa, T., and Suetsugu, S. (2007). The WASP-WAVE protein network: connecting the membrane to the cytoskeleton. *Nat.Rev.Mol.Cell Biol.* 8, 37-48.

Tarique, A.A., Logan, J., Thomas, E., Holt, P.G., Sly, P.D. and Fantino, E., (2015). Phenotypic, functional, and plasticity features of classical and alternatively activated human macrophages. *American journal of respiratory cell and molecular biology*, 53(5), 676-688.

Thrasher, A.J. (2002). WASp in immune-system organization and function. *Nat.Rev.Immunol.* 2, 635-646.

Takagi, T., and Doolittle, R.F. (1975). Amino acid sequence studies on plasmin-derived fragments of human fibrinogen: amino-terminal sequences of intermediate and terminal fragments. *Biochemistry* 14, 940-946.

Takeda, Y., Tachibana, I., Miyado, K., Kobayashi, M., Miyazaki, T., Funakoshi, T., Kimura, H., Yamane, H., Saito, Y., Goto, H., Yoneda, T., Yoshida, M., Kumagai, T., Osaki, T., Hayashi, S., Kawase, I., and Mekada, E. (2003). Tetraspanins CD9 and CD81 function to prevent the fusion of mononuclear phagocytes. *The Journal of cell biology* 161, 945-956.

Tang, L., and Eaton, J.W. (1993). Fibrin(ogen) mediates acute inflammatory responses to biomaterials. *Journal of Experimental Medicine* 178, 2147-2156.

Tang, L., Ugarova, T.P., Plow, E.F., and Eaton, J.W. (1996). Molecular determinants of acute inflammatory responses to biomaterials. *JCI* 97, 1329-1334.

Thevenot, P.T., Baker, D.W., Weng, H., Sun, M.W., and Tang, L. (2011). The pivotal role of fibrocytes and mast cells in mediating fibrotic reactions to biomaterials. *Biomaterials* 32, 8394-8403.

Tintut, Y., Patel, J., Territo, M., Saini, T., Parhami, F. and Demer, L.L., (2002). Monocyte/macrophage regulation of vascular calcification in vitro. *Circulation*, 105(5), 650-655.

Tsai, A.T., Rice, J., Scatena, M., Liaw, L., Ratner, B.D., and Giachelli, C.M. (2005). The role of osteopontin in foreign body giant cell formation. *Biomaterials* 26, 5835-5843.

Ugarova, T.P., Solovjov, D.A., Zhang, L., Loukinov, D.I., Yee, V.C., Medved, L.V. and Plow, E.F., (1998). Identification of a novel recognition sequence for integrin  $\alpha$ M $\beta$ 2 within the  $\gamma$ -chain of fibrinogen. *Journal of Biological Chemistry*, 273(35), 22519-22527.

Van Audenhove, I., Debeuf, N., Boucherie, C., and Gettemans, J. (2015). Fascin actin bundling controls podosome turnover and disassembly while cortactin is involved in podosome assembly by its SH3 domain in THP-1 macrophages and dendritic cells. *Biochim Biophys Acta* 1853, 940-952.

Van den Bossche, J., Bogaert, P., van, H.J., Guerin, C.J., Berx, G., Movahedi, K., Van den Bergh, R., Pereira-Fernandes, A., Geuns, J.M., Pircher, H., Dorny, P., Grooten, J., De, B.P., and Van Ginderachter, J.A. (2009). Alternatively activated macrophages engage in

homotypic and heterotypic interactions through IL-4 and polyamine-induced E-cadherin/catenin complexes. *Blood* 114, 4664-4674.

Van den Dries, K., Meddens, M.B., de Keijzer, S., Shekhar, S., Subramaniam, V., Figdor, C.G., and Cambi, A. (2013a). Interplay between myosin IIA-mediated contractility and actin network integrity orchestrates podosome composition and oscillations. *Nat Commun* 4, 1-13.

Van den Dries, K., Schwartz, S.L., Byars, J., Meddens, M.B., Bolomini-Vittori, M., Lidke, D.S., Figdor, C.G., Lidke, K.A., and Cambi, A. (2013b). Dual color superresolution microscopy reveals nanoscale organization of mechanosensory podosomes. *Mol Biol Cell* 24, 2112-2123.

Vignery, A., (2000). Osteoclasts and giant cells: macrophage-macrophage fusion mechanism. *International journal of experimental pathology*, 81(5), 291-304.

Vignery, A. (2011). Macrophage Fusion: The Making of a New Cell. In: *Cell Fusions: Regulation and Control*: Springer, 219-231.

Vogler, E.A., (1998). Structure and reactivity of water at biomaterial surfaces. *Advances in colloid and interface science*, 74(1-3), 69-117.

Vroman, L., Adams, A.L., Fischer, G.C. and Munoz, P.C., (1980). Interaction of high molecular weight kininogen, factor XII, and fibrinogen in plasma at interfaces.

Wang, Y., Brooks, P.J., Jang, J.J., Silver, A.S., Arora, P.D., McCulloch, C.A., and Glogauer, M. (2015). Role of actin filaments in fusopod formation and osteoclastogenesis. *Biochim.Biophys.Acta* 1853, 1715-1724.

Wang, J.T., Seydoux, G., Tulu, U.S., Kiehart, D.P., and Betzig, E. (2014). Lattice light-sheet microscopy: imaging molecules to embryos at high spatiotemporal resolution. *Science* 346, 1257998.

Ward, W.K., Li, A.G., Siddiqui, Y., Federiuk, I.F., and Wang, X.J. (2008). Increased expression of Interleukin-13 and connective tissue growth factor, and their potential roles during foreign body encapsulation of subcutaneous implants. *Journal of biomaterials science. Polymer edition* 19, 1065-1072.

Ward, W.K., Slobodzian, E.P., Tiekotter, K.L., and Wood, M.D. (2002). The effect of microgeometry, implant thickness and polyurethane chemistry on the foreign body response to subcutaneous implants. *Biomaterials* 23, 4185-4192.

- Ward, C.A., and Neumann, A.W., (1974). On the surface thermodynamics of a two—component liquid-vapor-ideal solid system. *Journal of colloid and interface science*, 49(2), 286-290.
- Wiesner, C., Faix, J., Himmel, M., Bentzien, F., and Linder, S. (2010). KIF5B and KIF3A/KIF3B kinesins drive MT1-MMP surface exposure, CD44 shedding, and extracellular matrix degradation in primary macrophages. *Blood* 116, 1559-1569.
- Wiesner, C., Le-Cabec, V., El, A.K., Maridonneau-Parini, I., and Linder, S. (2014). Podosomes in space: macrophage migration and matrix degradation in 2D and 3D settings. *Cell Adh Migr* 8, 179-191.
- Williams, D.F., (2009). On the nature of biomaterials. *Biomaterials*, 30(30), 5897-5909.
- Wang, N., Butler, J.P., and Ingber, D.E. (1993). Mechanotransduction across the cell surface and through the cytoskeleton. *Science* 260, 1124-1127.
- Wilson, C.J., Clegg, R.E., Leavesley, D.I., and Pearcy, M.J. (2005). Mediation of biomaterial-cell interactions by adsorbed proteins: a review. *Tissue Eng* 11, 1-18.
- Yang, L., Wang, L., Geiger, H., Cancelas, J.A., Mo, J., and Zheng, Y. (2007a). Rho GTPase Cdc42 coordinates hematopoietic stem cell quiescence and niche interaction in the bone marrow. *Proc.Natl.Acad.Sci.U.S.A* 104, 5091-5096.
- Yang, Z., Grinchuk, V., Urban Jr, J.F., Bohl, J., Sun, R., Notari, L., Yan, S., Ramalingam, T., Keegan, A.D., Wynn, T.A. and Shea-Donohue, T., (2013). Macrophages as IL-25/IL-33-responsive cells play an important role in the induction of type 2 immunity. *PloS one*, 8(3), 59441.
- Yang, C., and Svitkina, T. (2011). Filopodia initiation: focus on the Arp2/3 complex and formins. *Cell Adh.Migr.* 5, 402-408.
- Yagi, M., Miyamoto, T., Sawatani, Y., Iwamoto, K., Hosogane, N., Fujita, N., Morita, K., Ninomiya, K., Suzuki, T., Miyamoto, K., Oike, Y., Takeya, M., Toyama, Y., and Suda, T. (2005). DC-STAMP is essential for cell-cell fusion in osteoclasts and foreign body giant cells. *The Journal of experimental medicine* 202, 345-351.
- Yakovlev, S., Makogonenko, E., Kurochkina, N., Nieuwenhuizen, W., Ingham, K., and Medved, L. (2000). Conversion of fibrinogen to fibrin: mechanism of exposure of tPA- and plasminogen-binding sites. *Biochemistry* 39, 15730-15741.

Yokota, T., Sugawara, K., Ito, K., Takahashi, R., Ariga, H. and Mizusawa, H., (2003). Down regulation of DJ-1 enhances cell death by oxidative stress, ER stress, and proteasome inhibition. *Biochemical and biophysical research communications*, 312(4), 1342-1348.

Yona, S., Kim, K.W., Wolf, Y., Mildner, A., Varol, D., Breker, M., Strauss-Ayali, D., Viukov, S., Guilleims, M., Misharin, A. and Hume, D.A., (2013). Fate mapping reveals origins and dynamics of monocytes and tissue macrophages under homeostasis. *Immunity*, 38(1), 79-91.

Yonemura, S., Itoh, M., Nagafuchi, A., and Tsukita, S. (1995). Cell-to-cell adherens junction formation and actin filament organization: similarities and differences between non-polarized fibroblasts and polarized epithelial cells. *J Cell Sci* 108 (Pt 1), 127-142.

Zambonin-Zallone, A., Teti, A., Grano, M., Rubinacci, A., Abbadini, M., Gaboli, M., and Marchisio, P.C. (1989). Immunocytochemical distribution of extracellular matrix receptors in human osteoclasts: a beta 3 integrin is colocalized with vinculin and talin in the podosomes of osteoclastoma giant cells. *Experimental Cell Research* 182, 645-652.

Zeng, Z., Gong, H., Li, Y., Jie, K., Ding, C., Shao, Q., Liu, F., Zhan, Y., Nie, C., Zhu, W. and Qian, K., (2013). Upregulation of miR-146a contributes to the suppression of inflammatory responses in LPS-induced acute lung injury. *Experimental lung research*, 39(7), 275-282.

Zhao, Q., Topham, N., Anderson, J.M., Hiltner, A., Lodoen, G., and Payet, C.R. (1991). Foreign-body giant cells and polyurethane biostability: in vivo correlation of cell adhesion and surface cracking. *J Biomed Mater Res* 25, 177-183.

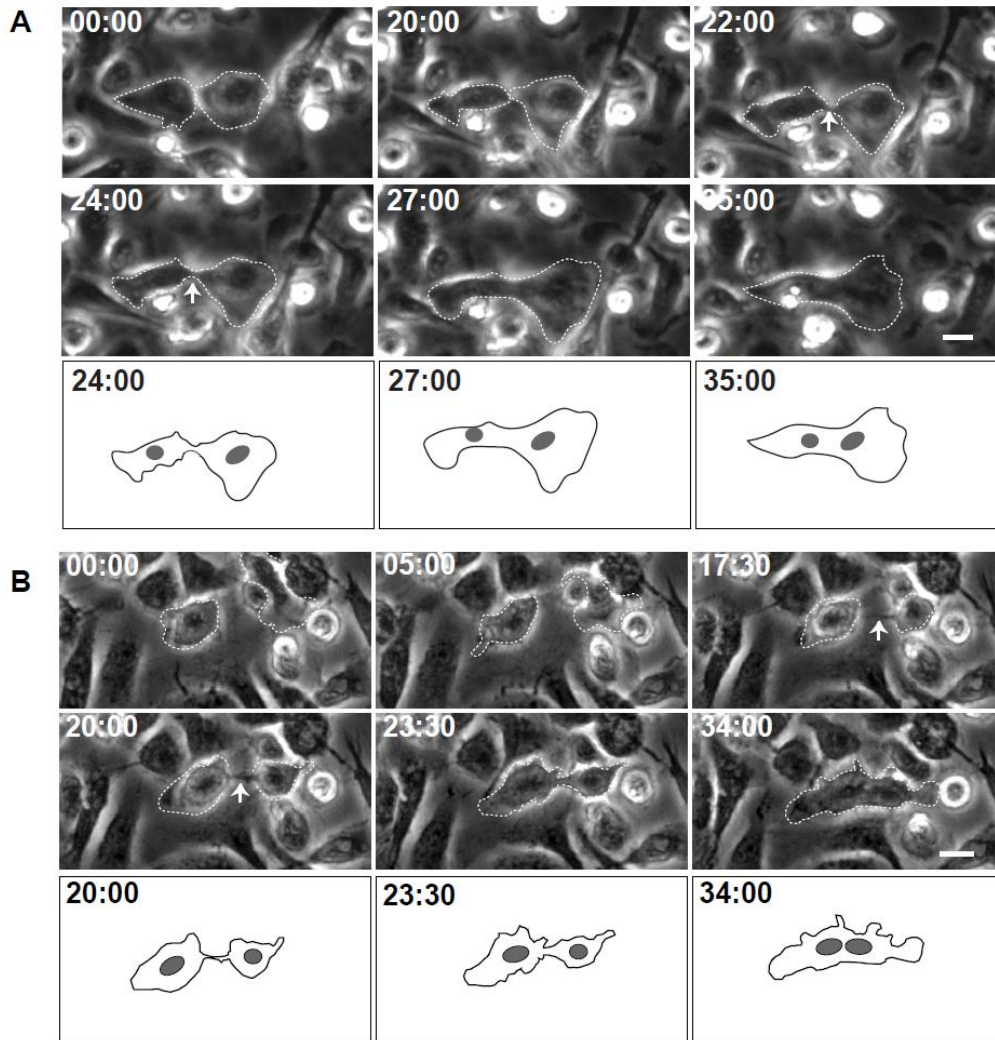
Zamarron, C., Ginsberg, M.H., and Plow, E.F. (1991). A receptor-induced binding site in fibrinogen elicited by its interaction with platelet membrane glycoprotein IIb-IIIa. *Journal of Biological Chemistry* 266, 16193-16199.

Zhang, L., Cao, Z., Bai, T., Carr, L., Ella-Menye, J.R., Irvin, C., Ratner, B.D., and Jiang, S. (2013). Zwitterionic hydrogels implanted in mice resist the foreign-body reaction. *Natural Biotechnology* 31, 553-556.

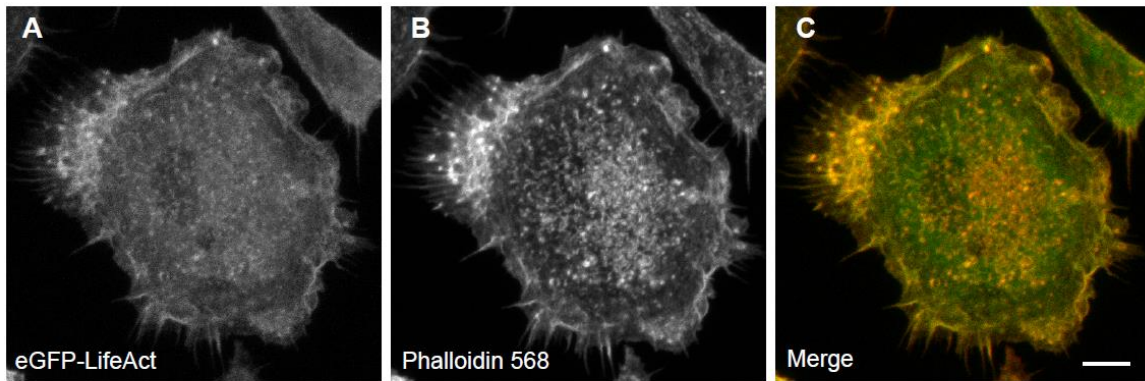


APPENDIX A

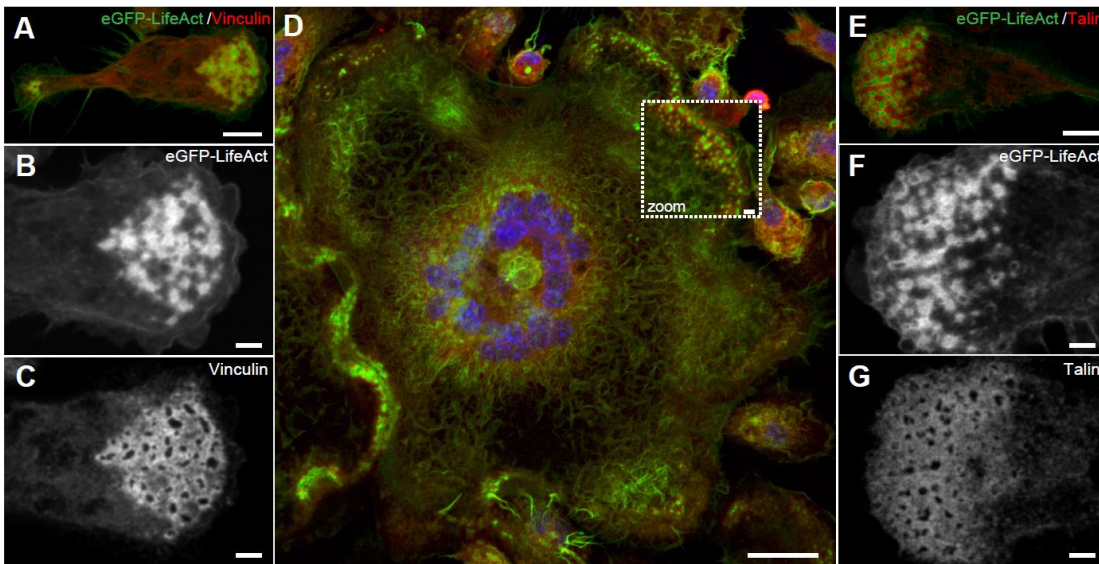
CHAPTER 2 SUPPLEMENTAL MATERIAL



**Supplemental Figure 1. Phase-dense protrusions initiating Type 1 fusion.** Live imaging of mononuclear macrophages undergoing fusion. Macrophages were isolated from the mouse peritoneum 3 days after TG injection, plated on a 35-mm Fluorodish and fusion was induced by IL-4. (A) A mononuclear macrophage extends a short phase-dense protrusion (white arrow) toward another macrophage before fusion. The lower panel is a diagram of frames at 24:00, 27:00 and 35:00 min illustrating morphological aspects of the fusion process. (B) Macrophage fusion mediated by a long protrusion (white arrows at 17:30-20:00 min). The lower panels show diagrams of frames at 20:00, 23:30 and 34:00 min. In each micrograph, time is shown in minutes:seconds. The scale bars are 10  $\mu$ m.

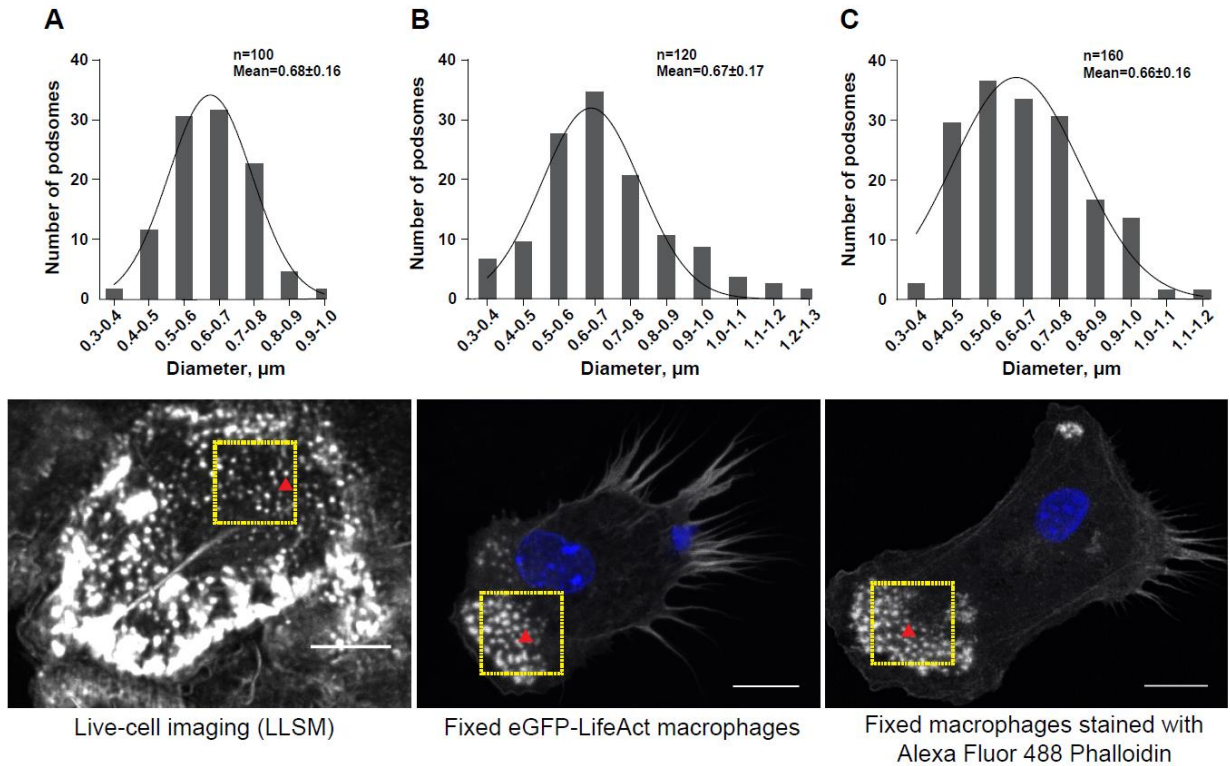


**Supplemental Figure 2: eGFP-LifeAct faithfully reports the distribution of F-actin in TG-elicited macrophages.** (A) The distribution of eGFP-LifeAct in a fixed and permeabilized macrophage 24 h after plating. (B) Alexa 568-conjugated phalloidin labeled structures. (C) The panel is an overlay of eGFP-LifeAct (green) and Alexa 568-Phalloidin (red). The majority of phalloidin-labeled structures appear to contain eGFP-LifeAct in fixed specimens. The scale bar is 10  $\mu\text{m}$ .



**Supplemental Figure 3. eGFP-LifeAct puncta in macrophages are podosomes.** (A) eGFP-LifeAct macrophage 48 h after the application of IL-4. Punctate eGFP-LifeAct structures (green) at the leading edge of a mononuclear macrophage contain vinculin (red). The scale bar is 7.5  $\mu\text{m}$ . (B) High magnification view of eGFP-LifeAct puncta shows the typical interconnected network with a core of eGFP-LifeAct and fine fibrils radiating from a central point. The scale bar is 2.5  $\mu\text{m}$ . (C) High magnification view of vinculin enriched around a core devoid of vinculin signal. The scale bar is 2.5  $\mu\text{m}$ . (D) Low magnification view of a MGC shows similar podosomes at the cell periphery. Nuclei are stained with DAPI (blue). The scale bar is 25  $\mu\text{m}$ . The scale bar for the zoomed box region is 2  $\mu\text{m}$ . (E) Punctate eGFP-LifeAct structures (green) at the leading edge of a mononuclear macrophage contain talin (red). The scale bar is 7.5  $\mu\text{m}$ . (F) High

magnification view of eGFP-LifeAct puncta. The scale bar is 2.5  $\mu\text{m}$ . (G) High magnification of view of talin enriched around a core devoid of talin signal. The scale bar is 2.5  $\mu\text{m}$ .



**Supplemental Figure 4. Distribution of the podosome size in samples of live and fixed macrophages.** Gaussian distribution of the podosome size obtained from live cell imaging using LLSM (A), from images of fixed eGFP-LifeActexpressing macrophages (B) and samples of fixed cells stained with Alexa Fluor 488-conjugated phalloidin (C). Only individual podosomes (red arrowheads) situated at some distance from the front of actin in the LLSM movies and away from the cell periphery in fixed samples were included in analyses. The scale bar is 10  $\mu\text{m}$ . Nuclei were stained with DAPI (blue).

Table 1




*Parameters of fusion-competent protrusions*

Number of analyzed protrusions	Type 1 fusion	Type 2 fusion	Type 3 fusion
Short	31 (94%)	85 (91%)	32 (89%)
Long	2 (6%)	8 (9%)	4 (11%)
Length of protrusions, $\mu\text{m}$	Type 1 fusion	Type 2 fusion	Type 3 fusion
Short	$2.6 \pm 0.7$	$2.8 \pm 1.2$	$2.6 \pm 0.7$
Long	$10.8 \pm 3.3$	$11.9 \pm 7.9$	$11.2 \pm 4.1$
Total fusion time from the first cell-cell contact to full integration, min	Type 1 fusion	Type 2 fusion	Type 3 fusion
Short	$59 \pm 31$	$48 \pm 22$	$68 \pm 48$
Long	$23 \pm 0.7^a$	$22 \pm 11^b$	$37 \pm 24^c$
Cell spreading, $\mu\text{m}^2$	Type 1 fusion	Type 2 fusion	Type 3 fusion
Mononuclear	$262 \pm 114$	$252 \pm 83$	–
Multinuclear	–	$1400 \pm 910$	$1760 \pm 1280$

<sup>a, b, c</sup> p=0.057, p= 0.001 and p=0.056 (long vs. short protrusions, respectively)

Table 2

*Patterns of macrophage fusion*

Pattern mediated by short protrusions*	Schematic showing cell polarity	Type 1 fusion	Type 2 fusion
Leading edge to the cell body		34%	31%
Leading edge to rear edge		23%	18%
Leading edge to leading edge		20%	45%
Other		23%	6%

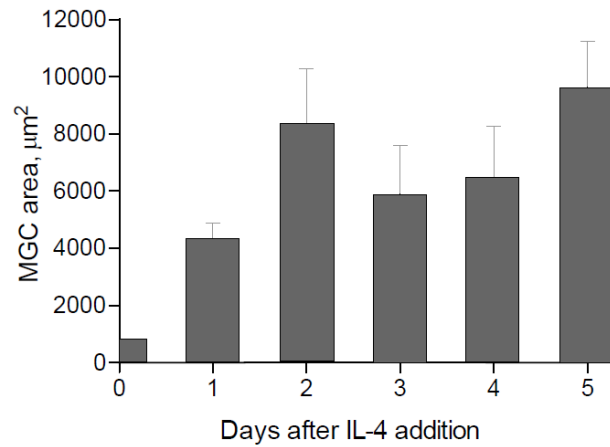
APPENDIX B  
CHAPTER 3 SUPPLEMENTAL MATERIAL

Supplementa Table 1

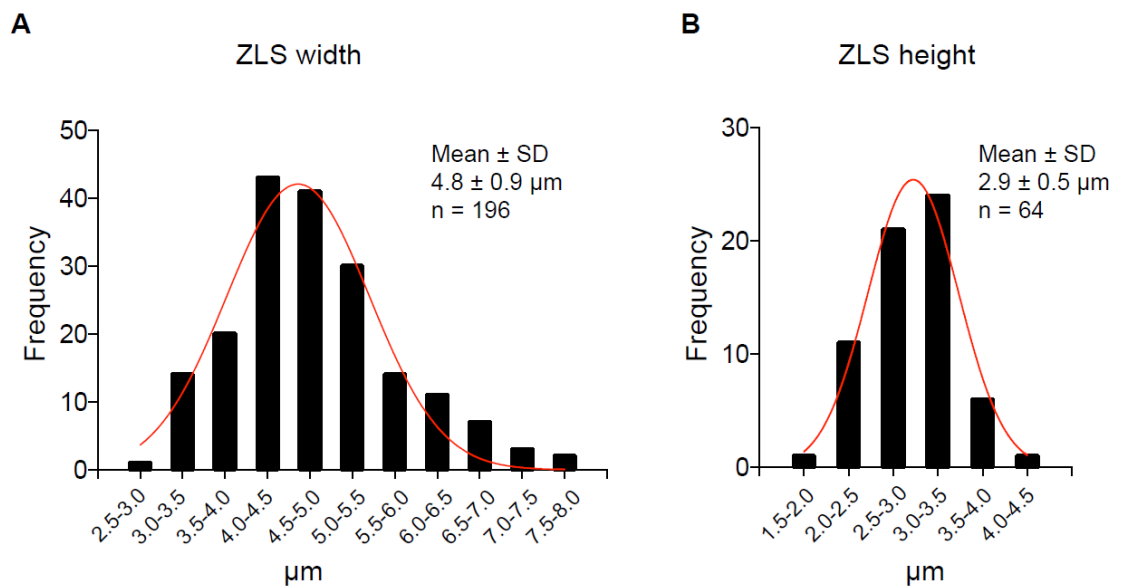
*Viability of macrophages cultured under different conditions<sup>a</sup>*

<b>Culturing conditions</b>	<b>Dead cells, %</b>	<b>Fusion index (%)</b>	<b>ZLS length/ 0.15 mm<sup>2</sup></b>	<b>Number of nuclei / 0.15 mm<sup>2</sup></b>
Media change every 2 days (no additional IL-4 added)	28 ± 11	29 ± 7	43 ± 33	289 ± 35
Media change every 2 days (additional IL-4 added with fresh media)	20 ± 1	27 ± 5	68 ± 76	243 ± 58
Media change (1:1) after 3 days (no additional IL-4 added with fresh media)	11 ± 6	25 ± 11	436 ± 391	322 ± 39
No media change	7 ± 0.5	18 ± 4	177 ± 124	315 ± 56

<sup>a</sup>Macrophages were isolated from the mouse peritoneum 3 days after TG injection, plated on paraffin-coated cover glass (P-surface) at 5000 cells/mm<sup>2</sup> in DMEM/F12 supplemented with 10% FBS and fusion was induced by the addition of IL-4 (10 ng/ml). Fusion indices and the length of ZLSs were determined after 5 days. The number of viable cells was determined by the trypan blue exclusion test performed on cells that remained attached to the surfaces after 5 days.

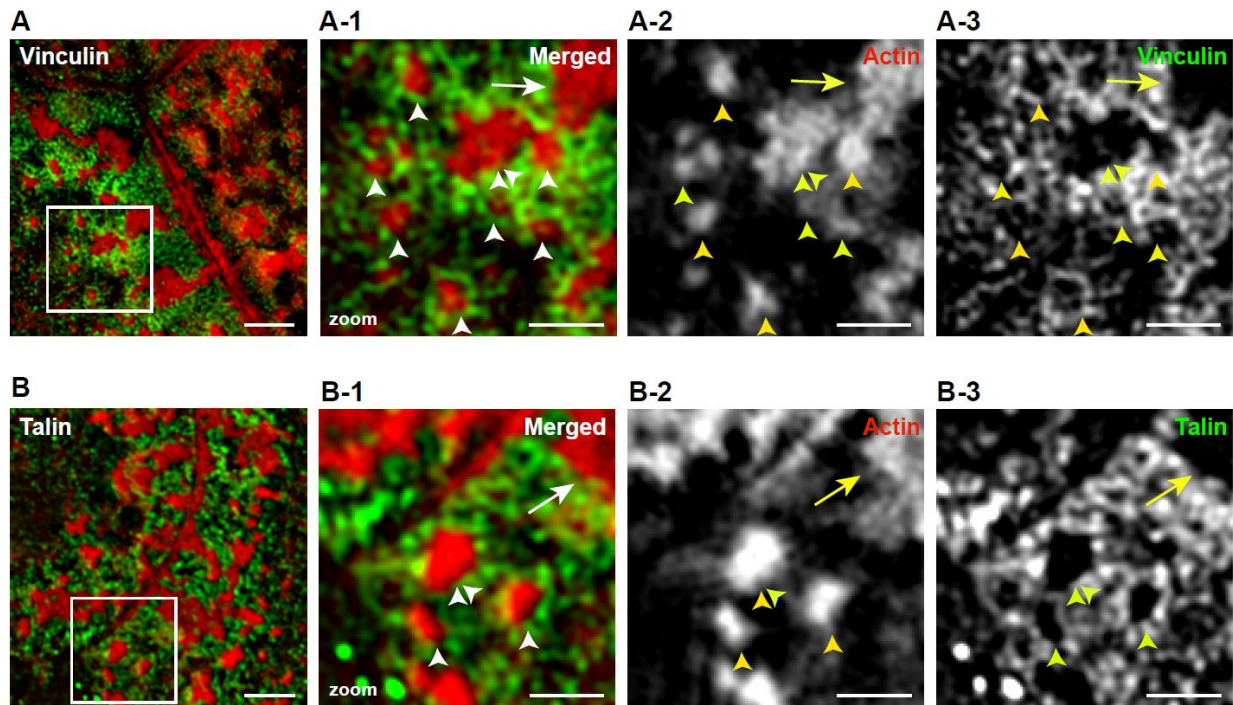


**Supplemental Figure 1. Determination of the MGC surface area.** TG-elicited peritoneal macrophages were plated on P-surface. After the addition of IL-4, the cells were fixed at different time points and incubated with Alexa 488-conjugated phalloidin and DAPI. The samples were imaged by confocal microscopy. Results shown are mean  $\pm$  SD of three independent experiments. Three-to-five random 20 $\times$  fields were used per sample to measure the MGC area using ImageJ software.

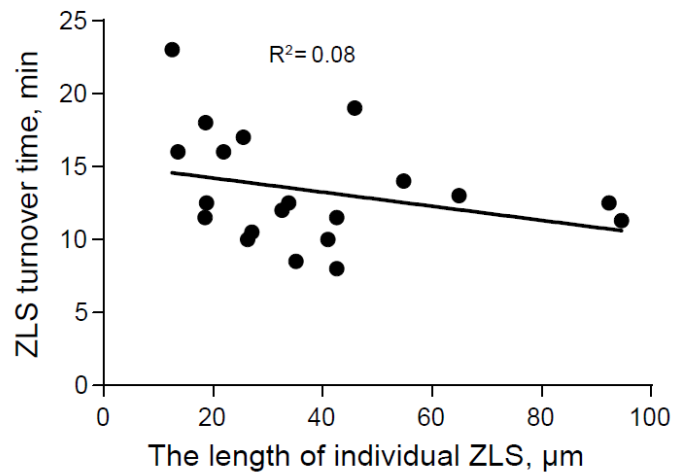


**Supplemental Figure 2. Dimensional parameters of ZLSs.** The histograms showing the normal distribution of ZLS width (A) and height (B) were generated based on confocal images and produced using GraphPad Prism Software.

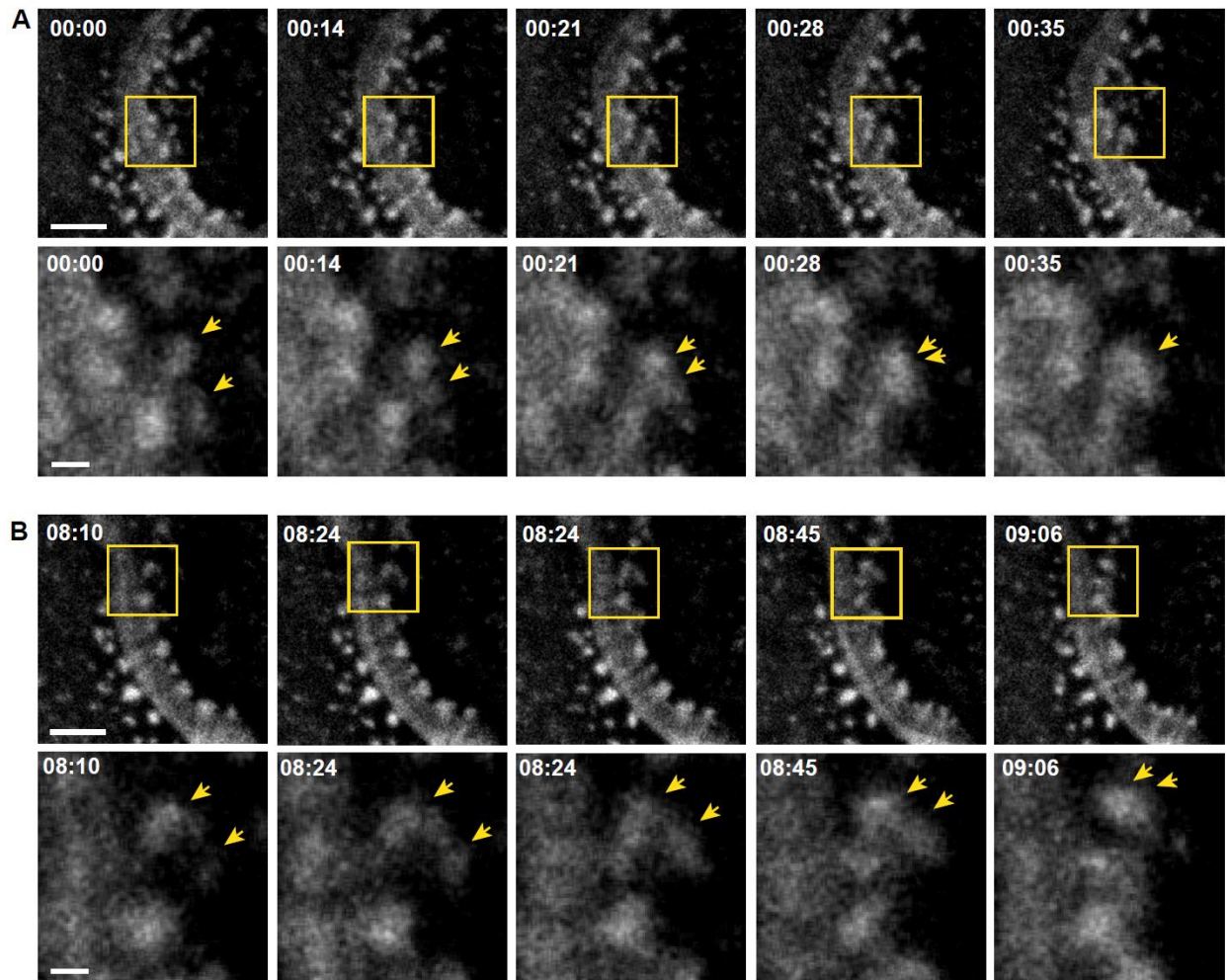




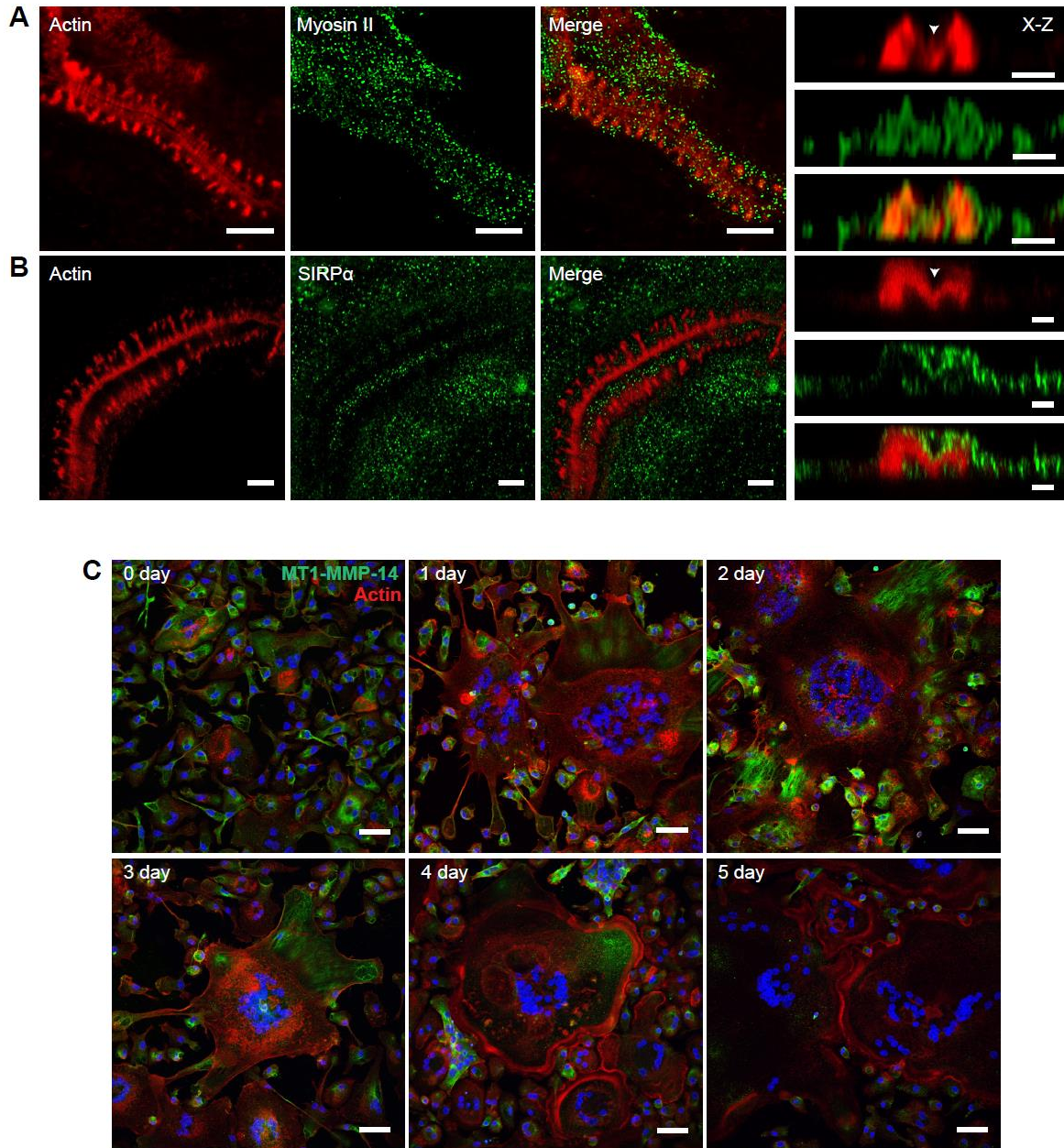
**Supplemental Figure 3. Actin puncta in the vicinity of ZLSs are podosomes.** (A) A representative confocal image of the ZLS formed in the 5-day culture of MGCs induced by IL-4 and incubated with an anti-vinculin antibody. The scale bar is 2  $\mu\text{m}$ . (A-1) A high magnification view of the boxed areas in **A** near the ZLS shows single podosomes (arrowheads) and a podosome cluster (a double arrowhead) containing several podosomes. Actin puncta (red) are surrounded by a ring of vinculin (green). A large actin globule in the ZLS is marked by an arrow. The scale bar is 1  $\mu\text{m}$ . (A-2) and (A-3) High magnification views of actin puncta and vinculin, respectively. Vinculin forms a ring around the actin core devoid of the vinculin signal. The scale bars are 1  $\mu\text{m}$ . (B) Actin puncta in the vicinity of ZLS are encircled by talin. The scale bar is 2  $\mu\text{m}$ . (B-1) A high magnification view of the boxed area in **B** shows single podosomes (arrowheads) and a podosome cluster containing two podosomes (a double arrowhead). Actin puncta (red) are surrounded by a ring of talin (green). A large actin globule in the ZLS is marked by an arrow. The scale bar is 1  $\mu\text{m}$ . (B-2) and (B-3) High magnification views of actin puncta and talin, respectively. Talin forms a ring around the actin core devoid of the talin signal. The scale bars are 1  $\mu\text{m}$ .



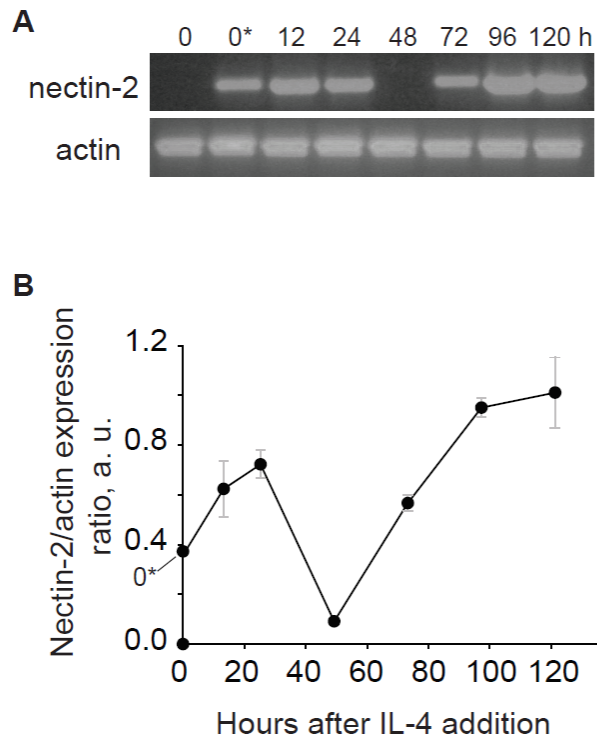
**Supplemental Figure 4. Correlation between the ZLS turnover time and ZLS length.** Live-cell video microscopy images were analyzed to determine the correlation between the ZLS turnover time (the time required for the full assembly and disassembly of a ZLS) and the ZLS length ( $\mu\text{m}$ ). No significant correlation was found.



**Supplemental Figure 5. Large globules in the ZLS grow by the addition of podosomes.** (A, B) Frames from two representative live-cell imaging experiments showing fusion of podosomes with a nascent large globule in the ZLS (*upper panel*). *Bottom panels*: high magnification images of the boxed areas. Arrows indicate fusing actin puncta. The scale bars in the upper panels are 5  $\mu\text{m}$  and 1  $\mu\text{m}$  in the lower panels.



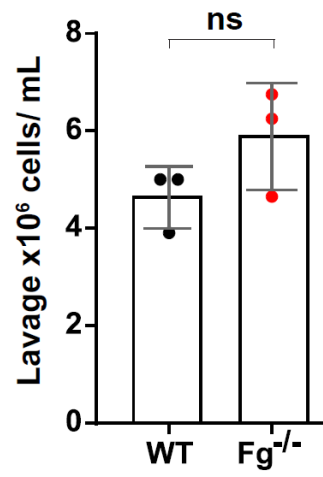
**Supplemental Figure 6. Distribution of Myosin II (A) and SIRP $\alpha$  (B) within the ZLS structures.** Representative confocal images of MGCs in the 5-day culture induced by the addition of IL-4 and incubated with anti-Myosin II (A) or SIRP $\alpha$  (B) mAbs. The x-z projections are shown in the right panels. The scale bars for x-y and x-z projections are 5  $\mu$ m and 2.5  $\mu$ m, respectively. The images were acquired using a 63 $\times$  oil objective. (C) The kinetics of MT1-MMP-14 distribution in mononuclear macrophages and MGCs. TG-induced peritoneal macrophages were cultured in the presence of IL-4 for 1-5 days, fixed and incubated with antibodies against MT1-MMP-14. The images were obtained by confocal microscopy using a 40 $\times$  oil objective. The scale bar is 50  $\mu$ m.



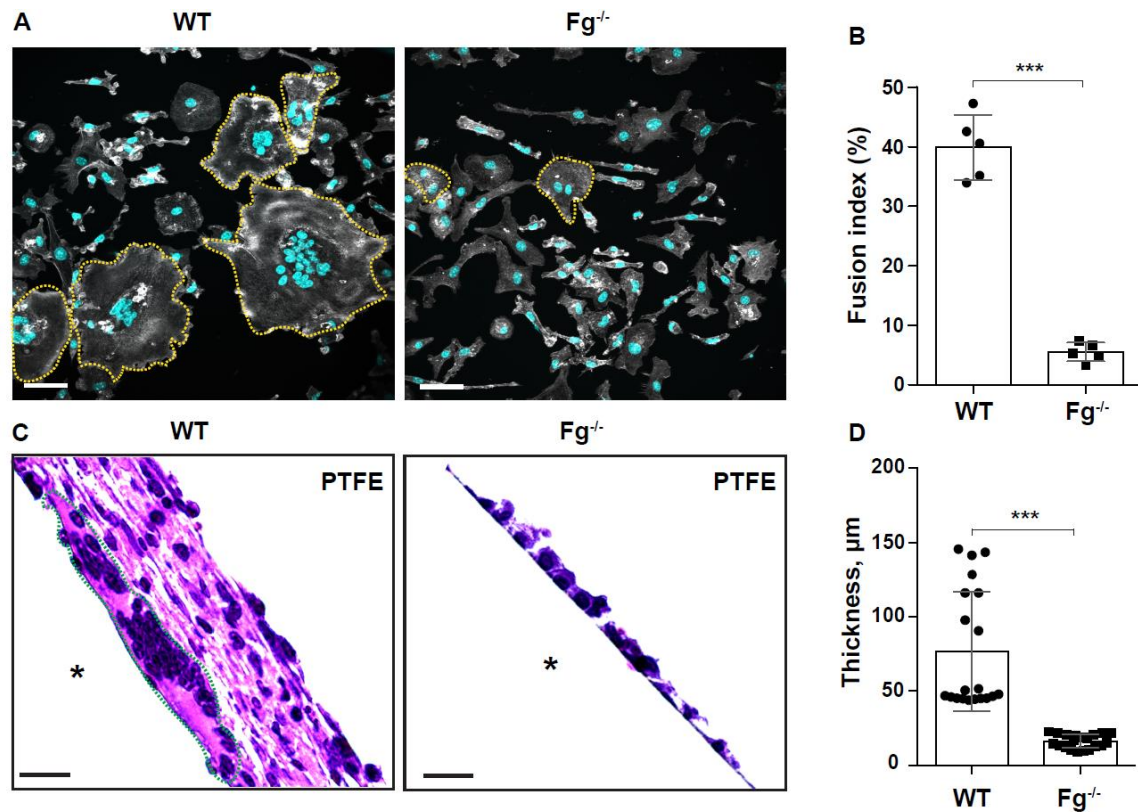
**Supplemental Figure 7. The kinetics of nectin-2 mRNA expression in fusing macrophages.** (A) Time course of E-cadherin mRNA expression in macrophages undergoing fusion in the presence of IL-4, as determined by RT-PCR. Signal intensities were normalized to that of  $\alpha$ -actin. (B) Fold change was determined relative to the control mRNA levels in freshly isolated TG-elicited macrophages before adhesion (0). 0\* denotes unstimulated macrophages adherent for 2 h before the addition of IL-4. Results shown are mean  $\pm$  SD of two independent experiments.

APPENDIX C

CHAPTER 4 SUPPLEMENTAL MATERIAL

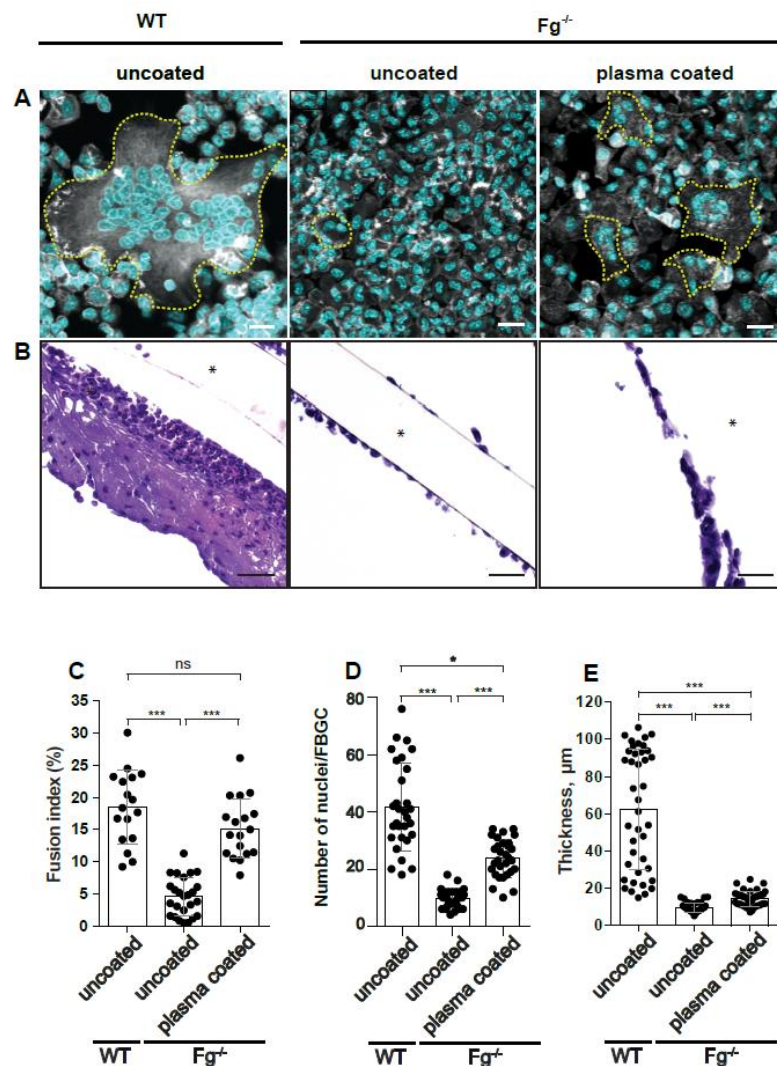


**Supplemental figure 1. The number of cells in the inflamed peritoneum of WT and Fg<sup>-/-</sup> mice.** Thioglycollate solution was injected into the mouse peritoneum and peritoneum lavage was collected after 72 hours. Results shown are mean  $\pm$  SD from three independent experiments (n=3 WT and n=3 Fg<sup>-/-</sup> mice). ns, not significant



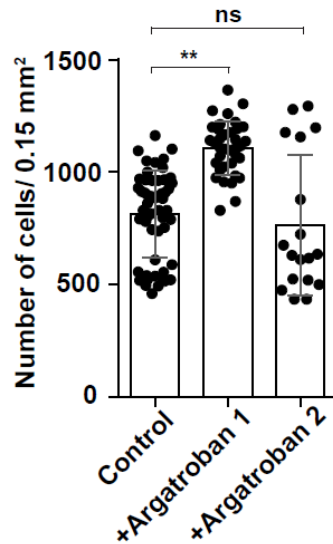
**Supplemental figure 2. The FBR to implanted PTFE biomaterials.** (A) PTFE sections were implanted in the peritoneum of wild type and *Fg*<sup>-/-</sup> mice for 7 days and explants were separated from the surrounding fibrinous capsule. Since PTFE plastic is nontransparent and consequently unamenable to immunocytochemistry, firmly adherent cells were removed from the surface using a cell scraper, centrifuged, and resuspended in DMEM/F-12. Cells were allowed to adhere to polylysine-coated coverslips and incubated with Alexa Fluor 546-conjugated phalloidin (white) and DAPI (teal). Representative confocal images are shown. FBGCs are outlined (yellow). The scale bar is 50 µm. (B) Macrophage fusion was assessed as a fusion index. Five to six random 20× fields were used per sample to count nuclei. (C) Explants were fixed, paraffin-embedded, sectioned, and stained according to a standard H&E method. Representative images of stained cross-sections are shown. The scale bar is 50 µm. (D) The thickness of granulation tissue around the implants retrieved from WT and *Fg*<sup>-/-</sup> mice was determined using ImageJ software. Ten random fields were used per sample to measure the thickness of cross-sections. Results shown are mean ± SD from two independent experiments (n=2 WT and n=2 *Fg*<sup>-/-</sup> mice). Mann-Whitney *U* test was used to calculate significance \*\*\*p < .001



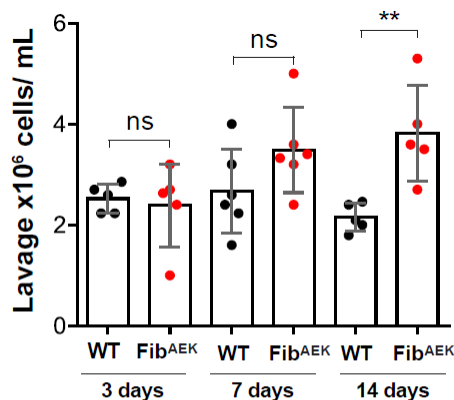


**Supplemental figure 3. Analyses of multinucleation and the granulation tissue formation of implants precoated with plasma.** PCFTE sections pre-coated with mouse plasma were implanted into Fg<sup>-/-</sup> mice for 3 days. Uncoated sections implanted in WT and Fg<sup>-/-</sup> mice served as controls. **(A)** Explants were separated from the surrounding fibrous capsule, fixed, and incubated with Alexa Fluor 546-conjugated phalloidin (white) and DAPI (teal). FBGCs are outlined (yellow). Representative confocal images are shown. **(B)** Representative images of the granulation tissue formed around different implants. **(C)** Fusion indices were determined as described in Materials and Methods. **(D)** The number of nuclei per FBGC was analyzed to

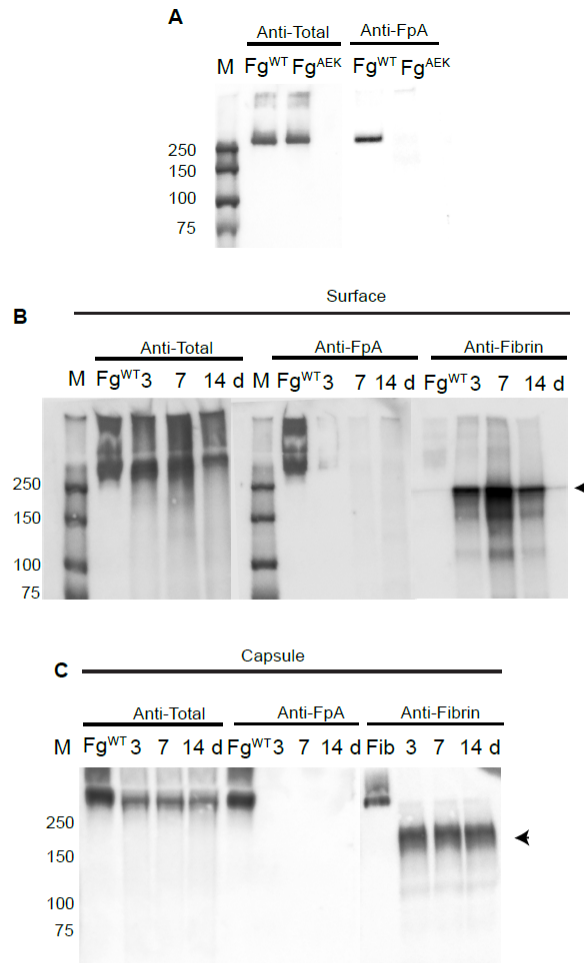
assess the extent of multinucleation. 30 FBGCs were analyzed from 6-8 fields. (E) The thickness of the granulation tissue formed around uncoated and precoated implants shown in B. The scale bar is 50  $\mu\text{m}$ . Results shown are mean  $\pm$  S.D. of four independent experiments (n=4 WT and n=4  $\text{Fg}^{-/-}$  mice). Two-tailed t-test and Mann-Whitney *U* test were used to calculate significance. ns, not significant,  $p < .05$ ,  $**p < .01$ ,  $***p < .001$



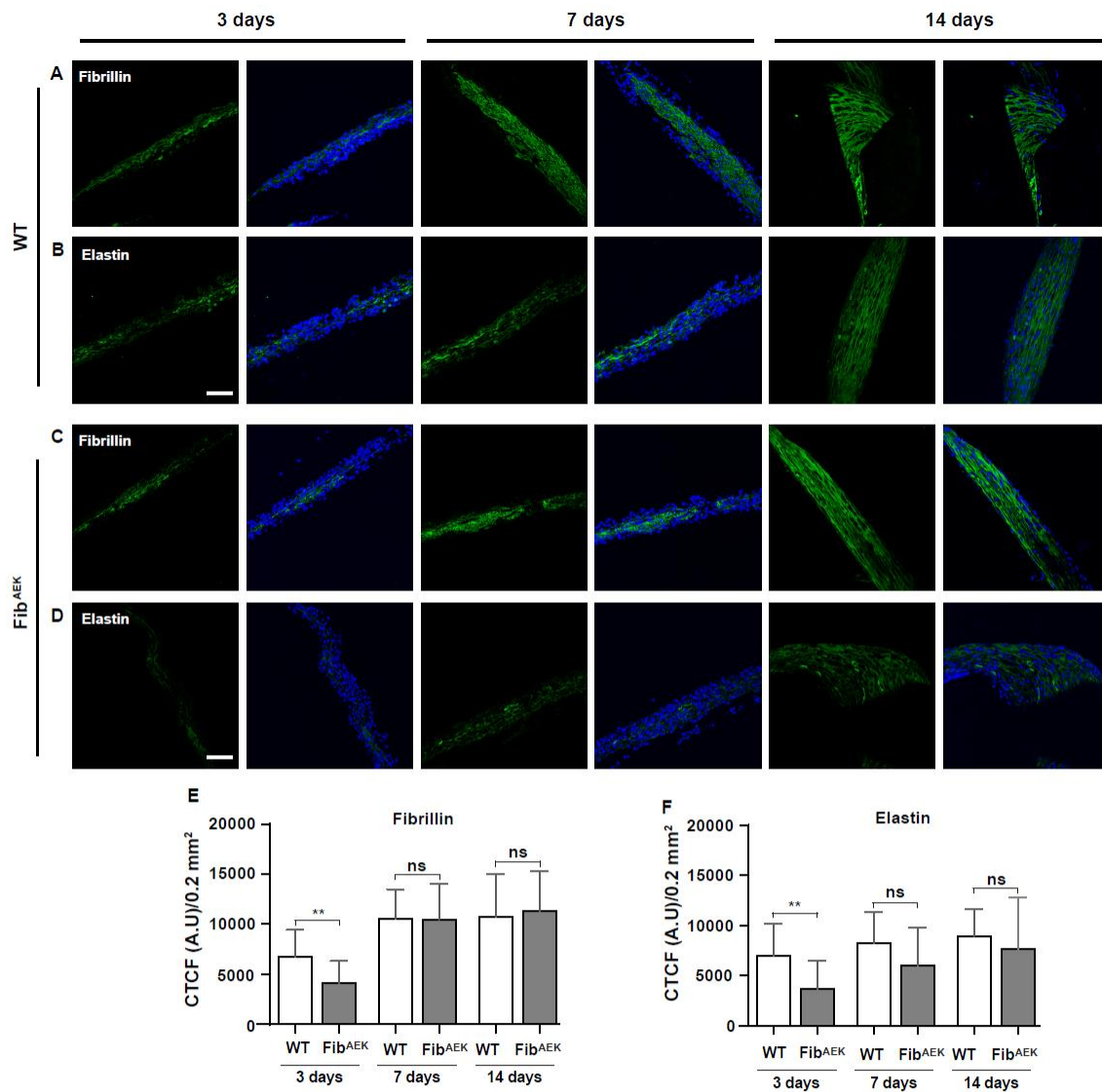
**Supplemental figure 4. Effect of argatroban on the total number of cells adherent to the surface of PCTFE biomaterials implanted in WT mice.** Argatroban (9 mg/kg and 18 mg/kg) was injected i.p. for 5 days before implantation of materials and subsequently for 7 days post-surgery. Control mice were injected with PBS. The number of cells on the surface of PCTFE explants retrieved from control and argatroban-treated mice was determined by counting nuclei. Results shown are mean  $\pm$  SD from three independent experiments (6 mice per group). Mann-Whitney *U* test was used to calculate significance. ns, not significant,  $**p < .01$



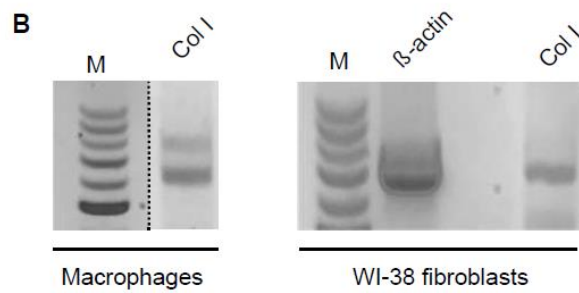
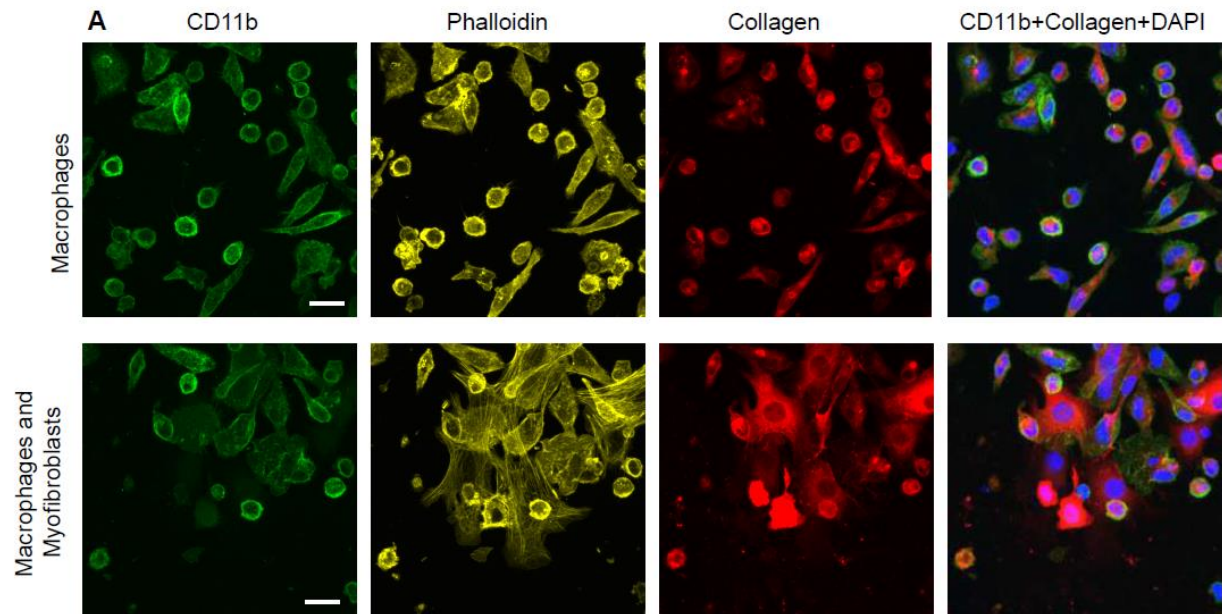
**Supplemental figure 5. The number of cells in lavage obtained from WT and FibAEK mice.** The peritoneal cells were collected from WT and FibAEK mice before the explantation of the PCTFE implants at various time points. Results shown are mean  $\pm$  S.D. of four independent experiments. n=5-6 (WT) and n=5 (FibAEK) mice. Mann-Whitney *U* test was used to calculate significance. ns, not significant,  $**p < .01$



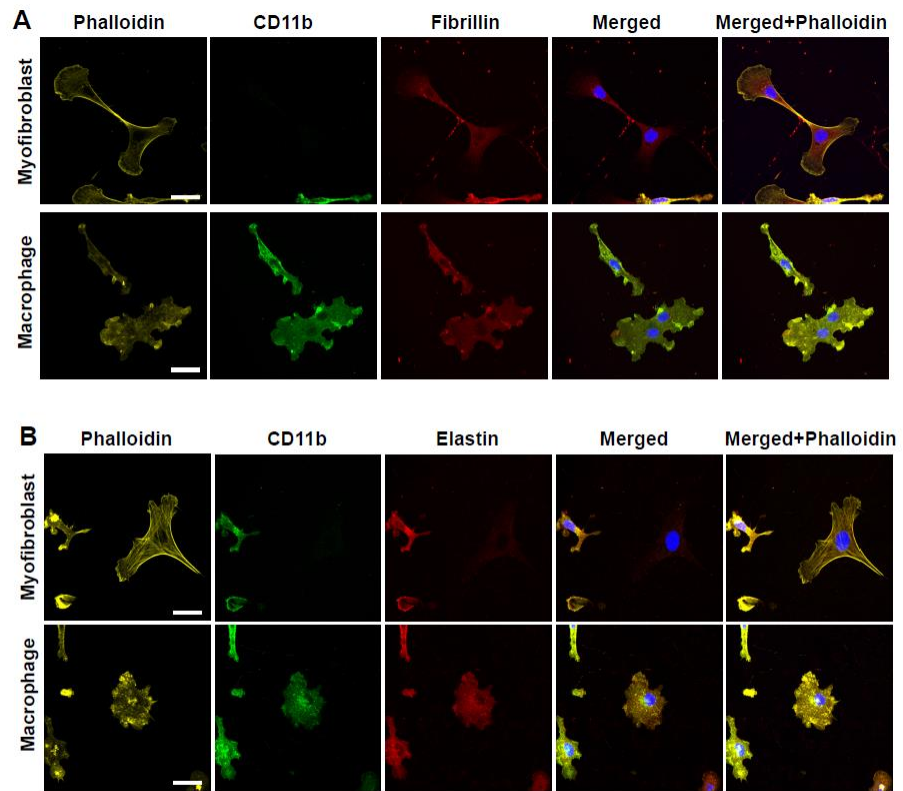
**Supplemental figure 6. Western blot analysis of fibrin(ogen) species deposited on the surface and in the capsule formed around PCTFE sections implanted into Fib<sup>AEK</sup> mice.** The specificity of antibodies recognizing total fibrinogen (anti-total Fg; 1: 50,000 dilution) and fibrinopeptide A (anti-FpA; 1:2000 dilution). **(A)** Purified mouse fibrinogen from WT and Fib<sup>AEK</sup> mice were electrophoresed on 7.5% polyacrylamide gel followed by Western blotting using fibrinogen- and FpA-specific antibodies. **(B)** Analysis of surfaces retrieved 3, 7, and 14 days after implantation. The fibrinous capsule was removed from the explanted material and exposed sections were placed into PBS containing protease inhibitors followed by the SDS-PAGE loading buffer and Western blotting using anti-total Fg, anti-FpA, and anti-fibrin antibodies. The arrowhead in the right panel shows the IgG-reactive product. The data shown are representative of samples obtained from four mice. **(C)** Analysis of fibrinogen species present in the capsule formed at different time points



**Supplemental figure 7. Deposition of fibrillin and elastin in the capsule formed around the implants in WT and Fib<sup>AEK</sup> mice.** PCTFE sections were implanted in WT and Fib<sup>AEK</sup> mice for 3, 7, and 14 days and the capsules formed were analyzed for the presence of fibrillin and elastin. (A and C) Representative immunofluorescence images of the samples incubated with antibodies that recognize fibrillin. (B and D) Representative immunofluorescence images of the samples incubated with antibodies that recognize elastin are shown. The scale bars are 50  $\mu$ m. (E and F) Quantification of fluorescence intensities of images of fibrillin and elastin deposition. Results shown are mean  $\pm$  S.D. from the areas of 0.2 mm<sup>2</sup>; n=100 for each sample. Two-tailed t-test was used to calculate significance. ns, not significant, \*\*p < .01



**Supplemental figure 8. Detection of collagen expression in macrophages isolated from the fibrous capsule.** (A) PCTFE sections were implanted in WT mice for 7 days and the cells in the capsule were isolated as described in Materials and Methods. The cells were allowed to adhere to the surface of a FluoroDish, fixed and incubated with anti-CD11b mAb M1/70 and anti-collagen polyclonal antibodies followed by Alexa Fluor 488- and Alexa Fluor 647-conjugated secondary antibodies. Cells also were stained with Alexa Fluor 568-conjugated phalloidin and DAPI. The scale bar is 15  $\mu$ m. (B) Detection of mRNA for collagen I in macrophages isolated from the capsule using RT-PCR. PCTFE sections were implanted in WT mice for 14 days and the cells in the capsule were isolated as described in Materials and Methods. Macrophages were separated from fibroblasts using magnetic beads. The PCR analysis was performed as described in Materials and Methods. WI-38 fibroblasts served as a control



**Supplemental figure 9. Macrophages express fibrillin (A) and elastin (B).** Cells isolated from a 14-day capsule formed in WT mice were allowed to adhere to the surface of a FluoroDish, fixed, and incubated with primary antibodies (anti-CD11b mAb M1/70, anti-fibrillin, and anti-elastin) followed by a secondary antibody. The scale bar is 15  $\mu$ m.